VICTORIA UNIVERSITY OF
WELLINGTON
TE HERENGA WAKA

Ultrafast refractive index change of novel semiconductor materials measured by frequency domain interferometry

---

A thesis

submitted in fulfillment of the
requirements for the degree of

Doctor of Philosophy
in
Physics

Author :	Ronnie R. Tamming
Supervisor :	Justin M. Hodgkiss
Second Supervisor :	Franck Natali

Wellington, New Zealand, September 2021

Ultrafast refractive index change of novel semiconductor materials measured by frequency domain interferometry

Ronnie R. Tamming

School of Chemical and Physical Sciences
Victory University of Wellington

September 2, 2021

Abstract

Ultrafast Transient Absorption Spectroscopy is a powerful tool to reveal excited state dynamics and semiconductor photophysics of semiconducting materials on femtosecond (10^{-15} s) timescales, including carrier recombination, hot carrier cooling, bandgap renormalisation and charge transfer. This technique uses a pump pulse to excite electrons within a material into a higher energy state and measures the state of the material by way of transmission of a probe pulse. This has provided insight into the photoexcitation and charge carrier dynamics of a broad range of materials such as organic semiconductors and halide perovskite materials.

This technique, however, faces two major obstacles. The first obstacle is the inability to distinguish the effects of the excited state absorption and reflection on the transmission of a material. With Transient Absorption measurements, the assumption is made that the change in transmission is the result of the imaginary part of the refractive index alone and does not consider the effect of the real part of the refractive index, which relates to the reflection. This is not an issue for materials with a low real refractive index, however, reflection effects can create significant artefacts on the Transient Absorption signal for materials with a high refractive index, such as perovskite materials. Attempts have been made to measure the excited state refractive index, however, these techniques are model dependent and therefore may not reflect the true excited state refractive index.

The second obstacle is the different requirements in spectrum and pulse energy for the pump and probe pulses used in this experiment. This results in the use of a combination of light sources, such as bulk supercontinuum generation, (Non)collinear Optical Parametric Amplifiers, and/or nonlinear optical fibres to generate these distinct pump and probe pulses. The use of multiple light sources, each with their own multitude of optical components, add to the complexity of the transient absorption spectroscopy system. In this thesis, we address these problems by implementing a Frequency Domain Interferometry system and a Multiple Plate Compression light source.

Firstly, the Frequency Domain Interferometer based on the Michelson interferometer is implemented in an existing Transient Absorption spectrometer. This is discussed in chapter 3, where this system is used to measure the optically induced change of the real part of the refractive index of $CsPbBr_3$ perovskite. From this, the excited state extinction spectrum is accessed, which provides valuable information regarding the suspected reflection artefacts observed in the Transient Absorption signal of this material.

Secondly, the Multiple Plate Compression lightsource is implemented in a Transient Absorption spectrometer in chapter 4. The Multiple Plate Compression is a novel light source capable of generating intense, stable, temporally compressed and spectrally broadband pulses, but has never been applied in the field of ultrafast spectroscopy before. The shot-to-shot stability and spectra of the pulses generated by two multiple plate compression systems are analysed. The Multiple Plate Compression Transient Absorption spectrometer is used on $MAPbI_3$ perovskite to demonstrate the application of this light source in ultrafast spectroscopy.

Finally, in chapter 5, the Multiple Plate Compression is used as a single light source for an improved Frequency Domain Interferometer system, based on the Sagnac interferometer. This technique is applied to obtain the optically induced change of the real part of the refractive index of pentacene. These results are then compared to the refractive index change obtained by a novel differential dielectric functions model.

Understanding of the complex refractive index change of materials has great implications for future optoelectronic device architecture. The analysis of the pulses generated by the multiple plate compression show that it is an excellent light source in the field of ultrafast Transient Absorption Spectroscopy. This paves the road for the implementation of this system as a light source in other spectroscopic techniques such as 2-Dimensional Electronic Spectroscopy and Impulsive Stimulated Raman Spectroscopy.

List of Publications

The contents of this thesis have resulted in the following publications:

1. **Ultrafast Spectrally Resolved Photoinduced Complex Refractive Index Changes in $CsPbBr_3$ Perovskites**, *Ronnie R. Tamming**, Justinas Butkus**, Michael B. Price, Parth Vashishtha, Shyamal K. K. Prasad, Jonathan E. Halpert, Kai Chen, and Justin M. Hodgkiss* - ACS Photonics 2019, 6, 2, 345-350
2. **Multiple-Plate Compression used in Transient Absorption Spectroscopy**, in 14th Pacific Rim Conference on Lasers and Electro-Optics (CLEO PR 2020), *R. R. Tamming, C. Lin, K. Chen, C. Lu, J. M. Hodgkiss, and S. Yang* - OSA Technical Digest (Optical Society of America, 2020), paper $C6B_4$
3. **Single 3.3 fs multiple plate compression light source in ultrafast transient absorption spectroscopy**, *Tamming, R.R., Lin, CY., Hodgkiss, J.M., Yang, SD., Chen, K., Lu, CH.* Sci Rep 11, 12847 (2021).

Other published research:

1. **Bandgap Control in Two-Dimensional Semiconductors via Coherent Doping of Plasmonic Hot Electrons**, *Yu-Hui Chen**, *Ronnie R. Tamming**, *Kai Chen, Zhepeng Zhang, Justin M. Hodgkiss, Richard J. Blaikie, Boyang Ding, and Min Qiu* Nat Commun 12, 4332 (2021).

---

[*] Both authors contributed equally to this work.

Acknowledgements

First of all, thank you Professor Justin Hodgkiss for giving me the opportunity to follow my passion and extend my knowledge in your group. Thank you for your guidance during this research adventure. I would like to thank Associate Professor Franck Natali for being my secondary supervisor.

I'm grateful for the MacDiarmid Institute for Advanced Materials and Nanotechnology for funding this research and the Victoria University of Wellington for providing state of the art research facilities.

Next I would like to thank everyone within the research group, in particular the postdocs, Dr. Kai Chen, Dr. Nicholas Monahan, Dr. Michael Price, Dr. Paul Hume, and Dr. Karen Thorn for the countless hours of discussions. Furthermore, I'd like to thank the other (former) students of the group, Dr. Justinas Butkus, Dr. Shreelakshmi Sandrabose, Dr. Silvina Pugliese, Aleksandra Ilina, Isabella Wagner, Clément Sester, Aleksa Djorovic and Sai Murali, for creating a fruitful research environment.

The next group of people I would like to thank are my close collaborators. Great thanks to Professor Shang-Da Yang, Sunny (Chao-Yang Lin) and Frank (Dr Chih-Hsuan Lu) for welcoming me with open arms in their lab and hosting me in Taiwan. It has been an amazing and precious time of my research during which I learned valuable research skills. Also great thanks to Arjun Ashoka for arranging the pentacene samples and providing the corresponding modelling data, and Dr. Parth Vashishtha for providing the perovskite samples.

And last but definitely not least, I would like to thank my family, both in the Netherlands and New Zealand, for their limitless support. To my father, Roel, who always believed in me with all of my endeavours, know that you will always be in

my heart. I would like to thank my mother and her partner, Jannie and Rob, and my siblings and their partners, René and Alexandra, Ingrid and Thijmen, for being there for me and supporting me in my journey. I'm also grateful for my nephew and nieces, Menno, Janouk and Jessie who all put a smile on my face every time I see them. I would like to thank my partner, Karen Thorn, her kids, Arthur, Leonard and Cassidy, and cats, Put and Boris, for their support and giving me a place in New Zealand that I call home.

Table of Contents

List of Figures

List of Tables

List of Abbreviations

(N)OPA (Noncolinear) Optical Parametric Amplifier.

BGR Bandgap Renormalization.

$CsPbBr_3$ Caesium Lead Bromide.

DOS Density of States.

FDI Frequency Domain Interferometry.
FROG Frequency-Resolved Optical Gating.
FWHM Full Width at Half Maximum.

GDD Group Delay Dispersion.
GSB Ground State Bleach.
GVD Group Velocity Dispersion.

HOMO Highest Occupied Molecular Orbital.

IRF Instrument Response Function.

KK Kramers-Kronig.

LUMO Lowest Unoccupied Molecular Orbital.

$MAPbI_3$ Methylammonium Lead Iodide.
MPC Multiple Plate Compression.

OPV Organic Photovoltaic.

PG-FROG Polarisation-Gated - Frequency-Resolved Optical Gating.
PIA Photoinduced Absorption.

TA Transient Absorption.
TAS Transient Absorption Spectroscopy.

Chapter 1

Introduction

1.1 Research motivation

The current energy demand is at an all time high and the projected increase of earth's human population, and the increase of the living standards in developing countries, will push the total energy consumption to even higher levels[1,2]. These developments result in an expected increase in energy demand of 28 % by 2040[3].

Currently, most of the energy demand is supplied for by burning fossil fuels such as coal, gas and oil[2]. Not only is this a non-renewable source of energy with a limited supply, but it is also the main contributor of greenhouse gasses[4]. These greenhouse gasses lead to climate change which results in the sea level rise and drastically changing weather conditions[5]. To avoid the severe consequences of climate change, 196 parties have signed the Paris agreement in which they promise to reduce greenhouse gas emissions to prevent the earth from warming more than 2 °C[6]. The reduction of energy consumption and the transition from fossil fuels to renewable energy sources are critical steps to achieve this goal.

To meet the increasing energy demand, novel renewable techniques are required to increase energy production or reduce energy consumption. The demand for these developments is further driven by the required reduction of the amount of greenhouse gasses emitted by burning fossil fuels to meet our current energy demand.

Semiconductor materials play an important role in this energy transition from fossil fuels to renewable energy. These materials are at the heart of devices such as solar cells, light-emitting diodes and computers. Traditional inorganic semiconductors, such as gallium arsenide and silicon, have been essential for the information society of present day and are the driving force between renewable energy production with solar cells. These materials, however, require complex fabrication techniques at high temperatures which results in large carbon emissions and high production costs[7].

Besides this, these materials are reaching their limits in power conversion efficiency, that is the available light to obtained energy efficiency, after decades of research[8].

Two new classes of semiconducting materials, Organic Photovoltaic (OPV) and photovoltaic perovskite materials, have raised a lot of interest over the past decade due to their high power conversion efficiency[9,10]. Single cell solar panels based on perovskite materials have increased their power conversion efficiency from 3.8 % in 2009 to over 25 % in just over a decade while organic semiconductor solar cells have a current record of 18.2 %[11,12]. These efficiencies are comparable to that of the single cell solar cells based on conventional gallium arsenide or silicon semiconductors which have been researched for over six decades[13,14].

Both of these materials have significant benefits over the conventional inorganic semiconductor materials. The absorption and emission spectra are tunable by adjusting the composition and/or dimensionality which allows for the use in specific light absorbers and tunable light-emitting diodes[15–19]. They are solution processible at room temperature[20–22], flexible[23,24], scalable for mass production[25], and the raw resources and processing steps are cheap[22,26].

Material knowledge gap

It is important to understand the chemical and physical properties of these novel photovoltaic materials in order to accurately measure and find ways to improve on their photovoltaic functions. One such measure is the real refractive index, n, or more specifically for this research, the excited state refractive index. This change in real refractive index has great implications regarding the design of device structures such as phase modulators and semiconductor laser cavities, and excited state transmission signal interpretation as it is directly related to the change in reflection[27–29]. The excited state refractive index of these classes of materials, however, have yet to be directly measured. Attempts, so far, have been made experimentally via transient reflection spectroscopy and ultrafast ellipsometry, but these techniques are model dependent, introducing uncertainties in the obtained excited state refractive index[29–31]. The ability to directly measure the excited state refractive index of semiconducting materials is highly motivating, as it could improve the understanding of the excited state dynamics. As the excited state dynamics reveal the loss and photon-to-energy conversion mechanisms present in these materials, proper interpretation of the obtained signals is essential. Also, the change of refractive index of a material might lead to unwanted optical path length changes and reflection effects. Therefore, understanding the complex refractive index will improve the function and design of the photovoltaic materials in real-life devices. In this research project, we discuss two configurations of an ultrafast spectroscopic technique that can directly measure the refractive index change of these semiconducting materials.

1.2 Method selection

The photoelectric conversion efficiencies, that is the conversion efficiency of light to usable energy or vice versa, of devices made with semiconducting materials can be improved if we understand the electronic response of these materials after photoexcitation. A widely used method of obtaining the photoresponse on a femtosecond timescale is Transient Absorption Spectroscopy (TAS). This technique uses optical pump and probe pulses to excite the sample and measure the excited state by the intensity of the transmission of the probe. This has provided insights in the excited state dynamics and relaxation mechanisms of OPV and halide perovskite materials, such as hot carrier cooling, exciton/charge recombination, bandgap renormalisation, singlet fission and charge transfer[29,32,33].

The assumption made with TAS is that the transmission of the probe is only dependent on the imaginary part of the refractive index, however, the spectrum of the probe pulse is modulated by the sample by both the real and imaginary part of the refractive index[34]. This means that photoinduced reflection effects are neglected in this type of experiment. This assumption is valid for materials with a low refractive index, however, this may not be valid for materials with a high refractive index, such as the next generation OPV and perovskite materials, where reflection effects might play a significant role[29,35].

To investigate the impact of the refractive index on the Transient Absorption (TA) spectrum, we have applied two configurations of the Frequency Domain Interferometry (FDI) technique[36,37]. This technique uses a broadband reference-probe pulse pair, with a fixed time delay, to obtain an interference pattern in the frequency domain. The pump pulse induces a change in the sample's real part of the refractive index, as observed only by the probe pulse, resulting in a change of optical path length, and thus time delay between the pulses. This is observed as a shift of the interference pattern, which is a direct result of the change in the relative phase between the reference and probe pulse.

The pulse requirements for both TAS and FDI experiments are a stable broadband (reference and) probe pulse(s), and a pump pulse with two opposing conditions, depending on the desired information[38]. These conditions are an intense narrow-band pump to resonate with specific energy levels within a sample, or a temporally compressed broadband pulse to observe kinetics with a high temporal resolution[39]. The currently available light sources, however, are limited to bulk supercontinuum, (Noncolinear) Optical Parametric Amplifier ((N)OPA) and nonlinear optical fibres, which each have limitations in terms of their experimental implementation. Bulk supercontinuum generates a broad spectrum, however, destructive nonlinear processes limits the achievable intensity of the pulses and the nonlinear crystal generates chirp within the supercontinuum, resulting in ps pulse durations[40]. (N)OPAs, on the other hand, can generate stable and intense pulses which are limited in the bandwidth due to phase matching conditions[41,42]. Nonlinear optical fibres can generate intense and broadband pulses, but applications are limited due to their sensitive input coupling and therefore low stability[43]. These individual limitations result in a multitude of light sources required for pump-probe spectroscopy systems.

Recently, the Multiple Plate Compression (MPC) has been introduced, providing us with a new light source[44]. The MPC uses a series of nonlinear crystal plates near a focal point of the beam to obtain a wave guiding effect and high intensities so that nonlinear broadening of the spectrum can occur. This system can generate intense broadband pulses with high stability. These pulses allow for easy temporal compression, down to the single cycle, due to the small travel distance through the nonlinear medium[45].

Technique knowledge gap

In TAS and FDI, various laser pulses, a pump, reference and probe, each with their own spectral and temporal attributes must be generated from a single femtosecond light source. The limitations of the previously available light sources demand a combination of light sources to generate the various pulses with differing requirements. The MPC is a novel light source that successfully generates intense, stable, broadband and temporally compressible pulses, meeting the requirements for all pump, reference and probe pulses, using a single straightforward optical layout. This light source, however, has never been used before in the field of ultrafast spectroscopy. This research presents the first application of the MPC in ultrafast spectroscopy by using it as a single light source for TAS and FDI.

1.3 Thesis outline

This research report is laid out as follows:

- The remainder of this chapter provides an introduction to semiconductors and describes the properties of the photovoltaic perovskite and OPV materials that are researched in this thesis.
- Chapter 2 provides the optical background for the techniques applied in this thesis. The theory of nonlinear optics and the ultrafast spectroscopic techniques used for this research are explained.
- Chapter 3 discusses the ultrafast refractive index change of Caesium Lead Bromide ($CsPbBr_3$) perovskite, as measured using the FDI technique. The obtained results are verified by retrieving the TA signal from the refractive index change and comparing these results to the spectrum from a TA measurement. Finally, the implications of the refractive index change in device architecture is discussed.
- Chapter 4 discusses the pulses generated by two different configurations of the MPC. These pulses are, for the first time, analysed on a shot-to-shot level to assess the application of this light source in the field of ultrafast spectroscopy.

After analysing the generated pulses, they have been used in TAS to showcase the application of this light source in the field of ultrafast pump-probe spectroscopy.

- Chapter 5 discusses the refractive index change of pentacene, as measured by an improved FDI technique. This technique uses the MPC as a single light source for the pump, reference and probe pulses, and an FDI system based on a Sagnac interferometer. The results are compared to the results of a novel differential dielectric functions model, capable of extracting the refractive index change from the TA and steady-state transmission signal.
- Chapter 6 summarises the results found during this research and provides an outlook for the MPC and FDI techniques.

1.4 Semiconductor physics

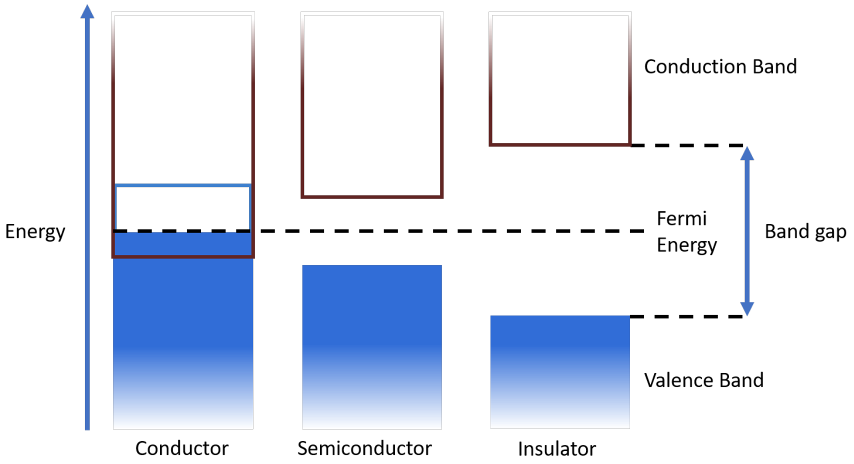

Figure 1.1: Representation of the band structures of a conductor, semiconductor and insulator. The blue band represents the filled states while the white band represents the empty states at zero Kelvin. The conductor shows that the Fermi level lies within an energy band. The semiconductor and insulator has the Fermi level between bands so that the states of the valence band is fully filled with electrons, and the conduction band is completely empty, with the size of the bandgap as a difference between these two materials.

All materials can generally be classified into three classes of materials depending on their electrical properties. These classes are metals, semiconductors and insulators, where the class of a material is determined by the electronic band structure of the material. The band structure of a material is the result of the broadening of the discrete energy levels of each atom or molecule within a lattice, due to the interaction between the surrounding atoms or molecules[46,47]. This is a result from the interaction of the electrons within the orbits of the atoms or molecules, lowering or increasing the energy of the distinct energy level. When an ensemble of atoms or molecules are placed close together, a large range of increased and decreased energy states are available within the material. A simplified depiction of these band structures is shown in figure 1.1[48]. These band structures show the available electron states within the material. At zero Kelvin, the electrons will occupy the lowest possible states, however, the Pauli exclusion principle prevents them to occupying only the lowest available state. Therefore, the electrons have to fill the energy states up to a certain level, which is defined by the Fermi energy.

For conductors, this Fermi energy lies within one of the electronic bands of a material, which results in a partially filled band. Therefore, the electrons are free to move through the lattice, resulting in the conductive property of conductors[48]. For semiconductors and insulators, this Fermi energy lies between two energy bands, which is a region without available electron states. This results in a fully occupied valence band and an empty conduction band, preventing the electrons from freely moving through the material. Both of these materials therefore act as an insulator at zero Kelvin. However, the difference between the semiconductor and insulator is the size of the bandgap, which is smaller for semiconductors so that it has a conductivity which is strongly dependent on temperature.

When the temperature of a material is increased, electrons will use the available energy from the environment to occupy states above the Fermi energy. The temperature dependent distribution of electrons is given by the Fermi-Dirac distribution:

$$f(E) = \frac{1}{\exp\left[(E - E_F)/k_B T\right] + 1}, \tag{1.1}$$

where E is the energy of electron states, E_F is the Fermi energy, k_B is the Boltzmann

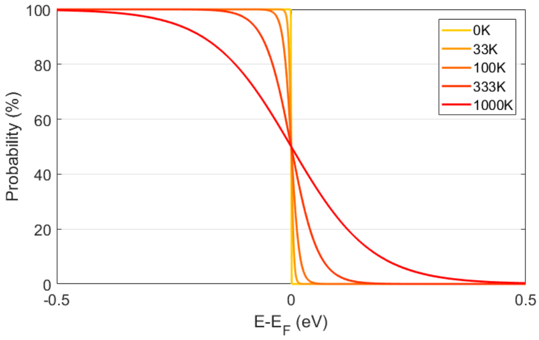

Figure 1.2: Fermi-Dirac distribution of electrons at various temperatures according to equation 1.1, with the energy scale set relative to the Fermi energy. This shows that the probability of carriers above the Fermi level increases with increasing temperature.

constant and T is the temperature of the electrons[49]. This distribution is shown in figure 1.2 for various temperatures and shows that carriers have a nonzero probability to occupy states above the Fermi energy. The smaller bandgap of semiconductors allows for the electrons to occupy states within the conduction band when the temperature is increased. These higher energy electrons leave holes, which are empty states, in the valence band. This enables free movement of the electrons and holes in the conduction and valence band respectively, resulting in a conductive behaviour.

1.5 Metal halide perovskites

Perovskite crystal structure

Perovskite materials are a class of materials with the perovskite atomic structure. The first discovery of this particular structure was in a calcium titanium oxide crystal ($CaTiO_3$), discovered in 1839. The generalised form for the perovskite structure is ABX_3. For the semiconducting metal halide perovskites, the A stands for a monovalent cation, B is a divalent metal cation and X is a halogen anion[50]. This structure has its A cation enclosed in corner sharing BX_6 cages as shown in figure 1.3 for the cubic perovskite structure. To obtain a stable perovskite structure, two size depen-

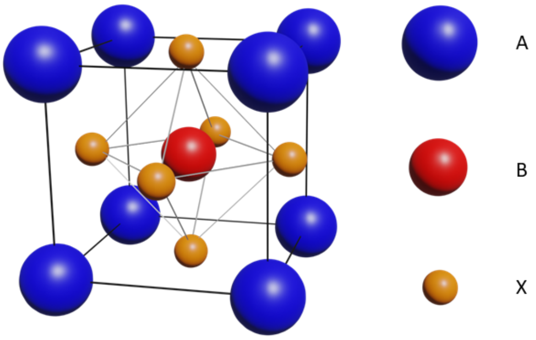

Figure 1.3: Cubic Perovskite crystal structure. Here, A represents a monovalent cation, B represents a divalent cation and X represents a monovalent anion.

dent empirical conditions are found which have to be fulfilled. These conditions lay boundaries on the Goldschmidt tolerance factor t and the octahedral factor μ and are given by

$$0.85 < t = \frac{r_A + r_X}{\sqrt{2}(r_B + r_X)} < 1.11, \tag{1.2}$$

and

$$0.442 < \mu = \frac{r_B}{r_X} < 0.895, \tag{1.3}$$

with r_A, r_B and r_X being the ionic radii for the A and B cations and the X anion respectively[51]. These conditions are a result of the physical constraints of the sizes of the used cations and ions to form a stable perovskite structure. Note that not all materials that conform to these conditions will arrange in the perovskite structure.

The choice for the B site cation is generally the large lead ion (Pb^{2+}) due to its higher stability and efficiency. However, environmental and health concerns are pushing for lead-free alternatives, such as tin (Sn^{2+}). The choice of these atoms results in a minimum size restriction to the A cation and therefore, the only suited single atom is caesium (Cs^{+}). Other options are the organic ions Methylammonium and Formamidinium. The X-site can be occupied by either iodide (I^{-}), bromide

(Br^-) or chloride (Cl^-). By choosing different cations and anions, or creating mixed compounds, the properties of the perovskite can be tuned[52,53].

Besides the composition, the dimensionality of the perovskites proves to be another great pathway to tune the properties[53]. Perovskite quantum dots, wires and platelets function in the quantum confinement regime. This confinement strongly influences the bandgap, exciton binding energy, carrier recombination rate and stability, providing great tunability of this material[17,54–56].

The tunability of these materials promise a bright future for these materials to be used in the next generation photovoltaic components such as solar panels, LEDs and lasers. However, stability issues have so far prevented commercial application of these materials[57]. The perovskites are bound together via ionic bonds, which partly explains the ease of the production of high quality crystals and high performance[58]. On the other hand, this also results in low decomposition temperatures, degrading the perovskite at room temperature. This creates an active field, preventing degradation via encapsulating and surface engineering[59,60].

Photovoltaic implications

The metal halide perovskites have an electronic structure with a bandgap in the eV range, with the Fermi energy between the valence and conduction band[48]. This results in a high electrical resistivity at room temperature, but a strong dependence on temperature or photoexcitation. The electronic structure for Methylammonium Lead Iodide ($MAPbI_3$) is given in figure 1.4 as obtained by density functional theory[61]. The electronic response is dominated by the valence band maximum and conduction band minimum, showing a bandgap of about 1.68 eV, being in agreement with absorption spectra[62].

The band structure around the bandgap is approximated by parabolic bands. It is still debated whether this bandgap is direct or indirect of nature. Experimental and numerical results have shown direct bandgap behaviour[63,64]. However, Rashba splitting effects might cause the bandgap to become indirect[65,66]. Wang *et al.*[67] proposed an intrinsic indirect bandgap via the Rashba splitting which turns to a direct bandgap under pressure. Local stresses in the lattice might explain the direct

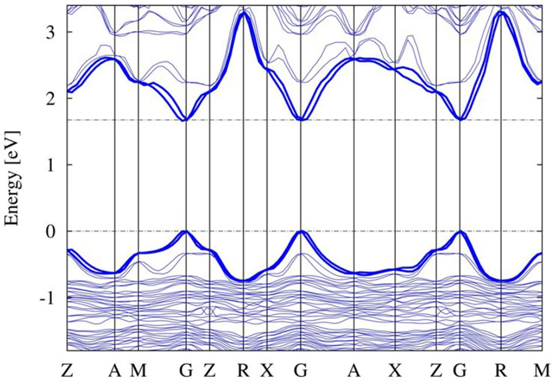

Figure 1.4: Electronic band structure for $MAPbI_3$ perovskite, obtained via relativistic density functional theory calculations. Reprinted with permission from Umari *et al.*[61], (2014) Springer Nature.

bandgap behaviour even while an indirect band is predicted. However, others claim that the splitting is intrinsically too small to have a significant effect on the band structure[68].

To obtain functional devices such as a solar cell or an emitting diode, the perovskite needs to be sandwiched between layers of other materials to extract the generated electrons and holes. An example is the device is shown in figure 1.5, from Kim *et al.*, who have deposited the $MAPbI_3$ perovskite between a layer of titainum dioxide (TiO_2) and 2,2′,7,7′-tetrakis(N,N-di-p-methoxyphenyl-amine)9,9′- spirobifluorene (spiro-MeOTAD) to create a solar cell structure[63]. The TiO_2, with the conduction band slightly below the conduction band of perovskite, functions here as an electron extractor (acceptor). Spiro-MeOTAD is an organic semiconductor and has the Highest Occupied Molecular Orbital (HOMO) above the valence band of the perovskite and therefore acts as the hole extractor (donor). This simple device structure has achieved a photocell efficiency of 9.7%.

Excited state dynamics

After photoexcitation of these materials, the electrons will go into an excited state in the conduction band and create holes in the valence band. These photogenerated electron-hole pairs can follow different recombination pathways as depicted

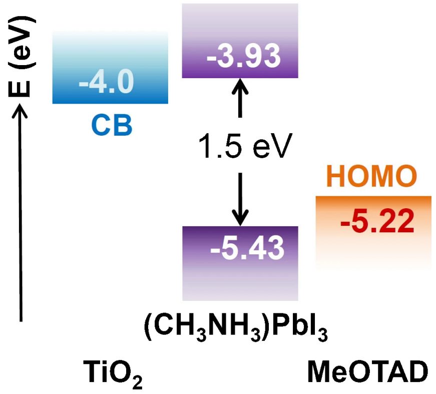

Figure 1.5: Example of a basic solar cell device band structure of MAPbI$_3$. The TiO$_2$ acts as an electron extraction layer (acceptor) while the spiro-MeOTAD acts as an hole extraction (donor) layer. This device structure achieved an photocell efficiency of 9.7 %. Reprinted with permission from Kim *et al.*[63], (2012) Springer Nature.

in figure 1.6. First, the electron-hole pair will either form an exciton, which is a electron-hole pair bound together via Coulomb interaction[69], or become free carriers depending on the composition of the perovskite. Which of the two excited states is more dominant is dependent on the ratio between the material specific exciton binding energy E_b and the lattice temperature where the binding energy is determined by the strength dielectric screening. This dielectric screening dampens the electric field strength of charge carriers, reducing the Coulomb binding between the electron and hole. In the case of $E_b < k_B T$, the available thermal energy in the system is larger than the binding energy and the excited carriers will form free charges. For bulk MAPbI$_3$, a wide range of values for E_b is found between 2 to 62 meV[70]. However, time-resolved spectroscopic and high-magnetic field experiments have shown that the generated photoexcited carriers mostly form free carriers at room temperature[71–74]. By changing the compound and dimension of the perovskite, the binding energy can be enhanced so that excitons are created instead[75].

The total charge carrier recombination dynamics is given by the rate equation

$$\frac{dn}{dt} = G - k_1 n - k_2 n^2 - k_3 n^3, \tag{1.4}$$

where n is the carrier density, G is the charge-density generation rate and k$_1$, k$_2$

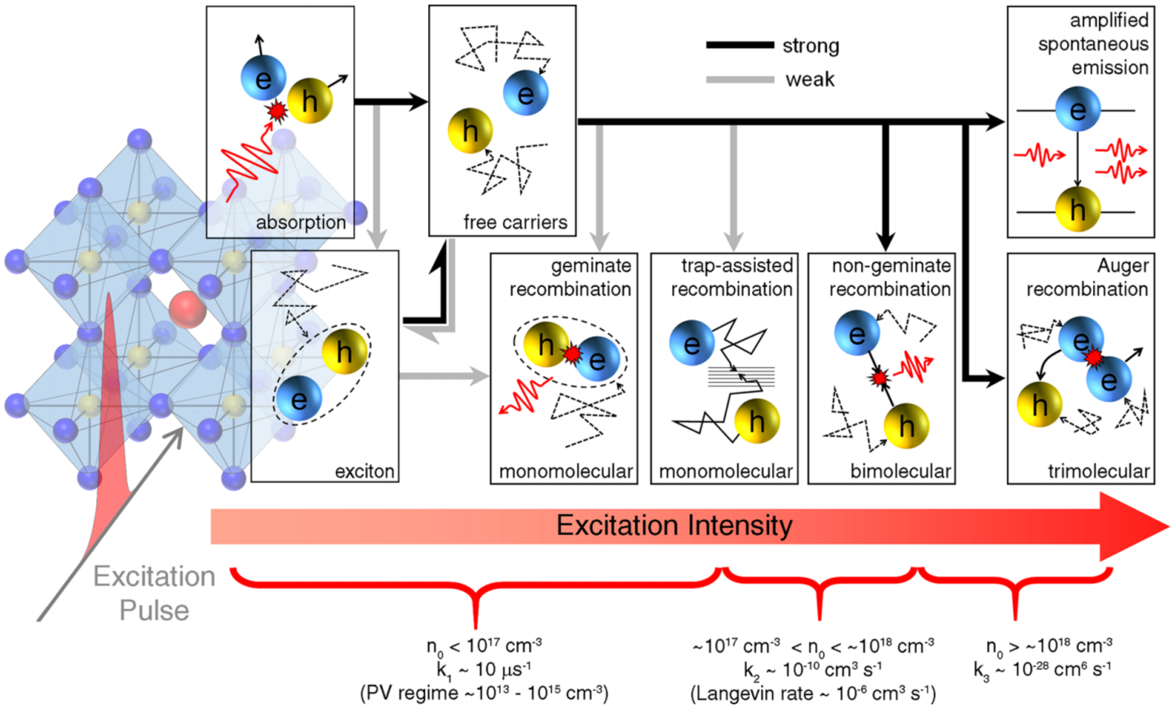

Figure 1.6: Different recombination pathways for $MAPbI_3$ perovskite after photoexcitation for different excitation intensities and their corresponding recombination coefficients. The weak and strong pathways are indicated by a grey and black arrow respectively. Reprinted with permission from Sum *et al.*[76]. Copyright 2016 American Chemical Society.

and k_3 are the monomolecular, bimolecular and trimolecular recombination rate constants respectively[77,78]. These different recombination pathways have different carrier concentration dependencies and will be briefly discussed.

Monomolecular recombination is the recombination of electron/hole pairs or excitons originating from a single excitation event and therefore has a recombination rate which is independent of carrier concentration. This recombination rate in these type of materials is very low[79]. This is explained by the free carrier behaviour and the long carrier diffusion length in this material, which enables the charges to spatially separate. Trap-assisted recombination is enabled by impurities and defects in the crystal structure. These defects, such as grain boundaries or native point defects (vacancies, interstitials, and antisites) create so called deep states[80]. These are energy levels within the bandgap trapping the charges, creating a pathway for non-radiative decay.

Because of the low exciton binding energy, the geminate recombination rate is very low and the monomolecular recombination in these materials most likely originates from trap-assisted recombination. The trap concentration is strongly dependent on the fabrication and therefore a broad range of rate constants, k_1, is found. Values are found between 1×10^6 and 250×10^6 s^{-1} for hybrid lead halide perovskites[70,77].

The bimolecular recombination is the recombination of two free carriers of opposite charge and is associated with the emission of a photon. This recombination rate is strongly dependent on the carrier density and is less dependent on the material processing. This results in a more consistent recombination rate constant, k_2, between various measurements than for geminate recombination. The bimolecular recombination rate constant for halide perovskites vary between 0.6×10^{-10} and 14×10^{-10} cm^3 s^{-1} at room temperatures, which compares to 4×10^{-10} cm^3 s^{-1} found for GaAs[77].

At higher intensities, trimolecular recombination (Auger recombination) becomes more dominant. Auger recombination is the recombination involving three carriers, two electrons (holes) and a hole (electron). By the recombination event of the hole and electron, the additional electron (hole) receives the released energy and is excited further up (down) the conduction (valence) band. This is a strong effect for perovskites with a recombination rate constant, k_3, of 1×10^{-28} cm^6 s^{-1}, which is a factor 25 higher compared to GaAs[77]. This recombination is a non-emissive decay pathway and the re-excitation of the carriers is suspected to be partially responsible for the long hot carrier lifetime[81].

Perovskite materials can also show amplified spontaneous emission[82,83]. This occurs at high fluence excitation, that is, when the free carrier density is high enough for population inversion and is the same effect as lasing. However, in contrast to lasing, amplified spontaneous emission is triggered spontaneously emitted photons rather than a decay due to a external electric field. This means that the initial photon that starts the cascade of amplified spontaneous emission can be emitted in any direction and can have any polarisation[69]. The following amplification of this electric field will then follow the direction and polarisation of the initial photon.

This excitation of perovskite will result in a change of both the real and imaginary part of the refractive index, which are related to the reflection and absorption respectively[29,84]. This change in refractive index and the resulting excited state reflection effect is investigated and discussed in chapter 3.

1.6 Organic photovoltaics

Organic semiconductors

OPVs are based on semiconducting organic molecules and polymers. This group of materials consist of (hetero) aromatic ring molecular materials such as buckyballs and nanotubes and conjugated polymers[85]. All of these materials have one thing in common, which is that they contain sequential single and double bonds between the carbon atoms, that is, they form the sp^2 hybridisation. These bonds result in conjugated π-bonds which allow for electron delocalisation and thus mobility within the molecule or polymer[86,87].

Rather than having an electronic structure consisting of bands, the available electron states of organic semiconductor molecules are more discrete, as depicted in figure 1.7[86]. These available energy states of organic molecules are the result of the molecular orbitals, where the HOMO is the highest occupied state and the Lowest Unoccupied Molecular Orbital (LUMO) is the lowest unoccupied state. In the solid state, the molecules are close enough to affect their neighbouring molecular orbitals, forming Davydov splitting of the LUMO and HOMO energy bands, indicated by the multiple lines above and below the LUMO and HOMO, respectively, in figure 1.7[88]. The bandgap of an organic semiconductor is given by the energy difference between the LUMO and HOMO levels.

Pentacene

The specific OPV molecule discussed in this research report is pentacene. Pentacene is an organic molecule consisting of five fused benzene rings and the molecular structure is shown in figure 1.8a. Pentacene is an intrinsic p-type semiconductor, which means that the Fermi level is closer to the HOMO than the LUMO[89]. This

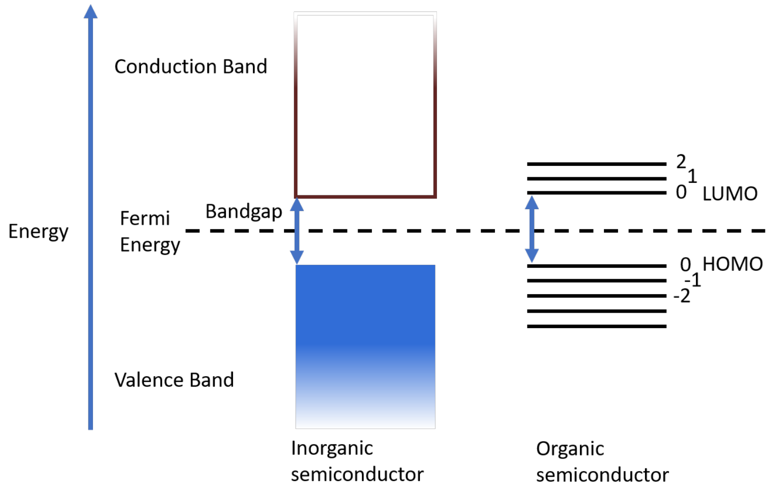

Figure 1.7: Representation of the band structure of inorganic and organic semiconductors. The inorganic semiconductor has a band structure due to the environmental interaction of each individual atom. The organic semiconductor consists of distinct energies originating from the molecular orbitals. The HOMO and LUMO represent the highest occupied and lowest unoccupied molecular orbital respectively.

material has a high charge carrier mobility with a measured hole mobility of up to 35 cm^2/V, making it an excellent candidate as a hole extraction layer[90].

The energy states of pentacene and possible transitions are shown in figure 1.8b, where S_x indicates a singlet state and T_x a triplet state[91]. These states are related to the spin of the ground state electron in the HOMO and the excited-state electron in the LUMO, where the singlet state has opposing spin and the triplet state has parallel spin of these electrons. Two electrons in their ground state (S_0) will have opposing spin due to the Pauli exclusion principle[48]. Because of the forbidden transition to the triplet state, for which the spin has to flip, the excitation of an electron only results in the excited singlet state (S_1), which can sequentially undergo relaxation to the ground state by emission of a photon, or transfer into the triplet state (T_2) via spin-orbit coupling. This intersystem crossing, however, is a slow process for isolated pentacene molecules (in a dilute solution) as this transition is spin forbidden[92]. The relaxation of T_2 to T_1 is achieved via internal conversion, where T_1 will eventually will relax back to the S_0, accompanied by another spin flip event. The TA signal of

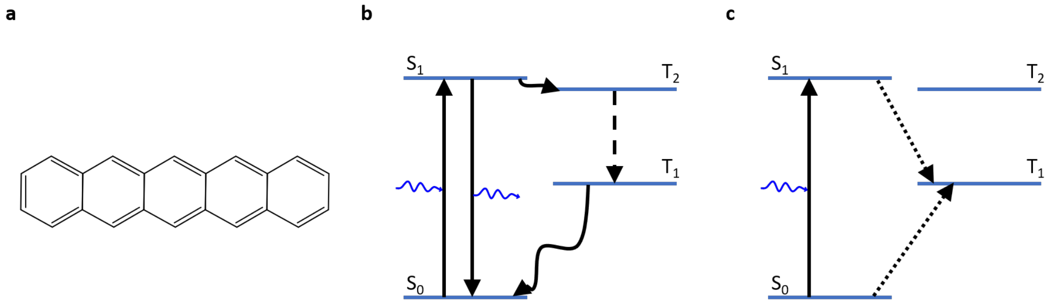

Figure 1.8: a) Chemical structure of pentacene. b) Electronic structure and possible energy transitions within pentacene. The transitions related to absorption/emission of a photon are indicated with a solid arrow, intersystem crossings with a wiggly black arrow and internal conversion with the dashed arrow. c) Diagram of singlet-exciton fission within pentacene indicated by the dotted arrow. Note that the second triplet is formed at a pentacene molecule neighbouring the initially excited molecule. Triplet-Triplet annihilation is the inverse process of singlet-exciton annihilation.

pentacene shows the same bleaching signal for the excited singlet and excited triplet states due to the depleted S_1 state and the forbidden optical transition from the S_0 to the excited triplet states[93]. Besides that, the excited singlet state can undergo relaxation via stimulated emission, which is superimposed on the TA bleach signal, making the observed TA signal difficult to interpret.

An interesting property of pentacene is the capability of singlet-exciton fission and triplet-triplet annihilation, which is the energy transfer from a single singlet (S_1) to two triplet states (T_1) and vice versa respectively[94–96]. This exchange between the singlet and triplet state is allowed as the energy level of the triplet state is similar to half that of the singlet state. The energy transitions of singlet-exciton fission are shown by the dotted lines in figure 1.8c, where the second triplet is created at a neighbouring pentacene molecule. The inverse of this transition is the triplet-triplet annihilation process. Singlet-exciton fission is both a fast and efficient pathway in this material as the generation of the two triplet states from a single singlet state can occur without a spin flip event, where two triplets with opposing spin are generated[97,98]. When the two triplets dissociate and diffuse to a donor/acceptor layer, two charges can be extracted from a single excitation event. This may help to break the Shockley-

Queisser limit, which is the calculated upper limit of the power conversion efficiency of a single active layer solar cell using the emission spectrum of the sun, where one photon is assumed to generate one electron-hole pair[99].

1.7 Conclusion

Increase of energy demand and emission of greenhouse gasses increases the need for renewable energy sources and ways to reduce energy consumption. One possible solution is to implement photovoltaic materials for solar panels and light-emitting diodes. Two new classes of materials, photovoltaic perovskite and OPV materials, have shown great promise for future implementation in these devices due to their flexibility, tunability, easy processing methods and have had a major increase in power conversion efficiencies over the last decade. However, to further improve their efficiency, it's important to understand the physical processes that occur after photoexcitation and the dependencies on the material properties. This information is often obtained via TAS where the assumption is made that the TA signal is purely a result from the change in absorption, ignoring effects from the real part of the refractive index, leading to misinterpretation of the obtained signal. In this thesis, we will discuss the FDI technique that can measure the change in the real part of the refractive index, which is directly related to the change in reflection, providing a deeper understanding of the excited state dynamics of these materials. Furthermore, the excited state refractive index has an impact on photovoltaic device design and thus understanding it will improve the efficiency of novel photovoltaic devices.

Chapter 2

Optics background and techniques

Ultrafast spectroscopy is the collective name of all spectroscopic techniques utilising femtosecond laser pulses to observe excited state dynamics on femtosecond to nanosecond timescales. Just like a stroboscope can show discrete moments of an event in an otherwise dark room on the timescale of seconds, ultrafast spectroscopists use femtosecond laser pulses to shed light on discrete moments at the femtosecond (10^{-15} s) timescales. These discrete moments are then combined to create a full image of the excitation and relaxation event of materials.

In this chapter, we discuss the relevant optical constants and their relations and the theory of nonlinear optics. Understanding the relation between optical constants is crucial for understanding the relevance of the real part of the refractive index on ultrafast spectroscopy. The nonlinear interactions discussed in this chapter are the processes that occur in solid-state supercontinuum generation, used for the probe in chapter 3, and within the MPC systems discussed in chapter 4 and used in chapter 5. After that, the ultrafast TAS and FDI techniques presented in this work are discussed as well as the relevant steps regarding data processing.

2.1 Relations between optical constants

When light encounters a medium, a couple of interactions can be observed. In linear optics, which is the conventional way of treating light-matter interactions, the light can be reflected, absorbed or transmitted[100,101]. Generally, the interaction is a combination of these three effects, resulting in

$$1 = R + A + T, \tag{2.1}$$

where R, A and T are the reflectance, absorbance and transmittance respectively. The ratio of these coefficients is determined via the wavelength dependent relative complex dielectric constant $\hat{\epsilon}(\omega)$ where the real part is related to the capability to store electrical energy while the imaginary part is related to the absorption, or damping, of the electric field. The real and imaginary part of the dielectric function, $\epsilon_1(\omega)$ and $\epsilon_2(\omega)$ respectively, are related to each other according to the Kramers-Kronig (KK) relations

$$\epsilon_1(\omega) - 1 = \frac{2}{\pi}\mathcal{P}\int_0^\infty \frac{\Omega\epsilon_2(\Omega)}{\Omega^2 - \omega^2} d\Omega, \tag{2.2}$$

which describe the response of a system after perturbation. In this equation, Ω describe all frequencies, ω is the wavelength for which the dielectric constant is calculated and $\mathcal{P}$ is the Cauchy Principal value. The real part of the dielectric constant is related to the susceptibility χ, which is proportional to the polarisability of a material via

$$\epsilon_1 = 1 + \chi. \tag{2.3}$$

To relate the dielectric constant to the reflectance, absorbance and transmittance of light in a material, it's convenient to express the dielectric constant in terms of the complex refractive index

$$\hat{n}(\omega) = n(\omega) + ik(\omega) = \sqrt{\hat{\epsilon}(\omega)}, \tag{2.4}$$

for which the assumption is made that the material is non-magnetised. This results in

$$n(\omega) = \sqrt{\frac{\sqrt{\epsilon_1^2(\omega) + \epsilon_2^2(\omega)} + \epsilon_1(\omega)}{2}} \tag{2.5}$$

and

$$k(\omega) = \sqrt{\frac{\sqrt{\epsilon_1^2(\omega) + \epsilon_2^2(\omega)} - \epsilon_1(\omega)}{2}}, \tag{2.6}$$

where ϵ_2 is the imaginary part of the dielectric constant.

At the interface of two materials, part of the light will be reflected and transmitted. The ratio between the reflectance and transmittance is given by Fresnel equations and is dependent on the real part of the refractive indices of the materials involved, n_1 and n_2, the angle of incidence, θ_i and polarisation of the light[48]. The transmittance, T, and reflectance, R, for P and S polarization are given by

$$T_P(\omega) = \frac{2n_1(\omega)\cos(\theta_i)}{n_2(\omega)\cos\theta_i + n_1\cos(\theta_t(\omega))}, \tag{2.7}$$

$$T_S(\omega) = \frac{2n_1(\omega)\cos(\theta_i)}{n_1(\omega)\cos\theta_i + n_2\cos(\theta_t(\omega))}, \tag{2.8}$$

$$R_P(\omega) = \frac{n_2(\omega)\cos(\theta_i) - n_1(\omega)\cos(\theta_t(\omega))}{n_2(\omega)\cos(\theta_i) + n_1(\omega)\cos(\theta_t(\omega))}, \tag{2.9}$$

and

$$R_S(\omega) = \frac{n_1(\omega)\cos(\theta_i) - n_2(\omega)\cos(\theta_t(\omega))}{n_1(\omega)\cos(\theta_i) + n_2(\omega)\cos(\theta_t(\omega))}, \tag{2.10}$$

where θ_t is the angle of the transmitted light, dependent on the ratio

$$\frac{n_1(\omega)}{n_2(\omega)} = \frac{\sin\theta_t(\omega)}{\sin\theta_i}. \tag{2.11}$$

This shows that the real part of the refractive index is directly related to the reflection and transmission ratio for a single boundary. In section 3.2, this is further elaborated on as two boundaries are close together, resulting in Fabry-Perot reflections.

Within the sample, only absorption plays a role. To calculate the total absorbance of a sample, we need to calculate the absorption coefficient $\alpha(\omega)$ using the complex refractive index

$$\alpha(\omega) = \frac{2\omega k(\omega)}{c}, \tag{2.12}$$

where c is the speed of light. This absorption coefficient is then used to calculate the absorption of light within the material, A, in equation 2.1, using

$$A(\omega) = 1 - \exp(\alpha(\omega)x), \tag{2.13}$$

with x being the thickness of the material.

2.2 Nonlinear optics

Linear optics is the conventional way of treating light-matter interactions[100]. This is described by the dipole moment per unit volume

$$\tilde{P}(t) = \chi^{(1)}\tilde{E}(t), \tag{2.14}$$

where $\chi^{(1)}$ is the linear susceptibility of the material and $\tilde{E}(t)$ is the time dependent optical electric field strength. The result of linear optics is that the frequency input and output is the same and that the output intensity scales with the input intensity.

Nonlinear optics, on the other hand, describes the nonlinear light-matter interactions which is a result from the physical limitation of the polarisability of a material, where the added polarisation of a material decreases with increasing electric field. It is described by a power series of the polarisation in the field strength as given by equation 2.14, resulting in

$$\begin{aligned}\tilde{P}(t) &= \chi^{(1)}\tilde{E}(t) + \chi^{(2)}\tilde{E}^2(t) + \chi^{(3)}\tilde{E}^3(t) + ... \\ &\equiv \tilde{P}^{(1)}(t) + \tilde{P}^{(2)}(t) + \tilde{P}^{(3)}(t) + ...,\end{aligned} \tag{2.15}$$

where $\chi^{(2)}$ is the second order and $\chi^{(3)}$ is the third order susceptibility and so on. Likewise, $\tilde{P}^{(1)}$ is the first order (linear) polarisation, $\tilde{P}^{(2)}$ is the second order polarisation and so on. The result of this is that new frequencies can be generated, as will be discussed in this chapter, and that the nonlinear processes will react in a nonlinear way to the intensity. To be able to calculate the nonlinear processes, two assumptions are made. The first assumption is that polarisation has an instantaneous response to the electric field. The second assumption is the slowly varying envelope approximation, which assumes that the envelope of a forward traveling pulse slowly varies in time[102].

2.2.1 Second order nonlinearity

The first observation of nonlinear optics was a second harmonic signal, generated by Franken *et al.* in 1961[103]. The second harmonic signal is a second order nonlinear response as a result from the second order nonlinear term:

$$\tilde{P}^{(2)}(t) = \chi^{(2)}\tilde{E}(t)^2. \tag{2.16}$$

In the case of second harmonic generation, the electric field contains a single frequency ω, described by

$$\tilde{E}(t) = Ee^{-i\omega t} + c.c., \tag{2.17}$$

where *c.c.* denotes the complex conjugate. Using this electric field with the second order polarisation term described in equation 2.16 we obtain

$$\tilde{P}^{(2)} = 2\chi^{(2)}EE^* + (\chi^{(2)}E^2e^{-2\omega t} + c.c.). \tag{2.18}$$

The second term of this equation indicates that the second order polarisation results in an oscillation at two times the original frequency. This mechanism is visualised in figure 2.1. The first term consists of a zero frequency component and is known as optical rectification, which results in a static electric field within the material.

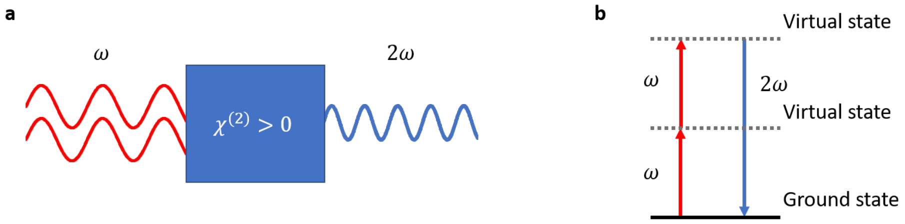

Figure 2.1: Principles of second harmonic generation with a) the geometry using a nonlinear crystal with $\chi^{(2)} > 0$, where two oscillating electric fields interact in the crystal, according to equation 2.18, to generate a single oscillating electric field at double the original frequency. b) A schematic of the energy levels involved in second harmonic generation.

Note that for centrosymmetric materials, the second order susceptibility is zero which can be shown by changing the sign of the electric field. Because of the inversion symmetry of centrosymmetric materials, the sign of the polarisation must change as well, resulting in

$$-\tilde{P}^{(2)}(t) = \epsilon_0 \chi^{(2)} (-\tilde{E}(t))^2 = \epsilon_0 \chi^{(2)} \tilde{E}^2(t). \tag{2.19}$$

This can only happen when $\chi^{(2)}$ is zero. Therefore, second harmonic generation can only occur in non-centrosymmetric materials.

In the case of sum-frequency, the electric field of two different frequencies interact to create a single new frequency according to

$$\omega_1 + \omega_2 = \omega_3, \tag{2.20}$$

with ω_i being the three wavelengths involved in this process and all larger than zero. The newly generated frequency, ω_3, is the result of the sum of both input frequencies, similar to second harmonic generation. Difference-frequency generation, however, generates a photon with a frequency equal to the difference in input frequencies according to

$$\omega_1 - \omega_2 = \omega_3. \tag{2.21}$$

In this case, ω_2 is the signal and ω_3 is called the idler. This shows that, by conservation of energy, creating a photon with frequency ω_3 will also result in an additional ω_2 photon. This ω_2 photon is a result from stimulated emission by the input ω_2 from the virtual state which is occupied after absorbing a photon with frequency ω_1. The energy difference, that is described in equation 2.21, is emitted as a photon with frequency ω_3.

2.2.2 Higher order nonlinearity and solid-state supercontinuum generation

The discovery of nonlinear optics has eventually given rise to supercontinuum laser pulse generation. A supercontinuum laser pulse is a pulse that contains a broad range of wavelengths. Figure 2.2 shows the spectrum of a broadband laser pulse generated via bulk supercontinuum generation[104]. The input is a 100 fs laser pulse, centred at 800 nm with a pulse energy of 310 nJ. This pulse is focused onto a YAG crystal, resulting in a spectrum spanning from 470 nm to 1400 nm. These pulses play a vital role in the field of ultrafast spectroscopy where they often serve as a broadband probe, allowing for the observation of a wide range of frequencies. Another use for the supercontinuum is as a broadband non-degenerate signal in a (N)OPA, where part of the supercontinuum is selected and amplified, accommodating large wavelength tunability.

Ever since the first observation of coherent supercontinuum generation, performed by Alfano and Shapiro[105], much effort has been put into understanding the mechanisms of supercontinuum generation and finding ways to generate broader, brighter and more stable white light. The development of the chirped pulse amplification technique[106], and the discovery of the kerr lens mode locking[107], allowed for the generation of intense femtosecond pulses. This resulted in great advancements in supercontinuum generation in gasses[108,109], liquids[108,110,111], solid state[112], and nonlinear optical fibres[113]. These, in turn, resulted in the development of the (N)OPA, and ultrafast spectrally resolved spectroscopic techniques amongst which are the TAS and FDI techniques discussed in this research report.

The generation of broadband coherent light pulses can be described via femtosec-

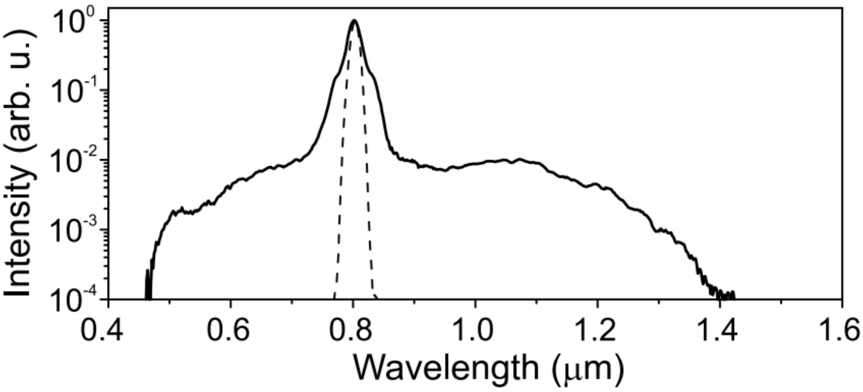

Figure 2.2: Example of a supercontinuum generated by bulk supercontinuum generation in a YAG crystal. Dashed line indicates the fundamental input pulse and the solid line indicates the generated supercontinuum pulse. Reprinted with permission from Springer Nature Customer Service Center GmbH, Springer Nature[104], 2019.

ond filamentation. This phenomenon is an intricate balance of nonlinear mechanisms which is described as *"a dynamic structure with an intense core, that is able to propagate over extended distances much larger than the typical diffraction length while keeping a narrow beam size without the help of any external guiding mechanism"*[114]. It depends on a combination of various interdependent nonlinear mechanisms. The mechanisms at play are self-focusing, self-phase modulation, self steepening, multiphoton absorption and ionisation, plasma defocusing, Group Velocity Dispersion (GVD) and Group Delay Dispersion (GDD), four-wave mixing and phase-matching. In this section, these fundamental mechanisms are discussed. As this topic is complex and extensive, complete books have been written on the field of supercontinuum generation. Here, an overview is given to provide conceptual understanding of the relevant nonlinear mechanisms. Full details and derivations about the mechanisms for supercontinuum generation can be found elsewhere[104,115,116].

Kerr lensing

An important mechanism to explain supercontinuum generation is self-focusing, also known as kerr lensing[117]. Self-focusing is related to the nonlinear refractive index of a transparent medium. The refractive index of a material is dependent on the intensity of the pulse according to

$$n(t) = n_0 + n_2 I(t), \tag{2.22}$$

where n_0 is the refractive index of the medium, and n_2 is the nonlinear refractive index related to the third-order optical susceptibility from equation 2.15 of the material according to

$$n_2 = \frac{3\chi^{(3)}}{4\epsilon_0 c n_0^2}, \tag{2.23}$$

where ϵ_0 is the permittivity of vacuum and c is the speed of light. This shows that, in a third-order nonlinear crystal, the refractive index increases (for $\chi^{(3)} > 0$) with the introduction of a laser pulse. The profile of the refractive index enhancement is dependent on the intensity profile of the beam, meaning that the centre of the (Gaussian) beam profile will have a higher refractive index with respect to the edges of the beam, creating a lensing effect. This lensing effect is further enhanced by the increase of intensity while the pulse propagates through the material by the self focusing, eventually leading to a singularity. However, diffraction and plasma defocusing will dominate the self-focusing when the intensity of the pulse increases, resulting in the defocusing of the beam[104,118,119]. If the intensity is in turn decreased, self-focusing will take over again and focus the beam, resulting in a oscillatory filamentation within a transparent nonlinear medium.

Self-phase modulation

Another mechanism at play is self-phase modulation. The refractive index change does not only impact the beam in the transverse direction of the beam pointing, but also in the propagation direction due to the time dependent intensity of the pulse[104,115,120]. This causes a time-dependent refractive index change, resulting in a nonlinear phase change within the pulse. This is called self-phase modulation as the intensity of the pulse itself modulates the phase. The phase change is given by

$$\phi_{nl}(t) = \frac{\omega_0}{c} n_2 \int_0^L I(t,z) dz, \tag{2.24a}$$

where ω_0 is the initial frequency, z is propagation distance and L is the thickness of the nonlinear medium[40,115]. Assuming a short travel distance through a nonlinear medium, the assumption can be made that the variation of the intensity over the propagation distance is negligible. This simplifies the phase change to

$$\phi_{nl}(t) = \frac{\omega_0 L}{c} n_2 I(t). \tag{2.24b}$$

The resulting frequency shift is given by[121,122]

$$\partial\omega = \frac{\partial\phi_{nl}}{\partial t}, \tag{2.25a}$$

or, using equation 2.24a

$$\partial\omega = \frac{\omega_0 L}{c} n_2 \frac{\partial I}{\partial t}, \tag{2.25b}$$

which, by assuming a Gaussian pulse of duration t_g and peak intensity I_0, results in

$$\partial\omega(t) = 4\frac{\omega_0 L}{c t_g} n_2 I_0 t \exp\left(-2\frac{t^2}{t_g^2}\right). \tag{2.26}$$

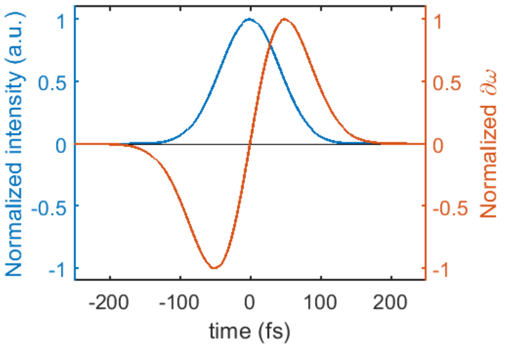

Figure 2.3: Normalised temporal intensity distribution (blue) and resulting self-phase modulation (red), according to equation 2.26, for a Gaussian temporal profile with a 100 fs (FWHM) pulse duration and positive n_2. Negative time represents the front of the pulse and positive time the tail of the pulse.

Equation 2.26 is plotted in figure 2.3 for a pulse duration of 100 fs and positive n_2. This shows that a decrease of the frequency at the front of the pulse and an increase of the frequency at the back of the pulse is generated.

Group velocity dispersion and group delay dispersion

One mechanism that lowers the supercontinuum generation efficiency is GVD. The group velocity of the pulse, that is the collective speed of a pulse envelope, is the inverse derivative of the wavenumber, $k = \omega n / c$, with respect to the angular frequency

$$v_g = \frac{\partial \omega}{\partial k}. \tag{2.27}$$

When light of different wavelengths pass through a medium, different wavelengths encounter different refractive indices resulting in different speeds of light within the medium. The amount of dispersion per unit length is called GVD and is calculated by the derivative of the inverse group velocity with respect to the frequency according to

$$\mathrm{GVD} = \frac{\partial}{\partial \omega} \frac{1}{v_g} = \frac{\partial^2 k}{\partial \omega^2}. \tag{2.28}$$

The GVD within a material leads to GDD. GDD is a measure of the chromatic dispersion, otherwise known as chirp, of the pulse and is given by the second derivative of the change in spectral phase with respect to the optical frequency:

$$\mathrm{GDD} = \frac{\partial^2 \phi}{\partial \omega^2}, \tag{2.29}$$

where the phase is the frequency dependent phase of the electric field, as will be elaborated on in the next section. The total amount of GDD added by a transparent medium is the amount of GVD of a material times the thickness of the material.

The refractive index dependent speed of light generally leads to the shorter wavelengths slowing down more than the longer wavelengths. This means that, when a material is placed in the beam path, the pulses stretch in time as the shorter wavelengths will lag behind the longer wavelengths. For pulses with no or positive chirp (long wavelengths leading the pulse), this causes temporal stretching, or chirping, of the pulse while propagating through a transparent medium, resulting in an increase of the GDD. This chirp increases the pulse duration, as will be discussed in the section 2.3.1. This reduces the pulse's temporal peak power, lowering the supercontinuum generation efficiency.

Self-steepening

One mechanism that has influence on the self-phase modulated broadening is self-steepening. Self-steepening occurs because of the time dependent refractive index change described in equation 2.22[123]. This causes the centre of the (Gaussian) pulse to slow down compared to the front and back of the pulse, as is the case when $Q > 0$. This creates a steep trailing edge as shown in figure 2.4a, where $Q = n_2 A^2 z / c\tau$ and $x = (t - nz/c)/\tau$, with τ being related to the temporal pulse duration, z the distance traveled through the nonlinear medium and $A^2 = |E|^2 / \cosh\left[(t - n/c)/\tau\right]$[124,125]. A so called optical shock-wave is formed when this edge becomes infinitely steep. The steepening of the trailing edge results in an asymmetric spectral broadening of the pulse, according to the derivative term of equation 2.25b. This results in a strong blue-shift of the frequencies, and a decrease of red shift, as shown in figure 2.4b.

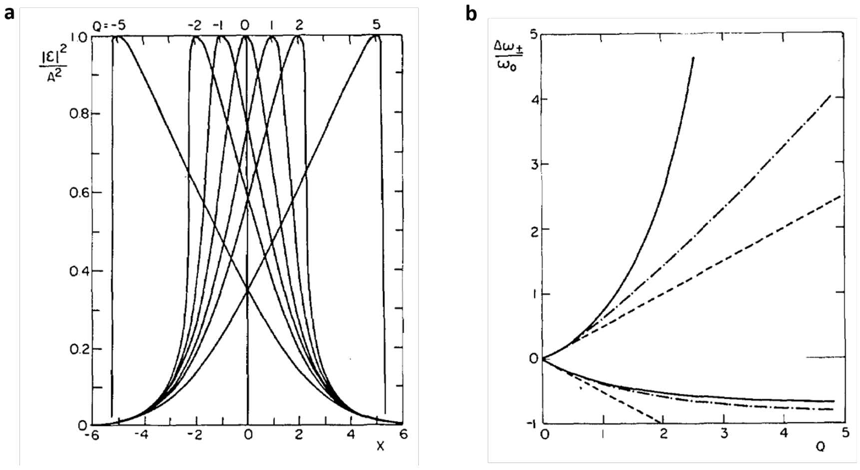

Figure 2.4: a) Self-steepening over travel distance for positive ($Q \propto n_2 > 0$) and negative ($Q \propto n_2 < 0$) nonlinear refractive index. b) Maximum red shift ($\Delta\omega_-$) and blue shift ($\Delta\omega_+$) without self-steepening (dashed line) and with self-steepening (solid line) for increasing Q. Reprinted with permission from Yang *et al.*[124] © The Optical Society.

Multiphoton absorption and plasma defocusing

An important defocusing mechanism is plasma defocusing. As the band gap between the valence and the conduction band of a dielectric material is larger than the photon energy, no photons can be directly absorbed. However, when the intensity of the beam within the filament becomes large enough, multiphoton absorption events occur that can overcome the band gap. The number of multiphoton absorption events increases with increasing intensity according to the rate equation

$$\frac{\partial \rho}{\partial t} = \frac{\beta_K}{K\hbar\omega_0} I^K, \tag{2.30}$$

where ρ is the conduction electron density, β_K is the multiphoton ionisation coefficient, K is the number of photons required to overcome the bandgap and I^K is the transition rate. The result of this is that a higher intensity causes a bigger relative photon loss due to a stronger multiphoton absorption.

These generated conduction electrons also have an impact on the refractive index of the medium. The refractive index including this plasma effect is described by

$$n(t) = n_0 - \frac{\rho(t)}{2n_0\rho_c}, \tag{2.31}$$

where $\rho_c = \epsilon_0 m_e \omega_0^2 / e^2$ is the critical plasma density for which the plasma becomes opaque to an electromagnetic radiation of frequency ω_0. This shows that an increase in conduction electrons, caused by an increase in multiphoton absorption, results in a decrease of the refractive index. This has the inverse impact of the kerr lensing effect and causes the beam to defocus until the intensity has decreased sufficiently for kerr lensing to take over again[126].

Besides the defocusing, the plasma effect on the refractive index has an impact on the phase as well according to the so called plasma-induced phase modulation. The phase modulation due to the photo-induced plasma is given by

$$\phi_{nl}(t) = -\frac{\omega_0 L}{c}\frac{\rho(t)}{2n_0\rho_c}, \tag{2.32}$$

assuming uniform free carrier distribution in the propagation direction. By using equation 2.25a and assuming a Gaussian temporal profile, we obtain the plasma induced frequency change

$$\partial\omega(t) = \frac{\omega_0 L}{c}\frac{\beta_K I_0^K}{K\hbar\omega_0 2n_0\rho_c}\exp\left(-\frac{2Kt^2}{t_g^2}\right), \tag{2.33}$$

which is always larger than zero. Therefore, the plasma induced broadening will result in a blue shift of the spectrum.

Four-wave mixing

Four-wave mixing is the mechanism where two or three photons interact to generate two or one photons with a different energy according to

$$\omega_1 + \omega_2 = \omega_3 + \omega_4, \tag{2.34}$$

where ω_i can be both positive and negative. This is a result from the third order term of the polarisation

$$\tilde{P}^{(3)}(t) = \epsilon_0 \chi^{(3)} \tilde{E}^3(t). \tag{2.35}$$

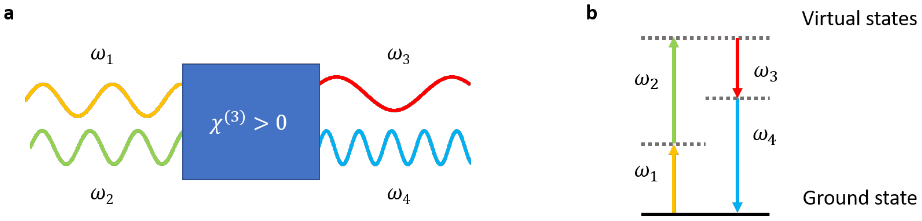

Figure 2.5: Principles of four-wave mixing with a) the geometry using a nonlinear crystal with $\chi^{(3)} > 0$, where two oscillating electric fields interact in the crystal, according to equation 2.34, to generate two oscillating electric field with higher an lower frequency than the two input pulses. b) A schematic of the energy levels involved in four-wave mixing.

As there is a multitude of possible interactions, we will discuss a single non-degenerate case. A full list of possible cases can be found elsewhere[100]. The interaction for this case, in which two frequencies $\omega_2 > \omega_1$ interact to create two new frequencies with $\omega_3 < \omega_1$ and $\omega_4 > \omega_2$, is depicted in figure 2.5. In this case, all interacting frequencies, ω_i, have different positive values. After this mixing event, the newly generated photons, with wavelengths lying outside of the input wavelengths, can participate again in this process, resulting in a cascade of new available wavelengths.

Phase-matching conditions

The generated frequencies are strongly dependent on phase-matching conditions. When photons with new frequencies are generated, these will travel at a different speed through the nonlinear crystal with respect to the input pulse according to

$$v(\omega) = c/n(\omega), \tag{2.36}$$

where $v(\omega)$ is the wavelength dependent speed of light in a medium. This results in a phase shift of the generated frequencies with respect to the induced polarisation. As the input pulse creates more of the new frequencies while propagating through the nonlinear crystal, in-phase with the induced electric field, these newly generated frequencies will phase-shift with respect to the earlier generated frequencies, resulting in deconstructive interference[102].

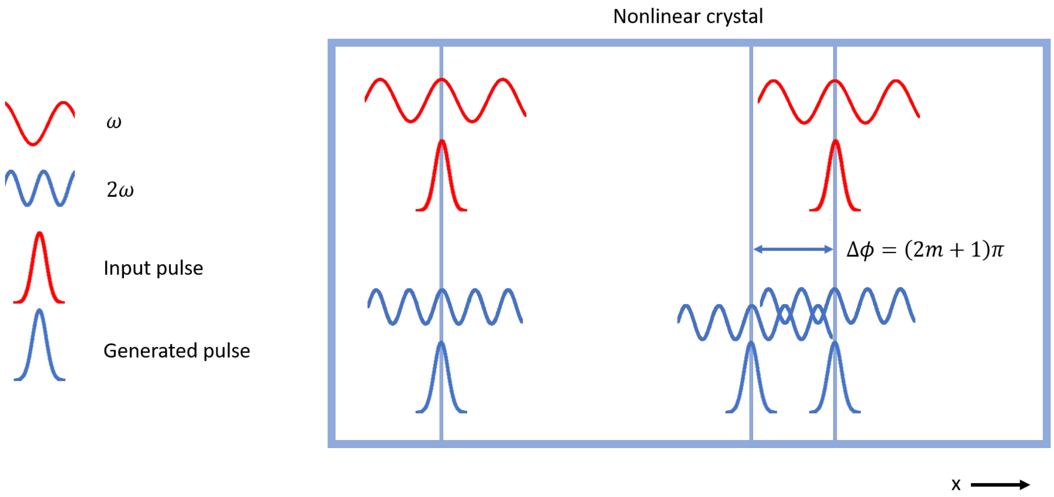

Figure 2.6: Result of phase shift during propagation through the nonlinear crystal. The newly generated wavelength (bottom) travels at a different speed than the source pulse (top). This generates an in-phase, out-of-phase oscillation of the newly generated wavelengths with respect to previously generated wavelengths which destructively interfere, lowering the overall conversion efficiency.

To illustrate this effect we will discuss the second harmonic generation as an example, however, this is an important mechanism for all of the generated wavelengths. Figure 2.6 shows a visualisation of what happens when phase-matching conditions are not met. Over the whole propagation length, the input pulse will generate the second harmonic signal, in-phase with the input pulse. By assuming $n_\omega < n_{2\omega}$, the input pulse will propagate through the nonlinear crystal faster than the generated pulse. Therefore, the input pulse goes in and out-of-phase with respect to the firstly generated second harmonic signal. This means that the newly generated second harmonic signal will also shift in and out-of-phase with respect to the previously generated second harmonic. This results in deconstructive interference of the previously and newly generated signal, reducing the efficiency of the second harmonic generation process.

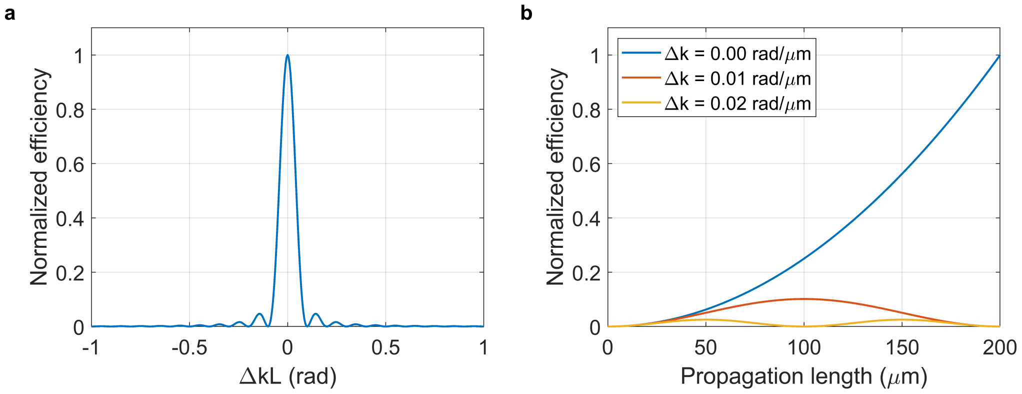

Figure 2.7: a) Conversion efficiency from phase-matching conditions calculated for fixed $L = 20\mu m$. A maximum conversion is achieved when $\Delta k = 0$, which is perfect phase-matching. b) Conversion efficiency for various Δk values. Only when $\Delta k = 0$ will the efficiency uniformly increase with increasing thickness. For other values, an oscillating pattern occurs due to in-phase and out-of-phase conditions.

To avoid this and achieve high conversion efficiency, phase-matching conditions need to be achieved. This is the case when the induced polarisation and the generated frequencies stay in-phase. The final generated intensity is given by

$$I(L,t) = \frac{c\mu_0\omega_0^2}{4}|P|^2L^2\,\mathrm{sinc}^2(\Delta kL/2), \tag{2.37}$$

with μ_0 the permittivity in vacuum, ω_0 the input frequency, L the propagation length through the nonlinear crystal and Δk the change in wave vector between the induced polarisation and generated field. As equation 2.37 shows that the irradiance is proportional to a sinc^2 function, the maximum generated irradiance is obtained when $\Delta kL = 0$ as shown in figure 2.7a. However, when L goes to zero, the conversion efficiency drops due to the L^2 term and no new frequencies are generated as shown in figure 2.7b. So a nonlinear crystal with nonzero thickness, $L > 0$, is required for which we will only obtain a uniformly increasing function when $\Delta k = 0$.

2.3 Pulse duration and Frequency-Resolved Optical Gating

2.3.1 Pulse duration

To analyse the pulse duration, we will have to understand the result of the sum of electric fields, given by equation 2.17, with a broad range of frequencies. In this case, we will also need to consider the phase of these frequencies, resulting in

$$\tilde{E}(t) = Ee^{-i(\omega t - \phi(t))} + c.c., \tag{2.38}$$

with $\phi(t)$ being the phase of the pulse. The electric field of a broadband laser pulse is a result of the sum of the electric fields of all the individual frequency components. Depending on the relative phase of these frequencies, these will result in constructive or deconstructive interference in the temporal domain. Due to the different frequencies, the electric fields can only be in-phase at one instance as shown in figure 2.8a. This results in constructive interference of all frequencies, generating a large intensity at the in-phase conditions while deconstructive interference of the varying terms cancel each other out outside of this region. The top plot of figure 2.8a shows the sum of the intensity of 10 spectral components. In this case, it is the transform limited pulse, which is when all electric field are in-phase and the pulse duration is limited only by the spectral width of the pulse.

Figure 2.8b shows the impact on the pulse duration when more and higher frequency components are present within the pulse. The relation between the spectral width and the temporal limit for a temporal Gaussian pulse is given by

$$t_p \Delta\omega \geq 0.441 \times 2\pi, \tag{2.39}$$

where t_p is the pulse duration measured by the Full Width at Half Maximum (FWHM) and $\Delta\omega$ is the spectral width[116]. Due to the increase of spectral width, the deconstructive interference occurs closer in time to the region where the electric field are

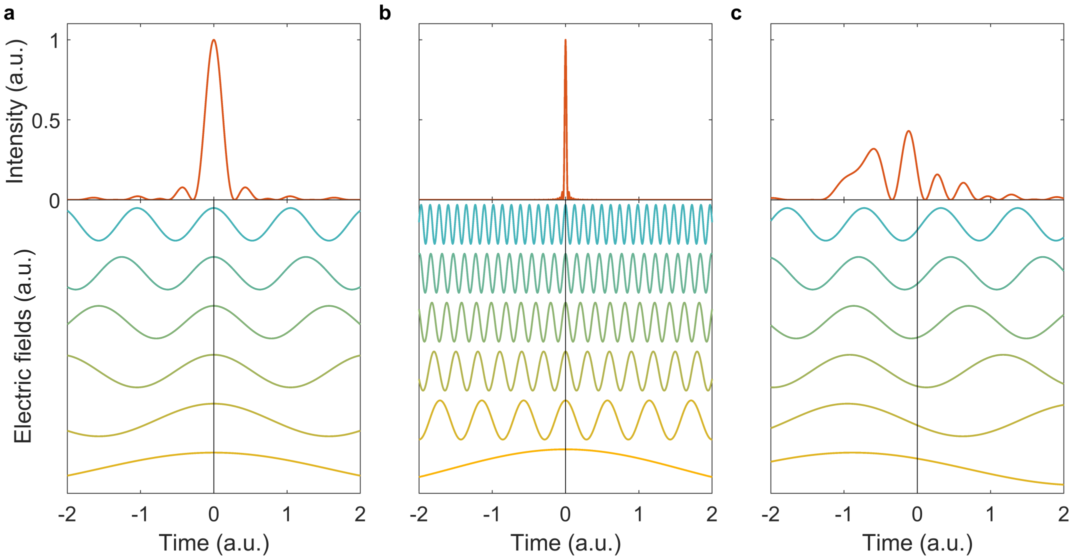

Figure 2.8: Models to show the relation between temporal compression and spectral broadening. Only 6 spectral components are displayed for clarity. a) Shows a compressed pulse at the top containing 10 spectral components with low frequencies as displayed at the bottom. b) Shows a compressed pulse at the top containing 100 spectral components as displayed at the bottom. c) Shows a pulse at the top containing 10 out-of-phase spectral components with low frequencies as displayed at the bottom.

in-phase. This shows that broadening of the pulse or having the same bandwidth in the spectral domain, as $\Delta\omega \propto \Delta\lambda^{-1}$, with higher centre frequency, can lead to a shorter pulse durations.

Unless accounted for, the pulse will contain a certain degree of spectral chirp described by the amount of GDD as discussed in section 2.2.2. This means that the phase of the individual spectral components is not the same. This case is shown in figure 2.8c, where both constructive and deconstructive interference of the electric fields of the spectral components occur over the whole time domain. This results in a less defined peak and longer pulse duration and gives an indication of the complexity of pulse shapes.

2.3.2 Polarisation-gated - Frequency-resolved optical gating

To measure the phase of the spectral components and determine the pulse duration, Trebino *et al.* have developed the Frequency-Resolved Optical Gating (FROG)[127,128]. This technique uses the instantaneous nonlinear interaction of two pulses in a medium to create a signal pulse, either via nonlinear diffraction, Kerr effect or higher order generation[129]. By temporally translating one of these pulses, the time dependent spectrum of the signal pulse is obtained. This signal pulse is dependent on the spectral and temporal distribution of both pulses used to generate it.

To measure the duration of these short pulses, and to optimise the chirp correction, we have analysed the supercontinuum pulses generated by the MPC, as discussed in chapter 4, with a Polarisation-Gated - Frequency-Resolved Optical Gating (PG-FROG) system[127,128,130]. This is a special type of FROG where the signal is generated via the optical Kerr effect within an instantaneous responding solid-state medium. This method is chosen because of its large spectral detection range, high temporal resolution, intuitive FROG traces and the lack of ambiguities[129].

The signal pulse is a result of the optical Kerr effect. The optical Kerr effect is the change of the refractive index of a material by the electric field of a laser pulse, as discussed in section 2.2.2. However, rather than inducing self-focusing, this effect is used to separate the parallel and perpendicular polarisation components of the probe pulse with respect to a pump pulse with a 45 ° polarisation angle[131]. The refractive index change of the material induces a phase shift between the parallel and perpendicular component of the probe pulse, only when the pump and probe pulses spatially and temporally overlap, resulting in a nonlinearly polarised beam. The signal pulse is obtained by implementing a polariser after the nonlinear crystal at a 90 ° polarisation angle with respect to the unperturbated probe beam, only transmitting the part of the beam that has been altered by the pump pulse.

The measured signal intensity of the PG-FROG is given by

$$I(\omega,\tau) = \left| \int_{-\infty}^{\infty} E(t)|E(t-\tau)|^2 \exp(-i\omega t)dt \right|^2, \tag{2.40}$$

where $|E(t-\tau)|^2$ is the gate function and $E(t)$ is the gated pulse. To extract $E(t)$, an iterative algorithm is applied using two constraints[132]. The first constraint is that the signal field has to match the pulse field of the gate and probe pulses, as given by

$$E_{sig}(t,\tau) = E(t)|E(t-\tau)|^2. \tag{2.41}$$

The second constraint is that this signal field, when used in equation 2.40, can reconstruct the signal intensity according to

$$I(\omega,\tau) = \left| \int_{-\infty}^{\infty} E_{sig}(t,\tau)\exp(-i\omega t)dt \right|^2. \tag{2.42}$$

This can be solved using an iterative error reduction algorithm that, when given the FROG traces and an initial guess of the complex electric field, can reproduce the spectrum and retrieve the temporal and spectral phase of the pulse.

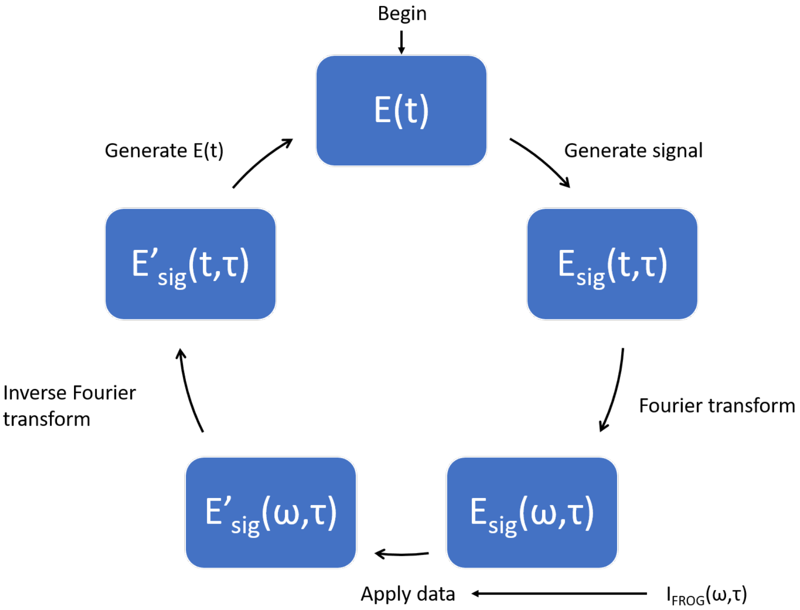

Figure 2.9: Error reduction algorithm steps to retrieve the PG-FROG traces.

The corresponding steps the algorithm takes are shown in figure 2.9[132–134]. The guess of the complex electric field is used to generate the signal field using equation 2.40, which is then Fourier transformed with respect to time to obtain the signal field in the frequency domain. The magnitude of this signal field is then replaced by the experimental FROG trace through

$$E'_{sig}(\omega,\tau) = \frac{E_{sig}(\omega,\tau)}{|E_{sig}(\omega,\tau)|}\sqrt{I_{FROG}(\omega,\tau)}, \tag{2.43}$$

while leaving the phase untouched. The inverse Fourier transform is then taken to get back to the complex signal field in the time domain. The new version of $E(t)$ is then generated by integrating $E'_{sig}(t, \tau)$ over τ and the loop starts again. This is repeated until the newly generated $E(T)$ is the same as the previously calculated $E(T)$.

2.4 Transient absorption spectroscopy

Ultrafast TAS is a technique that measures excited state dynamics of matter on ultrafast timescales. It uses a pump and probe pulse pair, where the pump pulse optically excites the electrons within a sample to a higher energy state and the probe measures these states by way of transmission.

2.4.1 Transient absorption spectroscopy system

The TAS system consists of a couple key components, schematically shown in figure 2.10. A broadband probe pulse and a pump pulse are focused and spatially overlapped at the focal point of the probe beam. This is confirmed by the beam profile as observed by a CCD camera at this focal point. The spotsize of the pump is kept larger than the waist of the probe to obtain a uniform excitation of the probed area.

The sample is placed at the focal point of the probe so that both beams spatially overlap inside the sample. To achieve this, the sample is moved through the focal point of the probe beam and the optimised position is found by maximising the observed TA signal. During the measurements, the samples reside inside a vacuum chamber under an active vacuum to prevent sample degradation caused by interaction with air.

After the sample, the transmitted probe is spectrally dispersed by either a grating or prism, as will be discussed in section 2.4.4, and focused onto a 1D detector to observe the transmission of individual spectral components. The 1D detector is electronically triggered by the laser amplifier to capture all individual laser shots. Because of this, sequential shot pairs can be used to calculate the TA signal to

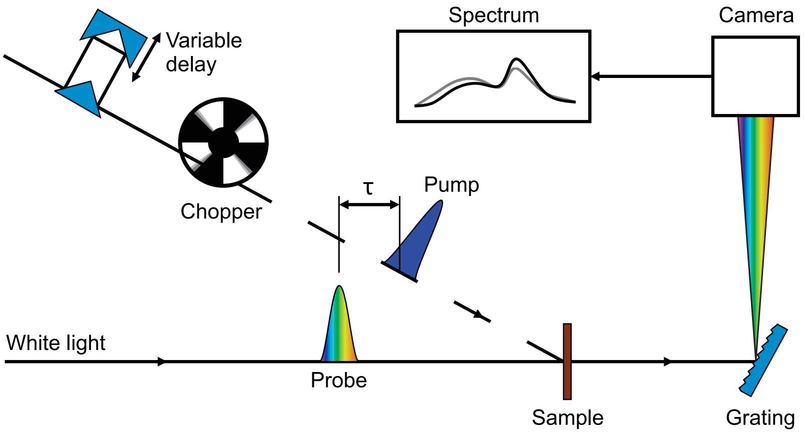

Figure 2.10: Schematic overview of the relevant components of a transient absorption spectrometer. The pump and probe pulses arrive at the sample with time difference, τ. Every other shot of the pump is blocked by a mechanical chopper and the arrival time is controlled via a mechanical delay stage. The probe is spectrally dispersed after the sample and the spectrum is collected by a 1D detector.

eliminate long term laser and environmental noise contributions.

The arrival time of the pump pulse is controlled using a computer controlled mechanical delay stage which adjusts the physical path length of the pump. By using that the speed of light is constant, the time delay, Δt, is varied by

$$\Delta t = \frac{2\Delta x}{c}, \tag{2.44}$$

where Δx is the change in distance. The factor of 2 is added because the delay is generated via a return trip. A mechanical chopper, running at half the laser frequency so that it blocks every other pump pulse, is used to measure the shot-to-shot modulation of the sample which increases the signal to noise ratio by using the highly correlated sequential shots[135]. The wavelength of the pump is tunable with the help of second or third harmonic generation, a (N)OPA or with the MPC. The latter will extensively be discussed in chapter 4.

The temporal limitation at the earliest timescales that can be observed by the TAS system is determined by the Instrument Response Function (IRF) duration. The IRF is a result of the direct nonlinear interaction of the pump and probe pulses in the sample and/or substrate when both pulses spatially and temporally overlap. This limits the earliest time delay that can be measured as this is not a response from the excited state of the material itself, but rather the direct interaction of the pump and probe pulses within a medium. This is defined by the convolution of the temporal profile of the pump and probe pulses as this only occurs when both pulses are overlapping in space ant time. These nonlinear effects can result in a large artifact on the obtained TA spectra by direct modulation of the probe pulse, rather than from the interaction with the excited state response of the sample. This means that to observe kinetics at a shorter timescale, a shorter pump pulse duration is required.

2.4.2 Transient absorption signals in semiconductor materials

There are several different mechanisms that contribute to the TA signal[136]. An overview of the different relevant mechanisms is given in figure 2.11 where the excited state mechanisms are shown for a material with parabolic energy bands. The TA signal constitutes of both positive and negative signals which correspond to an increase and decrease in the transmitted probe after excitation respectively.

First, an excited state population is generated by the pump pulse, as shown in figure 2.11a. Absorption of the pump pulse excites electrons from the valence band into the conduction band, leaving holes in the valence band. These charges could either be free carriers or bound excitons depending on the binding energy of the exciton and available energy in the system. The excited state population quickly rethermalises to comply with the Fermi-Dirac distribution as discussed in section 1.4.

As the excited electrons occupy states which were empty in the ground state, no more electrons can occupy the same state due to the Pauli exclusion principle, leading to a Ground State Bleach (GSB) as shown in figure 2.11b[48]. This is the so called state filling and leads to the Moss-Burstein effect, seemingly increasing the band gap. Because the energy states in the conduction band are occupied, and the energy states at the valence band are empty, absorption of the probe wavelength matching these energy transitions will be suppressed. This results in a positive signal of the TA spectrum as the excited state absorption is reduced.

On the other hand, there are two excited state mechanisms that show a negative result named under Photoinduced Absorption (PIA). These two mechanisms are the Bandgap Renormalization (BGR) and interband/intraband absorption. The BGR, or bandgap shrinkage, causes the valence band to move up and/or the conduction band to move down, as indicated in figure 2.11c, resulting in a smaller bandgap. This is a result of Coulombic interactions of the charges[137,138]. This counteracts the Moss-Burstein effect and, depending on the strength of both mechanisms, results in the effective bandgap to either increase or decrease. Interband/intraband absorption is the excitation of electrons (holes) in the conduction (valence) band into higher available energy states as depicted in figure 2.11d. This transition is not possible

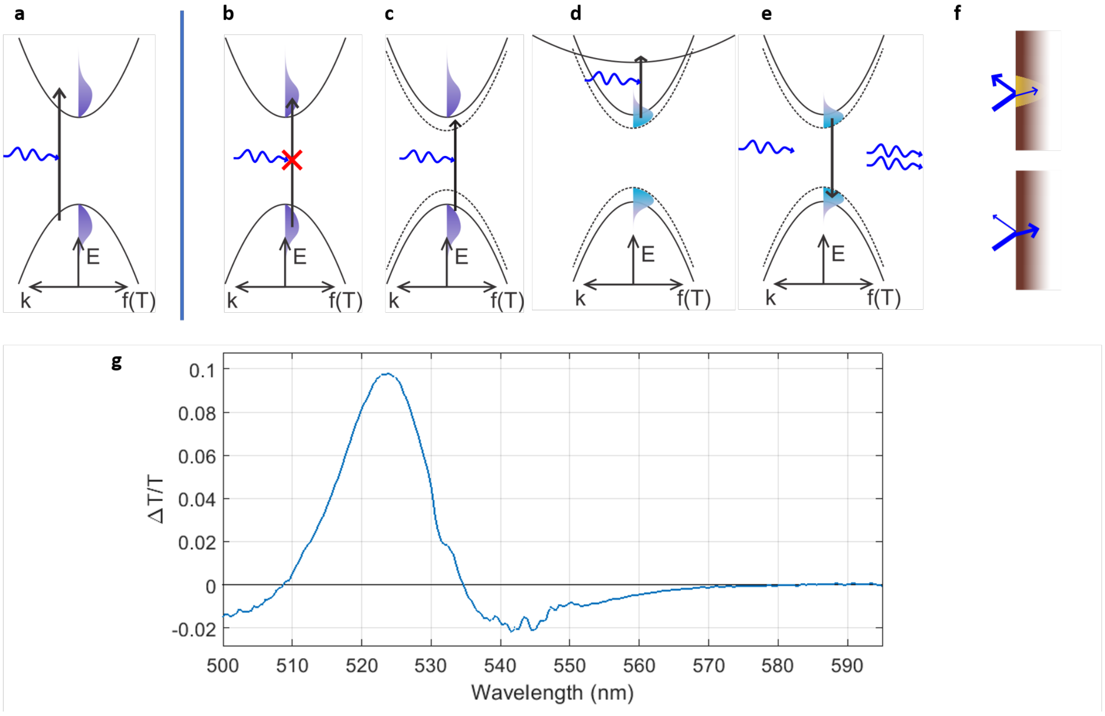

Figure 2.11: Schematic of the observed features of TAS, assuming the material has a parabolic band structure. a) Is the pump absorption event, b) is the ground state bleach (positive signal), c) is the bandgap renormalisation (negative signal), d) is the photoinduced absorption (negative signal) and e) is the stimulated emission (positive signal). f) Represents the change is reflection of the sample surfaces due to a modulated refractive index (either positive or negative). g) Example TA spectrum of a 72.5 nm thick layer of microcrystalline $CsPbBr_3$ perovskite, 1 ps after excitation at 400 nm with a fluence of $3.8\mu J/cm^2$.

in the ground state as the ground state to excited state is not resonant with this energy due to the bandgap, and there are no electrons (or holes) in the conduction (or valence) band to be excited. Therefore, the absorption of the photons with energy corresponding to the energy difference of the electrons (or holes) in the conduction (or valence) band and available higher energy states is increased, resulting in a negative signal.

The last absorption mechanism is stimulated emission, which is indicated in figure 2.11e. The photons of the probe will pertubate the matter (sample) with carriers in the excited state. This results in the stimulation of carriers to fall back to the valence band and emit a coherent photon. As this stimulated emission is highly directional, the newly created photons will travel coherently with the probe light, increasing its observed intensity. Therefore, this results in a seemingly lower absorption and has a positive signal.

Another effect, which is often ignored with TAS, is the change of the reflection of the probe, as indicated in figure 2.11f[136]. This is the result of the change in the real part of the refractive index by the excited state population, which induces the BGR, state filling and free carrier absorption[84,139]. These effects have a direct impact on the imaginary part of the refractive index, which is related to the real part of the refractive index via the KK relations[140]. This real refractive index change results in a wavelength dependent artefact which can either be positive or negative. When not taken into account, the refractive index induced signal can easily be misinterpreted as a change in the absorption for materials with a high refractive index, such as photovoltaic perovskites.

Figure 2.11g shows an example of a TA spectrum of a 72.5 nm thick layer of microcrystalline $CsPbBr_3$ perovskite layer 1 ps after excitation with a pump pulse at 400 nm with a fluence of 3.8 $\mu J/cm^2$. This spectrum contains a clear positive GSB signal centred at 523 nm, as indicated by figure 2.11b. The negative signal between 535 nm and 580 nm is the result of BGR, indicated by figure 2.11c, where the band edge shrinks due to the altered Coulomb interaction of the excited charges. This signal disappears within the first 2 ps as the charges will cool down to the shifted band edge filling these newly generated states. The last feature is the negative feature below 510 nm of which the origin remain ambiguous. Where Price *et al.* previously suggested this is from the change in reflection, indicated by figure 2.11f, others have suggested this is actually a result from the change in absorption[29,141,142]. This change in absorption is either from interband absorption, figure 2.11d, or the BGR, indicated in figure 2.11c, extending to energies above the state filling. This origin is further discussed in chapter 3, where the FDI is used to measure the impact that reflection has on the TA spectrum.

2.4.3 Pulse requirements and preparation

One of the key components of this technique is a stable broad supercontinuum probe[38]. This is used to obtain the kinetics over a large spectral range, allowing for the observation of the excited state dynamics on a broad range of energy levels within the material. This supercontinuum is typically generated by bulk supercontinuum generation or a (N)OPA[38,143].

As for the pump pulse, an intense tunable pump pulse is required to bring the material to an excited state. There are two opposing operating conditions for the pump pulse. The first option is a tunable narrowband pulse, resonating with specific energy transitions within the material. This, for example, is important to examine charge transfer within an organic semiconductor blend[144]. These pulses are usually generated by a (N)OPA, which amplifies a small spectral part of a supercontinuum or uses the resulting idler[38]. The second option is a broadband pump pulse to allow for temporal compression to the femtosecond duration[136]. These short pulses result in a short IRF duration, which allows the observation of kinetics on the shortest of timescales. The conventional way of generating these short pump pulse is with a (N)OPA or nonlinear optical fibres.

Bulk supercontinuum generation is achieved by focusing a pulse into a nonlinear crystal, broadening the beam as discussed in section 2.2.2. The bulk supercontinuum generation can result in a larger than octave spanning supercontinuum as discussed in section 2.2.2[145]. The (N)OPA can generate wavelength tunable, easily compressible and intense pulses by amplifying part of a bulk supercontinuum via four-wave mixing[146]. As for the nonlinear optical fibres, they can produce an intense and broad supercontinuum by using a nonlinear gas and a long path length[43]. All of these techniques, however, have their respective drawbacks as will be discussed in chapter 4.

2.4.4 Spectrometer

The supercontinuum probe is measured by a spectrometer, depicted in figure 2.12. The beam is first focused onto a slit to create an object of fixed size and then projected to the Fourier plane. The slit width partly determines the optical resolution of the spectrometer by setting the object size. After collimation, a dispersion element is used to separate the spectral components. This can either be a prism (figure 2.12a), or a grating (figure 2.12b). The prism has the benefit of having a high throughput but generates nonlinear dispersion while the grating has lower throughput, but generates linear dispersion. A lens, or concave mirror, is used to focus the different spectral components onto a 1D detector.

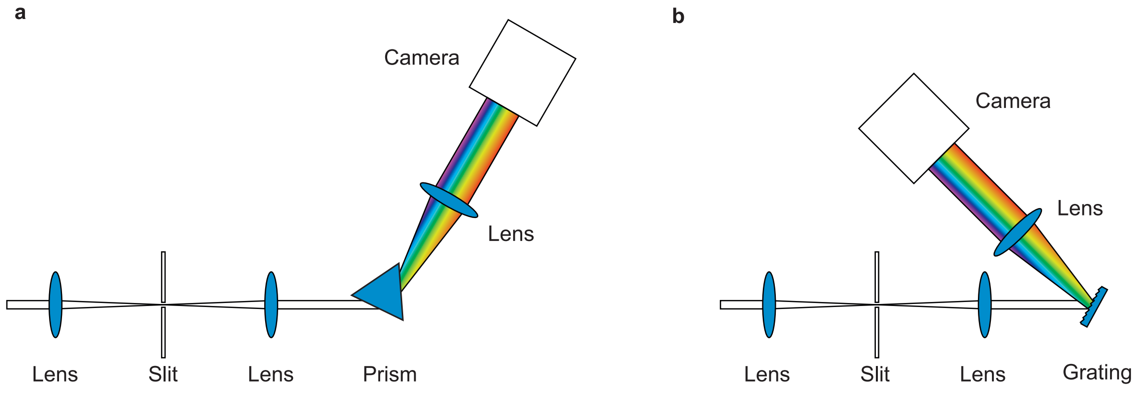

Figure 2.12: Two configurations of a spectrometer. The light is focused onto a slit to set the object size on the detector. The light is then collimated and dispersed via a a) prism or b) grating. The light is then focused onto a 1D detector which collects the spectra.

For the prism spectrometer, the dispersion is determined by the difference in refractive index of the prism for different spectral components. The total beam deviation δ from its original path for each wavelength can be calculated according to

$$\delta = \theta_i + \sin^{-1}\left[\sin(\alpha)\sqrt{n(\lambda)^2 - \sin^2(\theta_i)} - \sin\theta_i \cos\alpha\right] - \alpha, \tag{2.45}$$

where θ_i is the angle of incidence and α is the apex angle of the prism[147].

In the grating spectrometer configuration, a blazed reflective diffraction grating is used. Here, the dispersion is determined by the groove density of the grating according to the grating equation:

$$m\lambda = d[\sin(\theta_i) + \sin(\theta_o)], \tag{2.46}$$

where m is the order of the reflection, d is the groove spacing, θ_i is the input angle and θ_o is the output angle. Using the output angle, we can calculate the dispersion on the camera

$$\frac{d\lambda}{dL} = \frac{d\cos(\theta_o)}{mF} \times 10^6, \tag{2.47}$$

where $d\lambda$ is the total spectral range, dL is the width of the dispersed beam and F is the focal length of the imaging lens.

2.4.5 Data processing

A 1D detector runs at the same readout frequency as the laser amplifier repetition-rate output to allow acquisition of each individual shot. The output of each shot is a single vector with the measured intensity of the probe pulse for each pixel. The pixel numbers are converted to wavelength as discussed later in section 2.4.5. All the individual shots are collected to calculate the TA signal by using sequential shots.

A small portion of the pump, after the chopper, is collected by a photodiode to measure the state of the pump of the individual shots. This reference value is used to indicate the acquired shots as pump "on" (1) or pump "off" (0). On top of that, it serves as an error check to detect possible missed shots.

The TA signal is calculated as

$$\frac{\Delta T}{T}(\lambda, t) = \frac{T^*(\lambda, t) - T(\lambda)}{T(\lambda)}, \tag{2.48}$$

where $T^*(\lambda, t)$ is the excited-state transmission for various pump time delays and $T(\lambda)$ is the ground state transmission. The TA signal is calculated for each sequential excited and ground state probe pair to eliminate any long-term laser fluctuations with sequential shots having higher correlation. This is further be discussed in section 4.4.4 where the correlation of the MPC supercontinuum is discussed. The obtained TA signals are then averaged per time point. The time dependent spectra are then put in series to obtain a surface of the excited state response.

Background subtraction

The camera detects the supercontinuum probe on top of a dark background and light pollution in the room. The dark background is a signal level that the camera measures without any light arriving on the detector, while light pollution is the light from any external light source within the room that reaches the detector. These noise contributions have a significant impact on the TA signal as the relative change in transmission is artificially reduced without background correction as the measured intensity for both ″on″ and ″off″ shots is increased by a fixed amount. Therefore, a background measurement is taken whilst blocking only the probe before each measurement. This has as an added benefit that potential pump scattering for the ″on″ shots can be measured as well. By subtracting the ″on″ and ″off″ background from the corresponding shots, the true probe spectrum can be observed.

Wavelength calibration

For this research, two methods of wavelength calibration are used. The first method is with the use of bandpass filters. These filters only allow a small spectral region, typically a Gaussian shape with a FWHM of 10 nm, to pass through. By using different band pass filters, specific pixels of the camera can be assigned to the wavelengths corresponding to the centre wavelengths of these filters. Depending on the spectrometer configuration, either the prism equation (equation 2.45) or linear interpolation is used to fit the wavelength calibration curve.

The second method is to use an external light source. For this experiment, a grating spectrometer (SpectraPro 2150, Princeton Instruments) is used, with the capability to set the centre wavelength for given grating specifications. This spectrometer has a rotation-controlled grating which can translate the spectrum across the detector, which enables the use of a single continuous wave laser with known emission wavelength to calibrate the axis. By setting the spectrometer to the continuous wave laser wavelength, the centre position on the camera is recorded. By then rotating the grating to another centre wavelength, the wavelength from the continuous wave laser is translated to another pixel on the camera. Using the linear dispersion from the grating, $\Delta\lambda / \Delta pixel$ can be extracted over the full spectral range. By using the set wavelength at the centre pixel, the corresponding wavelengths of the full pixel range can be extrapolated.

The bandpass filter method is used for relatively low resolution spectrometer experiments as the width of the bandpass filters result in relatively wide Gaussian profiles on the camera compared to a continuous wave laser. The benefit however is that it requires no external light source and thus requires no separate alignment procedure. However, when high resolution is required, the continuous wave laser procedure is the only reliable option.

Chirp correction

The supercontinuum probe is generated in a nonlinear solid-state crystal with a wavelength dependent refractive index. This wavelength dependent refractive index results in a different optical path length of the various wavelengths within the crystal which generates GDD of the pulse. This means that the generated pulse has obtained a chirp, which is a delay of the spectral components of the probe with respect to one another. Therefore, the arrival time of the probe at the sample is dependent on the wavelength, with a delay of up to a couple picoseconds[38]. When the pump delay is adjusted, with respect to the probe arrival time, different wavelengths observe time zero at different time delays, which is observed with TAS as a wavelength dependent time zero. The effect of this chirp is shown in figure 2.13 for a monolayer of tungsten disulfide (WS_2) placed on a plasmonic structure under resonant conditions[148]. This shows that the temporal pump-probe overlap occurs earlier for the shorter wavelengths, as the signal appears before the negative signal at 650 nm appears.

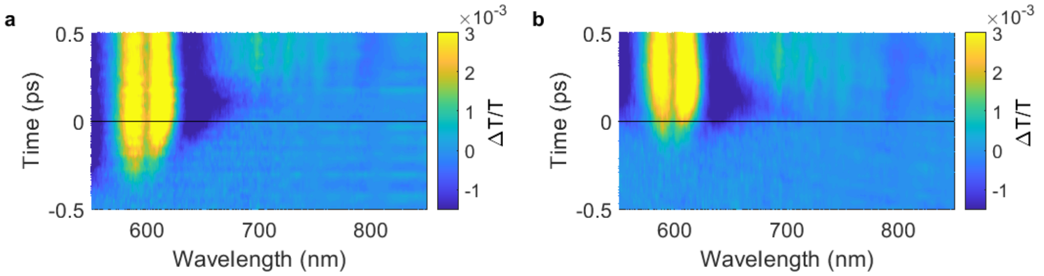

Figure 2.13: The effect of chirp correction of a TA spectrum. This spectrum is the TA spectrum of a plasmonic-WS_2 heterostructure with a probe angle of 22 degrees and a 400 nm pump pulse with a fluence of 12 μJ/cm^2 [148]. Here, a) is the original spectrum and b) is the chirp corrected spectrum.

This chirp needs to be corrected for to accurately describe the time dependent TA spectra, especially at early times. To achieve this, a convolution of a Gaussian pump pulse and (bi)exponential decay is fitted through the data to approximate the kinetics for every wavelength from which the peak position of the Gaussian pump is extracted. A second degree polynomial is fitted through all of these peak positions to approximate the wavelength dependent delay. Finally, the estimated time zero is set to a uniform time zero by subtracting the obtained time delay from the corresponding individual wavelength components. The result of this is shown in figure 2.13b, where we can see that both the positive and negative signal appear at the same time delay.

2.5 Differential phase spectroscopy

Transient absorption spectroscopy measures the modulation of the transmission of a probe pulse after excitation of the sample. This technique measures solely the amplitude of the signal and thus ignores any phase information. FDI on the other hand is a technique that is capable of extracting the phase information by introducing a broadband time-delayed reference-probe pulse pair, rather than a single probe, to obtain an interference pattern in the frequency domain[36,149]. There are three benefits of this technique related to its dependency on the phase rather than the intensity of the probe pulse. The first is the insensitivity to reflection effects on the transmission introduced by the transient refractive index as a result of excitation of the sample during pump-probe spectroscopy. The second is that pump scattering onto the detector does not contribute to the interference signal as the pump and probe are temporally separated after time zero. The last benefit is that any stimulated emission does not contribute to the phase change and thus the signal obtained by the FDI is decoupled from the stimulated emission.

2.5.1 Interference

Interference is an often used technique to extract the phase information of two beams of light in steady state spectroscopy. In previous studies, a Michelson interferometer was used to extract the ground state refractive index of materials or the thickness of the material[150,151]. Later, this technique has been implemented in the field of ultrafast spectroscopy using a broadband laser pulse to extract the phase information[36].

When two beams of light are co-polarised, temporally and spatially coherent and spatially overlapping, interference will occur. This is the case for all of our experiments as we use a polariser before the spectrometer and use a coherent light source. In this section, we will briefly derive the interference equation of two light beams with the same single wavelength[147].

We can write the wave equations for two beams of coherent light as

$$\mathbf{E}_1(\mathbf{r},t) = \mathbf{E}_{01}\cos(\mathbf{k}_1 \cdot \mathbf{r} - \omega t + \phi_1), \tag{2.49a}$$

and

$$\mathbf{E}_2(\mathbf{r},t) = \mathbf{E}_{02}\cos(\mathbf{k}_2 \cdot \mathbf{r} - \omega t + \phi_2), \tag{2.49b}$$

where $\mathbf{E}_1$ and $\mathbf{E}_2$ are the electric field strength of the two beams, ω is the frequency, t is time and ϕ_1 and ϕ_2 are the initial phases. As we measure the irradiance (time average of the magnitude of the electric field strength squared), rather than the sum of the electric field, we can evaluate the irradiance, $\mathbf{I}$,

$$\mathbf{I} = \left\langle \mathbf{E}^2 \right\rangle_T = \left\langle \mathbf{E}_1^2 + \mathbf{E}_2^2 + 2\mathbf{E}_1 \cdot \mathbf{E}_2 \right\rangle_T, \tag{2.50}$$

where $\mathbf{E}$ is the sum of the electric fields. From here, we can isolate $\langle 2\mathbf{E}_1 \cdot \mathbf{E}_2 \rangle_T = \mathbf{I}_{12}$, which is the interference term. From here on, we assume a collinear geometry

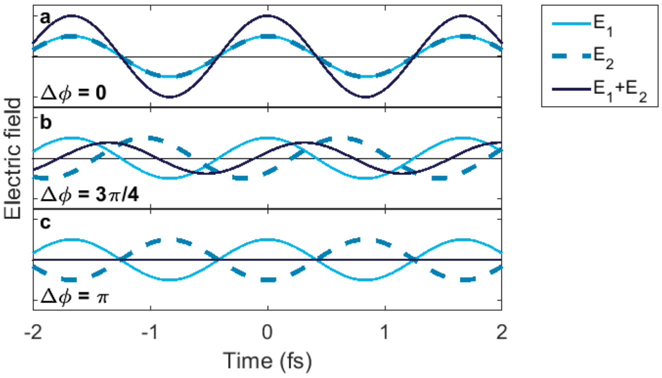

Figure 2.14: Overview of the effect of interference of two electric fields, according to equation 2.52, with different amount of phase delay for a wavelength of 500 *nm*.

($k_1 = k_2$), which is always the case for the performed experiments, and an ideal case of equal electric field strength. By using this assumption and that the time average of the electric field is half of the maximum field strength, $I_1 = I_2 = E_2/2$, we can evaluate the scalar interference term, which is the result of the cross term of equation 2.50, as

$$I_{12} = E^2 \cos \Delta\phi, \tag{2.51}$$

where $\Delta\phi$ is the phase difference between the two beams. This gives us the total irradiance

$$I = I_1 + I_2 + 2\sqrt{I_1 I_2} \cos \Delta\phi. \tag{2.52}$$

From this interference equation, there are three possible scenarios depending on the phase difference $\Delta\phi$, illustrated with the electric fields in figure 2.14: constructive interference ($\Delta\phi = 0, \pm 2\pi, ..$), deconstructive interference ($\Delta\phi = \pm 1\pi, \pm 3\pi, ..$) or an intermediate phase for all other values for $\Delta\phi$. It is important to note that any incoherence or temporal mismatch will result in a reduction of the interference contrast, that is, the difference in peak and valley values.

2.5.2 Frequency domain interference

Whereas in section 2.5.1 the assumption was made for a single wavelength, we can expand the interference term to become wavelength dependent. This is done by

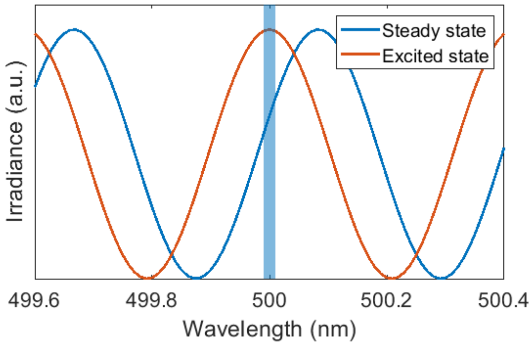

Figure 2.15: Interference model according to equation 2.52, extended in the frequency domain by using equation 2.54, for excited and ground state. The parameters for this model are a time delay of 2 ps between the reference and probe for the ground state. For the excited state, an exaggerated $\Delta n = 1$ over the whole spectrum for a material with a thickness of 100 nm is used, resulting in $\Delta\phi = -0.2\pi$ at 500 nm.

defining the relative phase:

$$\Delta\phi(\lambda) = -\frac{2\pi}{\lambda}\Delta\,\mathrm{OPL}, \tag{2.53}$$

where Δ OPL is the optical path length difference of the two pulses. For laser pulses, this can be written in the time-domain as

$$\Delta\phi(\omega) = -\omega T, \tag{2.54}$$

with T being the time delay between the two pulses. From this we can see that the phase difference is dependent on wavelength if we introduce a path length difference, or time delay, between the two pulses. The result of this is an interference in the frequency domain shown as the ground state interference in figure 2.15 for an optical path length difference of 596 μm, or 2 ps.

When a piece of material, i.e. sample, is introduced between the interferometer and detector, the increase of optical path length of both beams is equal. When we (optically) excite the sample between the reference and probe pulse, the refractive index observed by the probe may be modulated, depending on the optical properties of the material. The change in optical path length because of this excitation is given by

$$\Delta\,\mathrm{OPL}(\omega) = \Delta n(\omega) l, \tag{2.55}$$

where Δn is the change in refractive index and l is the thickness of the material. Note that the spatial profile of the probe beam has to measure the same $\Delta n(\omega)$ to obtain an acurate value, therefore, the probe spot has a diameter which is typically four times as small as the pump spot diameter. From equation 2.53 we know that the phase is directly related to the optical path length, and thus, by combining equations 2.53 and 2.55, we obtain

$$\Delta n(\omega) = -\frac{\Delta\phi(\omega) c}{\omega l}, \tag{2.56}$$

which shows a direct relation between the change of phase of the probe pulse and the refractive index. The result is a phase shift of the probe while that of the reference remains constant, resulting in a shift of the interference pattern. This is shown by the excited state in figure 2.15, where a refractive index change of 0.2 over the whole spectrum is simulated on a sample with a thickness of 100 nm.

2.5.3 Frequency domain interferometry system

A schematic of the important components of the ultrafast FDI setup is shown in figure 2.16. This setup a straightforward adaptation of an existing TAS system where the white light probe is split into a reference and probe pair with a Michelson interferometer. With the two arms set at different length, a fixed time delay is set between the two pulses. The grating then stretches the short broadband pulses due to the dispersion of the white light into its different frequency components[116]. This stretching results in temporal overlap on the detector as described in section 2.3, creating an interference pattern in the frequency domain from which the phase at each wavelength can be obtained.

Optical excitation of the sample is set around the probe arrival time, but has to arrive after the reference pulse to avoid modulation of the reference pulse. The pulse sequence is schematically shown in figure 2.17. The excitation event can alter the refractive index, resulting in a phase shift between the reference and probe as discussed previously.

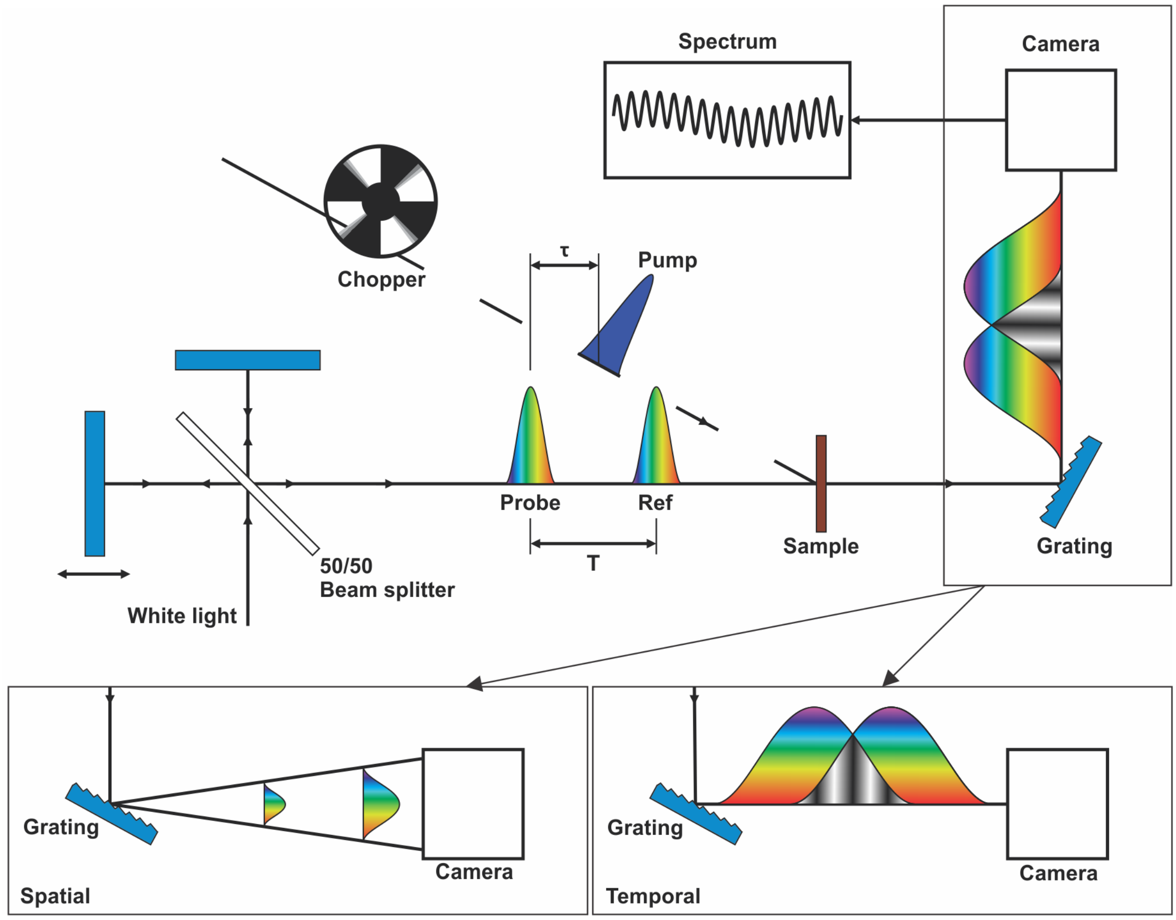

Figure 2.16: Schematic overview of the relevant components of a frequency domain interferometer. The pump and probe pulses arrive at the sample with time difference τ, while the reference and probe pulses arrive with time difference T. Every other shot of the pump is blocked by a mechanical chopper and the arrival time is controlled via a mechanical delay stage. The reference and probe pulses are spectrally dispersed after the sample using a grating, indicated in the box on the bottom left. This temporally stretches the reference and probe pulses so that they overlap, indicated by the box on the bottom right. This overlap creates an interference pattern in the frequency domain, which is collected by a 1D detector.

2.5.4 Phase extraction method

Knowing that there is a direct relation between the refractive index and the phase of the interferogram, we need a way to extract the phase information. Tokunaga *et*

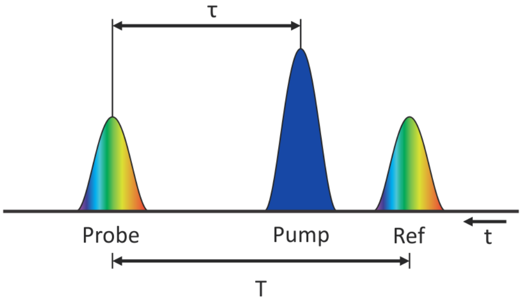

Figure 2.17: Schematic of the pulse sequence used in the frequency domain interferometer. A leading reference pulse arrives at the sample before the pump. Finally, the probe pulse arrives to observe the excited-state.

al.[36] used the shift of the minima of the interferogram to extract the phase. The estimated error due to intensity change is

$$\delta\Delta\Phi \approx \frac{-\exp(-\Delta k \pm 1)\delta dk/d\omega}{T + d\Delta\Phi/d\omega}, \tag{2.57}$$

with $\Delta\Phi = -\Delta n\omega x/c$ and $\delta\Delta\Phi$ being the differences between the actual and measured $\Delta\Phi$. In this equation, the minima corresponds to the -1 case while the maxima corresponds to the +1 case, resulting in a smaller error for the minima. This is a robust method, however, it limits the spectral resolution at which the phase can be acquired. The spectral resolution for this method can be increased by increasing the time delay between the reference and probe pulse creating an interference with a shorter period. However, increasing the time delay will reduce the temporal overlap of the reference and probe on the detector resulting in lower contrast between the maxima and minima of the interference as displayed in figure 2.18.

To overcome the limitation of spectral resolution, we have implemented a phase extraction method based on the discrete Fourier transform,

$$X_k = \sum_{m=0}^{N-1} x_m \exp(-\frac{i2\pi}{N}km), \tag{2.58}$$

where N is the number of samples, m is the considered sample, x_m is the value of the signal at time m, k is the considered frequency and X_K is the final obtained complex

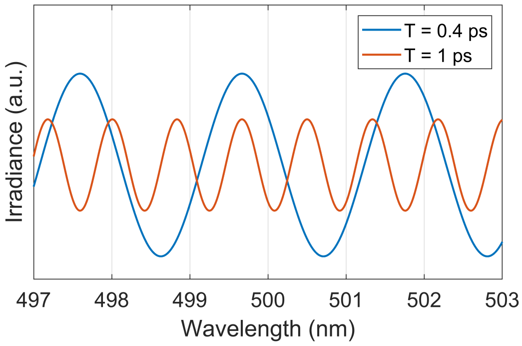

Figure 2.18: The effect of different time delay, T, between reference and probe on the interference pattern. Increased time delay decreases the period of the interference pattern, but lowers the interference contrast by decreasing the temporal overlap.

number containing amplitudes and phase of the frequencies that can reconstruct the signal[152]. A diagram of the steps of the Fourier method is displayed in figure 2.19 and has shown the same result as the minima analysis with significant higher spectral resolution[153].

This method selects a small spectral window containing at least one full oscillation of the interference pattern. A larger window will increase the accuracy of the phase extraction method as more oscillations are present, reducing the impact of noise within the spectral window. However, the inclusion of more frequency components will artificially smooth the obtained $\delta\phi$ as the frequency of the oscillations change with the probe wavelength. Including too many frequency components can broaden the dominant frequency, introducing errors in finding the actual frequency of the centre wavelength. The average of the signal within the window is then subtracted to achieve oscillations around zero to prepare the data for additional padding. After this, the spectrum is multiplied by a Hanning window to eliminate the effect of discontinuous (nonzero) boundary values. This spectrum is then padded by zero values to obtain more accurate amplitudes of the frequencies. This implemented method is empirically found to resolve a more consistent phase compared to no processing or either only applying the Hanning window or padding.

By taking the Fourier transform, the dominant frequency of the window is ex-

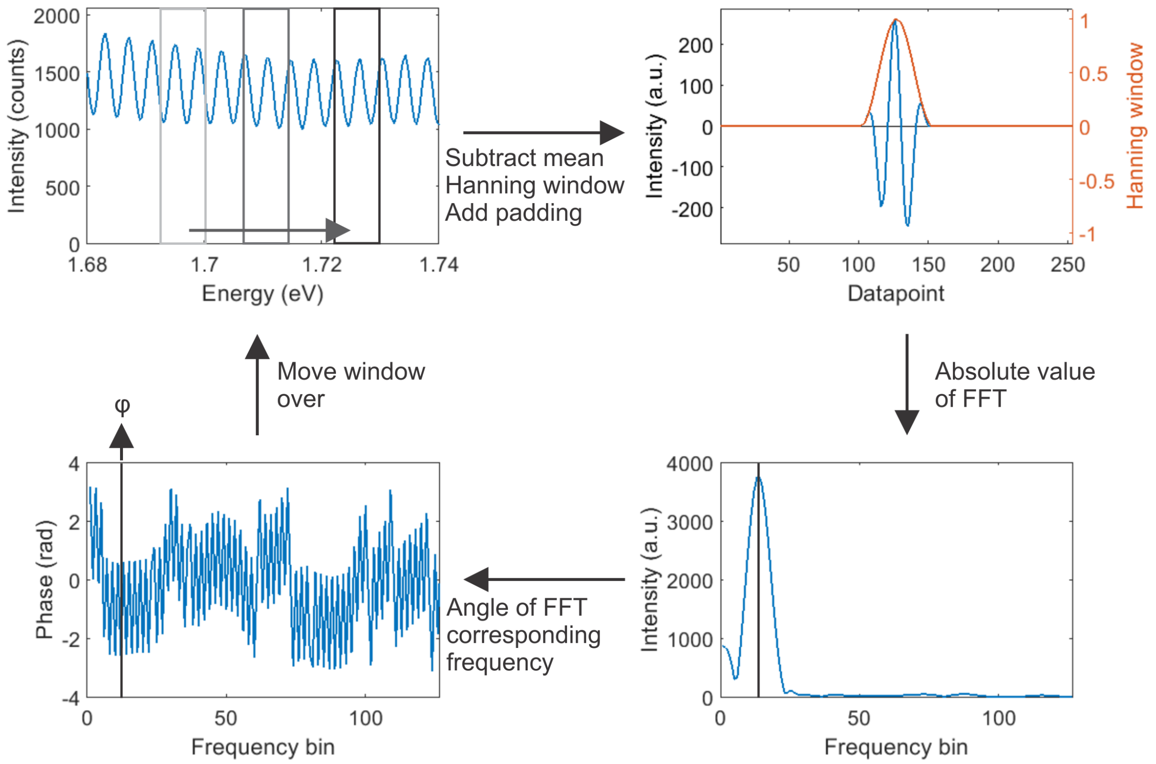

Figure 2.19: Step by step process to extract the phase. First, a window is selected. Then, the mean is subtracted and the window is multiplied by a Hanning window to remove the impact of nonzero values at the edge of the window. Then the window is padded by zeros to artificially increase the intensity contrast. The dominant frequency is extracted by taking the Fourier transform and its corresponding phase is stored. This is repeated until the whole spectrum has been analysed, for every time point for both excited and ground state. The difference in phase is obtained by subtracting the phase of the ground state from the excited-state

tracted by finding the frequency with the highest intensity of the absolute value of X_k. The phase of this frequency is extracted by the corresponding argument of X_k. By doing this for both excited and ground state, the change of phase is extracted. The Matlab code written for extraction of the change in phase and refractive index can be found in appendix A.

2.6 Conclusion

In this chapter, the relations between optical constants and the reflection, transmission and absorption are discussed. Furthermore, the field of nonlinear optics is introduced including second harmonic generation and supercontinuum generation. Detail is given on the origin and effects of Kerr-lensing, self-phase modulation, self-steepening, four-wave mixing, phase-matching, group velocity dispersion and group delay dispersion on supercontinuum generation.

Three ultrafast spectroscopic techniques are discussed: PG-FROG, TAS and FDI. The PG-FROG is capable of measuring the duration of ultrafast laser pulses, using an optical Kerr-gate. The TAS measures the change in transmission of a broadband probe pulse travelling through a sample between the ground state and excited state. The FDI measures the change in the phase of a broadband probe pulse, related to the real part of the refractive index, after traveling through a sample in the ground state and excited state. This technique extracts the phase of the probe pulse by obtaining the frequency domain interference between the probe and a unperturbated reference pulse.

Chapter 3

Direct measurement of the ultrafast photoinduced refractive index change of $CsPbBr_3$ Perovskite

The contents of this chapter have resulted in the following publication:

Ultrafast Spectrally Resolved Photoinduced Complex Refractive Index Changes in $CsPbBr_3$ Perovskites, *R.R. Tamming*, J. Butkus*, M.B. Price, P. Vashishtha, S.K.K. Prasad, J.E. Halpert, K. Chen and J.M. Hodgkiss* **- ACS Photonics 2019[154]†**

3.1 Introduction

Perovskite photovoltaic materials have shown great promise for solar cell applications due to their high power conversion efficiency[155,156]. On top of that, they are easily tunable for light-emitting diodes[157,158] and show the capability to be used in lasers[16,159]. Therefore, these materials are extensively studied by using ultrafast spectroscopy to obtain an insight into the key parameters such as BGR[29], hot carrier cooling[29,160,161], diffusion lengths[73,162], and carrier recombination rates[73].

One of the techniques used to unravel the excited state dynamics is TAS, which is discussed in section 2.4. With this technique, the assumption is made that the difference in transmission is solely coming from the change of absorption of the sample, and thus ignoring the change of the real part of the refractive index. This is true for materials with low real refractive indices, such as early organic photovoltaic materials. However, this assumption breaks down once the refractive index increases which is the case for the more efficient perovskite photovoltaic materials. The transient refractive index results in reflection artefacts which can have a significant impact on the TA signal of these materials[29,141]. Besides artefacts in the TA signal, the change

---

*Both authors contributed equally to this work.

†Justinas Butkus provided the setup and performed the measurements. Parth Vashishtha provided the samples. Ronnie Tamming performed the data analysis and further modelling.

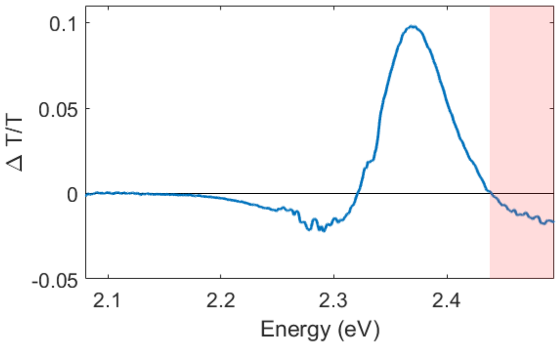

Figure 3.1: Transient absorption signal of microcrystalline $CsPbBr_3$ perovskite with a thickness of 72.5 nm at 400 fs. The sample is pumped at 400 nm with a fluence of 3.8 $\mu J/cm^2$. The origin of the signal indicated by the pink box is still under debate.

in refractive index can have great implications for the development of novel devices, such as optical switches, photodetectors, modulators, photovoltaic cells and laser cavities[53,84,139].

The transient absorption spectrum of $CsPbBr_3$ is shown in figure 3.1, where the origin of the negative signal at the area indicated in pink is still under debate. Attempts to decouple the absorption and reflection contributions to the TA signal have been made with inconclusive outcomes. Price *et al.* have measured both the transient transmission and reflection spectra simultaneously of a $CH_3NH_3PbI_3$ perovskite sample and report a strong reflection effect, especially in the photoinduced absorption signal above the band edge[29]. This technique, however, is model dependent, difficult to implement and suffers from scattering of polycrystalline samples. Their claim of the reflection effect is rebutted by Ghosh *et al.*[141], who have measured large suspended perovskite nanocrystals, to avoid scattering, and films on substrates with different refractive indices and found nearly no impact on the transient transmission signal. This is backed up by Anand *et al.*[142] who have modelled the refractive index change. While there are models to estimate the transient refractive index from the different excited state dynamics, such as carrier generation, band filling, plasma intraband transitions and Coulombic carrier interactions[84,163,164], measurements that have directly obtained the true excited-state dielectric constants, just like ellipsometry directly measures the dielectric constant of the steady state spectrum[165], are lacking.

In this chapter, the FDI, an adaptation of TAS, is used to directly measure the real part of the refractive index, which has not yet been applied to modern semiconductor materials[36]. The working principles of FDI are discussed in section 2.5. This technique is applied here to $CsPbBr_3$ perovskite films to extract their transient refractive index. This is then fed into the KK relations to obtain the excited-state imaginary part of the refractive index, which is directly related to the change in absorption. Basic Fresnel equations are then used with the complex refractive index to successfully reconstruct the TA signal to show the reliability of this technique.

Finally, the real carrier temperature and cooling is extracted and the values of the change of refractive index are used to estimate the impact on semiconducting laser cavities, showing that a significant design change is required for optimal emission. Also, the efficiency change of a concentrating solar cell is estimated. This shows a strong decrease of power conversion efficiency with increasing excitation density due to the increase in reflection.

3.2 Theory

The FDI system, first developed by Tokanuga *et al.*[36], uses the difference of the phase of an identical reference and probe pulse pair to directly measure the photoinduced modulation of the real part of the refractive index. The theory of the FDI technique and the data processing steps required to obtain the change in the refractive index are discussed in section 2.5. Here, we discuss the relation between the real and imaginary part of the refractive index, related to the reflection and absorption of the material respectively.

Kramers-Kronig relations

The real part and imaginary part of the linear refractive index are related via the KK relations[166]. This is a dispersion relation given by

$$n(\omega) - 1 = \frac{c}{\pi}\mathcal{P}\int_0^{\infty} \frac{\alpha(\Omega)d\Omega}{\Omega^2 - \omega^2}, \tag{3.1}$$

where $n(\omega)$ is the wavelength dependent real refractive index, $\mathcal{P}$ is the cauchy principal value and $\alpha(\Omega)$ is the absorption coefficient over all frequencies Ω.

The KK relation always holds for linear optics, in contrast to nonlinear optics for which the relation is only satisfied with certain causality conditions[149]. These conditions are normally not met for regular ultrafast spectroscopic methods due to its nonlinear nature. Besides this, the obtained signals generally contain a contribution from both the real and imaginary part of the refractive index, which effects can only be separated using models. However, they are fulfilled by using this FDI setup with a weak probe field as the reference pulse arrives at the sample before the strong perturbation field[149]. The boundary conditions for this state that no change in charges can be generated before time zero and that the population of carriers after time zero is in quasi-equilibrium, that is, slowly changing compared to the duration of the probe pulse. This assumption is valid throughout this thesis as the timescale of the kinetics occurring within the discussed samples is on a timescale that is several orders of magnitude larger than the probe duration. Thus, this setup allows the recovery of the change in imaginary part of the refractive index from the real part of the refractive index. Finally, the change in absorption coefficient can be used to calculate the change in imaginary refractive index according to

$$\alpha(\omega) = \frac{2\omega \Delta k(\omega)}{c}. \tag{3.2}$$

Practically, this is calculated using the Hilbert function from Matlab using the code provided by Djorović *et al.*[167].

Fresnel equations

The (excited) complex refractive index can be used to calculate the total transmission and reflection spectrum of a sample using Fresnel equations[101]. To calculate these spectra, the specific sample configuration is used. This is a three layer system with the substrate, sample and air, with their respective complex refractive index.

The equations used to calculate the steady and excited state transmission are fully derived in the book by Born and Wolf[101]. These calculated transmissions for a perpendicular probe beam are then used to calculate the TA signal according to equation 2.48. The used conventions are

$$n_1 = 1.48 \quad (3.3) \qquad \hat{n}_2 = n_2(1 + k_2 i) \quad (3.4) \qquad n_3 = 1, \quad (3.5)$$

where n_1 is the refractive index of the substrate, $\hat{n}_2$ is the complex refractive index of the sample as used for the remainder of this calculation, with n_2 and $n_2 k_2$ the real and imaginary part of the refractive index, respectively, and n_3 is the refractive index of vacuum. To do this, it is convenient to set

$$\hat{n}_2 = u_2 + i v_2, \tag{3.6}$$

from which we obtain

$$u_2 = \sqrt{\frac{n_2^2(1 - k_2^2) + \sqrt{(n_2^2(1 - k_2^2)^2 + 4n_2^4 k_2^2}}{2}}, \tag{3.7}$$

and

$$v_2 = \sqrt{\frac{-n_2^2(1 - k_2^2) + \sqrt{(n_2^2(1 - k_2^2)^2 + 4n_2^4 k_2^2}}{2}}. \tag{3.8}$$

By using the transmission of a single interface

$$t_{12} = \tau_{12} \exp\left(i \chi_{12}\right) = \frac{2n_1}{n_1 + u_2 + i v_2}, \tag{3.9}$$

where χ_{12} is the phase of the light after the first interface, we obtain the transmission for the first interface. The second interface is obtained by replacing the subscripted numbers:

$$\tau_{12} = \sqrt{\frac{(2n_1)^2}{(n_1 + u_2)^2 + v_2^2}}, \quad (3.10) \qquad \tau_{23} = \sqrt{\frac{4(u_2^2 + v_2^2)}{(n_3 + u_2)^2 + v_2^2}}, \quad (3.11)$$

where τ_{12} and τ_{23} are the transmissions of the first and second interface respectively. The corresponding phases of the transmitted light at the boundaries are given by

$$\tan \chi_{12} = \frac{v_2}{n_1 + u_2}, \qquad (3.12) \qquad \tan \chi_{23} = \frac{v_2 n_3}{u_2^2 + v_2^2 + u_2 n_3}, \qquad (3.13)$$

for the first and second interface respectively. When now considering the coefficient for reflection

$$\rho_{12} = r_{12} \exp\left(i\phi_{12}\right) = \frac{n_1 - u_2 - iv_2}{n_1 + u_2 + iv_2}, \tag{3.14}$$

it is possible to calculate the reflection at each interface via

$$\rho_{12} = \sqrt{\frac{(n_1 - u_2)^2 + v_2^2}{(n_1 + u_2)^2 + v_2^2}}, \qquad (3.15) \qquad \rho_{23} = \sqrt{\frac{(n_3 - u_2)^2 + v_2^2)}{(n_3 + u_2)^2 + v_2^2}}, \qquad (3.16)$$

and the corresponding phase changes are given by

$$\tan \phi_{12} = \frac{2 v_2 n_1}{u_2^2 + v_2^2 - n_1^2}, \qquad (3.17) \qquad \tan \phi_{23} = \frac{2 v_2 n_3}{u_2^2 + v_2^2 - n_3^2}. \qquad (3.18)$$

Furthermore, it is convenient to set

$$\eta = \frac{2\pi}{\lambda} d_m, \tag{3.19}$$

where d_m is the thickness of the sample and λ is the wavelength of light. From here, the total transmission and reflection coefficients can be calculated according to

$$t = \tau \exp\left(i\delta_r\right) = \frac{\tau_{12}\tau_{23} \exp\left(-v_2\eta\right) \exp\left(i(\chi_{12} + \chi_{23} + u_2\eta)\right)}{1 + \rho_{12}\rho_{23} \exp\left(-2v_2\eta\right) \exp\left(i(\phi_{12} + \phi_{23} + 2u_2\eta\right)}, \tag{3.20}$$

and

$$r = \rho \exp\left(i\delta_r\right) = \frac{\rho_{12} \exp\left(i\phi_{12}\right) + \rho_{23} \exp\left(-2v_2\eta\right) \exp\left(i(\phi_{23} + 2u_2\eta)\right)}{1 + \rho_{12}\rho_{23} \exp\left(-2v_2\eta\right) \exp\left(i(\phi_{12} + \phi_{23} + 2u_2\eta)\right)}, \tag{3.21}$$

respectively. The final transmission and reflection ratios are given by

$$T = \frac{n_3}{n_1}|t|^2 = \frac{n_3}{n_1}\frac{\tau_{12}^2\tau_{23}^2 \exp\left(-2\nu_2\eta\right)}{1+\rho_{12}^2\rho_{23}^2 \exp\left(-4\nu_2\eta\right)+2\rho_{12}\rho_{23}\exp\left(-2\nu_2\eta\right)\cos(\phi_{12}+\phi_{23}+2u_2\eta)}, \tag{3.22}$$

and

$$R = |r|^2 = \frac{\rho_{12}^2 \exp\left(2\nu_2\eta\right)+\rho_{23}^2 \exp\left(-2\nu_2\eta\right)+2\rho_{12}\rho_{23}\cos(\phi_{23}-\phi_{12}+2u_2\eta)}{\exp\left(2\nu_2\eta\right)+\rho_{12}^2\rho_{23}^2 \exp\left(-2\nu_2\eta\right)+2\rho_{12}\rho_{23}\cos(\phi_{12}+\phi_{23}+2u_2\eta)}, \tag{3.23}$$

respectively.

3.3 Michelson frequency domain interferometer

The FDI setup is an adaptation of the TA setup and is depicted in figure 3.2[36]. The 100 fs pulses, centred at 800 nm, are generated by a Ti:sapphire amplifier system (MaiTai, Spitfire, Empower, SpectraPhysics). A beam splitter (not shown) is used to select a small portion of the beam for the probe. The pump is then sent down a delay stage with a retro reflector to control the time delay. After this, the second harmonic signal, indicated by the blue line, is generated using a Barium Borate crystal to excite the sample above the band edge. A wire grid polariser and a $\lambda/2$ waveplate are used to set the pump polarisation to the magic angle (54.7 °) with respect to the probe polarisation and attenuate the pump. Finally, a concave mirror loosely focuses the pump onto the sample to a spot size with a diameter of 600 μm FWHM.

The probe is focused on a YAG crystal to generate a broad supercontinuum as discussed in section 2.2.2, indicated by the yellow line. A physical beam block is placed, 150 mm from the YAG crystal, to block most of the the bright fundamental while transmitting most of the generated supercontinuum wavelengths. This beam is then refocused using a concave mirror and collimated by an off-axis parabolic mirror. The collimated probe then passes through a Michelson interferometer, which uses a broadband 50/50 beam splitter to create a reference-probe pulse with equal intensity to generate optimal interference contrast. The probe pulse for this experiment is delayed 2 ps relative to the reference pulse to balance between the observable temporal range and interference contrast. Both beams are sent down to the same path and

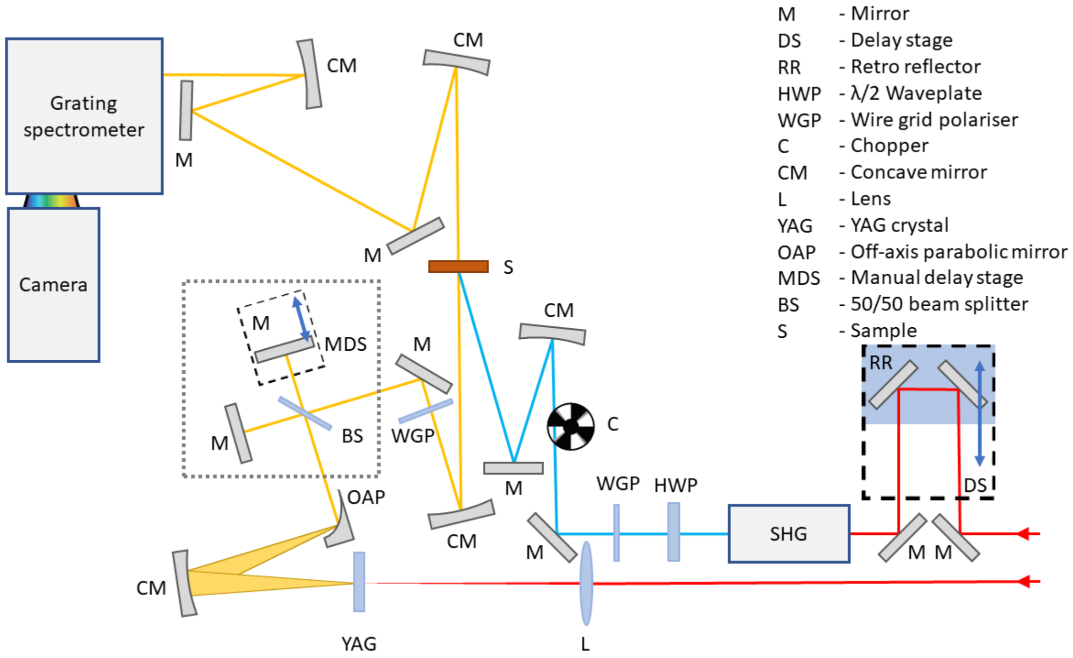

Figure 3.2: Schematic of the setup used for the FDI experiment. All optical components are listed on the right, ordered by following the beampath (first pump path, then probe path). The gray dotted box indicates the Michelson interferometer, which is the only change made to the existing TAS setup.

focused onto the sample to a spot size of 150 μm FWHM using a concave mirror. The reference and probe are then collimated and focused onto the entrance slit of a grating spectrometer (SpectraPro 2150, Princeton Instruments). This spectrometer is equipped with a 1,200 gr/mm grating to disperse the pulses into their spectral components. These components are projected on a 1D linescan camera (LightWise LW-ELIS-1024A-1394) resulting in a 0.02 nm/pixel resolution.

3.4 Results and discussion

3.4.1 Obtained frequency domain interference and phase change

The interference pattern observed by the FDI is shown in figure 3.3a. This figure shows both the reference and probe signal and the signal for the probe alone. The

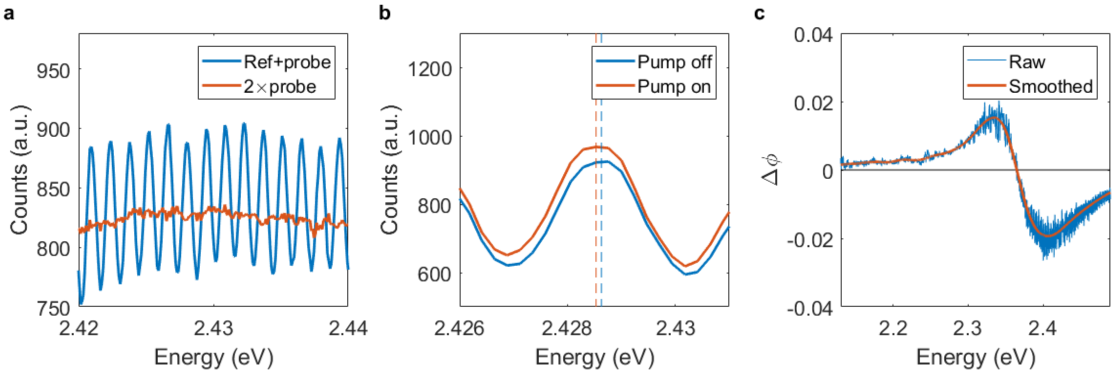

Figure 3.3: a) Observed spectra of the FDI system for the reference and probe pulses arriving at the detector (blue) with a 2 ps delay between the pulses, and just the probe pulse (red). The signal for the probe has been doubled as the intensity of the probe pulse is half that of the reference and probe pulses combined. b) The observed interference pattern without (blue) and with (red) pump pulse of microcrystalline $CsPbBr_3$ perovskite, 1.5 ps after excitation. The sample is pumped at 400 nm with a fluence of 3.8 $\mu J/cm^2$. The peak positions are indicated by the dashed line in their respective colours. This shows that a small phase shift of the interference pattern is observed after excitation.

latter is multiplied by two to equal the intensity observed by the detector, as half of the probe pulse is used for the reference pulse. This shows that a clear interference pattern is observed on the detector.

When introducing a pump pulse on the $CsPbBr_3$ perovskite sample, the refractive index of this sample is modulated. This results in a change of optical path length of the probe with respect to the reference pulse which is reflected by a shift of the interference pattern. This shift corresponds to the change of phase between the reference and probe pulse according to equation 2.53 and is shown in figure 3.3b. The change of phase is extracted for the whole spectrum by using the method described in section 2.5.4, and is shown in figure 3.3c. The obtained data is smoothed before further analysis steps to eliminate the fluctuations obtained by the Fourier phase extraction method. From this phase change, the change of refractive index is obtained by using equation 2.56.

3.4.2 Retrieved (complex) refractive index change

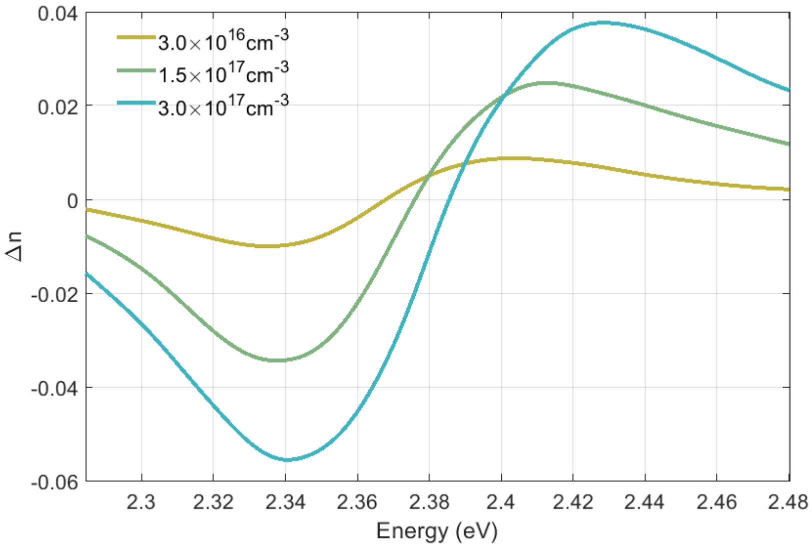

Figure 3.4: a) Fluence dependent refractive index change of microcrystalline $CsPbBr_3$ at 400 fs after excitation by a 400 nm pump pulse. The fluences used are 0.76 μJ/cm^2, 3.8 μJ/cm^2 and 7.6μJ/cm^2, indicated from light green to blue.

The obtained change in refractive index is shown in figure 3.4 for $CsPbBr_3$ microcrystalline perovskite film with a thickness of 72.5 nm, measured at multiple locations by a Dektak 150 profilometer, 400 fs after excitation. The sample is prepared by Dr. Parth Vashishtha and the full procedure can be found in appendix A.3[154]. The sample is excited at 400 nm with fluences of 0.76 μJ/cm^2, 3.8 μJ/cm^2 and 7.6 μJ/cm^2, resulting in an estimated carrier density of 3×10^{16} cm^{-3}, 1.5×10^{17} cm^{-3} and 3×10^{17} cm^{-3} respectively. These transients show a derivative-like shape of the real refractive index with a zero crossing near the band edge of 2.37 eV. This shows that the refractive index does indeed change around the band edge and indicates that the change in reflection does have an impact on the spectral shape of the features present in the TA spectrum.

From here, we show the measurement with an excitation fluence of 3.8 μJ/cm^2 for the following analysis. The time dependent real part of the refractive index is shown in figure 3.5a. This is used with the KK relations to obtain the imaginary part of the

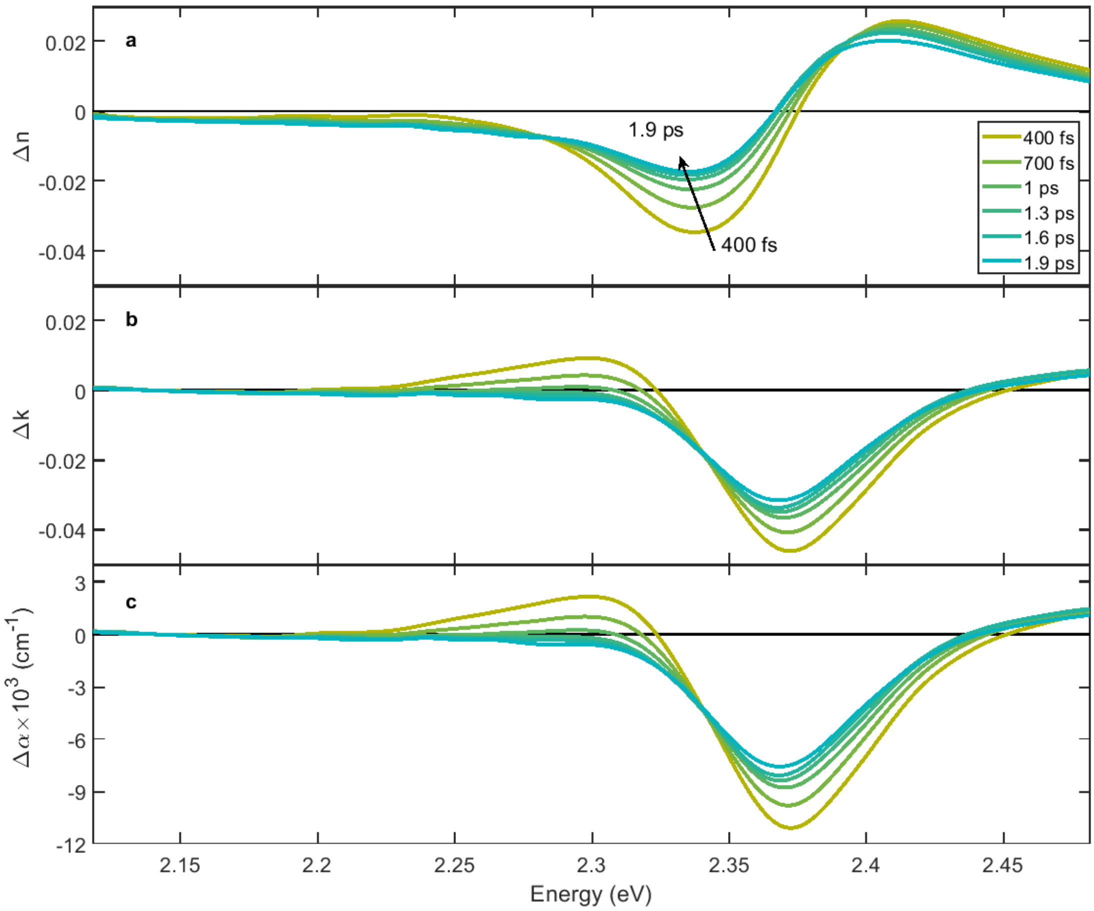

Figure 3.5: a) Obtained change in the real part of the refractive index of microcrystalline CsPbBr$_3$ from 400 fs to 1.9 ps with 300 fs steps. b) The corresponding retrieved change in the imaginary part of the refractive index via KK relations. c) The calculated change in absorption coefficient. The sample is pumped at 400 nm with a fluence of 3.8 μJ/cm^2

refractive index. Unfortunately, the spectral range available with this system did not fully capture the response on the high energy side. As the KK relations assume that the response is zero at $\omega = 0$ and $\omega \to \infty$, extrapolation of the signal is required. As the low energy side is almost zero, this side is extended with zeros. On the high energy side, however, the signal is nonzero. Therefore, we have extrapolated the data to go to zero, assuming that the effect of the second band edge on this spectral region is negligible. This assumption is supported when considering the energy difference between the band edges (5.5 eV)[168], and the small extent of the change in refractive index below the first band, which is up to ∼0.26 eV. The extrapolation of the spectral window to zero and infinity frequency, approximated by 10,000 eV and 0 eV respectively, is done in three ways: padding with zeros, linear extrapolation and an exponential decrease. The zero padding causes a significant drop of the imaginary part of the refractive index signal at the last 0.02 eV of the spectrum in comparison to the other methods due to the discontinuous step. Both linear and exponential extrapolation to zero have the same (initial) decrease as the decrease at the edge of the spectrum. These spectra are further padded by additional zeros to comply with the KK assumption at infinite frequency. These two methods show very little difference between themselves in retrieving the the transient imaginary refractive index. As the difference of the retrieved transient imaginary refractive index is small, the linear extrapolation is used for the calculation of the imaginary part.

Furthermore, $\Delta\alpha(\Omega)$ has to fall off faster than $1/\Omega^2$. Assuming that the change in the refractive index is a local perturbation, as discussed above, the measured spectrum is not impacted by the perturbation of other energy bands. From here, we can describe the $\Delta\alpha$ spectrum with an ensemble of individual Lorentz oscillators at all wavelengths within the observed spectrum. As a Lorentzian lineshape falls of faster than $1/\Omega^2$, we can see that this condition holds as well[149,169].

The obtained change in the imaginary part of the refractive index and absorption coefficient is shown in figure 3.5b and c. The change in absorption coefficient shows strong resemblance to the observed TA spectrum, shown in figure 3.6a. A strong increase of absorption below the band edge is observed, which completely disappears within the first picosecond. This feature has been assigned to the BGR, which is a well-known feature in perovskite materials[29]. The fast decrease is caused by hot-carrier cooling, where carriers with energy $E > E_g$ lose energy by emission of phonons to relax to the band edge. The strong decrease in absorption at 2.36 eV is the result of GSB. Again, a quick reduction at the ps timescale of this signal is observed, where the high energetic carriers relax back to the newly generated band edge. Lastly, an increase in absorption is observed above the band edge. This shows that at least part of this signal is a result of the change in absorption and thus not solely due the change in reflection.

3.4.3 Comparison with a measured transient absorption signal

The change in complex refractive index is added to the steady state refractive index from Ahmad *et al.*[170] to calculate the excited state refractive index. These are then used with Fresnel equations including Fabry-Perot reflections to calculate both excited and steady state transmission and reflection spectra. The Fresnel equations are discussed in section 3.2. These equations model a three layered structure which includes the sample layer, the substrate on which it is spin-coated and the vacuum on the other side of the sample.

These Fresnel equations have only one free parameter which is the thickness of the sample. From the steady state and excited-state transmission spectra, the TA signal is calculated in the same way as the measured transmission spectra described by equation 2.48. The result is shown in figure 3.6a, with the thickness of the sample set to 72.5 nm to best match the measured TA spectrum. For consistency, this thickness is also used to calculate the refractive index change from the phase change. This shows strong consistency between the directly measured TA spectrum and the retrieved TA spectrum from the refractive index change, which is a good indication of the reliability of this technique.

For this research, the contributions of transient transmission and transient reflection at the high energy side of the bleach is the main part of interest. To analyse the individual contributions of transmission and reflection, the change in transmission and reflection is calculated in the same way as in the paper from Price *et al.*[29] and is shown in figure 3.6b. Both the steady and excited state refractive index are used to calculate the change of transmission and reflection, normalised to the sum of steady state transmission and reflection. In this region, the calculated transient reflection spectrum shows a very small change in reflection at the PIA region, above 2.43 eV in figure 3.6, indicating that the reflection in this region remains almost unchanged. This suggests that, in agreement with the recent results from Ghosh *et al.*[141], the transient reflection is not largely responsible for the observed PIA signal.

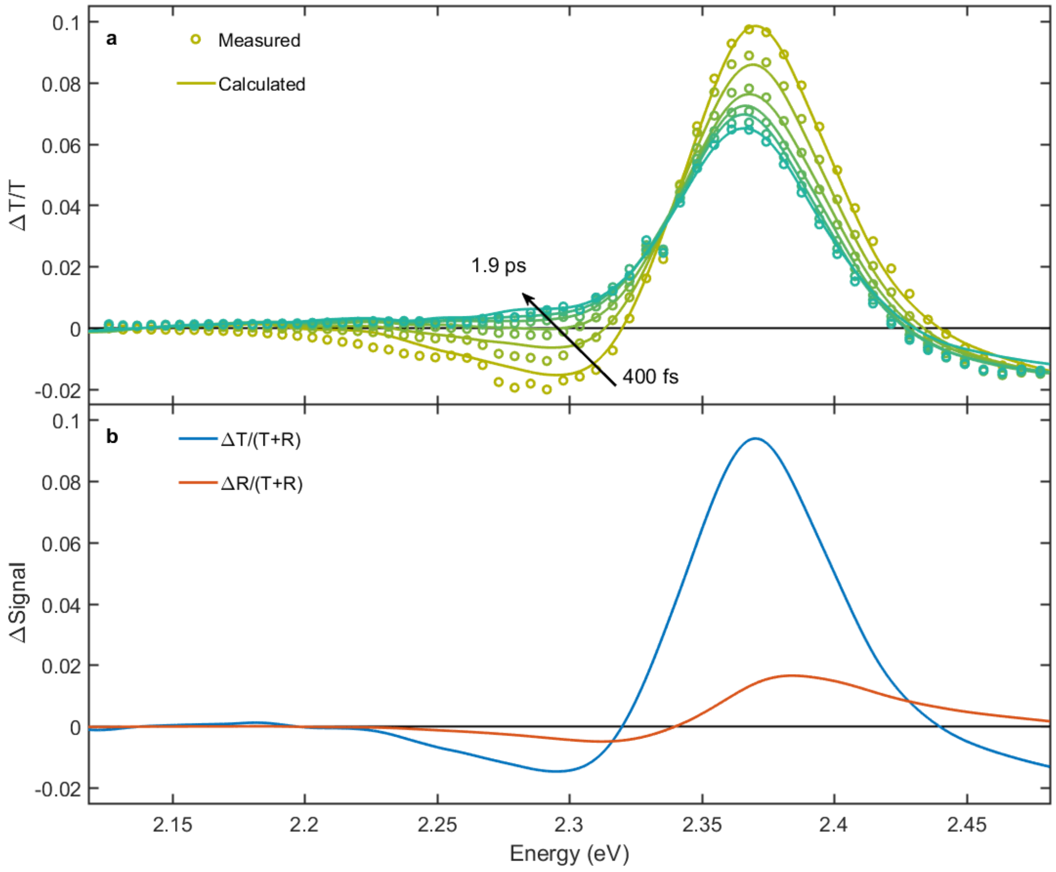

Figure 3.6: a) Calculated and measured transient transmission spectra at different time delays with 300 fs intervals on a thin film of microcrystalline $CsPbBr_3$ perovskite with a fluence of 3.8 $\mu J/cm^2$ at 400 nm. b) Corresponding calculated transient transmission and reflection spectra at 400 fs.

3.4.4 Origin of the photoinduced absorption signal

To support this claim, we have created a model which could explain the observed PIA signal. Pogna *et al.*[171] have found that the BGR dominates the TA spectrum for 2D transition metal dichalcogenide materials. Similarly, others have found strong evidence of BGR for perovskite in this region[78,172]. Therefore, we have extended this to the $CsPbBr_3$ perovskite to see what the effect of BGR would be on the Δk signal.

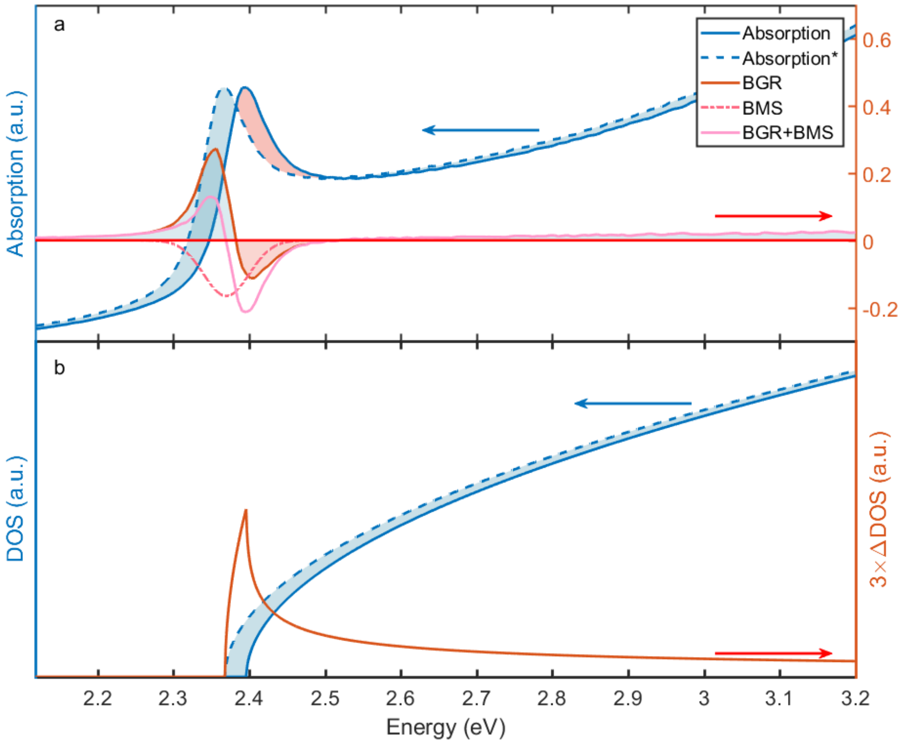

Figure 3.7: a) Model to show the effect of the extended bandgap renormalisation at the high energy side of the bleach. This model includes the effect of bandgap renormalisation on the (excited-state) absorption spectrum in (dashed) blue, and it's resulting change in absorption in red. The state filling is indicated by the pink dashed line and the sum of these mechanisms is shown in pink. b) Change of Density of States (DOS) for a parabolic band edge with a BGR of 25 meV. Reprinted with permission from Tamming *et al.*[154]. Copyright 2019 American Chemical Society.

The model, shown in figure 3.7a, shows the effect of BGR and state filling on the $\Delta\alpha$ spectrum. The BGR is modelled by shifting the steady-state absorption spectrum of the sample, while the state filling is modelled by a Gaussian, which is a similar shape to the GSB observed in the TA spectrum of figure 3.6. Here, the bandgap shift is assumed to be 25 meV, which is in the order of magnitude found by Yang *et al.*[172], indicated by the blue dashed line. From this, we observe an enhanced absorption below the exciton peak energy, near 2.4 eV, and a decreased absorption at the peak energy and above. However, when going to higher energies, the absorption increases again due to the extended BGR. When considering the state filling (pink dash-dotted line) we get a final spectrum, indicated with a solid pink line, which shape looks remarkably like the early time Δk spectrum in figure 3.5b. Note that the effect of state-filling is arbitrarily chosen and serves the purpose of giving an impression of the combined effect of BGR and state filling on the Δk shape.

As the band structure of perovskites is approximated by parabolic bands, we have used the parabolic band approximation to show the effect of BGR when extended to higher energies shown in figure 3.7b. This shows that this shift creates a large amount of new states (ΔDOS) below the band edge, however, the amount of newly generated states goes down with increasing energy. This is in good agreement with TA measurements and supports the hypothesis that BGR is the main contribution to the high energy PIA[142,172].

3.4.5 Impact on high carrier concentration devices

At the bleach however, the reflection effect interferes with the TA signal. The slope of the high energy side of the bleach is often used to estimate the carrier temperature by fitting the Fermi-Dirac distribution[29,173,174]. The additional reflection in this region has an impact on the shape of the GSB, altering the estimated carrier temperature using this method. To validate this hypothesis, we have fitted the Fermi-Dirac distribution, given by equation 1.1, to the edge of the bleach between 2.415 eV and 2.45 eV for both the measured TA and $\Delta\alpha$ spectra. The fits are shown in figure 3.8a and 3.8b for a couple of time points. From the Fermi-Dirac distribution, the carrier temperature is obtained as shown in figure 3.8c. This shows that the estimated initial carrier temperature is higher for the TA signal. Besides the increased temperature, the corresponding carrier cooling rate is also found to be overestimated.

Finally, we look at the impact of the change of the refractive index on high carrier concentration device structures. These are devices that operate under conditions which result in a high density of carriers within the semiconductor, such as laser cavities and concentrating solar cells. The latter uses focusing mirrors to concentrate the sunlight of a large area onto a small solar cell to reduce the size of the active component and thereby reduce the cost of solar cell systems.

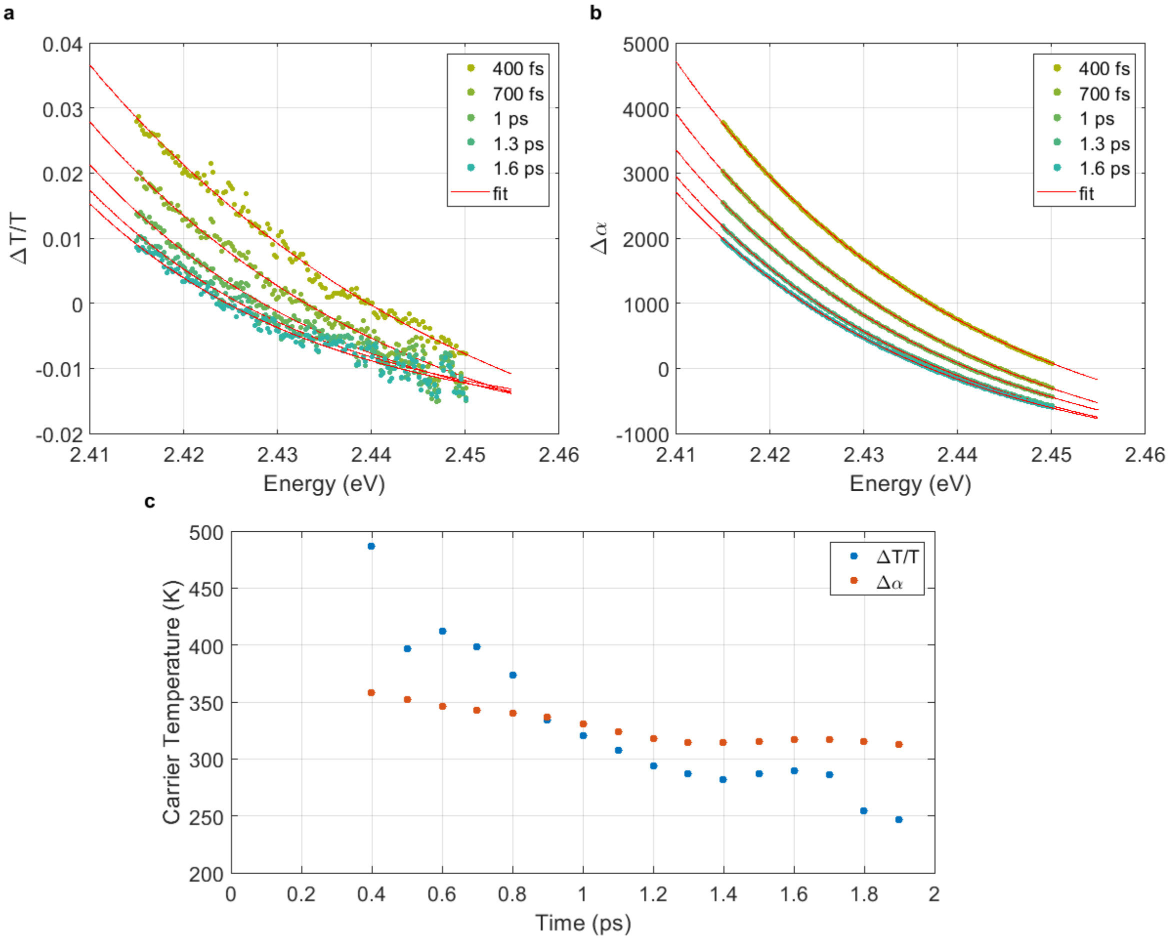

Figure 3.8: a) And b) shows the fitting the carrier temperature by the Fermi-Dirac distribution (equation 1.1) between 2.15 and 2.45 eV, which is at the high energy side of the GSB for the $\Delta T/T$ and $\Delta\alpha$, respectively. c) The obtained carrier temperature for the different time delays, showing higher estimated carrier temperature from the refractive index impacted $\Delta T/T$ signal.

For a simple semiconductor laser cavity, the resonant emission wavelength is given by

$$\lambda_0 = \frac{2nL}{m}, \tag{3.24}$$

where n is the real part of the refractive index, L is the length of the cavity and m is an integer[28]. This condition shows that a multiple of half a period of the desired wavelength must fit within the cavity to obtain resonant emission. The observed stimulated emission peak of $CsPbBr_3$ at room temperature is around 530 nm (2.34 eV)[82,175], which is in the region of largest Δn change as seen in figure 3.5a. By using the steady state real refractive index of 2.2 at this wavelength[170], we obtain a resonant cavity length which is a multiple of 120.5 nm. Our highest measured fluence experiment, which resulted in a carrier density of approximately 3×10^{17}cm^{-3}, resulted in a refractive index change of -0.06 in this region. This results in an optimal cavity length which is a multiple of 123.4 nm. The fluence used (7.6μJ/cm^2) to obtain this refractive index change is well below the lasing threshold of $CsPbBr_3$, which is over tenfold higher[176,177]. This would result in an even stronger modulated Δn and thus a longer resonant cavity length.

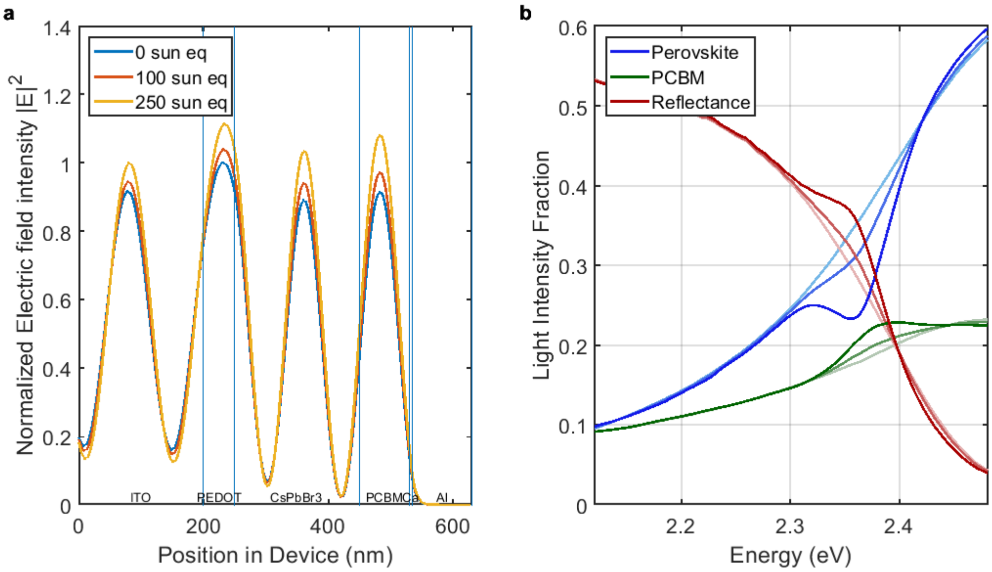

Figure 3.9: Structure of the perovskite solar cell and the electric field distribution of light with a wavelength of 532 nm within the device according to the model from Burkhard *et al.*[178]. The thickness of the materials is, from left to right, 200 nm, 50 nm, 200 nm, 80 nm, 5 nm and 95 nm. b) Contributions of absorption and reflection for steady state, 100 sun equivalents and 250 sun equivalents as estimated by Wang *et al.*[179], from light to dark. The estimated short circuit currents, assuming 100 % internal quantum efficiency, are 1.5376 mA/cm^2, 1.5024 mA/cm^2 and 1.4276 mA/cm^2. Reprinted with permission from Tamming *et al.*[154]. Copyright 2019 American Chemical Society.

Besides applying Perovskite materials in laser cavities, they are also being considered for concentrating solar cells. Therefore, we have evaluated the effect of the refractive index on a solar cell device structure. This is done with the help of a model published by Burkhard *et al.*[178], which uses the transfer matrix method to estimate the active layer absorption[180,181]. This model uses the real and imaginary part of the refractive of all layers of a solar cell structure to calculate the electric field within each layer, taking into account internal reflections and transmissions, absorption and interference. In this case, the internal quantum efficiency is assumed to be 100 %. This is not fully representing the device, but it provides a good indication of the change in charge generation efficiency. The device structure modelled and resulting electric field within the structure for a wavelength of 532 nm is shown in figure 3.9a. This is calculated for the steady and excited state refractive indices of the $CsPbBr_3$ layer obtained with the FDI. The used fluences are translated to sun equivalents by using the calibration of Wang *et al.*[179]. Here, one sun equivalent equals the amount of charges that would be present within the material under the illumination of a sun simulator light source. The number of charges for this experiment is calculated by the fluence of the pump and the absorption coefficient of the $CsPbBr_3$ sample and divided by the amount of charges under one sun illumination to obtain the equivalent value. The device structure is based on previous work in which perovskite/PCBM heterostructures show good solar cell efficiency[182,183].

The resulting total absorption and reflection of this device is shown in figure 3.9b for the spectral range measured with the FDI. This shows that absorption of the $CsPbBr_3$ decreases drastically when illuminated by 250 sun equivalents. This is partly compensated for by the increased absorption within the PCBM due to the enhanced electric field within this layer. However, only the ground state refractive index of PCBM is used for this model. The interesting part is the increased reflection under high illumination, resulting in a larger loss of the device. The calculated short circuit current shows a decrease of 2.3 % and 6.5 % for 100 and 250 sun equivalents respectively, which is a result of the combination of real and imaginary part of the refractive index. This shows that the full complex refractive index needs to be taken into account when considering high carrier density operation.

3.5 Discussion and conclusion

In this chapter, we have shown the direct photoinduced refractive index change of $CsPbBr_3$, measured via a simple adaptation to TAS. The ultrafast FDI returns the phase change of the probe pulse after photoexcitation with respect to the reference pulse, from which the refractive index change is calculated. By using the steady and excited state refractive index with basic Fresnel equations, the steady and excited state transmission and reflection is calculated. From this, the TA spectrum is retrieved and compared with a TA spectrum of the same sample. These spectra are in agreement with one another, showing the reliability of this system.

Previously, people have tried to decouple the effect of reflection on the PIA above the band edge. This research has excluded that the change of reflection is the main contribution of this PIA signal. Instead, a simple model is discussed that suggests that this signal arises from the extended BGR, as previously found by others. The refractive index change, however, has an impact on the shape of the TA spectrum by reflection artefacts. The shape is often used to extract the carrier temperature where by fitting the Fermi-Dirac distribution to the $\Delta\alpha$ instead, these reflection artefacts are eliminated and a more representable carrier temperature is extracted.

There is a limitation of the temporal range of this technique, which is governed by the reference-probe delay time. The maximum delay time is determined by the temporal overlap of the reference and probe on the detector where the interference contrast decreases with decreasing overlap. This limitation can be overcome by spatial separation, or temporal separation and recombination of the reference-probe pair.

The spatial separation of the reference and probe at the sample position can be achieved by implementing a differential interference contrast microscope system in the probe path[184]. For this case, Rochon prisms can be used to generate and recombine the reference-probe pair. Between these prisms, the sample is placed at the focal point of both beams and only excited at one of the two probe arms. This method has been considered and discarded as it requires thick optical components, generating strong chirp of the supercontinuum probe.

The temporal separation and recombination of the reference and probe pulses has been implemented and is described in full detail in chapter 5. This chapter discussed the details of a Sagnac-FDI system which is used to generate a long reference-probe delay at the sample whilst being fully compensated for when leaving the interferometer. A birefringent crystal is then used to set a time delay between reference and probe to obtain interference in the frequency domain.

Chapter 4

Multiple plate compression light source in ultrafast transient absorption spectroscopy

The contents of this chapter have resulted in the following publications:

- **"Multiple-Plate Compression used in Transient Absorption Spectroscopy" in 14th Pacific Rim Conference on Lasers and Electro-Optics (CLEO PR 2020),** ***R. R. Tamming, C. Lin, K. Chen, C. Lu, J. M. Hodgkiss, and S. Yang*** **- OSA Technical Digest (Optical Society of America, 2020), paper $C6B_4$**[185]
- **Single 3.3 fs multiple plate compression light source in ultrafast transient absorption spectroscopy,** ***Tamming, R.R., Lin, CY., Hodgkiss, J.M., Yang, SD., Chen, K., Lu, CH.*** **Sci Rep 11, 12847 (2021).**

4.1 Introduction

TAS relies on a pump and probe pulse pair, with distinct properties, to excite the sample and observe the kinetics of this excited state by way of transmission[38]. The conventional light sources for TAS, bulk supercontinuum, (N)OPA and nonlinear optical fibres, are discussed in section 2.4.3. These light sources, however, all have their respective drawbacks.

As for bulk supercontinuum generation, the focusing of the beam inside a nonlinear crystal can lead to destructive mechanisms, setting a limit to the input energy and thus output energy[186]. This results in an available spectral density, that is the energy available in the pulse per nanometer, of the supercontinuum in the pJ/nm per pulse range. This makes it hard, or even impossible, to measure samples with a high absorption coefficient which are often the materials of interest for photovoltaic applications, or add optical components in the probe beam required for experiments such as FDI[154,187,188]. On top of that, the generated pulses obtain a large and nonlinear chirp and are therefore hard to compress using chirped mirrors alone. Therefore, expensive and complex optical components are required to compensate for this chirp and compress the pulse[189].

The pulses generated by the (N)OPA are limited by their spectral range due to phase matching conditions. This can partly be overcome by implementing complex phase controlling schemes, however, this adds to the multitude of optical components already required for the (N)OPA itself[42,190]. Due to the phase matching conditions, a broadband (N)OPA will generate pulses with front tilt, spatial chirp and angular dispersion[191].

The nonlinear optical fibre uses a pressurised gas within a hollow core fibre. Within this gas, various nonlinear processes compete, such as chaotic four-wave mixing and modulation instabilities, which occur over a long travel distance[113]. This results in supercontinuum generation which is extremely sensitive to the input coupling and amplifies the input noise. Therefore, large shot-to-shot spectral and temporal fluctuations are expected in the resulting supercontinuum[192–194]. Because of the varying requirements of the pump and probe pulses, and the limitations of these existing light sources, a combination of these techniques is required for a single TAS system.

Recently, a new light source has been developed by our collaborators that overcomes these drawbacks. The MPC is method to generate a broad and stable supercontinuum[44]. This technique utilises the high nonlinear coefficient of a series of thin nonlinear plates to step-wise achieve strong spectral broadening, spanning the visible spectrum into the near infrared. These plates act as a waveguide by using the self-focusing within the plates to maintain a small beam waist for a long distance. Optical breakdown within the material is avoided as the self-focal point of the pulse lies at a point after each plate[195]. This prevents the intensity within the plates from reaching the multiphoton absorption and ionisation, and optical breakdown threshold. Therefore, a higher input pulse energy, and thus output pulse energy, than bulk supercontinuum can be used[196]. Additionally, these pulses are easily temporally compressible, down to the single cycle[197].

In this chapter, we will analyse and discuss the use of the MPC as a single temporally compressed broadband light source for the field of ultrafast pump-probe spectroscopy. This light source has never been applied in TAS before, therefore thorough evaluation of the generated supercontinuum pulses is required. To analyse the pulses, we have built two separate MPC-TAS systems. The first system is based on a single-stage MPC, provided by our collaborators, Mr. Chao-Yang Lin, Dr. Chih-Hsuan Lu and Prof. Shang-Da Yang from the Tsing Hua University in Hsinchu, Taiwan. The second system uses a double-stage configuration and is built in our own lab. The spectrum and shot-to-shot stability of the generated supercontinuum pulses are evaluated, and real TA measurements are discussed to show the potential of the MPC in ultrafast pump-probe spectroscopy.

4.2 Multiple plate compression background

The MPC relies on the various nonlinear effects within the plates that lead to supercontinuum generation. The supercontinuum generation is a result of the complex interplay of self-focusing, self-phase modulation, self steepening, multiphoton absorption and ionisation, plasma defocusing, GVD, four-wave mixing and phase matching, similar to bulk supercontinuum generation. A comprehensive overview of these nonlinear effects is given in section 2.2.2.

The MPC is first described in 2014 by Lu *et al.*[44] who have used a series of 4

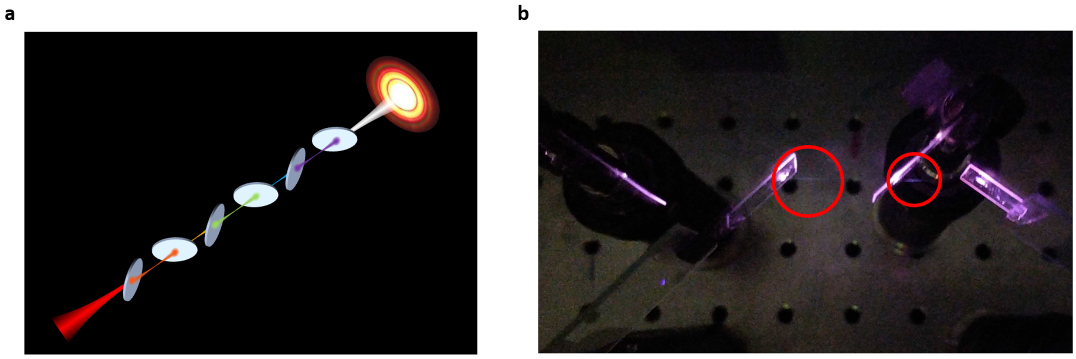

Figure 4.1: a) Schematic of the MPC and broadening of the pulse. Thin plates are placed at Brewster's angle near the focal waist of the input pulse. The output is a bright white centre with concentric rings surrounding it. b) Photo of the first stage of the double-stage MPC, containing four quartz plates with a thickness of 200 μm, described in section 4.5. The red rings indicate the locations where plasma is generated in the air.

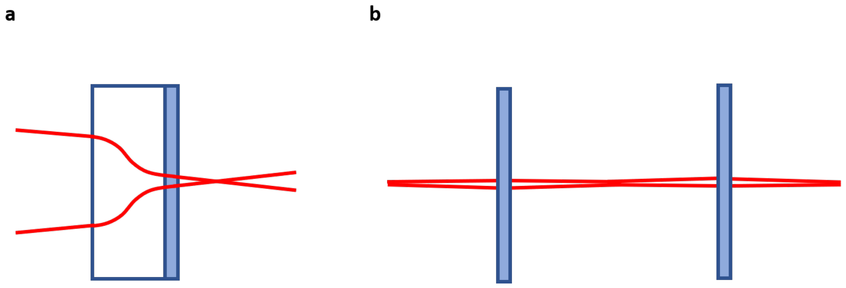

Figure 4.2: a) Self-focusing of the pulse in a bulk crystal leads to an intensity high enough for nonlinear broadening to occur. The blue box indicates the effective length for efficient supercontinuum generation. b) MPC plates placed near the focal points where the intensity is sufficiently high for nonlinear broadening while avoiding optical damage.

fused silica plates, with a thickness of 0.1 mm, near the waist of a focusing beam to obtain spectral broadening of the pulse. A schematic of this technique is shown in figure 4.1a for the case of 6 plates. These plates were placed at Brewster's angle to reduce losses from reflections and with alternating orientation to allow for physical space and compensate for lopsided sideways spatial beam stretching. This lopsided sideways stretching is caused by the time-dependent sideways nonlinear refractive index change, where the beam will bend towards the side where the beam interacts with the plates first. They discovered that, by strategically placing the plates, they could generate an intense (76 μJ/pulse) octave-spanning spectrum from 450 nm to 980 nm at the -20 dB intensity level whilst avoiding optical damage or multiple filamentation. They reported that the nonlinear self-focusing within the plate creates a new focal point beyond the solid-state medium and therefore multiple filamentation, multiphoton absorption and ionisation, and optical damage can not occur within the plates[195,198]. Figure 4.1b shows a photo of the first stage of the double-stage MPC described in section 4.5. The pulse travels from left to right and the bright line indicated by the red circles is plasma generated in air at the focal point behind the second and third plate. This allowed them to use an input peak power of 5.6 GW, which is 2,800 times higher than the critical peak power of fused silica, to generate this supercontinuum[199].

The total travel distance through these nonlinear media (0.4 mm) is much shorter than that of typical bulk supercontinuum generation (>1 mm). Therefore, the nonlinear interaction length is shorter and a weaker interaction is expected. However, the pulse input energy density, and thus the spatiotemporal intensity, can be made higher throughout the whole thickness of the plate due to the shorter travel distance[195]. This is unlike bulk supercontinuum, which uses the self-focusing of the pulse within the crystal to obtain sufficient intensity to initialise the nonlinear broadening. Therefore, efficient broadening only occurs at the end of the crystal as shown schematically in blue in figure 4.2a[40].

With the MPC, however, we can place the plates at the intensity sweet spots generated after the self-focusing as shown in figure 4.2b. Equations 2.24b and 2.25b, from section 2.2.2, show that the instantaneous phase change and the spectral broadening are dependent on the intensity and change of intensity respectively. This predicts a stronger broadening of the pulse via self-phase modulation with higher intensity. Besides this, the nonlinear refractive index is also dependent on the intensity according to equation 2.23, resulting in a more effective self-steepening and self-focusing for the MPC. On top of that, the thin plates will result in smaller dispersion of the pulse and thus maintains the high temporal peak power. As the nonlinear interactions can occur over the whole plate length, this method requires less material to achieve a broadening similar to bulk supercontinuum[195].

4.3 Single-stage multiple plate compression

4.3.1 Single-stage multiple plate compression - transient absorption spectrometer

To characterise the stability and use of the MPC in the field of pump-probe spectroscopy, an MPC-TAS system was built. A schematic overview is displayed in figure 4.3. The build consists of 2 main parts. The first part is the MPC, indicated by the dotted box, and is provided by our collaborators. The second part, the TA spectrometer, is the bottom of the system. These components are built separately and were put together in the lab of our collaborators.

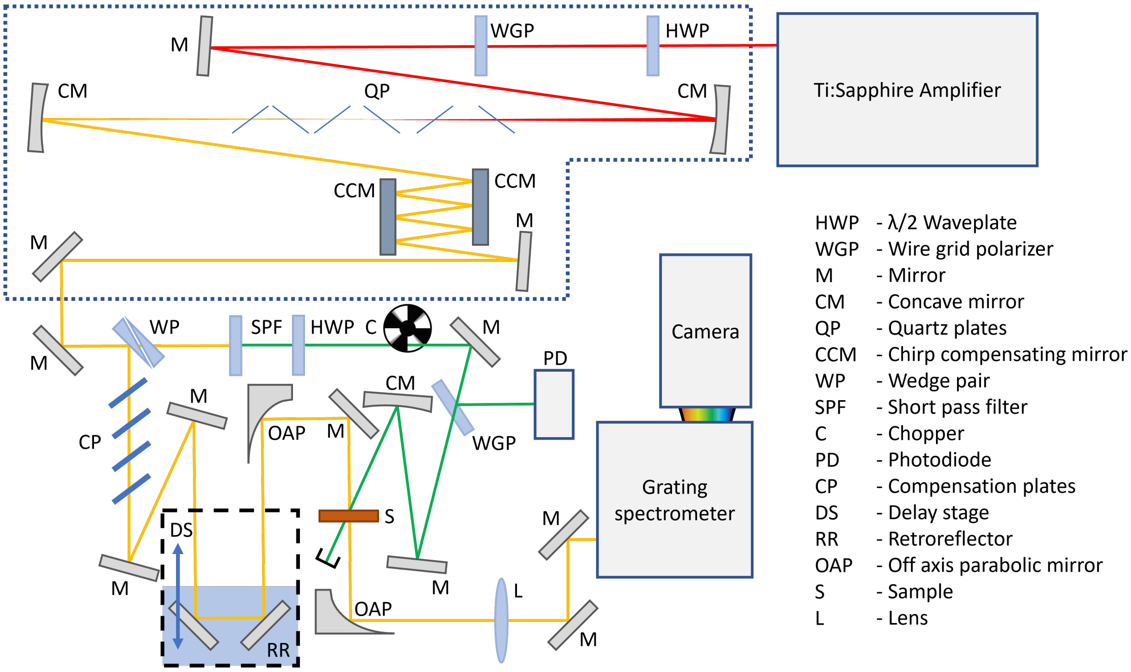

Figure 4.3: Schematic of the MPC-TAS system used to characterise the MPC supercontinuum. All optical components are listed on the right, ordered by following the beampath (first pump path, then probe path after splitting). The MPC part is indicated in the dotted box while the TAS is outside.

The driving laser for this system is a Ti:Sapphire amplifier system (FemtopowerTMHEPRO CEP). This system generates pulses with a bandwidth of 30 nm, centred at 790 nm, and with a pulse duration of 25 fs at a 1 kHz repetition rate. The output pulse power is tuned to 200 μJ per pulse using a $\lambda/2$ waveplate (WP) and a wire grid polariser (WGP), set at P-polarisation. This beam is then focused by a concave mirror (CM) onto a series of thin (50 μm) z-cut quartz plates (QP). This material is chosen as it has a high damage threshold and, from the experience of our collaborators, has shown the longest stability of the materials they have tested whilst generating a broad spectrum. The plates are then positioned one by one near the focal point at Brewster's angle. The position of the plates is set by looking at the broadening of the generated spectrum and the stability of the spectrum. The exact placement of these plates is done by using translation stages, however, placement errors of ± 0.5 mm are acceptable for each sequential plate, making it a robust technique with a straightforward alignment procedure. Misalignment, however, will result in a narrower spectrum with less conversion effiency. After the 6 quartz plates, a concave mirror is placed to collimate the beam. A combination of chirp compensation mirrors (CCM) are placed after the supercontinuum generation to temporally compress the pulse. A set of commercially available chirped mirrors compensate for 720 fs^2 linear GDD at 700 nm and one set of custom designed chirped mirrors compensate for the higher orders dispersion.

After the broadband pulses are generated and compressed, the beam is split into a pump and a probe beam. This is done by a dispersion compensating wedge pair (WP), where the first back reflection is used for the probe and the transmitted beam is used for the pump. The longer wavelengths of the pump are then suppressed using a 750 nm short pass filter (SP) to eliminate the strong 790 nm fundamental wavelength. A $\lambda/2$ waveplate and a wire grid polariser are used to tune the intensity and polarisation to the magic angle (54.7 °) relative to the P-polarised probe. This angle is set to avoid polarization and photoselection effects[200]. This allows for the observation of the excited species rather than effects from the lattice. The pump then passes through a chopper (C) running at half the amplifier output frequency to block every other shot, resulting in shot-to-shot modulation of the excitation of the sample. The captured shots are indicated with the pump ″on″ (excited state) or ″off″ (ground state) by using a photodiode (PD), connected to a digitiser (Glaz-PD, Syntertronic), which captures the back reflection of the wire grid polariser after the chopper. Finally, the pump is loosely focused to a spot size of 1 mm FWHM onto the sample to create a large uniform excitation profile. This is possible due to the high spectral density of the MPC supercontinuum pulses.

The probe beam follows a different path than the pump beam. As the pump path passes through transmissive optics, the supercontinuum has been negatively chirped to precompensates for the GVD of the optical components. The probe, however, does not travel through any optical components. Therefore, the negative chirp is compensated with the use of glass compensation plates (CP). In this case, the shortest probe duration is found when using 4 soda-lime glass microscope slides (1.1 mm) placed at Brewster's angle. The probe is then sent onto a retroreflector (RR) which is mounted on a mechanical delay stage (DS) (XMSL210-S, Newport) to control the probe arrival time. To avoid the effect of beam drift, a CCD camera (acA1300-60gmNIR, Basler ace) is placed at the sample position and the position and spot size of the probe remains constant at the front and back of the stage. An off axis parabolic mirror (OAP) is used to focus the probe onto the sample and another one is used to collimate the probe after the sample. After collimation, a variety of filters (not shown) can be used to attenuate the probe in certain spectral regions to avoid saturation of the camera.

A grating spectrometer (SpectraPro 2150, Princeton Instruments) is used to disperse the probe beam. An achromatic doublet (L) (f = 150 mm) is used to focus the probe onto the entrance slit of the spectrometer. An 800 gr/mm grating is installed in the spectrometer to disperse the supercontinuum over the 30.7 mm width of the detector (S11639-01, Hamamatsu) of a high speed camera (Glaz Linescan-II, Synertronic). The camera is electronically triggered by the amplifier to capture each individual shot. Because of the electronic delay of the wires, the trigger is set to capture the following shot using an integration window of 10 μs.

4.3.2 Polarisation-gating - frequency-resolved optical gating

To characterise the pulse duration, a home-built PG-FROG is used, based on the work of Trebino[129]. The theory behind the PG-FROG is described in section 2.3. The PG-FROG is chosen because it is capable of measuring temporally short pulses with a large spectral width. It requires fairly high pulse intensities which the MPC can easily produce. Here, we have used the compressed fundamental MPC output as a Kerr gate pulse and the MPC output, with additional optical components present in the TAS system, as the probe pulse. A schematic overview of the system is depicted in figure 4.4.

After this, the beam is split into a pump and probe, indicated by yellow and blue respectively, via a chirp compensating wedge pair (WP). The pump is sent over a mechanical delay stage with a retroreflector to control the time delay. A wire grid polariser is used to set the pump pulse polarisation at a 45 ° angle with respect to the probe pulse. A concave mirror is used to tightly focus the pump onto a quartz

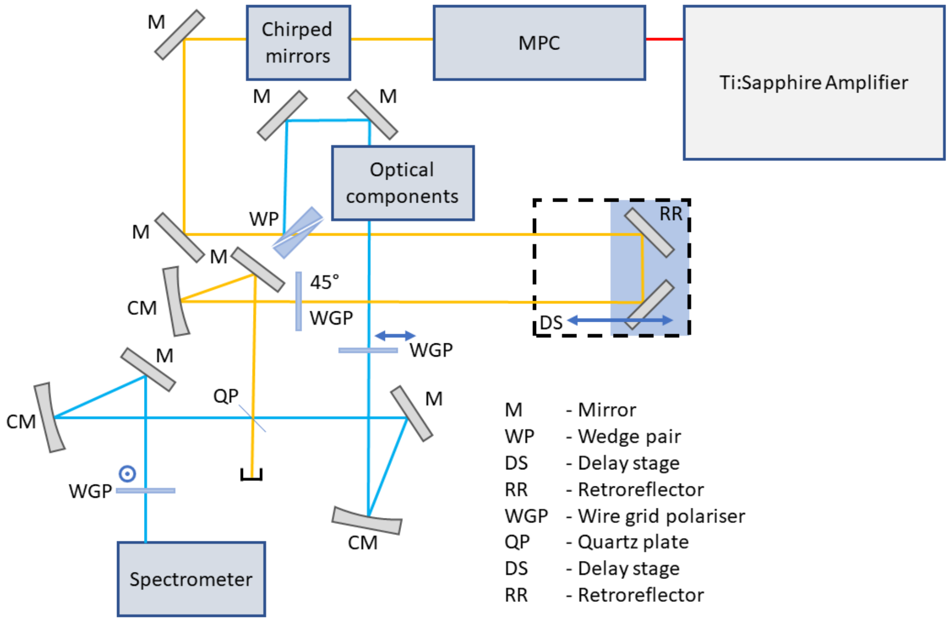

Figure 4.4: Schematic of the experimental setup used to characterise the MPC. All optical components are listed on the right, ordered by following the beampath (first pump path (yellow), then probe path (blue) after splitting). The quartz plate to obtain the FROG signal has a thickness of 100 μm.

window with a thickness of 100 μm. The probe passes through the same set of optics as the pump and probe path of the TAS system for their respective pulse duration measurement. This ensures we actually measure the pulse duration at the sample position rather than the MPC output.

A set of wire grid polarisers are placed around the quartz window, set at the cross-polarisation condition, to eliminate all probe light passing through. Therefore, the spectrometer (Ocean Optics HR4000), placed after the second polariser, won't detect anything. However, once the pump and probe overlap, spatially and temporally, on the quartz plate, the optical Kerr effect will occur, slightly changing the polarisation of the probe. This results in a leakage of the probe pulse through the second wire grid polariser which is detected by the spectrometer. By changing the delay of the pump, a time-dependent spectrum is obtained. After obtaining the spectral trace, our collaborators have applied a least squared generalized projection algorithm to retrieve the phase and pulse duration.

4.4 Single-stage - Results and discussion

4.4.1 Spectral broadening

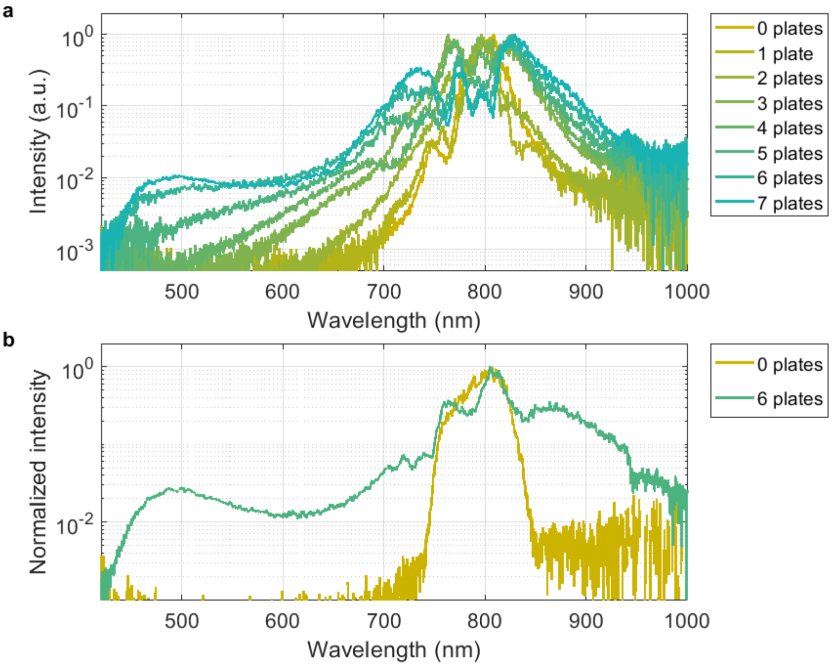

Figure 4.5: a) Normalised spectrum of the single stage MPC for zero to 7 plates. This measurement is taken after the other measurements described in this chapter, hence the 7 plate system instead of 6 described in the main text. b) spectrum for the actual used MPC conditions for zero and 6 plates. Each quartz plate has a thickness off 50 μm.

First, we analyse the spectral broadening caused by the individual plates of the MPC. The spectra for increasing amounts of plates is shown in figure 4.5a. The final spectrum after passing through 7 plates spans from 450 nm to over 1000 nm, limited by the spectral range of the spectrometer. Here, only the bright centre of the pulse is selected. Note that this is one more plate than described in the previous section. Due to the limited time available in the lab of our collaborators, we have not performed a plate-dependent spectrum measurement for the actual setup described in this chapter. This measurement has been performed by our collaborators prior to the measurements further described in this chapter, with different laser input conditions. However, the mechanisms behind the broadening remain the same. The final spectrum obtained for the 6 plates MPC is recorded and shown in figure 4.5b.

The resulting spectrum is similar to the spectrum obtained via numerical calculations using the nonlinear mechanisms described in section 2.2.2, showing that the supercontinuum is generated in a similar fashion as bulk supercontinuum[195]. The first two plates only broadens the pulse around the fundamental frequency. The symmetric broadening indicates that this broadening is dominated by the self-phase modulation and four-wave mixing[44,195]. This is further supported by the formation of the dip in the spectrum around the fundamental frequency, which is the result of the red and blue shift at the front and back of the pulse respectively, depleting the centre wavelength[116]. With the addition of more plates, a strong broadening occurs with a blue pedestal, similar to the results of bulk supercontinuum generation[104]. This is a fingerprint of the self-steepening assisted self-phase modulation[145]. The high nonlinear refractive index within each plate contributes to self-steepening of the pulse so that this effect accumulate after travelling through a couple of plates. On the other hand, each plate generates GVD leading to an increase of the GDD, meaning that the beam gets chirped. This lowers the peak intensity by temporal stretching, reducing the effect of the nonlinear interactions. Therefore, adding more plates does very little to the spectral broadening and increases the losses of the MPC by parasitic effects, such as multiphoton absorption and additional surface reflections.

With an input pulse energy of 200 μJ and the output pulse power is 87 μJ, a 44 % conversion efficiency is achieved. By using the measured spectrum and the total output power, we can estimate the spectral density, which is given by the energy available per nanometer per pulse. The resulting spectral density, using the 87 μJ pulse energy, is shown in figure 4.6. The minimum spectral density within the supercontinuum is 14.5 nJ/nm at 605 nm, excluding the edges of the spectrum. This is high compared to bulk supercontinuum, for which which pJ/nm levels are

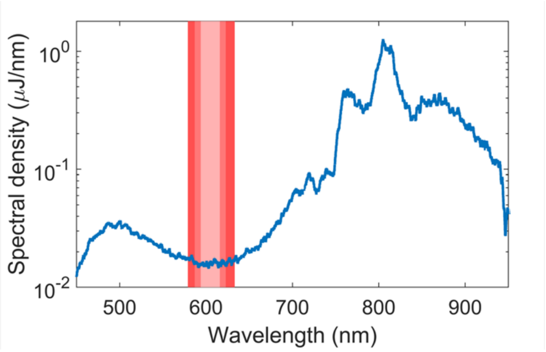

Figure 4.6: Spectral density of the supercontinuum generated by the MPC. The pink to red lines indicate spectral windows with a width of 22 nm, 36 nm and 54 nm. These result in 50 fs, 30 fs and 20 fs transform limited pulses respectively. The corresponding available pulse energies within these windows are 353 nJ, 575 nJ and 880 nJ. Reprinted with permission from Tamming *et al.*[201], (2021) Scientific Reports.

typically achieved[202]. This high spectral density and the broadband nature of the pulses generated by the MPC are useful for TAS as it complies with both pump and probe requirements which allows us to use a single MPC light source to generate both the pump and probe pulses for the TA experiment.

The broadband pulse, when used as a probe, allows for the observation of a broad spectral range, whereas the high spectral density enables us to measure samples with a high absorption coefficient, which would absorb most of the photons. The increased photon count allows for the loss of photons while preserving a high signal to noise. This also provides the opportunity to add more optics in the path of the supercontinuum to perform more complex pump-probe measurements, such as FDI.

As for the pump, the MPC can be used to generate a tunable narrowband pulse, which is required when the excitation of specific species within a sample is required. The high spectral density means that there is much energy within a small spectral range. This allows the selection of a spectral region of the supercontinuum by either using band pass filters, for discrete tuning, or a combination of low and high pass filters for variable tuning.

To simulate the available energy per pulse using this method, we have integrated over small regions of the spectrum centred around 605 nm, which is the region of lowest spectral density. The windows are square functions with a width of 22 nm, 36 nm and 54 nm, corresponding to a transform limited pulse durations of 50 fs, 30 fs and 20 fs respectively. These windows are indicated in figure 4.6 by the pink to red lines. The corresponding pulse energies are 353 nJ, 575 nJ and 880 nJ. Focusing this to a spot size with a diameter of 500 μm FWHM, results in the fluences of 175 μJ/cm^2, 294 μJ/cm^2 and 451 μJ/cm^2 respectively. These values are summarised in table 4.1. These fluences are sufficient for most TA measurements[32,72,203]. When higher fluences are required, tighter focusing of the beam is possible.

	Bandwidth	Pulse duration	Pulse energy	Fluence
Pink	22 nm	50 fs	353 nJ	175 μJ/cm^2
Middle	36 nm	30 fs	575 nJ	294 μJ/cm^2
Red	54 nm	20 fs	880 nJ	451 μJ/cm^2

Table 4.1: Selected excitation bandwidths around 605 nm and their respective pulse durations, pulse energies and fluences obtained for a spot size with a diameter of 500 μm FWHM.

The broad spectral nature also allows for temporal compression of the pulse, as will be discussed in the next section. Combined with the high spectral density, these pulses can serve as a short pump in TA measurements, resulting in a short IRF duration and thus high temporal resolution.

4.4.2 Polarisation-gating - frequency-resolved optical gating

The obtained PG-FROG traces for the probe and pump pulses are shown in figure 4.7a and 4.7b. The lower intensity at longer wavelengths for the pump is a result of the short pass filter in its path. After collecting these spectra, our collaborators have retrieved the spectrum and phase of the pulses with the help of an least squared generalized projection algorithm. The result of this is shown in figure 4.7c and 4.7d for probe and pump pulses respectively. This shows an almost linear phase for both spectra, indicating an even temporal shift which has no impact on the final pulse duration, but temporally shifts the pulse position[102]. The fluctuations of the retrieved spectra are a result of the broad spectrum and the therefore relative

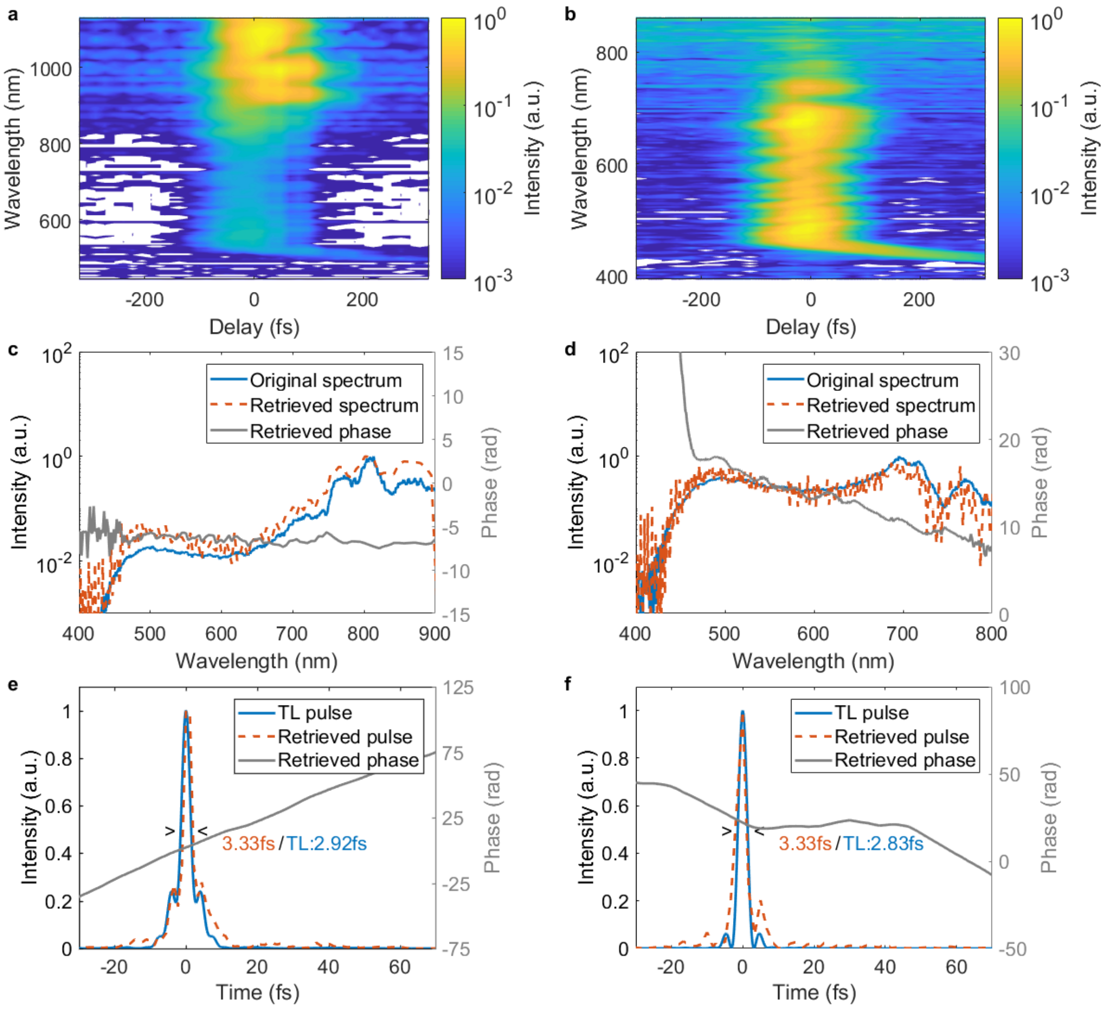

Figure 4.7: The obtained PG-FROG traces for the a) probe and b) pump pulses. The different spectrum available for both pulses is the result of a short pass filter in the pump path to block most of the MPC driving frequencies. The integrated spectrum and the retrieved spectrum and phase from the least squared generalized projection algorithm for the c) probe and d) pump pulses. The linear phase shows that the pulses are close to their transform limit, which is the shortest possible pulse duration with the measured spectrum. The calculated transform limited temporal pulse profile and retrieved temporal pulse profile and phase for the e) probe and f) pump pulses. Adapted with permission from Tamming *et al.*[201], (2021) Scientific Reports.

low spectral resolution of the spectrometer. These fluctuations, however, have little impact on the retrieved pulse durations as the overal spectral shape, and the spectral bandwidth, is approximated accurately. Note that the 450 nm to 400 nm region of the pump has a sharp increase in phase. This has very little effect on the final pulse duration due to the low intensity of these wavelengths with respect to the rest of the spectrum.

Finally, the duration of the pulses is calculated and shown in figure 4.7e and 4.7f for probe and pump pulses respectively and is shown to be 3.3 fs for both pulses. This is very close to the corresponding transform limits, which are 2.92 fs for the probe and 2.83 fs for the pump. The transform limit is the theoretically shortest pulse duration possible with the measured spectrum and is calculated by addition of all available frequency components and their intensities for the in-phase condition. This shows that, by using these pulses for TAS, a high temporal resolution can be obtained.

The probe has a longer transform limited pulse, even though it has a broader available spectrum. This can be explained by the large intensity difference between the 800 nm region and the 500 nm region. Because of this large intensity difference, full deconstructive interference around the in-phase position, as discussed in section 4.2, is not possible.

The phase of these pulses is only defined when there is a nonzero intensity, therefore, only the phase close to the pulse has to be considered. Also here, an almost linear phase is obtained for both pulses. This indicates that the pulses are close to the transform limit and that there is a spectral shift of the centre frequency with respect to the chosen centre wavelength for the least squared generalized projection algorithm[102].

4.4.3 Stability and spectral density

Lu *et al.* have reported the stability over several hours of this system, resulting in a 0.83 % standard deviation of the total power of this system as recorded by a power meter[44]. However, the power meter measures the sum of the spectral components on a relative slow timescale, which is expected to be dominated by the frequency of

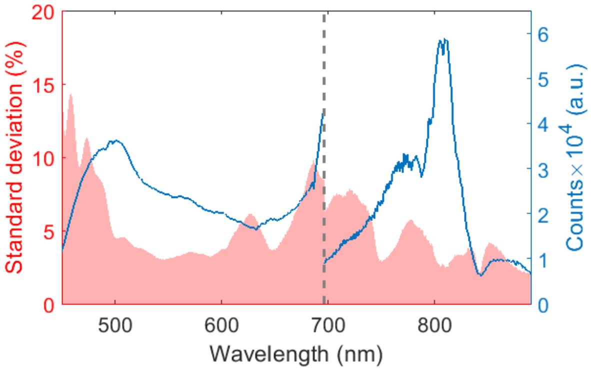

Figure 4.8: Spectrum of the pulses generated by the MPC in blue. The spectra of two separate measurements are merged at 696 nm to capture more photons over the whole spectral range to reduce the background noise of the camera. The relative standard deviation is given in pink, with an average of 4.6 % between 490 nm and 890 nm. Reprinted with permission from Tamming *et al.*[201], (2021) Scientific Reports.

the input pulse of the MPC due to its higher intensity.

To obtain a better understanding of the shot-to-shot stability of the spectral components generated by this system, we have captured the spectra of the individual pulses generated by the MPC. For the analysis, we have collected multiple sets of 2,000 shots that are generated by the MPC, with a total acquisition time of 2 seconds, using the MPC-TAS system described in section 4.3. This is done separately for two spectral regions to avoid saturation of the camera around the MPC input frequencies and having very few counts on the detector for the short wavelength region. The average of the captured spectra for a set of 2,000 shots is shown in figure 4.8, where the gray dashed line indicates 696 nm, which is where the two measurements are merged. The spectrum is cut off at 470 nm and 890 nm due to the physical width of the detector.

Figure 4.8 also shows the standard deviation of the amount of counts, given as the percentage of the mean. An average standard deviation of 4.6 % is obtained between 490 nm and 890 nm. The total noise is the sum of the camera noise, Poisson statistics and the actual laser fluctuations. To show that the measured standard deviation is dominated by the laser fluctuations, we have estimated the individual contributions

	Noise contributions at 600 nm		
	Electronic noise	Shot noise	Laser fluctuations
Value	$I_0 = 20,137$ counts	$N^*_{ph} = 3.11 \times 10^4$	$I_0 = 20,137$ counts
Error	13.1 counts	$\sqrt{N_{ph}} = 176$	612 counts
Relative error	6.51×10^{-4}	$1/\sqrt{N_{ph}} = 5.67 \times 10^{-3}$	3.04×10^{-2}

Table 4.2: Individual noise contributions of the obtained standard deviation spectrum for the pixel corresponding to 600 nm. *For this wavelength, the conversion efficiency of the CMOS is 79%. Adapted with permission from Tamming *et al.*[201], (2021) Scientific Reports.

of these noise components according to the estimation from Kanal *et al.*[135]. These individual contributions are summarised in table 4.2 for the pixel corresponding to 600 nm.

The error in electronic noise is estimated by the dark noise of the camera. For this experiment, we have used the Synertronic Linescan-II camera with a Hamamatsu S11639-01 linear CMOS. This detector has a 16 bit output (65,536 bins), with a typical read out noise of 0.4 mV and a typical 2 V maximum output voltage. This results in a dark noise of 13.1 counts, giving a relative error of 6.51×10^{-4}.

The shot noise is a result of the Poisson statistical error of the measured photons. To calculate this, we need to calculate the amount of photons arriving at the detector. The camera is a 16 bit, has a 2 V readout range, an output of 25 μV/e$^-$ and has a conversion efficiency of 79 % (0.79 e$^-$ per photon) at this wavelength. From this, we obtain a total of 3.11×10^4 photons detected by this pixel. The standard error of Poisson statistics is given by the square root of the total amount of photons, and the relative error is the inverse of the standard error, resulting in a relative error of 5.67×10^{-3}.

As for the laser fluctuation, we can only estimate this using the measurements we have which includes the previously mentioned noise contributions. Therefore, we first assume that the measured error, calculated by the standard deviation, is only from the laser fluctuations. The calculated relative error of 3.02×10^{-2}, calculated via the relative standard deviation, shows that the total noise is an order of magnitude larger than the noise from the shot noise. This validates the assumption that the measured error is dominated by laser fluctuations and that the relative standard deviation shown is a representation of the actual laser noise.

4.4.4 Temporal correlation

For ultrafast spectroscopy, the lowest noise level is achieved when all shots are exactly the same. As for TAS, this would completely eliminate the noise originating from the laser fluctuation. However, small fluctuations within the laser cavity, vibrations or even airflow within the room all contribute to small fluctuations of the laser output conditions. These small fluctuations can have a significant impact on the pulses generated via the MPC due to the nonlinear nature of this system. From this, we expect shots that are closer in time to be more similar to each other than shots that are separated further in time as the environmental conditions will have changed less[135].

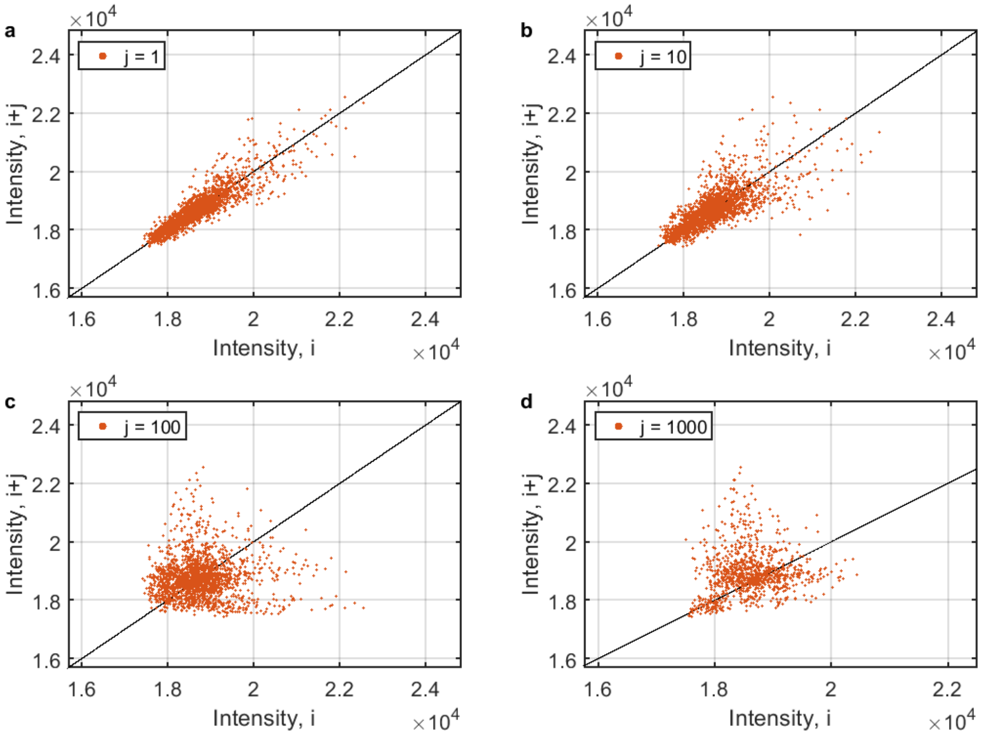

Figure 4.9: Intensity of shots i and $i+j$ for a) j = 1, b) j = 10, c) j = 100 and d) j = 1000 for the pixel corresponding to 650 nm. The black line indicates intensity(i) = intensity($i+j$).

Figure 4.9 shows the relation between the intensity of the pixel corresponding to 650 nm within the pulse as generated by the MPC. This figure shows the intensity of shot $i + j$ plotted against shot i for different shot differences j. For a highly correlated system, all of the data points will be close to the black line, which indicates that the intensity of shot i is the same as for shot $i + j$. This shows that, as expected, the intensity of the shots start to differ more with increasing shot difference. This immediately shows the benefit of using a chopper in the pump path to block every other shot and being able to use sequential shots for the calculation of the TA signal.

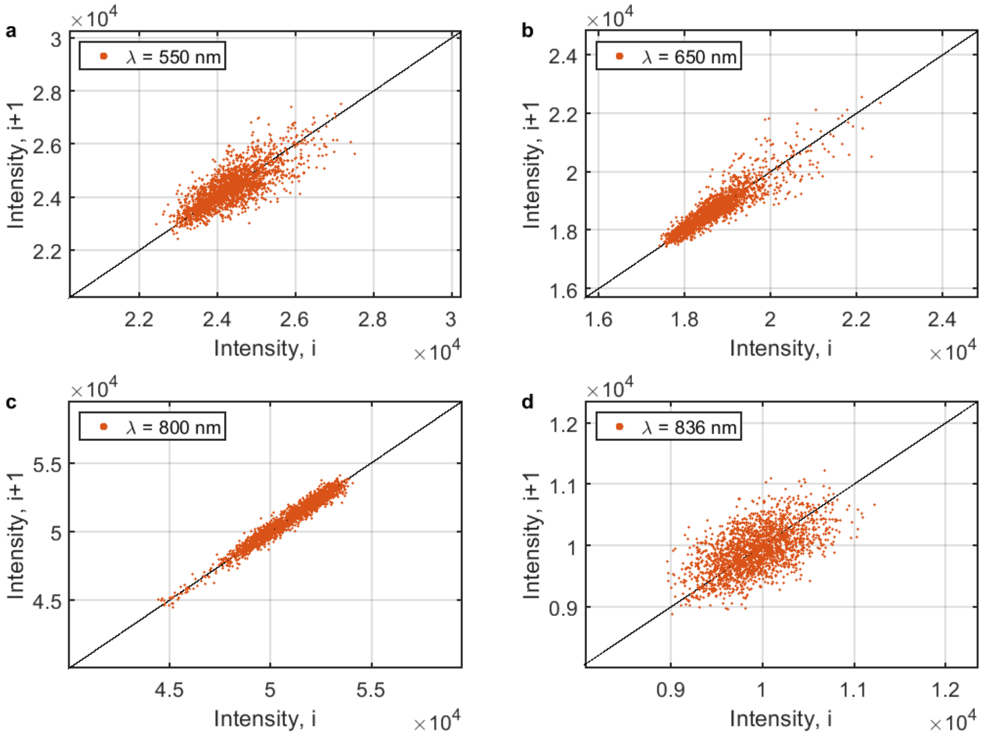

Figure 4.10: Intensity of the probe for 2000 shots at a) 550 nm, b) 650 nm, c) 800 nm and d) 836 nm. Black line indicates intensity(i) = intensity($i + 1$)

The time dependent correlation is not the same for the various wavelengths as the different wavelengths are generated via a different combination of nonlinear mechanisms. The effect of these different mechanisms are impacted by the intensity and spatial distribution of the input beam by different amounts. Therefore, we have plotted the intensity of sequential shots for different wavelengths in figure 4.10. This shows that the pulse is better correlated for 800 nm than any of other wavelengths. The 800 nm is generated by the laser and only a relative small portion contributes to the supercontinuum generation. However, a small fluctuation of the MPC input beam will result in larger fluctuations for the generated wavelengths due to the nonlinear processes involved.

So far, the correlation has been discussed in a qualitative manner by comparing the intensities of various shots. To analyse the whole spectral range in a quantitative manner, the Pearson correlation function is used[204]. This is calculated by the covariance of the intensities divided by the product of the standard deviation given by

$$\gamma_{\lambda,j} = \frac{\sum_{i=1}^{n-j}[(E_{\lambda,i} - \bar{E}_\lambda)(E_{\lambda,i+j} - \bar{E}_\lambda)]}{\sqrt{\sum_{i=1}^{n-j}(E_{\lambda,i} - \bar{E}_\lambda)^2}\sqrt{\sum_{i=1}^{n-j}(E_{\lambda,i+j} - \bar{E}_\lambda)^2}}, \tag{4.1}$$

with $\gamma_{\lambda,j}$ being the correlation coefficient and $E_{\lambda,i}$ and $E_{\lambda,i+j}$ being the intensities of wavelength λ at the ith and $(i + j)$th shot, respectively. This results in a value between -1 and 1, where -1 is fully anti-correlated, 0 means not correlated and 1 is fully correlated.

The result of the wavelength and shot difference dependent Pearson correlation function on this set of shots is shown in figure 4.11a. The calculated correlation contained a 120 Hz oscillation as a result from room lighting and the power supply and has readily been removed via a frequency filter. The correlation at set shot differences is shown in the top panel, showing the different correlations over the whole spectral range. Figure 4.11b shows the correlation coefficient of the wavelengths depicted in figure 4.10. This shows that, indeed, the intensity of 800 nm has the highest initial correlation. Whilst the initial correlation is vastly different, the decay of the correlation is similar over the whole spectral range.

The average correlation coefficient over the whole spectral range is shown in figure 4.11c. The average correlation between sequential shots is 0.77, which is higher than the $\bar{\gamma} \approx 0.5$ previously reported for bulk supercontinuum with a 1 kHz system[204,205]. On top of that, the correlation is kept high on a longer timescales, where it takes about 35 shots (35 ms) to half the correlation of the shots[135]. This

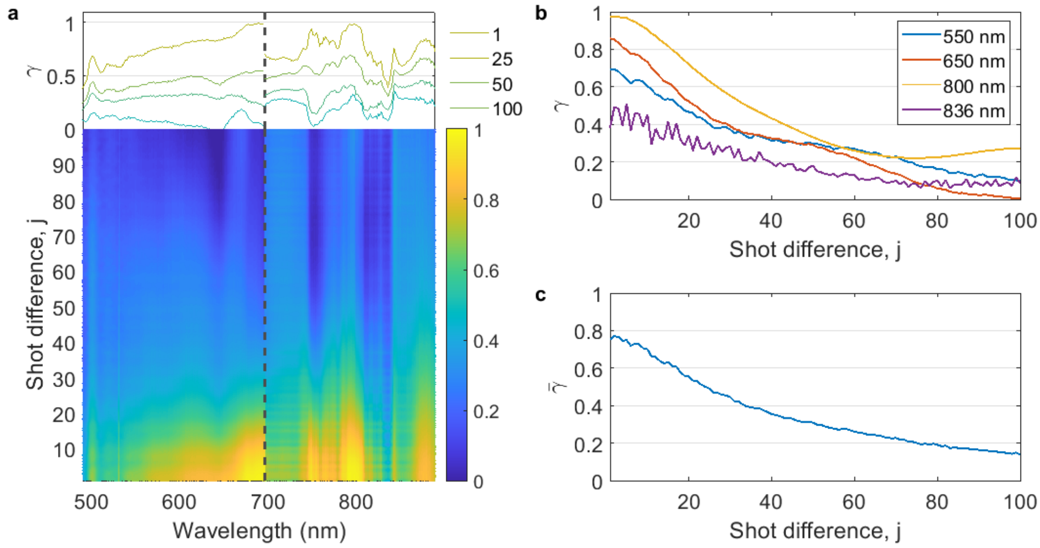

Figure 4.11: a) The correlation coefficient surface (bottom) calculated according to equation 4.1 and slices at indicated shot differences (top). b) The correlation coefficient for various wavelengths. c) The average correlation coefficient over the entire spectral range. Adapted with permission from Tamming *et al.*[201], (2021) Scientific Reports.

shows the potential for this system to partially overcome the requirement of shot-to-shot modulation of the sample, which is hard, or even impossible, to achieve for high repetition rate lasers, and instead use the average of a small set of ground and excited-state shots to calculate the TA signal.

4.4.5 Transient absorption noise baseline measurement

Finally, the TA signal is calculated using a series of 2,000 shots. Here, the pump beam is blocked once again to only collect the noise resulting from the probe beam. The calculated TA signal between 490 nm and 890 nm is shown in red in figure 4.12, where the blue line is the same spectrum as analysed for the pump (figure 4.8).

This calculated TA spectrum contains pseudo structures, which has a consistent shape and appeared at the same wavelength with unpredictable amplitudes for different data sets. This pseudo structures match the regions of higher standard deviation from figure 4.8 and low correlation in figure 4.11. Others have reported

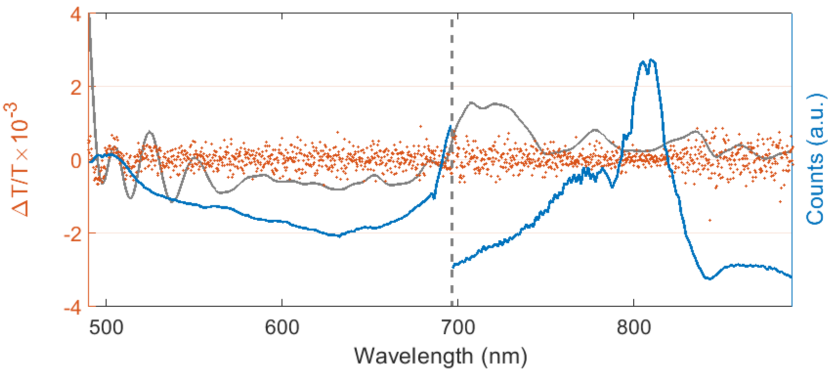

Figure 4.12: Probe spectrum (blue) and ΔT/T spectrum (red) obtained for 1,000 shot pairs. The obtained TA spectrum contains a background signal (pseudo structures), indicated in gray, which are obtained via spline curve (0.1) fitted through the ΔT/T spectrum and are subtracted from the actual ΔT/T spectrum. The origin of these pseudo structures and its impact on the obtained TA signal is discussed in the main text. Adapted with permission from Tamming *et al.*[201], (2021) Scientific Reports.

similar pseudo structures for bulk supercontinuum and assigned them to be a result of spectral correlation[204,206]. Bradler *et al.* found similar wiggles at the short wavelength region and a negative feature above[204]. These correlations create the larger structures in the TA spectrum, often misinterpreted as actual excited state features, by generating a coherent noise as the intensity of individual wavelengths are dependent on their neighbouring wavelengths. These pseudo structures can be eliminated by using a referencing scheme, where part of the probe is captured by a separate detector to reference the shot-to-shot probe fluctuations[204,205]. This has the added benefit of reducing the TA background noise by increasing the correlation of sequential shots over the whole spectrum, up to 0.92 as recorded by Dobryakov *et al.*[205]. This, however, requires a second identical 1D detector and is out of the scope of this research.

For the sake of analysing the ΔT/T signal, we have subtracted the pseudo structures from the signal. These pseudo structures are fitted by a rough smoothing spline curve (0.1) using the Matlab curve fit toolbox. A good measure of the noise level is the root mean square given by

$$\mathrm{RMS}_{\lambda} = \sqrt{\frac{1}{n}\sum_{i}\left(\left[\frac{\Delta T}{T}\right]_{\lambda,i}\right)^{2}}, \tag{4.2}$$

with n being the number of measurements and $\left[\frac{\Delta T}{T}\right]_{\lambda,i}$ being the TA intensities for wavelength λ and shot-pair i. The average root mean square noise between 490 nm and 890 nm is 2.6×10^{-4}, which is similar to other TAS systems using bulk supercontinuum[205].

4.4.6 Spectral correlation of the MPC supercontinuum

To further investigate the origins of the pseudo structures, we have calculated the spectral correlation. The generated wavelengths within the supercontinuum are dependent on other wavelengths within the pulse. Therefore, researching the dependency between the wavelengths can give an insight into the supercontinuum generation processes occurring within the MPC plates. The spectral correlation is given by

$$\gamma_{\lambda_1,\lambda_2} = \frac{\langle E_{\lambda_1}E_{\lambda_2}\rangle - \langle E_{\lambda_1}\rangle\langle E_{\lambda_2}\rangle}{\sqrt{(\langle E_{\lambda_1}^2\rangle - \langle E_{\lambda_1}\rangle^2)(\langle E_{\lambda_2}^2\rangle - \langle E_{\lambda_2}\rangle^2)}}, \tag{4.3}$$

with E_{λ_i} the intensity of wavelength λ_i[110].

The result of the spectral correlation is shown in figure 4.13 and can provide an insight into the nonlinear processes participating in the generation of the supercontinuum[207–209]. The contour plot shows the spectral correlation, i.e. how the intensity of wavelength λ_1 relates to λ_2. A slice at 475 nm is shown in the left plot to provide a better interpretation of the data. Besides understanding the supercontinuum generation processes, it helps to explain the pseudo structures observed in the TA spectrum shown in figure 4.12. Comparing these two figures reveals that the pseudo structure show great resemblance to the features in the spectral correlation plot. For example, there are spectral wiggles observed in both correlation and pseudo structures between 450 and 520 nm and a broad negative pseudo structure between 520 and 670 nm, corresponding to the spectrally correlated wavelength region in

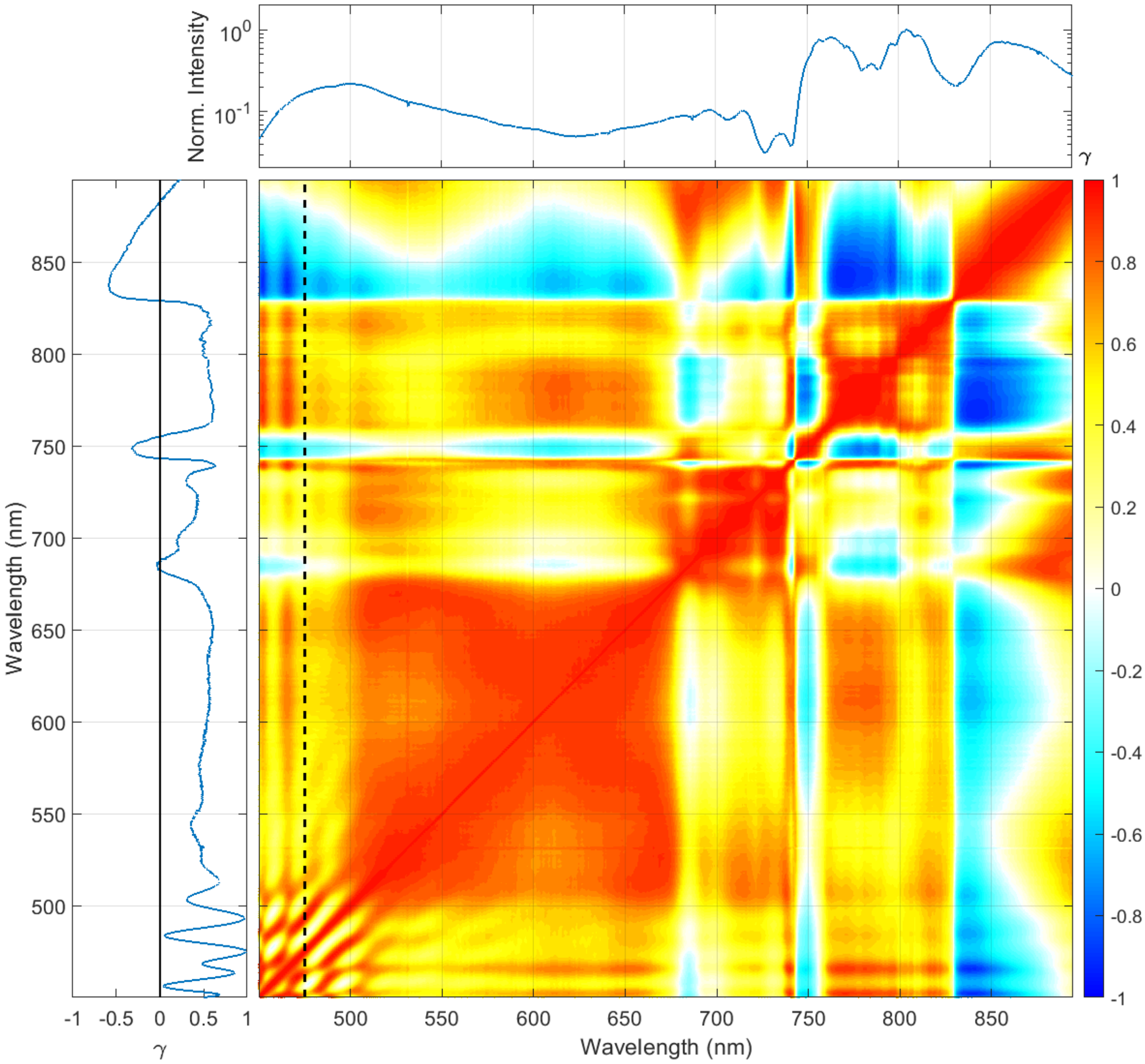

Figure 4.13: Average spectral correlation calculated according to equation 4.3. Top shows the average spectrum for which the correlation is calculated. Left shows the spectral correlation of 475 nm, indicated by the black dashed line in the surface plot.

figure 4.13. This shows that the TA signal can be improved when the effect of spectral correlation can be eliminated with, for example, referencing the probe pulse[204].

The obtained spectral correlation shows resemblance to bulk supercontinuum generation, suggesting that similar processes occur in both supercontinuum generation strategies[204]. Appendix B.1 shows this spectral correlation for the following explanation with the regions of interest indicated.

The fundamental wavelengths, around 790 nm, is anti-correlated to the surrounding wavelengths (indicated in figure B.1). This is the result of self-phase modulation and four-wave mixing of the fundamental wavelength, where the generation of the wavelengths around the fundamental requires depletion of the fundamental wavelength[207]. This is also observed by the plate dependent spectra where a dip in the spectrum is obtained at 800 nm while the surrounding wavelengths increase in relative intensity as can be seen in figure 4.5[204]. The positive correlation in the top right (>830 nm) is a result of self-phase modulation and four-wave mixing, where the generation of wavelengths longer than the input wavelengths results in turn in the generation of more and longer wavelengths.

The short wavelength region (<750 nm) show a strongly intercorrelated signal which shows that a similar interaction is likely the cause for this entire region (indicated in figure B.2). In this case, it can be assigned to the anti-Stokes shift caused by self-steepening[210]. As for the region between 450 nm and 500 nm, a similar oscillatory signal is observed as for the pseudo structures in figure 4.12. These features show resemblance to the combination of self-phase modulation and four-wave mixing observed in nonlinear optical fibres[211,212].

The shorter wavelength range and the wavelengths surrounding the fundamental are anti-correlated (indicated in figure B.2). The photons with shorter wavelength are mostly a result of self-steepening assisted self-phase modulation while the long wavelengths are a result of direct self-phase modulation and four-wave mixing. The anti-correlated behaviour is explained by figure 2.4b, which shows that the self-steepening decreases the spectral broadening into the longer wavelength. Therefore, a stronger self-steepening will result in a weaker red shift.

4.5 Double-stage multiple plate compression

4.5.1 Double-stage multiple plate compression setup

After these first results, we have built a similar system in our own lab. In this case, a Ti:Sapphire amplifier system (MaiTai, Spitfire, Empower, SpectraPhysics) generating pulses at a 3 kHz repetition rate, with a 100 fs duration and an 11 nm bandwidth centred around 805 nm.

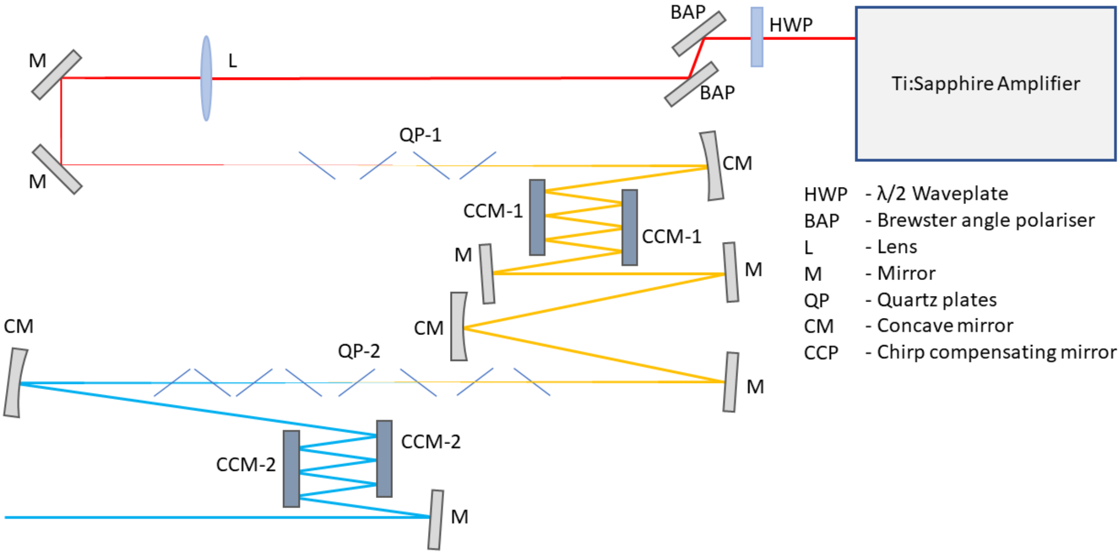

Figure 4.14: Schematic of the double-stage MPC. All optical components are listed on the right, ordered by following the beam path. The input pulse energy is tuned by a $\lambda/2$ waveplate and Brewster's angle polarisers. The pulse is focused with a long focal length (f = 1000 mm). Four quartz plates are placed, at Brewster's angle, near the focal point of the beam to obtain a bandwidth supporting 30 fs pulse duration. This beam is collimated by a concave mirror and temporally compressed using a set of chirp compensating mirrors. Another concave mirror focuses the beam and a series of five quartz plates are placed near the focal point to obtain further broadening. After collimation, this pulse is again temporally compressed using chirp compensating mirrors.

Due to its limited initial bandwidth, and (therefore) long pulse duration, it is not possible to achieve the large broadening using a single MPC stage. This is due to the lower spatiotemporal peak power, weakening the nonlinear interactions within the plates. Additionally, the dispersion generated within each plate lowers the spatiotemporal peak power, preventing the use of a single series with many plates. Therefore, a double-stage MPC is constructed as shown in figure 4.14, where the pulses are temporally compressed between the two stages.

The intensity and polarisation of the input beam is set by using a $\lambda/2$ waveplate and a pair of Brewster's angle reflection polarisers. The beam is then focused using a thin lens (L) (f = 1,000 mm) onto 4 thin (200 μm) z-cut quartz plates (QP-1). These plates are placed near the focal point, at Brewster's angle. Again, the placing of the first plate and the distance between the sequential plates is determined by balancing the spectral broadening and stability of the spectrum. A concave mirror (CM) (f = 500 mm) is then used to collimate the broadened pulse. This pulse is compressed using a combination of chirped mirrors (CCM-1). A set of commercially available chirped mirrors is used to compensate for 500 fs^2 GDD at 800 nm and a pair of custom chirped mirrors is used to compensate for the higher order dispersion. The beam is then focused (f = 1,500 mm) onto the second stage, consisting of 5 z-cut quartz plates (QP-2) with a thickness of 200 μm. The position of the first plate and distance between the plates is again determined by the balance between spectral broadening and the stability of the spectrum. The beam is then collimated by a concave mirror (f = 500 mm) and sent through a second stage of commercial chirp compensating mirrors (CCM-2), compensating for 275 fs^2 GDD at 700 nm.

4.5.2 Transient absorption spectrometer

For the double-stage MPC, a different TAS system is used than for the single-stage MPC. The main components are similar, however, this system is designed to be compatible with the Sagnac-FDI system, which will be discussed in chapter 5. The system is shown in figure 4.15.

The supercontinuum, generated by the double-stage MPC, is sent through a chirp compensating wedge pair where the first back reflection is used as a probe pulse

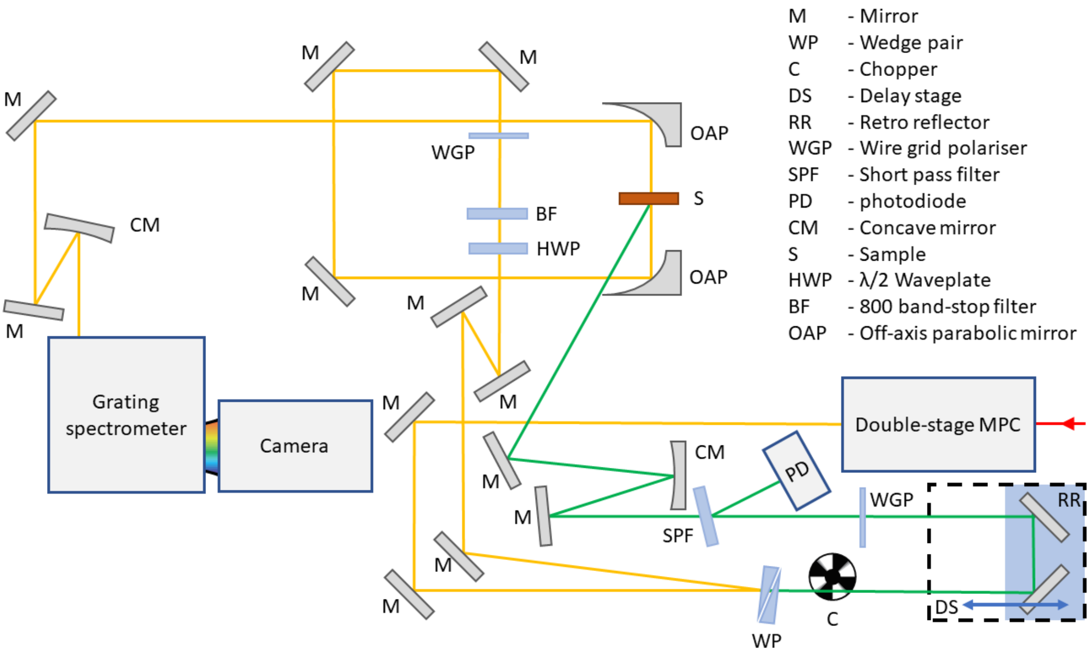

Figure 4.15: Schematic of the experimental setup used to characterise the pulses generated by the double-stage MPC. All optical components are listed on the right, ordered by following the beampath (first pump path, then probe path after splitting).

and the transmitted pulse is used for the pump. The pump is then chopped using a mechanical chopper to obtain sequential excited state and ground state shots. The time delay is set by a retroreflector on a computer controlled mechanical delay stage. A wire grid polariser in the pump path is set to obtain magic-angle (57.4 °) excitation with respect to the probe. The strong fundamental is then blocked out by a 750 nm short pass filter and the reflection of this filter is captured by a photodiode to index the shots as ”on” and ”off”. A concave mirror (f = 500 mm) is used to focus the pump onto the sample. The position of the concave mirror can be adjusted to tune the spot size while a variable ND-filter wheel (not shown) is used to adjust the pump intensity.

The probe is sent through wire grid polariser to obtain a P-polarised beam. An 800 nm band-stop filter is used to eliminate a large portion of the intense fundamental 805 nm. Then, a pair of off-axis parabolic mirrors (f = 101.6 mm) is used to focus the probe onto the sample and collimate the beam after. Finally, the probe is sent into a spectrometer (SpectraPro 2150, Princeton Instruments) and the individual shots are being captured by a fast linescan detector (Glaz LineScan-I-gen2, Synertronic with Hamamatsu S13014 CMOS).

4.6 Double-stage - Results and discussion

4.6.1 Spectral broadening

As mentioned in section 4.3 the pulse is broadened by inserting thin plates. For the double-stage MPC, we have used a series of four and a series of five z-cut quartz plates with a thickness of 200 μm for the first and second stage respectively. With the insertion of every plate, the laser pulse broadens as shown in figure 4.16. Here, the first stage broadens the spectral width of the pulse from 11 nm to $\sim$30 nm. Further broadening is inefficient at this point as each plate contributes to more dispersion of the pulse, lowering the temporal peak power.

The obtained spectrum after the first stage has two features which are an indication of self-phase modulation. The dip occurring in the spectrum at 815 nm and the symmetric broadening as described by equation 2.26[116]. The slight asymmetry towards the longer wavelengths is an indication of the four-wave mixing, which results in a spectral broadening which is slightly moving the centre towards the red.

To overcome the dispersion limitation, these generated pulses are temporally compressed to achieve a high peak intensity required for further broadening of the spectrum. The compression is done by a set of custom chirped mirrors to compensate for the higher order chirp and a set of commercial chirped mirrors to compensate for 500 fs^2 GDD at 800 nm. The actual chirp has not been measured, however, the chirp compensation was optimised by focusing (f = 150 mm) the beam in air and comparing the length of the generated plasma, where a longer plasma trail indicates higher peak intensity due to stronger self-focusing of the beam. The total compensation is adjusted by the amount of bounces on the commercial chirped mirrors.

After the compression of the pulse after the first stage, the second stage broadens the spectrum further. With the insertion of the third plate of this stage, a clear yellowcoloured ring is observed and the spectrum stretches out. A spectral broadening spanning between 500 nm and 950 nm is achieved for a total of 5 plates in the second stage. Adding more plates does not broaden the spectrum further as each plate contributes to the dispersion, reducing the peak energy. The duration of this pulse has not been measured as there is no delay stage available in the lab during this research with high enough precision. However, the calculated shortest possible pulse duration with the spectrum after the fifth plate of the second stage is 3.8 fs.

The reduced spectral range of this spectrum, when comparing to the single-stage MPC, is likely due to the use of thicker plates. These were picked as the amplifier system driving this MPC generates a certain degree of spatial chirp in the pulses. That is, the pulse does not have a perfect Gaussian-like (TEM_{00}) spatial energy distribution. This results in a nonuniform spatial intensity distribution within the plates, lowering the achieved spatiotemporal peak power. Therefore, a longer travel distance within the medium is required to achieve sufficient self-focusing to achieve the required intensity for supercontinuum generation. To compensate for this, we have used thicker, 200 μm, plates to allow for a longer travel length through the high nonlinear

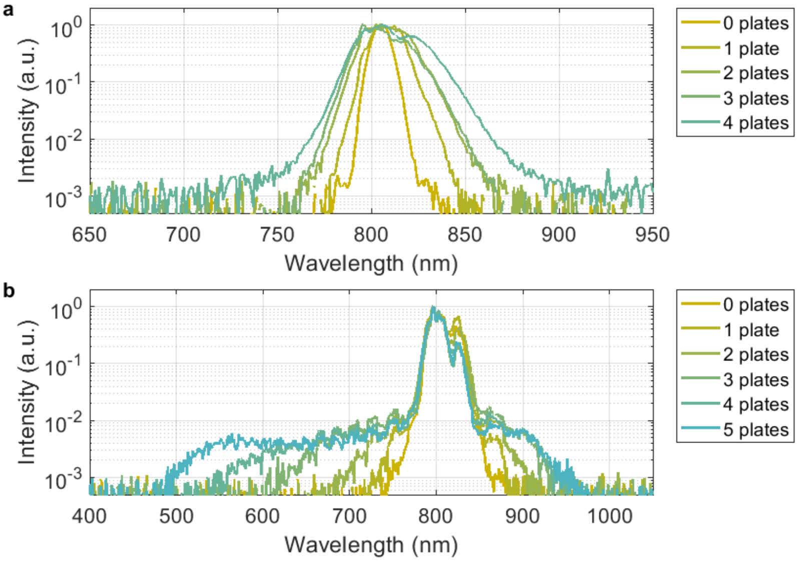

Figure 4.16: Example of the spectral broadening for a) the first MPC stage and b) second MPC stage as discussed in section 4.5.1. Each quartz plate has a thickness off 200 μm.

coefficient material. This, however, induces more dispersion of the pulse, lowering the temporal intensity while traveling through the plates and thereby lowering the spectral broadening, and lowers the conversion efficiency due to phase-mismatching.

4.6.2 Stability and spectral density

For the pulses obtained by the double-stage MPC, the spectral density is calculated as well in a similar fashion described in section 4.4. With an input energy of 197 μJ per pulse, the total output energy after the final compression stage is 71 μJ per pulse, resulting in a 36 % conversion efficiency. This is lower than for the single-stage MPC, which can be expected from to the additional compression and MPC stage in this system.

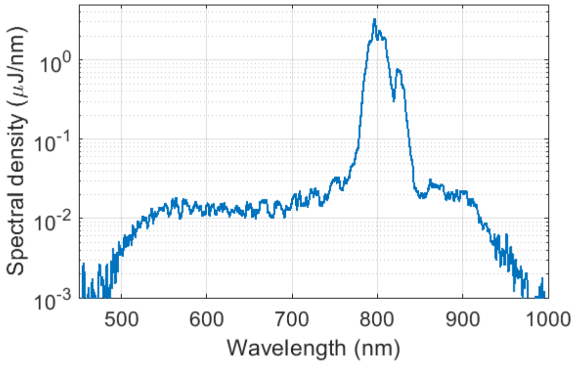

Figure 4.17: Estimated spectral density for the double-stage MPC system. The spectral density is calculated by equalling the integral of the spectrum to the total pulse power (71 μJ per pulse).

The resulting spectral density is shown in figure 4.17. Here we see that the spectral density over the whole generated range is over 10 nJ/nm, which at a similar level as the spectral density of the single-stage MPC shown in figure 4.6. The slightly lower spectral density is a result of the two-stage system, where additional losses are expected from reflections of the plates and the compression stage.

To analyse the use of the double-stage MPC within the field of pump probe spectroscopy, we have again gathered multiple sets of 2,000 shots as well using the system described in section 4.5. To reduce the intensity of the fundamental wavelengths, we have implemented a physical beam block in the centre of the pulse after the MPC. This will induce spatial chirp, however, this does not impact the supercontinuum process or the stability of the pulses.

The obtained spectrum and relative standard deviation is shown in figure 4.18. This shows that the obtained probe spectrum spans from about 520 nm to 980 nm with an average standard deviation over this spectrum of 4.5 %, similar to that of the single-stage MPC (4.6 %) shown in figure 4.8. The standard deviation of the spectrum also shows a similar shape to that of the single-stage MPC, indicating that similar nonlinear processes occur within this MPC system. The low standard deviation near the 805 nm region corresponds to the input wavelengths, which will have a lower noise level as this region is not generated via the nonlinear processes within the MPC.

4.6.3 Transient absorption noise baseline measurement

To obtain an understanding of the noise level of this system, we have calculated the TA signal while blocking the pump pulse. The spectrum used and the corresponding TA signal is shown in figure 4.19. The average root mean square noise level of the TA spectrum between 550 nm and 930 nm is 1.6×10^{-4}, which is lower than that of the single-stage MPC (2.6×10^{-4}), therefore we expect an even higher signal to noise level

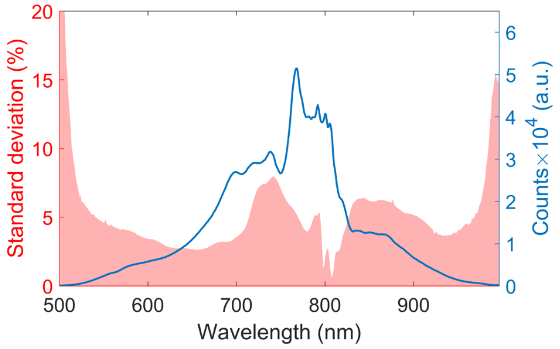

Figure 4.18: Average spectrum of 2,000 shots generated by the MPC in blue. The standard deviation of these shots is given in pink, with an average relative standard deviation of 4.5 % between 520 nm and 980 nm.

while performing a TA measurement. This is assigned to the higher repetition rate of the laser, for which we expect lower shot-to-shot input fluctuations.

This TA spectrum shows a small pseudo-structure, similar to the ones observed in the single-stage MPC. The intensity, however, is smaller and is therefore not subtracted from the TA signal to obtain the root mean square noise. This pseudo-structure matches the wavelength region of high standard deviation observed in figure 4.18, suggesting they both originate from the spectral correlation of the MPC supercontinuum. As the pseudo-structures are consistent structures with fluctuating intensities, it is still important to understand their origin[206].

4.6.4 Spectral correlation of the MPC supercontinuum

To analyse these pseudo-structures, we have calculated the spectral correlation of this data set by equation 4.3. The spectral correlation is shown in figure 4.20. The spectrum is obtained while blocking the centre of the beam by a physical beam block, where the 750 to 950 nm of the supercontinuum is the most intense, creating a flat spectrum compared to the spectrum shown in figure 4.16b. This is done to allow for a higher photon count on the detector of the wavelengths with lower spectral density while avoiding saturation of the camera. The spectral correlation shows several distinct features which are indicated in appendix B.2. It is important to remember that this is a double-stage MPC, where the generation of the supercontinuum occurs

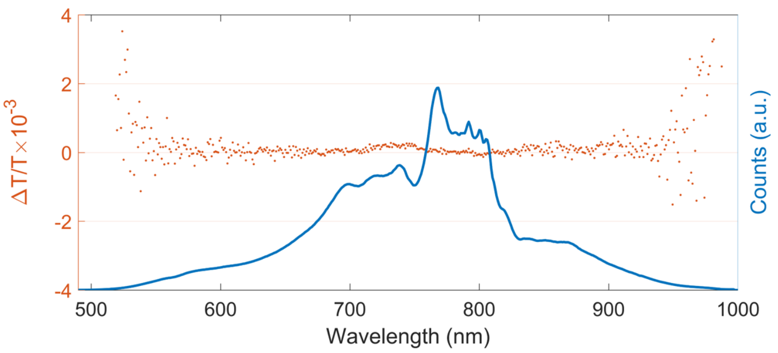

Figure 4.19: Spectrum in blue and calculated $\Delta T/T$ in red for 1,000 shot pairs generated by the double-stage MPC. A small pseudo-structure in the TA signal can be observed at 720 nm.

in two distinct sequential steps.

The area near the driving wavelengths, around 805 nm, and the neighbouring wavelengths are anti-correlated (indicated in figure B.3). This shows that self-phase modulation and four-wave mixing are the dominant mechanisms in the first stage of the MPC, similar to that observed in the single-stage MPC. These neighbouring wavelengths play a significant role in the further broadening of the pulse in the second stage.

The correlated signal in the longer wavelength range (>810 nm), is the result of self-phase modulation and four-wave mixing of the pulse towards longer wavelengths, similar to that of the single-stage MPC. The positive triangle shape in the bottom-left corner of this region, at 820 nm, is the result of the first stage while the rest of the frequencies is a result of the second stage. This corresponds to the observed plate dependent spectrum, shown in figure 4.16.

The shorter wavelength region (<775 nm) is the region that is generated via the self-steepening assisted Stokes-shift in the second stage (indicated in figure B.4). This is the same as found for the single-stage MPC, however, this plot shows large negative correlation within the region of positive correlation. This negative correlation and the negative correlation of the longer wavelengths (>810 nm) with respect to the input frequency of the second stage is a result of four-wave mixing and self-phase modulation of the second stage input pulse. The anti-correlation is a result from the depletion of the input wavelengths is required to generate the neighbouring wavelengths. This is similar to the single-stage MPC or the first stage of this MPC, where the wavelengths around the input wavelength are negatively correlated. The four-wave mixing and self-phase modulation competes with the self-steepening of the pulse. The region generated by self-steepening does not show the same square positive correlation as the single-stage MPC as the positive correlation of self-steepening competes with the self-phase modulation and four-wave mixing. This shows that the small pseudo-structure in figure 4.19 around 750 nm is likely to be a result of the competition between self-phase modulation and four-wave mixing, and self-steepening.

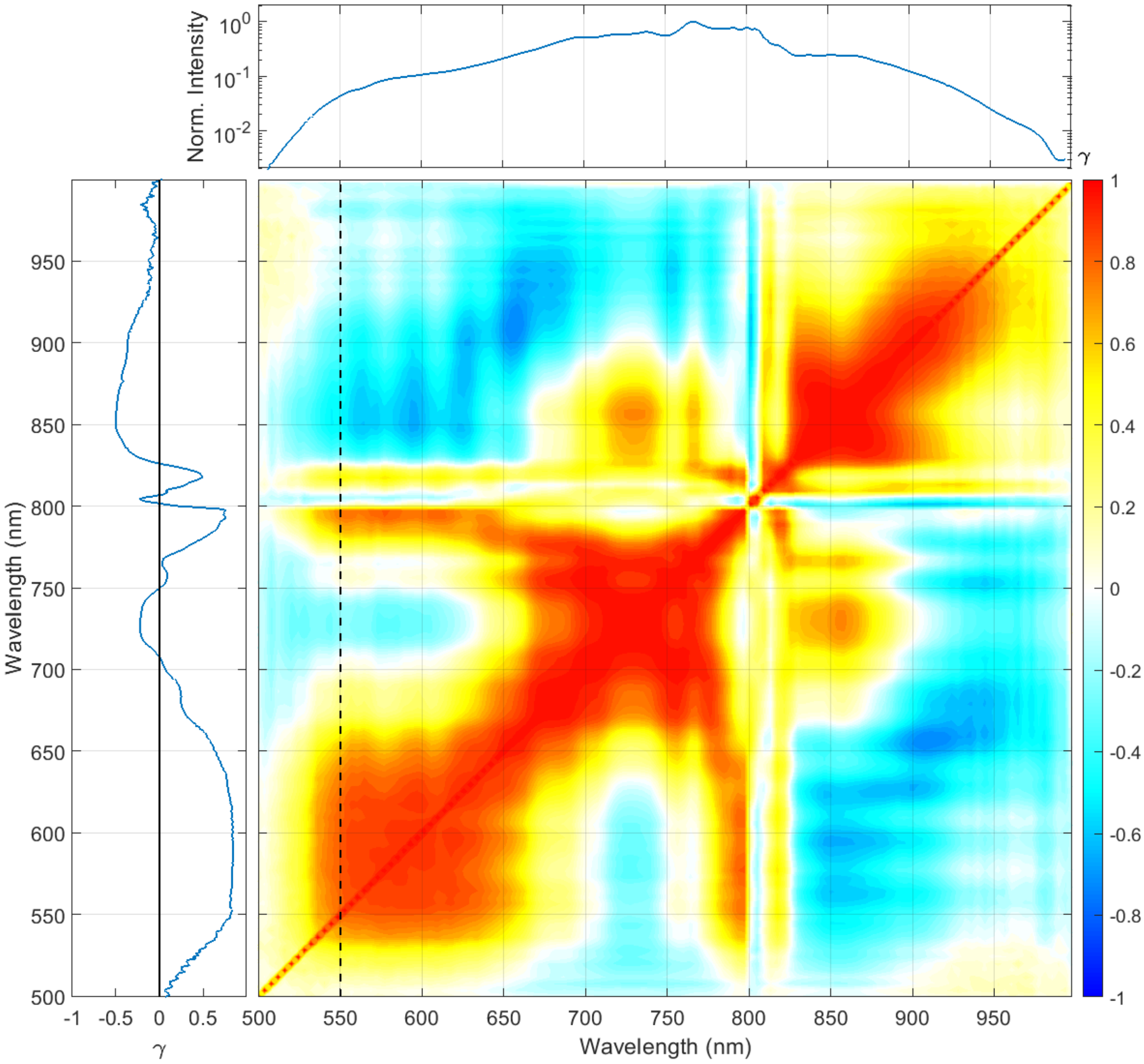

Figure 4.20: Average spectral correlation calculated according to equation 4.3. Top shows the average spectrum for which the correlation is calculated. left shows the spectral correlation of 550 nm, indicated by the black dashed line in the surface plot.

4.6.5 Comparison of single-stage and double-stage MPC

The first system is based on a single-stage MPC, which broadened the 25 fs pulses, centred at 790 nm with a 30 nm bandwidth to pulses with a spectrum spanning from 490 nm to over 1000 nm and a 3.3 fs pulse duration. These pulses have a high spectral density (>14.5 nJ/nm) which enabled the use of a single MPC light source to generate both pump and probe pulse for TAS.

The second system is based on a double-stage MPC. This system broadened the 120 fs pulses, centred at 805 nm with an 11 nm bandwidth to a bandwidth of 500 nm to 950 nm. This is achieved in two broadening and temporal compression steps, where broadening and temporal compression occur sequentially. Here, a similar minimum spectral density (>10.5 nJ/nm) is obtained as for the single-stage MPC, thus showing it to be a great candidate as a single light source for TAS as well.

For the application in TAS, it is important to understand the shot-to-shot stability and baseline noise level of the system. These parameters determine the achievable signal-to-noise level while performing an experiment. The average standard deviation of 2,000 shots is measured for both the single-stage and double-stage MPC and are found to be 4.6 % and 4.5 % respectively. A $\Delta T/T$ noise level of below 3×10^{-4} root mean square noise is achieved using 1,000 shot pairs for both systems, demonstrating the high sensitivity of this system.

4.7 Example measurement of $MAPbI_3$

Finally, to see the MPC-TAS system in action, a TA measurement is taken on a $MAPbI_3$ perovskite microcrystalline thin film on a fused silica substrate, whose excited state properties are well studied and have a well-known TA response[142,213–215]. The single-stage MPC setup, as described in section 4.3, is used for this measurement as both MPC systems show similar properties, such as the spectral broadening, TA noise baseline, and shot-to-shot standard deviation, while this system has the added benefit of having a known pulse duration of 3.3 fs. The application of the double-stage MPC as a single light source in FDI is discussed in chapter 5.

The resulting pump spectrum after the short pass filter is shown in figure 4.21a. A large part of this spectrum overlaps with the ground state absorption of $MAPbI_3$ perovskite films as obtained by Umari *et al.*[61], also shown in this figure. The fluence used in this experiment is 20 μJ/cm^2 and was achieved by the short pass filter, a neutral optical density filter with OD=1, almost fully detuning the $\lambda/2$ waveplate and using an excitation spot size with a diameter of 1 μm FWHM. This shows that the pulses generated with the MPC light source are extremely bright.

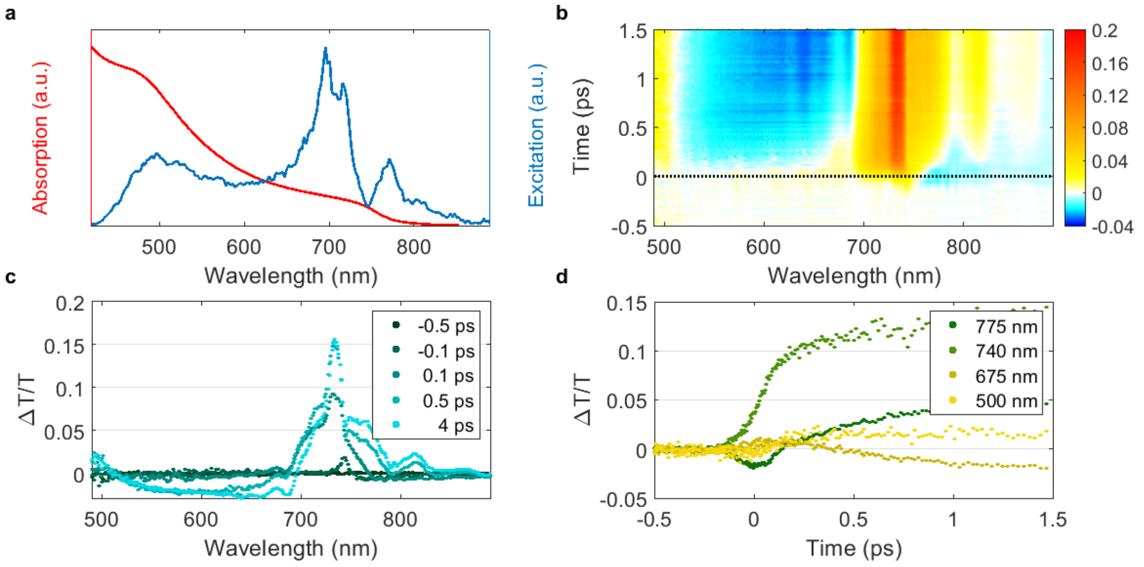

Figure 4.21: TA results from the single-stage MPC-TAS on a thin film of $MAPbI_3$ perovskite with only 1,000 shot pairs (2 second acquisition time) per time point. a) Absorption spectrum of $MAPbI_3$ and excitation spectrum of the pump. b) TA surface obtained for $MAPbI_3$ with an excitation fluence of 20 $\mu J/cm^2$. c) Spectral slices at the indicated time delays, calculated by the mean of an interval of 3 time points. d) Kinetics at the indicated wavelengths, where a 5 pixel average (1.25 nm) is used to obtain the kinetics.

The surface plot of the resulting TA spectrum is shown in figure 4.21b. This shows that with the intensity of a single back reflection, even with the high absorption coefficient of $MAPbI_3$ perovskite, the spectrum from 490 nm to 890 nm is obtained. Here, the 890 nm cut-off is due to the physical size of the detector. This spectrum shows the typical features obtained with TA of $MAPbI_3$ perovskite, such as the GSB at 740 nm and at 500 nm, and the PIA between 500 nm and 700 nm. At early times, the BGR at 775 nm and the hot carriers between 500 nm and 700 nm are observed[142]. This becomes more apparent when looking at the spectral slices at various time delays as shown in figure 4.21c. Note that for TA, chirp correction of the probe pulse is generally required due to the chirp of the pulse up to a couple ps[38]. In this case, no chirp correction is applied to this data, indicating the short probe pulse duration.

A big advantage of the MPC as a supercontinuum light source for both pump and probe is shown in figure 4.21d, where temporal slices at the interesting features described above are presented. These slices are obtained by averaging the $\Delta T/T$ signal for 5 pixels around the wavelength indicated in the plot, with a resolution of 0.25 nm per pixel.

First, at 775 nm, the signal becomes negative due to the BGR while, after 400 fs, it turns into a positive signal due to the state filling caused by carriers cooling to the band edge. These carriers lose energy and cool down to the band edge by electron-phonon scattering on the ps time scale. A similar signal is observed at 500 nm, where a small negative signal appears around time zero. This wavelength lies just above the second band edge of $MAPbI_3$ perovskite[142]. This indicates that this is due to the BGR of the second band edge, quickly followed by a positive signal induced by the cooling of hot carriers, causing the state filling effect. Due to the small amplitude and short life time of this negative feature, it is often obscured with regular TA measurements. This is due to either the long pump pulse duration, generating an IRF with a long duration, or limited spectral range of the TAS system due to the high absorption coefficient of $MAPbI_3$ perovskite in this region.

When considering the GSB at 740 nm, we can observe a distinct two-fold rise time. These fast rise component ($<$100 fs) is due to the carrier thermalisation, where the carriers undergo fast scattering from an anomalous energy distribution to a Fermi-Dirac distribution[29]. The second slower rise component ($>$1 ps) is, similar to the positive signal at the BGR due to hot carriers cooling down. This is further verified by comparison of the kinetic trace at 675 nm, which shows a decrease of the state filling towards the negative PIA signal at the same time scale as the slow rise of the GSB. This two fold rise time is only observed in TA when using short pump pulse durations, as the carrier thermalisation process occurs on such a fast time scale[216].

4.8 Discussion and conclusion

In this chapter, we have built two MPC-TAS systems to demonstrate the capabilities of the MPC as a single light source for both the pump and probe pulse in the field of TAS. The MPC has never before been applied in the field of ultrafast spectroscopy and therefore investigation of the shot-to-shot stability is required. This is an important parameter for ultrafast pump-probe spectroscopy, and for the field of ultrafast spectroscopy in its entirety, as it determines the achievable signal-to-noise level.

To research the feasibility of the application of the MPC in the field of ultrafast spectroscopy, we have collected series of shots and analysed the shot-to-shot stability to estimate shot noise level of the pulses generated by the MPC. The obtained relative standard deviations over the whole spectra for both the single- and double-stage MPC are 4.6 % and 4.5 % respectively for 2,000 shots. The expected noise levels obtained with both MPCs is below the 3×10^{-4} level for 1,000 shot pairs which is well below the typical TA signal, proving that the MPC is a suitable light source for TAS experiments.

The spectral correlation and the spectral broadening of the systems are explained and compared and show a similar correlation spectrum between the two different systems. The spectral correlation provides a better understanding of the interaction of the various dominant nonlinear processes occurring within the MPC plates. Understanding these dominant nonlinear processed can help with future improvements of the MPC system.

The single-stage MPC only shows self-phase modulation and four-wave mixing in the first three plates. When sufficient self-steepening is achieved, strong broadening to the blue side occurs after the third plate, resulting in a bright blue pedestal.

As for the double-stage MPC, the first stage only shows the four-wave mixing and self-phase modulation effects, broadening the pulse near the input wavelengths. This intermediate pulse has similar properties to that of the single-stage MPC input. The second stage achieves sufficient self-steepening after the third plate. The spectral correlation of the second stage is explained in a similar fashion to that of the single-stage MPC, showing that four-wave mixing and self-phase modulation are competing with self-steepening.

The results of this chapter show that the MPC is a bright, broadband, temporally compressible and stable light source. These properties show potential for the use of the MPC as a single light source in multi-dimensional spectroscopy, such as 2-Dimensional Electronic Spectroscopy[217]. These properties are also required for laser ablation techniques, where a compressed pulse is used to remove material from a solid-state material while avoiding heating effects within the remaining material[218]. These, and further possible applications are discussed in section 6.

In the next chapter, we have combined the double-stage MPC with an improved FDI technique. This system overcomes the limitation of the spectral density of the reference-probe pulse pair by using the bright MPC. The duration of the IRF is reduced by using the short pulses generated by the MPC. Furthermore, the time delay of the reference and probe pulses at the sample position and detector is decoupled by using a Sagnac interferometer and birefringent crystals.

Chapter 5

Ultrafast refractive index change of pentacene by multiple plate compression-Sagnac-frequency domain interferometry

5.1 Introduction

In chapter 3, we have obtained the change of the real refractive index of $CsPbBr_3$ perovskite upon photoexcitation using a FDI setup[154]. This system is used to directly measure the relative phase of the interference in the frequency domain of broadband reference and probe pulses, avoiding the need of modelling required for transient reflection or ultrafast ellipsometry measurements[29]. This current system, however, has two limitations which will be addressed in this chapter.

The first limitation is the temporal range of this technique, which is determined by the maximum time delay of the reference and probe pulses so that they temporally overlap after the grating[36]. The two pulses are required to have some temporal overlap at the detector to create an interference pattern, setting an upper limit to the time delay of the probe. The pump has to excite the sample between the reference and probe arrival times to obtain an unperturbated reference and perturbated probe pulse. Therefore, only kinetics at a timescale up to the reference-probe time delay can be measured.

The second limitation is that the FDI spectrometer requires high resolution to observe the smallest of phase changes. This is obtained by using a highly dispersive grating, which means that every pixel measures the photons of only a small spectral range. To obtain a reliable signal, a high photon count on each pixel is required. Bulk supercontinuum can generate a broad spectrum, but has a spectral density in the pJ/nm range. This complicates the application of the FDI system on highly absorbing samples, which are the samples of interest for photovoltaic applications.

In this chapter, a Sagnac-FDI system is combined with the MPC described in chapter 4 to overcome these limitations[37]. The use of the Sagnac interferometer temporally separates the reference and probe pulses at the sample position and recombines the pulses afterwards. To obtain interference in the frequency domain, a birefringent wedge pair is used to set the time delay at the detector. This decouples the reference-probe delay from the delay at the detector and allows for the observation of timescales beyond the 2 ps previously achieved.

Besides this, the Sagnac interferometer has an added benefit of being a common path interferometer. This means that both pulses travel along the same path ″seeing″ the same optical components within a couple nanoseconds. Because of this, these pulses are passively phase matched as both pulses are subjected to the same small mechanical vibrations and fluctuations of the environment within the interferometer which occur on a microsecond to millisecond timescale[219].

The MPC generates broadband pulses with an overall high spectral density, in the tens of nJ/nm range[44,220]. This enables the use of a single MPC system to generate the pump, reference and probe pulses, all with sufficient intensity. The supercontinuum pulses generated by the MPC is also easily temporally compressible to a couple of femtoseconds in duration, which is used to reduce the IRF duration of the system and measure kinetics on a shorter timescale[45].

The MPC-FDI is applied to measure the optically induced refractive index change of pentacene. This material is chosen as it has a complex TA response and thus an expected complex refractive index change, showing the capability of the FDI system. The measured refractive index change is used to validate the refractive index change obtained from a differential dielectric functions model developed by Arjun Ashoka from the University of Cambridge, United Kingdom.

Model to retrieve the excited state complex refractive index

The refractive index of a material is directly coupled to the absorption coefficient via the KK relations, as discussed in section 3.2[221]. These KK relations are applied to calculate the ground state refractive index after measuring the steady state absorption coefficient, or the absorption coefficient from the refractive index obtained by ellipsometry[222–224].

The use of the KK relations for steady state measurements is allowed as the system is not strongly perturbated before the probing event. For transient absorption, however, the causality condition of KK is broken as the signal is not the isolated real or imaginary part of the refractive index[149,221]. Because of this, it is not possible to directly retrieve the change in refractive index from the transient absorption signal by applying the KK relations.

To circumvent this issue, our collaborator Arjun Ashoka, from the University of Cambridge, United Kingdom, has developed a model to retrieve the change of the refractive index from the ground state transmission and TA signal. This model uses KK consistent Lorentz oscillators and variational oscillators to fit the transmission signal[169,225]. These oscillators are KK consistent as they simulate the electrons as natural damped oscillators, following causality. This is then combined with the TA signal and a rewritten TA equation via calculus of variations to obtain the change in the dielectric functions. This model requires no input parameters, other than the sample thickness, and does therefore not suffer from biased user input. This model is applied to the $CsPbBr_3$ perovskite from chapter 3.4 and pentacene to retrieve the real refractive index to compare the results with the refractive index change obtained by the FDI system.

5.2 Theory

5.2.1 Sagnac interferometer for temporal separation at the sample

The Sagnac interferometer is suited to generate a time delay between the reference and probe required for FDI. This is done by placing the sample off-centre within the interferometer as shown in figure 5.1a. The spatial movement of the pulses through the interferometer is indicated by the arrows shown in the schematic of the interferometer. The movement of the pulses within the interferometer is displayed

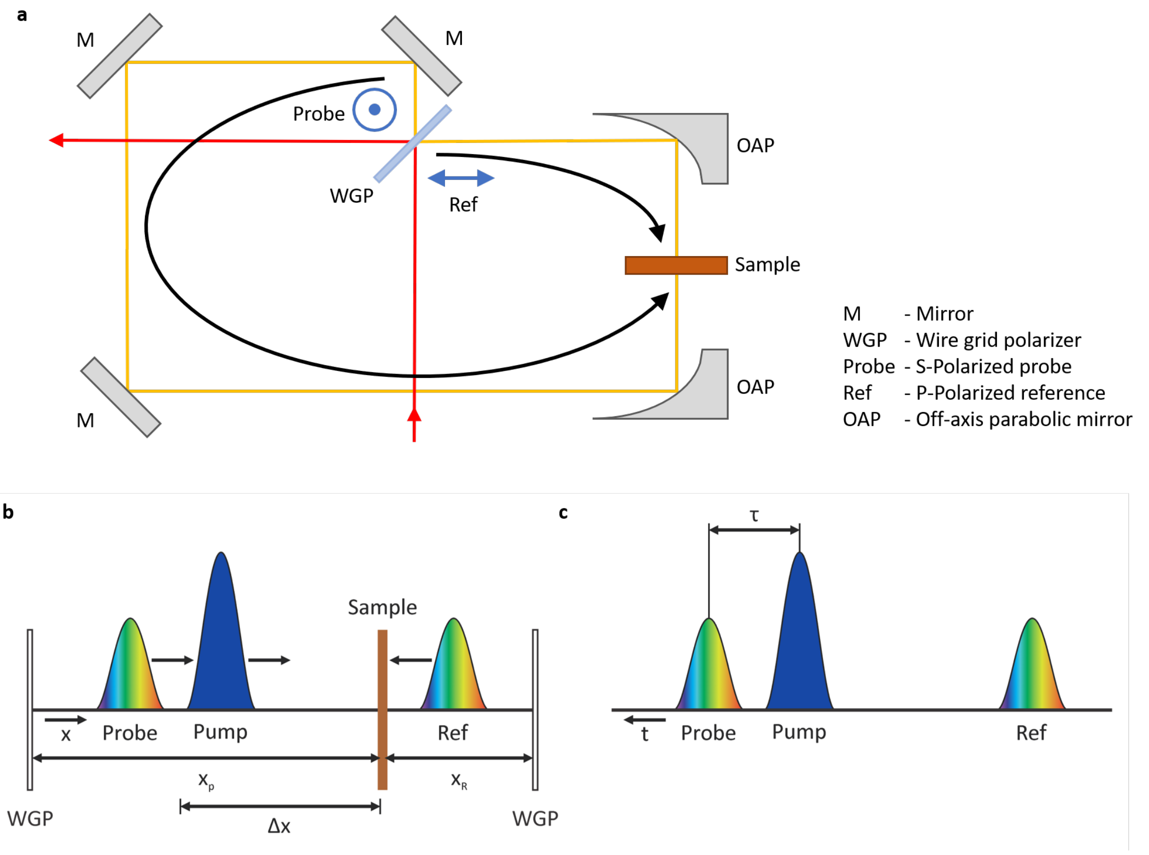

Figure 5.1: a) The Sagnac-interferometer path (indicated in yellow) with the S-polarised probe pulse transmitted and moving counter-clockwise and the P-polarised reference pulse moving clockwise. b) Spatial overview of the pulses when they have just entered the Sagnac interferometer. The single wire grid polariser for splitting and recombination of the reference-probe pair is indicated by WGP and the x-axis indicates the travel direction of the probe pulse (counter-clockwise). The arrows indicate the direction of movement of the pulses. c) Temporal overview of the pulses at the sample position.

in figure 5.1b. The x-axis indicates the loop in the Sagnac interferometer with the traversing direction of the probe pulse. The polarisers on either side of this diagram represent the single beam splitting and recombination wire grid polariser of figure 5.1a. The probe travels in the anti-clockwise direction and the reference in the clockwise direction through the interferometer, as indicated by the arrows. Note that the pump pulse is not actually passing through the interferometer, but is shown this way in this diagram for clarity.

Both reference and probe arrive back at the wire grid polariser, at the opposite side of the diagram in figure 5.1b, at the same time as the total path length within the interferometer is the same for both pulses. This cancels out the reference-probe time delay observed at the sample. This fully decouples the time delay at the sample position from the time delay at the camera, which has previously limited the temporal range of the Michelson-FDI system. Instead, we have used the polarisation of the pulses to create a time delay with the use of a birefringent wedge pair (BWP), as discussed in section 5.2.2. The wire grid polariser also acts as a filter for potential polarisation changes of the reference probe pulses within the sample due to anisotropy, only reflecting and transmitting the polarisation state of the input reference and probe pulses respectively.

This diagram shows that the reference arrives at the sample after travelling distance x_R and the probe after distance x_P. The total time delay between the reference and probe arrival time is now determined by the path difference Δx according to

$$T_{\text{diff}} = \frac{\Delta x}{c} = \frac{x_P - x_R}{c}. \tag{5.1}$$

The pulse sequence in the temporal domain is shown in figure 5.1c, showing that this system has the same pulse sequence as obtained for the Michelson-FDI system as discussed in section 2.5, but without the reference-probe delay restriction.

5.2.2 Birefringence for temporal separation at the detector

The Sagnac configuration temporally recombines the reference and probe pulse, resulting in a phase shift of π over the whole spectrum as a result of the double reflected beam[226]. However, to generate an interference in the frequency domain, a time delay has to be generated. Therefore, we have designed and used a birefringent wedge pair, which has a different refractive index depending on the polarisation of the beam[227]. In this case, we have used 2 wedges made from Barium Borate, with a thickness varying from 0.3 mm to 3.5 mm, resulting in a total variable thickness between 0.6 mm and 7 mm. The refractive indices for ordinary (n_o) and extraordinary (n_e) polarisation is shown in figure 5.2a, together with the difference in refractive index[228]. The resulting wavelength dependent time delay for a 2.5 mm thick crystal is displayed in figure 5.2b.

This wedge pair does not impact the beam pointing while giving the option of tuning the time delay by translating the wedges, resulting in a longer or shorter effective crystal in the beam path as indicated in figure 5.2c. This also shows that a different delay is obtained over the spectral range. However, the spectral windows used in the Fourier analysis to obtain the phase, as discussed in section 2.5.4, are narrow. For this experiment, we have used a fixed window size of 0.01 eV, resulting in a window of 7 nm at 950 nm and 2 nm at 500 nm. The total range of time delays within these windows are 0.36 fs and 0.61 fs for a 2.5 mm crystal respectively. Compared to the time delay generated by these wedges (1 ps), this variation is extremely small. Therefore, the variation of delay between the wavelengths within this window can be ignored.

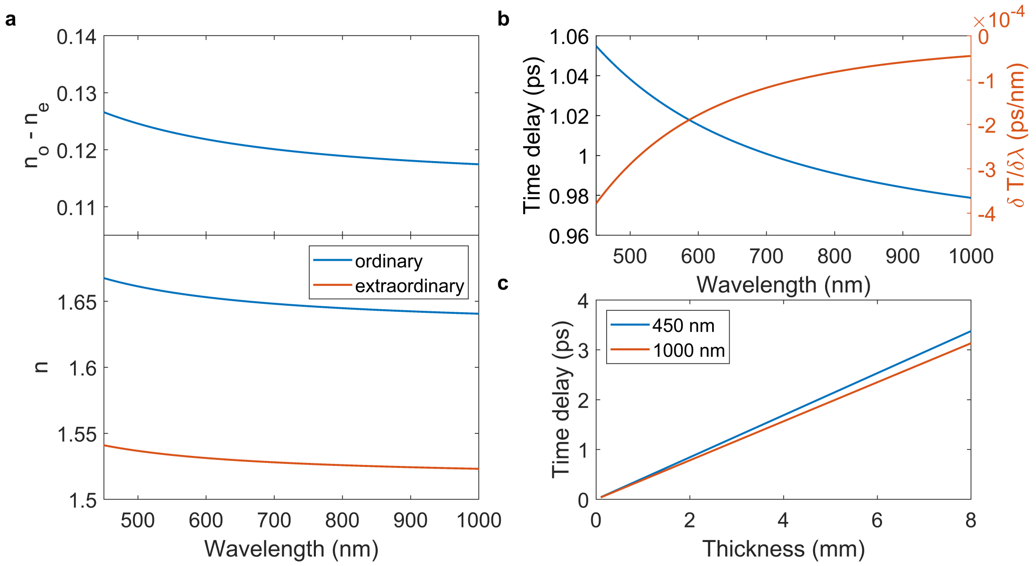

Figure 5.2: a) Refractive index of Barium Borate for ordinary and extraordinary polarisation. b) Wavelength dependent delay for a 2.5 mm thick Barium Borate crystal. c) Time delay generated for the extremes at 450 nm and 1000 nm for varying crystal thickness.

5.3 Experimental setup

5.3.1 Sagnac - Frequency domain interferometer

The Sagnac-FDI system designed to overcome the temporal limitation is shown in figure 5.3. This system is the same system as the MPC-TAS system that was used to measure the stability of the double-stage MPC. The full description of the MPC that drives this experiment is given in section 4.5. The FDI part of this experimental setup is also compatible with the TAS system described in section 4.5, with a couple of small adjustments.

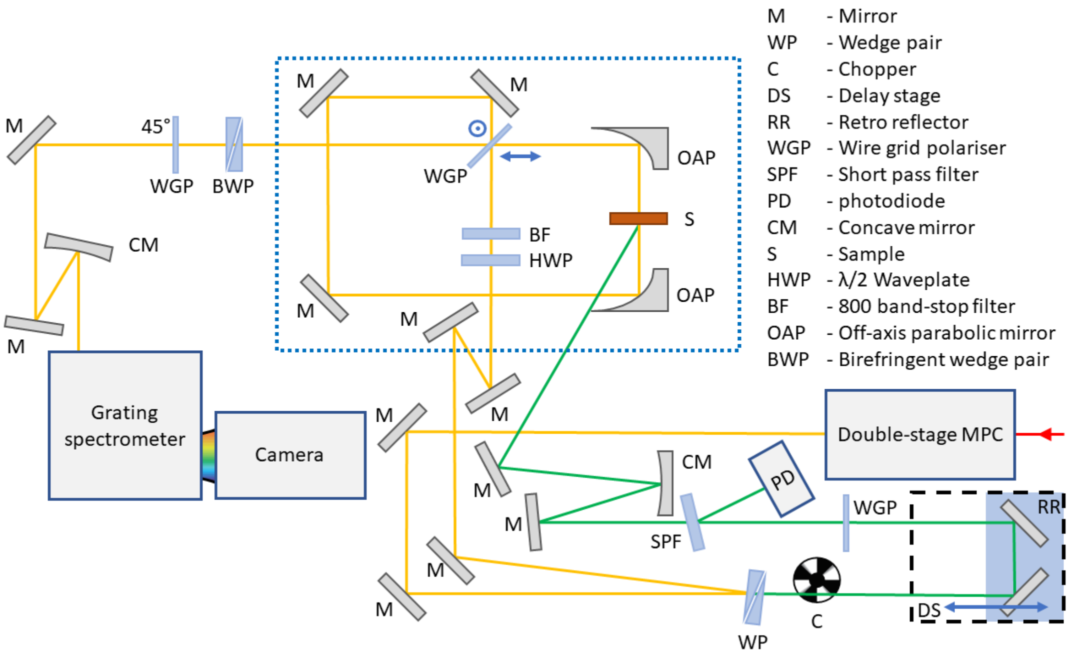

Figure 5.3: Schematic of the Sagnac-FDI system. All optical components are listed on the right, ordered by following the beampath (first pump path, then probe path after splitting).

The wire grid polariser (WGP) in the probe path is now set to intersect the probe so that both the transmission and reflection arrive back at this wire grid polariser. The reflection is set to the P-polarisation and the transmission to the S-polarisation, forming the reference and probe pulse pair. This forms the Sagnac-interferometer part of this setup, indicated by the blue dotted box, and is explained in section 5.2.1[219].

The energy distribution of the P- and S-polarised pulses is tuned by a $\lambda/2$ waveplate to provide maximum contrast in the interference pattern.

After the interferometer, birefringent wedges are places to generated a time delay between the reference and probe pulse. After these birefringent wedges, a wire grid polariser is placed at a 45° polarisation angle with respect to both the reference and probe pulses to align the polarisations of the two pulses. This polarisation alignment maximizes the interference contrast at the detector, allowing for more accurate measurements.

After this, the reference-probe pair is focused by a concave mirror (CM) onto the slit of a grating spectrometer (SpectraPro 2150, Princeton Instruments). A grating with 1,200 gr/mm is used to obtain the high spectral resolution (4.17 nm/mm) required for this experiment. The resulting spectra are captured by a high speed 1D linescan camera (Glaz LineScan-I-Gen-2, Synertronic with Hamamatsu S13014 CMOS), providing a resulting resolution of 0.088 nm/pixel. The total spectral range detected by the camera with this configuration is 45 nm. To obtain the full spectrum, multiple sets of measurements are taken while shifting the spectrum by 30 nm between each measurement, to obtain sufficient (15 nm) data overlap. These individual measurements are then processed to obtain the individual $\Delta\phi$ spectra. With the spectra merged together by weighting the data to Sigmoid functions at the overlapping wavelengths. This process is checked by plotting the obtained Δn spectra at various time delays. This showed deviations within the noise level between the spectra where the spectra are merged and no large discontinuities were found between the spectra.

5.3.2 Differential dielectric functions

The model from our collaborator is capable of extracting the change in real part of the refractive index from the ground state transmission and TA signal. This model uses the combination of coarse Drude-Lorenz oscillators to roughly fit the dielectric functions from the transmission signal, and a set of equidistant variational oscillators to fit the residuals. These variational dielectric functions are then used, in combination with the TA and transmission spectra, to calculate the change in

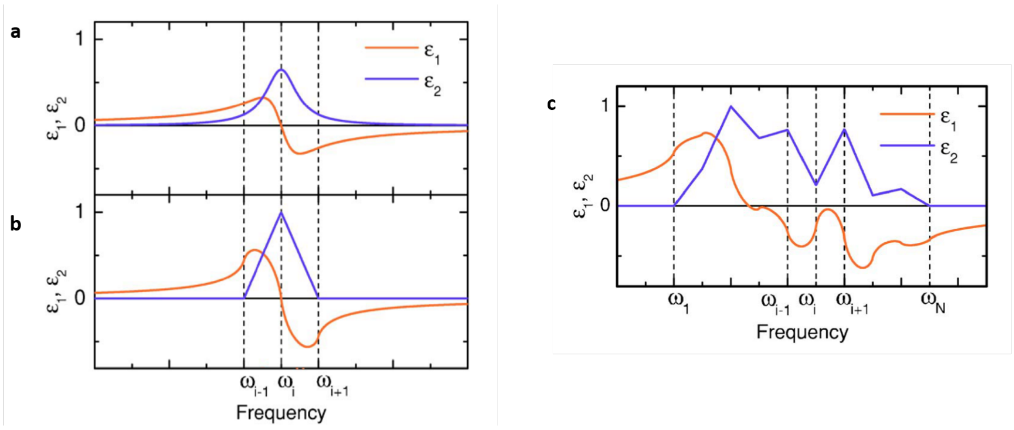

Figure 5.4: a) The dielectric functions for a classic Lorentz oscillator model where ϵ_1 and ϵ_2 extend to neighbouring frequencies. b) The dielectric functions for a variational oscillator where ϵ_2 only affects the region around the centre frequency, decoupling the neighbouring oscillators and allowing for easier computation. Here, ϵ_1 is obtained via KK relations. c) The sum of multiple variational oscillators, ϵ_2 and the corresponding ϵ_1 obtained via KK relations. Reprinted from Kuzmenko[169], with the permission of AIP Publishing.

dielectric functions.

Variational dielectric functions

The Drude-Lorentz oscillator model is often applied to fit the dielectric function of materials. It is combined with the KK relations to retrieve the real from the imaginary part or vice versa. The Drude-Lorentz oscillators formula is given by

$$\epsilon(\omega) = \sum_{k=1}^{N} \frac{\omega_{p,k}^2}{\omega_{0,k}^2 - \omega^2 - i\omega\gamma_k}, \tag{5.2}$$

where $\omega_{p,k}$ is the plasma frequency, $\omega_{0,k}$ is the oscillator frequency and γ_k is the linewidth[169]. The obtained real (ϵ_1) and imaginary (ϵ_2) dielectric function for a single Lorentz oscillator is shown in figure 5.4a. This shows that this single oscillator, with a width $\gamma_i = (\omega_{i+1} - \omega_{i-1})/2$, has nonzero values of the dielectric function at the neighbouring frequencies. This makes the oscillators interdependent and makes it computationally hard to fit the data, especially when large numbers of oscillators are considered[140]. Therefore, this oscillator is used to only capture the main spectral features, resulting in a large residual[229,230].

To account for the residual, numeric alternatives to this oscillators are used with their weight mainly around ω_i. This is achieved by using a triangular profile for ϵ_2, as shown in figure 5.4b, with ϵ_1 obtained via the KK transformations[169]. With this, we can write equation 5.2 as

$$\epsilon_{\text{var}}(\omega) = \sum_{i=2}^{N-1} \epsilon_i^{\Delta}(\omega). \tag{5.3}$$

This enables us to exactly fit ϵ_2 to the obtained spectra, provided that sufficiently small intervals $\Delta\omega$ are considered. These individual oscillators have no physical meaning on their own, however, the total dielectric function of all oscillators combined will be able to accurately represent the dielectric function of a material. The total dielectric functions, ϵ_{total}, is the sum of the coarse Lorentzian oscillators and the variational oscillators according to

$$\epsilon_{\text{total}} = \epsilon_{\text{coarse}}(\omega) + \epsilon_{\text{var}}(\omega). \tag{5.4}$$

Because of the decoupled variational oscillators, these dielectric functions are capable of fitting fine features whilst overcoming the computational limitations.

Obtaining the change of refractive index

The transmission of the probe, T, is dependent on the real and imaginary dielectric functions. Using the linearity of the KK relations, we can write the change in transmission, ΔT as a function of the change of dielectric functions[231]. With this, the normalised change in transmission, via calculus of variations, can be written as

$$\frac{\Delta T}{T} = \frac{1}{T}\left(\frac{\partial T}{\partial \epsilon_1}\Delta\epsilon_1 + \frac{\partial T}{\partial \epsilon_2}\Delta\epsilon_2\right). \tag{5.5}$$

Here, we can treat $\Delta\epsilon$ as regular dielectric functions with the addition of two assumptions regarding $\Delta\epsilon(\omega)$. The first assumption is that $\Delta\epsilon(\omega)$ can both be positive and negative and the second assumption is that $\Delta\epsilon_\infty$, from equation 5.2, is zero.

Equation 5.5 shows a relation between the change in the dielectric functions ($\Delta\epsilon$), transmission (T), TA signal ($\Delta T/T$) and the derivative of the transmission with respect to the real and imaginary part of the dielectric function ($\partial T/\partial \epsilon_1$ and $\partial T/\partial \epsilon_2$). We can directly measure the transmission and the TA signal from the sample, and the ground state dielectric functions are obtained by fitting the oscillators onto the transmission spectra. By taking the derivative of the transmission to the respective real or imaginary dielectric function, we can extract the values for the partial derivatives. From here, the change in dielectric functions can be evaluated. The complex refractive index is related to the dielectric function according to

$$\tilde{n} = \sqrt{\tilde{\epsilon}}, \tag{5.6}$$

with $\tilde{n}$ and $\tilde{\epsilon}$ the complex refractive index and complex dielectric functions respectively. By using partial derivation to both the real and imaginary part of the refractive index, we obtain

$$\Delta\tilde{n} = \frac{1}{2\sqrt{\tilde{\epsilon}}}\Delta\tilde{\epsilon}, \tag{5.7}$$

via which the change in the complex refractive index is calculated.

5.4 Results

5.4.1 Differential dielectric functions on CsPbBr$_3$ perovskite

To initially test the differential dielectric functions model, we have applied it to the CsPbBr$_3$ perovskite TA data from chapter 3. This is done as the data is readily available and the spectral response of the refractive index is relatively simple. The result is shown in figure 5.5, where both the model and FDI measurement are shown at a time delay of 500 fs.

The model uses the same TA data obtained for the analysis in chapter 3. This allows us to compare the results obtained with the FDI and the model with the same sample and excitation conditions. The transmission of the sample has been approximated by the known ground state refractive index of CsPbBr$_3$ as the actual transmission itself was not measured at the time[170]. This introduces a single model dependent parameter, which is the thickness of the sample and set at 72.5 nm to match the thickness obtained in chapter 3. The model agrees with the results from

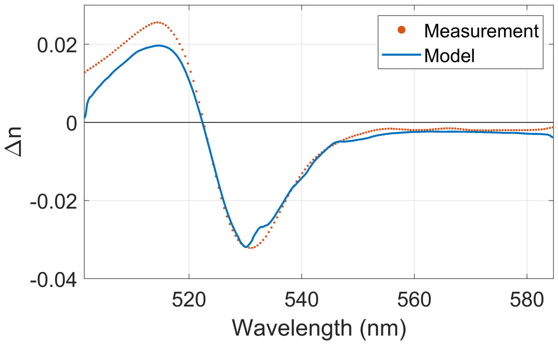

Figure 5.5: Refractive index change obtained by the Michelson-FDI measurement on $CsPbBr_3$ as discussed in chapter 3 and the resulting refractive index change obtained by the differential dielectric functions model at a time delay of 500 fs.

the FDI measurement regarding the refractive index change with a small deviation at the shorter wavelength, without any signal scaling of the obtained Δn spectrum. The deviation is probably a result of the mismatch of the actual ground state refractive index and the one obtained from Ahmad *et al.*[170]. This shows that the model is capable of predicting the transient refractive index of a material with a relative simple Δn response upon excitation fairly well, with a small underestimation at the short wavelength region.

5.4.2 Frequency domain interferometry on pentacene

As the transient refractive index of $CsPbBr_3$ closely resembles a single Lorentz oscillator, it can be accurately approximated, even without applying the variational dielectric functions to the residual. Pentacene, on the other hand, has a more complex TA spectrum as it has multiple absorption peaks in the visible region[232]. On top of that, the thickness of pentacene sample can be accurately controlled via thermal evaporation, eliminating any uncertainty about the sample thickness[233]. To test both the model and the Sagnac-FDI system under more challenging sample conditions, we have applied the FDI technique on an evaporated pentacene film with a thickness of 100 nm on a spectrosil substrate.

The absorption and excitation of the pentacene sample is shown in figure 5.6a, showing that part of the excitation is on resonance with the electronic transitions of the pentacene. The resulting refractive index change surface, after applying the Fourier phase retrieval algorithm, discussed in section 2.5.4 and a Fourier long pass filter, is shown in figure 5.6b. The long pass filter is applied as the Δn spectrum contains oscillations in the spectral domain as a result from the Fourier phase extraction method[154]. An excitation fluence of 400 μJ/cm^2 was used for this experiment. This surface shows the refractive index change over a 500 ps time delay, which is enabled by using the Sagnac interferometer configuration. A strong signal at time zero is observed, which corresponds to the IRF of the MPC-FDI system. This IRF signal is caused by the nonlinear refractive index of the substrate which modulates the optical path length of the probe beam when the probe and pump temporally overlap. Note that no chirp correction is required for this data due to the small chirp of the MPC probe pulse. This is shown by the duration of the IRF of the Δn spectrum, which only appears when pump and probe overlap, being close to time zero for all observed spectral components.

The kinetics at 640 nm and 700 nm is shown in figure 5.6c. Here, the sharp peak from the IRF at time zero is clearly visible. A clear signal is observed with a minimum Δn of -7×10^{-3}, and a maximum of 2.5×10^{-3}. The obtained spectral slices at set time delays are shown in figure 5.6. This shows the decrease in signal over the first 100 ps. The dip in the region around 790 nm is probably the result of a strong intensity spike of the spectrum at this spectral window, which dominated the transmission signal. Therefore, the Fourier analysis method could not reliable extract the frequency of the interference pattern in this region.

5.4.3 Differential dielectric functions on pentacene

The spectral slice of the refractive index change obtained by FDI at 500 fs time delay is compared to the differential dielectric functions model. For this data, no Fourier filter is applied, revealing the actually signal of the FDI. This spectrum contains 13 individual measurements with a 45 nm bandwidth. Between these windows, small discontinuities are observed before merging the data with Sigmoid functions. This effect can be reduced by reducing the amount of windows required to capture

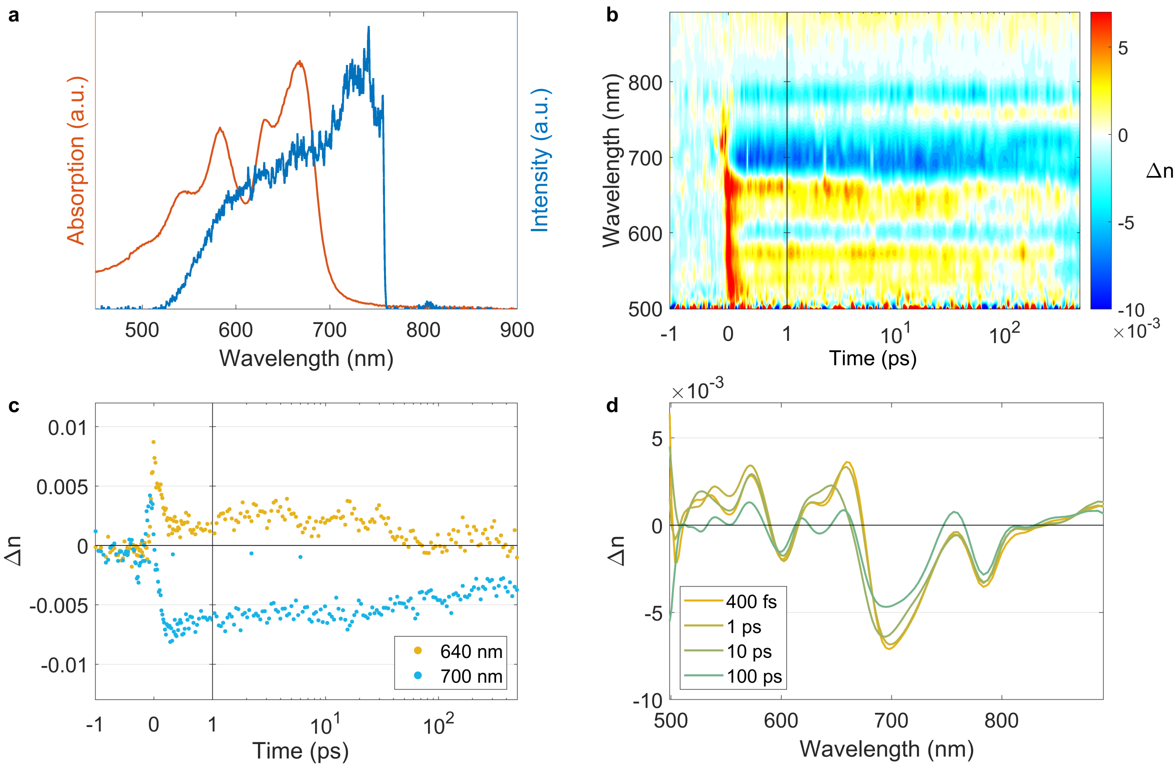

Figure 5.6: a) Absorption spectrum (red) of pentacene and pump pulse spectrum (blue). b) Obtained refractive index change of pentacene for a pump fluence of 1.8 mJ/cm^2. c) Kinetic traces at 640 nm and 700 nm. d) Spectral slices at the indicated time delays.

the whole spectrum, which has the added benefit that overall measurement time will decrease, thereby decreasing the impact of the long term laser instability. For this experiment, the spectral width is limited by the width of the detector and the reduction of the spectral windows can be achieved by using a camera with a larger physical detection size to capture a broader range. This issue will be addressed with future experiments by using a camera with a wider detection range, capable of measuring at least 100 nm in a single measurement with the current spectrometer configuration. The pixel width of the new camera will also be half that of the current camera, improving the resolution or, by using a grating with less dispersion, increasing the detectable spectral range even further.

The resulting refractive index change is shown in figure 5.7 for a time delay of

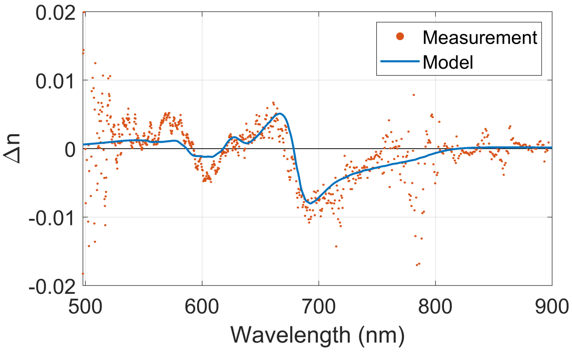

Figure 5.7: Refractive index change of pentacene using the Sagnac-FDI on a layer of pentacene with a thickness of 100 nm and the calculated refractive index change via the differential dielectric functions model at 500 fs.

500 fs. This plot also shows the result obtained by the differential dielectric functions model, calculated with the data obtained by Rao *et al.*, who have excited the pentacene with an excitation wavelength of 490 nm and a fluence of 80 μJ/cm^2 [232]. Even with the completely different fluence, the model shows great spectral agreement with the refractive index change measured with the FDI, with a small deviation at the short wavelength region, from 500 nm to 620 nm. The difference between the model and the FDI results at 790 nm is explained by the error of the phase extraction at this wavelength due to the intensity spike of the probe at this region. Therefore, the phase retrieval algorithm could not accurately determine the phase change in this wavelength region.

The intensity is also similar between the experiment and the model, even with the vastly different fluence for the TA experiment used for the model (80 μJ/cm^2) and the FDI experiment (400 μJ/cm^2). This can be explained by the pump spectrum being partially off resonance as shown in figure 5.6, the low absorption coefficient of the 100 nm thick pentacene, with a maximum optical density of 0.5 so that only a small portion of the pump is absorbed. Furthermore, the lower refractive index of pentacene will result in a smaller absolute change of the refractive index. On top of that, the pentacene can work as a saturable absorber which lowers the expected carrier density [234]. This saturable absorber effect occurs due to the depletion of the valence band, which prevents further excitation of the sample. This suggests that the same refractive index change could be expected for the lower fluence used for the TAS experiment.

Interestingly, the region between 700 nm and 750 nm does show a change in the refractive index, while having a low absorption coefficient, as shown in figure 5.6a. A weak PIA band is formed at this region, indicating a small absorption increase[232]. The extent of the refractive index change means that this region would be suitable for an optical phase modulator. For this type of devices, materials are used which weakly absorb the light but adjusts the phase changing the refractive index[27,235]. For pentacene, the phase can be controlled by optical excitation where the total phase shift is set by changing either the excitation density or the time delay. This shows that this technique is capable of measuring the ultrafast refractive index change of, and thus time-dependent phase change induced by, materials designed for phase modulators.

5.5 Discussion and conclusion

In this chapter, the Sagnac-FDI, an improvement of the Michelson-FDI, is implemented. The Sagnac interferometry configuration decouples the reference-probe time delay at the sample position from the reference-probe time delay at the detector. By increasing the path length of the probe pulse to the sample relative to the reference pulse path length, a longer temporal range is available, allowing for the observation of dynamics occurring on a longer timescale. Besides the decoupling of the time delays, the Sagnac configuration is advantageous due to the common path configuration, where instabilities of the system are passively compensated for.

A single MPC system is used to generate the pump, reference and probe pulses of the FDI. The high resolution of the spectrometer (0.088 nm/pixel) requires a reference and probe source with a high spectral density. A single back reflection of the pulses generated by the MPC of a wedge pair provided sufficient photons for both the reference and probe pulses to obtain an interference pattern which could be reliably read out between 500 nm and 900 nm. The transmitted pulse was used as the pump pulse, exciting the sample with a fluence of 1.8 mJ/cm^2 over a spectrum spanning from 520 nm to 750 nm.

The Sagnac-FDI is applied to measure the refractive index change of pentacene. This is done by performing multiple measurements with a 45 nm bandwidth to obtain sufficient resolution. Because of this, small discontinuities between the spectral windows are observed as a result of the noise level of the system. This will be improved in the future by using a camera with a larger detector, or smaller pixel size, to expand the spectral width or resolution of this system.

The results obtained with the FDI are compared to the results of a differential dielectric functions model. This model uses the Lorentz oscillators and variational oscillators and the TA signal. The oscillators are used to closely approximate the transmission signal and obtain the ground state dielectric functions. Combined with the TA signal, the change in dielectric functions are obtained, which are directly related to the change of the complex refractive index.

The obtained change in the refractive index spectrum of both the FDI and the differential dielectric functions model are in strong agreement. This shows that the model is able to predict the refractive index change when the TA and transmission signal can be obtained.

Pentacene has a low absorption coefficient in the region between 700 nm and 750 nm with a weak PIA signal. The change in refractive index upon photoexcitation, however, is nonzero. This means that this region could be used for optical phase modulators, where the phase of transmitting light can be controlled. The ultrafast response, up to 500 ps, measured by the FDI provides an insight in the available switching time of this system and shows that the amount of phase change can be adjusted by controlling the pump-probe time delay.

The differential dielectric functions model uses the TA signal which utilises the change in the intensity of the probe pulse. This signal contains, on top of the reflection and transmission signal, contributions from stimulated emission and potential scattering as well. Therefore, the model is not able to resolve the refractive index change of samples with a strong stimulated emission signal or samples that generate large scattering. The FDI, on the other hand, does not use the intensity of the probe pulse, but measures the relative phase of a reference and probe pulse pair.

Because of insensitivity to the intensity, the FDI is capable of retrieving the refractive index without reflection, scattering and stimulated emission artefacts. By using the KK relations and Fresnel equations, as discussed in chapter 3 and summarised in appendix 3.2, the TA signal can be obtained. The difference between this calculated and a measured TA signal will be the effect of stimulated emission that is superimposed on a measured TA signal. This could be used to isolate the stimulated emission in a TA signal, which is related to the photoluminescence of a sample, effectively obtaining the ultrafast photoluminescence signal.

Chapter 6

Summary and outlook

6.1 Summary

In this report, two main ultrafast optical techniques, the MPC and the FDI, are discussed. The MPC has been used for the first time in the field of ultrafast spectroscopy. Whereas previous results have shown great long term stability (0.83 % standard deviation measured by power meter), the spectrum dependent shot-to-shot stability was still unknown[44,196]. Here, we have shown that the single-stage MPC generates a broad spectrum, spanning from 450 nm to over 1,000 nm with an average spectral standard deviation of 4.6 % between 490 nm and 890 nm for 2,000 shots. A pulse duration of only 3.3 fs has been achieved using chirped mirrors alone, allowing for observations at short timescales. A long lasting temporal correlation is found, showing the option of pulse integration of small sets of pulses generated by a high repetition rate lasers, where shot-to-shot modulation of the sample might not be possible[135]. The calculated root mean square noise of the TA signal is calculated and found to be about 2.6×10^{-4} for 1,000 shot pairs, well below the typical TA signal level. As for the double-stage MPC, a spectrum spanning from 520 nm to 980 nm has been generated with an average spectral standard deviation of 4.5 %. A root mean square noise of the TA signal of 1.6×10^{-4} has been achieved for 1,000 shot pairs between 550 nm and 930 nm. These results show that the MPC is an excellent broadband light source within the field of ultrafast spectroscopy.

Two configurations of the FDI have been used to extract the refractive index change of $CsPbBr_3$ and pentacene. The first technique is based on a Michelson interferometer and the second is based on a Sagnac interferometer. The Michelson-FDI is a more straightforward adaptation of TA and uses a second-harmonic pump and bulk supercontinuum probe. This FDI system has been applied on $CsPbBr_3$ perovskite to investigate the impact the change of the real part of the refractive index has on the TA signal. For this material, it has been suggested that the PIA at the high energy side of the GSB is a result of the change in reflection, rather than a result of the imaginary part of the refractive index. The results obtained with the FDI, however, show that the change in reflection goes to zero at this region. This system, however, is limited in the available temporal range due to the coupling of the reference-probe pulse delay at the sample position and at the detector.

To overcome this limitation, a Sagnac-FDI system has been implemented, where the time-delay of the reference and probe pulses at the sample and detector are decoupled. This allows for the observation of longer timescales and thus observe long timescale dynamics. This system also implements the MPC as a single light source for the pump, reference and probe pulses. A single MPC system provides intense, stable and broadband light pulses required for this experiment. This MPC-Sagnac-FDI technique has been applied on pentacene, which is expected to have complex excited state refractive index spectrum. The results are compared to a novel differential dielectric functions model, that estimates the refractive index from the TA signal and ground state transmission signal. The FDI measurement and model show great agreement of the results, indicating that both techniques obtain the true change in refractive index.

6.2 Outlook of Multiple plate compression

The application of the MPC for both TAS and FDI experiments, and the analysis of the generated pulses, has shown that the MPC is an excellent light source in the field of pump-probe spectroscopy. Thanks to the pulses' stable, intense, temporally compressible and broadband nature, it meets all requirements for both the pump and probe pulses for these experiments. Because of this, the various light sources required, with their multitude of optical components, can be replaced by a single MPC light source, vastly reducing the complexity of these spectroscopy systems.

Further ultrafast spectroscopic techniques

The proof of concept of the MPC in ultrafast pump-probe spectroscopy paves a road for the application of the MPC as a light source in other ultrafast spectroscopic techniques, such as 2 dimensional electronic spectroscopy and impulsive stimulated raman spectroscopy[236,237]. Both of these techniques require intense broadband pulses with sub-10 fs durations. Conventionally, these pulses are generated using a (N)OPA which can generate intense and compressible pulses, but suffers from the available spectral bandwidth, front tilt, spatial chirp and angular dispersion[191,237,238].

The MPC can generate an easily compressible broadband pulses, down to the single cycle[45]. This octave spanning supercontinuum has high shot-to-shot and long term stability with high spectral density[44]. Therefore, the use of the MPC for these techniques allows for the observation of kinetics at a larger spectral range, shorter pulse durations and higher pump intensities than previously obtained.

High repetition rate lasers

A recent development in the field of spectroscopy is the high repetition rate fibre laser[239]. These lasers produce pulses with hundreds of μJ pulse energies and a 200 fs duration at up to a 40 MHz pulse repetition rate [240]. These high repetition rate lasers open up new possibilities for both background free measurements, such as transient grating photoluminescence and pump-probe spectroscopy[135,241], where the high repetition rate vastly reduces the experimental time required for a single experiment. The data quality also increases as the expected noise level drops significantly at these high repetition rates due to the reduction of the $1/f$-electric noise, dominating at low frequencies[242].

The MPC has recently been tested with an Ytterbium: Potassium Gadolinium Tungstate (Yb:KGW) fibre laser[45]. A two-staged MPC achieved spectral broadening to 700 nm bandwidth at a 100 kHz repetition rate. The resulting pulse energy directly after the supercontinuum generation is 27 μJ per pulse, with a transform limited pulse duration of 3.77 fs. The long temporal correlation found in this research allows for nonsequential pulses to be used for the calculation of the TA signal. This shows that the MPC, in combination with the high repetition rate lasers, can provide temporally compressed broadband pulses with high average power applicable in the field of ultrafast high-repetition rate spectroscopy.

Micromachining

A completely different technique that can benefit from the MPC light source is femtosecond micromachining. Femtosecond laser ablation is a technique which focuses short and intense pulses onto a solid-state material to drill micrometer sized holes[243]. The focused laser pulse creates an incredibly high temperature ($>10^4$ K) free electron gas by absorption of the pulse[244,245]. This ionises the lattice which results in the Coulombic repulsion of the material, leading to expansion and vaporisation of the ions, also known as the Coulomb explosion. This happens on a sub-100 fs timescale, much faster than the timescale of 1 ps for electron-phonon interactions, thereby avoiding a temperature increase and melting of the area around the pump focal point. This strong expansion blasts the freed ions away from the sample which, combined with the low lattice temperature, leaves a clean hole in the sample with little to no debris[246].

This technique requires stable and high repetition rate lasers. Fibre lasers generate pulses at the MHz repetition rate with mJ pulse energy, making them excellent candidates for machining applications[240]. However, the narrow bandwidth of these lasers limits the achievable temporal compression of the pulses. By using the MPC in combination with these fibre lasers, stable, intense pulses with femtosecond pulse durations and at a high repetition rate can be produced. These ultrashort pulses have a high temporal peak power which will result in a low ablation threshold and a clean hole, without affecting the surrounding sample area[247].

6.3 Outlook of Frequency domain interferometry

6.3.1 Possible improvement

2D detector

The FDI discussed in this thesis is capable of reliably retrieving the excited state refractive index. However, the spectral resolution is currently limited by the combination of the pixel size of the detector, time delay and Fourier window. For a high phase resolution, a single period of the interference pattern should contain as many data points as possible. According to equation 2.54, this can be achieved by reducing the time delay between the reference-probe pulse pair[36]. However, if the time delay between reference and probe pulses is set too short, a large spectral window has to be taken for the Fourier analysis which reduces the spectral resolution. This results in a balance between the spectral resolution and phase resolution.

Both spectral and phase resolution can be improved individually if they can be decoupled. This can be achieved by using a fast 2D detector rather than a 1D linescan detector, where the spectrum is dispersed in one (horizontal) direction while the time delay of the probe is generated in the other (vertical) direction by slight misalignment of one of the mirrors within the interferometer[37]. Here, each wavelength component, along the horizontal axis, will contain its own interference pattern, in the vertical axis. Therefore, the spectral resolution is determined by the horizontal dispersion while the phase resolution is set by the vertical angle at which the reference-probe pair arrive at the detector. However, this can only be achieved with a probe pulse containing high spectral density, therefore, the MPC is an excellent light source for this modification.

6.3.2 Applications

Optical phase modulator

The first application is hinted at in section 5.4, where the refractive index change of pentacene is observed in a region of weak absorption (700 nm to 800 nm). This region can be used to change the phase of light of a wavelength within this region while avoiding strong absorption, which are the requirements for an optical phase modulator[27]. This device has a broad range of applications such as optical information processing, quantum optics and even biosensing[235,248,249].

The results of performing FDI on pentacene shows that this technique is an excellent tool to measure the refractive index change of novel materials which are developed for optical phase modulators on an ultrafast timescale[27,250]. Understanding the ultrafast response provides information regarding the switching response time and allows for a new means of phase control, besides the excitation density, by tuning the time delay between the excitation and probe pulses.

Lasing

TAS measures the sample by the intensity of the transmission of a probe pulse. This means that, beside the transient reflection effects, TA signals also include a potential positive stimulated emission signal, as discussed in section 2.4. These stimulated emission signals are close to, or directly on top of the GSB, making it difficult to distinguish between kinetics of the GSB and the stimulated emission[136,232].

Being able to distinguish between the stimulated emission and GSB is very useful for OPV materials, where the positions of the GSB for both singlets and triplets, and the stimulated emission, often overlap. For OPV, all stimulated emission is a result from the relaxation of the singlet state because the triplet to ground state transition is a forbidden transition[251]. Therefore, the kinetics of the singlet state can be extracted by isolating the stimulated emission signal.

The FDI uses the relative phase of a reference-probe pulse pair, rather than the intensity of the probe, and is therefore insensitive to an intensity change of the probe. Potential stimulated emission is in-phase and co-directional with the probe pulse, increasing its intensity and thereby reducing the interference contrast, but leaving the phase of the interference pattern unchanged[252]. Therefore, by taking an FDI measurement and extracting the imaginary part of the refractive index via KK transformations, we can calculate the TA signal without stimulated emission. By subtracting of the obtained TA signal from the TA signal from an actual TA measurement, the time dependent intensity and spectrum of the isolated stimulated emission signal is extracted.

Ultrafast metrology

Spatial white light interferometry has been used to measure the refractive index change of a material during micromachining[253]. This provides information about the resulting optical path length of a material, related to the thickness and refractive index. Currently, a complex microlensing technique is required to generate a sufficiently intense supercontinuum to obtain the spatial information with high signal to noise level. This supercontinuum generation step, that results in a supercontinuum with a pulse duration of several ps, can be replaced by the MPC, generating intense pulses with high intensity and sub-10 fs durations at high repetition rate[45,254]. This technique can be implemented in combination with micromachining to monitor the progress of micromachining in real-time.

Appendices

Chapter A

Frequency Domain Interferometry

A.1 Matlab code: $\Delta\phi$ extraction

A.1.1 Import data and calculate $\Delta\phi$

```matlab
clear all
Folder = 'E:\20201127_Pentacene\Measurement\';
FolderInfo = dir(Folder);
[datasets,~] = size(FolderInfo);
datasets = datasets-2;
Thickness = 100*10^-9; % meter
User_Input.padding = 2; % 0 is no processing, 1 is hanning window, 2 is hanning+padding
User_Input.Window = 0.01;


for m = 1:datasets-1 %except BG folder
clearvars -except datasets FolderInfo Folder m User_Input
Folder2 = strcat(Folder,FolderInfo(m+2).name);
filename = '\raw';
file = strcat(Folder2, filename);
h5information = h5info(file);
[numSets,~] = size(h5information.Groups.Datasets);
time = f_importTime(Folder2);

numTime = length(time);
numRuns = numSets./length(time);

%% Background
FolderInfo = dir(Folder);
[NumberItems,~] = size(FolderInfo);

```

```
%% Import background
for n=1:NumberItems
    if strcmp(FolderInfo(n).name, 'BG') == 1
        Background = f_Background(Folder);
        Background.on = Background.on(1:512);
        Background.off = Background.off(1:512);
    end
end

%% Automated wavelength calibration
Wavelength = f_Calibrate_axes(str2num(FolderInfo(m+2).name));
Energy = 1240.8./Wavelength;

for n = 1:numSets

    Shot = strcat('/Camera_0/',h5information.Groups.Datasets(n).Name);
    raw = double(h5read(file,Shot));
    raw = raw(1:513,:); %for 512 pixel camera
    [Pixels, shots] = size(raw);
    if n==1
        if ~exist('Background')
    Background.on = zeros(Pixels-1,1);
    Background.off = zeros(Pixels-1,1);
        end
        if length(Energy) > Pixels
            Energy = Energy(1:2:end);
            Wavelength = Wavelength(1:2:end);
        end
    end
    Reference = raw(1,:)>1;
    TempData = raw(2:Pixels,:)';
    [numShots, numPixels] = size(TempData);

   k=1;
    if Reference(1) == 1
       for N = 1:2:length(Reference)
           if Reference(N) == 1 && Reference(N+1) == 0
               keep(k) = 1;
```

```
                k = k+1;
            else
                keep(k) = 0;
                k = k+1;
            end
        end
    else
        for N = 1:2:length(Reference)
            if Reference(N) == 0 && Reference(N+1) == 1
                keep(k) = 1;
                k = k+1;
            else
                keep(k) = 0;
                k = k+1;
            end
        end
   end

    keep = logical(keep);
    clear Data tempData
    if Reference(1) == 1
        tempData.on = (TempData(1:2:end,:)-Background.on');
        tempData.off = (TempData(2:2:end,:)-Background.off');
    else
        tempData.on = (TempData(2:2:end,:)-Background.on');
        tempData.off = (TempData(1:2:end,:)-Background.off');
    end
    Data.on = tempData.on(keep,:);
    Data.off = tempData.off(keep,:);
    [FFT_Energy, ~, dphi(n,:)] = f_Fourier_Averaged(Energy, Data,
        User_Input);
    dTTMatrix = mean(Data.on)./mean(Data.off)-1;
    dTTtemp(n,:) = (dTTMatrix);
end


Alldn = -dphi.*(1240.8./FFT_Energy).*10^-9./(2*pi*Thickness);

```

```
%% average different runs
if floor(numRuns) ~= 1
    for n = 1:floor(numRuns)                                                    %In case uncomplete run, remove last run
    splitdn(n,:,:) = Alldn(n*numTime-(numTime-1):numTime*n,:);
    splitdTT(n,:,:) = dTTtemp(n*numTime-(numTime-1):numTime*n,:);
    end
    dn = squeeze(mean(splitdn));
    dTT = squeeze(mean(splitdTT));
else
    for n = 1                                                                   %In case uncomplete run, remove last run
    splitdn(n,:,:) = Alldn(1:numTime,:);
    splitdTT(n,:,:) = dTTtemp(1:numTime,:);
    end
    dn = squeeze(splitdn);
    dTT = squeeze(splitdTT);
end

save(strcat(FolderInfo(m+2).name,'.mat'))
end

function [time] = f_importTime(Folder)
[importTime,~] = xlsread(strcat(Folder,'\Processed_1.csv'), 'A:A');
[~, keep] = unique(importTime, 'stable');
keep = keep(2:end);
time = importTime(keep);
end
```

A.1.2 Background extraction

```
function[BG] = f_Background(folder)
%% Background
%input is folder of the data, output is a structure with the background for the on and off shots.
BGfolder = strcat(folder,'\BG');

```

```
if ~exist(BGfolder, 'dir')
    BG.on = h5read(file,'/Camera_0/BackGround/BackGround');
    BG.off = BG.on;
else
    BackgroundFile = strcat(BGfolder,'\raw');
    Background = double(h5read(BackgroundFile, '/Camera_0/00'));
    [pixels, shotsBG] = size(Background);
    PDThreshold = mean(Background(1,:));
    BG.off = [];
    BG.on = [];
    for n=1:shotsBG
        if Background(1,n) < PDThreshold
            BG.off = [BG.off Background(2:pixels,n)];
        else
            BG.on = [BG.on Background(2:pixels,n)];
        end
    end
    BG.on = mean(BG.on,2);
    BG.off = mean(BG.off,2);
end
```

A.1.3 Wavelength Calibration

```
function [WL] = f_Calibrate_axes(Used_Center)

%% Manual inputs
Folder = 'E:\20201127_Pentacene\WLCalibration';
Laser_Wavelength = 655; %nm


%% Rest
FolderInfo = dir(Folder);
[NumberItems,~] = size(FolderInfo);


if strcmp(FolderInfo(NumberItems).name, 'BG') == 1
    Background = f_Background(Folder);
    Background.on = Background.on(1:512);
```

```
end

%figure
for n = 3:NumberItems-1
    WL(n-2) = str2double(FolderInfo(n).name);
    filename = '\raw';
    file = strcat(Folder,'\', FolderInfo(n).name, filename);
    h5information = h5info(file);
    Shot = strcat('/Camera_0/',h5information.Groups.Datasets(1).Name);
    raw = double(h5read(file,Shot));
    Spectrum = mean(raw(2:513,:),2)-Background.on;
    Spectrum = (Spectrum./max(Spectrum))';
    hold on
    CameraSize = length(Spectrum);
    %scatter(1:length(Spectrum), Spectrum, 'filled')
    [fitresult, coeffval] = f_WLfit(Spectrum);
    %plot(fitresult)
    Pixel(n-2) = coeffval(2);
end

Calibration_Center = Laser_Wavelength == WL;
Center_Pixel = Pixel(Calibration_Center);
Center_WL = WL(Calibration_Center);
nmperPixel = -mean(diff(WL)./(diff(Pixel)));


WL = Laser_Wavelength-Center_Pixel.*nmperPixel;
WL = WL+nmperPixel.*(1:CameraSize);
WL = WL+(Used_Center-Laser_Wavelength)+1;
```

A.1.4 Fourier phase extraction

```
function[FFT_Energy, FFT_Data, dphi] = f_Fourier_Averaged(Energy, Signal,
    User_Input, varargin)

if Energy(1) > Energy(end)
    Energy = flip(Energy);
    Signal.on = flip(Signal.on,2);
```

```
    Signal.off = flip(Signal.off,2);
end

HEnergy = interp1(Energy, Energy, Energy(1):min(diff(Energy)):Energy(end));
Signal.on = mean(Signal.on);
Signal.off = mean(Signal.off);

for n = 1%:numshots
    HSignal.on(n,:) = interp1(Energy, Signal.on(n,:), HEnergy);
    HSignal.off(n,:) = interp1(Energy, Signal.off(n,:), HEnergy);
end

Window = User_Input.Window;

n = 1;
left = 1;
[~, right] = min(abs((HEnergy(left)+Window)-HEnergy));
stepsize = floor((right-left)/3);
%stepsize = 1;
k=1;
while right < length(HEnergy)
    Cropped_Energy = HEnergy(left:right);
    Cropped_Signal.on = HSignal.on(n,left:right);
    Cropped_Signal.off = HSignal.off(n,left:right);

    if n == 1
        %FFT_Energy((left-1)/stepsize+1) = mean(Cropped_Energy);
        FFT_Energy(k) = mean(Cropped_Energy);
    end

    if User_Input.padding == 2
        FFT_Signal.on = fft([zeros(1,100) (Cropped_Signal.on-mean(Cropped_Signal.on)).*hann(length(Cropped_Signal.on))' zeros(1,100)]);
        FFT_Signal.off = fft([zeros(1,100) (Cropped_Signal.off-mean(Cropped_Signal.off)).*hann(length(Cropped_Signal.on))' zeros(1,100)]);
```

```
        [~, FFT_Signal.max.on] = max(abs(FFT_Signal.on(50:ceil(end/2))));
        [~, FFT_Signal.max.off] = max(abs(FFT_Signal.off(50:ceil(end/2))));
        FFT_Signal.Angle.on = angle(FFT_Signal.on(FFT_Signal.max.on+49));
        FFT_Signal.Angle.off = angle(FFT_Signal.off(FFT_Signal.max.on+49));

    elseif User_Input.padding == 1
        FFT_Signal.on = fft((Cropped_Signal.on-mean(Cropped_Signal.on)).*hann(length(Cropped_Signal.on))');
        FFT_Signal.off = fft((Cropped_Signal.off-mean(Cropped_Signal.off)).*hann(length(Cropped_Signal.on))');
            [~, FFT_Signal.max.on] = max(abs(FFT_Signal.on(2:ceil(end/2))));
        [~, FFT_Signal.max.off] = max(abs(FFT_Signal.off(2:ceil(end/2))));
        FFT_Signal.Angle.on = angle(FFT_Signal.on(FFT_Signal.max.on+1));
        FFT_Signal.Angle.off = angle(FFT_Signal.off(FFT_Signal.max.on+1));

    else
        FFT_Signal.on = fft((Cropped_Signal.on-mean(Cropped_Signal.on)));
        FFT_Signal.off = fft((Cropped_Signal.off-mean(Cropped_Signal.off)));
        [~, FFT_Signal.max.on] = max(abs(FFT_Signal.on(2:ceil(end/2))));
        [~, FFT_Signal.max.off] = max(abs(FFT_Signal.off(2:ceil(end/2))));
        FFT_Signal.Angle.on = angle(FFT_Signal.on(FFT_Signal.max.on+1));
        FFT_Signal.Angle.off = angle(FFT_Signal.off(FFT_Signal.max.on+1));
    end

    FFT_Data.on(n,k) = FFT_Signal.Angle.on;
    FFT_Data.off(n,k) = FFT_Signal.Angle.off;
    left = left+stepsize;                                          %set new left position of window

    [~, right] = min(abs((HEnergy(left)+Window)-HEnergy));          %set
```

```
        new right position of window

    k = k+1;
end

dphi = (FFT_Data.on-FFT_Data.off);
A = dphi > 0.5*pi;
A2 = dphi < -0.5*pi;
dphi(logical(A)) = NaN;
dphi(logical(A2)) = NaN;
```

A.2 Matlab code: Merge Δϕ and calculate Δn

```
clear all
Folder = 'H:\PhD\DIC_FDI\Processed_Data\20201127_Pentacene\
    RawProcessed_Referenced_Highres_padding_hanning';
FolderInfo = dir(Folder);
[NumberItems,~] = size(FolderInfo);
User_input.timeoffset = 480.85; %set timezero to zero
User_Input.Thickness = 100*10^-9; %thickness of sample


%% import data
for n = 1:NumberItems-2
    Import = open(strcat(Folder, '\', FolderInfo(n+2).name));
    Data(n).time = Import.time;
    Data(n).Energy = Import.FFT_Energy;
    %Data(n).dn = -Import.dn;
    Data(n).tempdphi = -Import.dphi; %%%%%%%%%%%%%%%%THIS IS INVERTED

    if floor(Import.numRuns) ~= 1
    for N = 1:floor(Import.numRuns)  %In case uncomplete run, remove last
        run
        split(N).dphi = Data(n).tempdphi(N*Import.numTime-(Import.numTime
            -1):Import.numTime*N,:);
        splitdphi(N,:,:) = split(N).dphi(:,:)-mean(split(N).dphi(1:10,:))
            ;
```

```
    end
    Data(n).dphi = squeeze(mean(splitdphi));
    else
    Data(n).dphi = squeeze(Data(n).tempdphi);
    end
    clear splitdphi
    %Data(n).dphi = Data(n).dphi-nanmean(Data(n).dphi(1:10,:));
    Data(n).dn = -Data(n).dphi.*(1240.8./Data(n).Energy).*10^-9./(2*pi*User_Input.Thickness);
end



%% set uniform energy axis
[minEnergy,~] = min([Data.Energy]);
[maxEnergy,~] = max([Data.Energy]);
[dEnergy,~] = min(abs(diff([Data.Energy])));
Energy = minEnergy:dEnergy:maxEnergy;

 Matrix = NaN(length(Energy), length(Data(1).time).*length(Data));
for n = 1:NumberItems-2
    [~, lower(n)] = min(abs(Energy-Data(n).Energy(1)));
    [~, upper(n)] = min(abs(Energy-Data(n).Energy(end)));
    Data(n).CroppedEnergy = Energy(lower(n):upper(n));
    for N = 1:length(Data(1).time)
        if sum(~isnan(Data(n).dphi(N,:))) > 2
            Data(n).Interpolated(:,N) = interp1(Data(n).Energy, Data(n).dphi(N,:), Data(n).CroppedEnergy, 'spline', 'extrap');
        else
            Data(n).Interpolated(:,N) = NaN(length(Data(n).CroppedEnergy),1);
        end
    end
    [~, Croppedlower(n)] = min(abs(Energy-Data(n).CroppedEnergy(1)));
    [~, Croppedupper(n)] = min(abs(Energy-Data(n).CroppedEnergy(end)));
end

%% Merge data by sigmoid functions
```

```
for n = 1:NumberItems-2
            Data(n).Weight = ones(1,length(Energy));
    if n == NumberItems-2
        overlapwidth = upper(n)-lower(n-1);
        Sigmoid = -sigmoid(1:overlapwidth, ceil(overlapwidth./2), 10./(0.6.*overlapwidth))+1;
        Data(n).Weight(1,upper(n)-overlapwidth+1:upper(n)) = Sigmoid;
    elseif n == 1
        overlapwidth = upper(n+1)-lower(n);
        Sigmoid = sigmoid(1:overlapwidth, ceil(overlapwidth./2), 10./(.6.*overlapwidth));
        Data(n).Weight(1,lower(n):lower(n)+overlapwidth-1) = Sigmoid;
    else
        overlapwidth = upper(n)-lower(n-1);
        Sigmoid = -sigmoid(1:overlapwidth, ceil(overlapwidth./2), 10./(0.6.*overlapwidth))+1;
        Data(n).Weight(1,upper(n)-overlapwidth+1:upper(n)) = Sigmoid;
        overlapwidth = upper(n+1)-lower(n);
        Sigmoid = sigmoid(1:overlapwidth, ceil(overlapwidth./2), 10./(.6.*overlapwidth));
        Data(n).Weight(1,lower(n):lower(n)+overlapwidth-1) = Sigmoid;
    end
end

for n = 1:NumberItems-2
    Matrix(Croppedlower(n):Croppedupper(n),n.*length(Data(1).time)-(length(Data(1).time)-1):n.*length(Data(1).time)) = Data(n).Interpolated;
end

for n = 1:length(Data(1).time)
    for N = 1:NumberItems-2
        tempdphi(N,:) = Matrix(:,(n-1)+N.*length(Data(1).time)-(length(Data(1).time)-1))'.*Data(N).Weight;
    end
    dphi(:,n) = sum(tempdphi,'omitnan');
end

```

```
%% calculate dn and store data
dphi = dphi-nanmean(dphi(:,1:10),2);
Wavelength = 1240.8./Energy;
dn = -dphi.*(1240.8./Energy').*10^-9./(2*pi*User_Input.Thickness);

time = Data(1).time*10^12;
time = time+User_input.timeoffset;

[m,M] = size(dn);
SaveData = NaN(m+1, M+1);
SaveData(2:end,2:end) = dn;
SaveData(2:end,1) = Wavelength;
SaveData(1,2:end) = time;
SaveData(2:end,:) = flip(SaveData(2:end,:));

%dlmwrite('Processed_Data.txt',SaveData)
```

A.3 Sample preparation

The microcrystalline $CsPbBr_3$ thin film is prepared by Dr. Parth Vashishtha. The procedure is copied from the supplementary information of Tamming *et al.*[154].

Materials: Oleic acid (90 %), Cesium carbonate (99 %), 1-Octadecene (90 %), cesium bromide (99.9 %) PbBr2 (99.99 % trace metal basis), oleylamine (99 %), anhydrous hexane (95 %), anhydrous toluene (99.8 %), Titanium diisopropoxide bis (acetylacetonate) 75 wt. % in isopropanol, 1-butanol (99.8 %, Sigma–Aldrich), anhydrous Dimethyl sulfoxide (DMSO) (99.9 %), micro-90, acetone, Isopropyl alcohol and anhydrous acetonitrile (99.8 %) were purchased from Sigma-Aldrich.

Synthesis: Synthesis of NCs also involves the synthesis of cesium oleate precursor. In a typical synthesis method 0.4 g cesium carbonate, 15 mL 1-octadecene and 1.3 mL oleic acid were loaded in a 25 mL 3 neck round bottom flask. The entire solution was degassed at 120 °C for 1 h and then the reaction temperature was increased to 150 °C for 30 mins under N_2. Cesium oleate was transferred from the round bottom flask to a schlenk tube and stored in the N_2 glove box. For the NC's synthesis, $PbBr_2$ (0.376 mmol), 10 mL 1-octadecene were loaded in a 50 mL 3 neck round bottom flask and degassed it for 1 h at 120 °C. Simultaneously, 1 mL oleylamine and 1 mL oleic acid were degassed in a glass vial at 120 °C for 1 h. After that, oleic acid and oleylamine were injected in to the reaction flask under N_2 and the temperature was increased to 170 °C. 0.8 mL Cesium oleate was heated to 100 °C, and hot injected in to the reaction flask. After 20 s the flask was cooled down with the ice bath.

Purification: Growth solution was centrifuged at 10000 RPM for 10 mins and the supernatant was discarded. The precipitate was dissolved in 6 mL of toluene and about $\sim$ 2 mL of acetonitrile was used as an antisolvent. The solution was centrifuged again at 8000 RPM and the toluene/acetonitrile step was followed one more time. Eventually, Nanocrystals precipitate was dried under vacuum for 5 mins and dissolved in anhydrous hexane for further characterisation.

Fabrication of $CsPbBr_3$ microcrystalline films: glass substrates were sequentially cleaned in micro-90 (concentrated cleaning solution) diluted solution, distilled water, acetone, and Isopropyl alcohol by ultra-sonication of 20 mins for each step. A compact TiO_2 layer was fabricated by spin-coating of 0.15 M titanium diisopropoxide bis (acetylacetonate) solution in 1-butanol at 4000 rpm for 30 s followed by annealing at 125 °C for 5 min. For the preparation of $CsPbBr_3$ layer, 128 mg CsBr and 220 mg $PbBr_2$ were dissolved in 2 mL of DMSO and then spin coated on the TiO2 coated glass film at 2000 RPM for 60 s followed by the annealing at 100 °C for 30 mins in N_2 glove box.

Chapter B

Multiple plate compression spectral correlation

B.1 Single-stage MPC

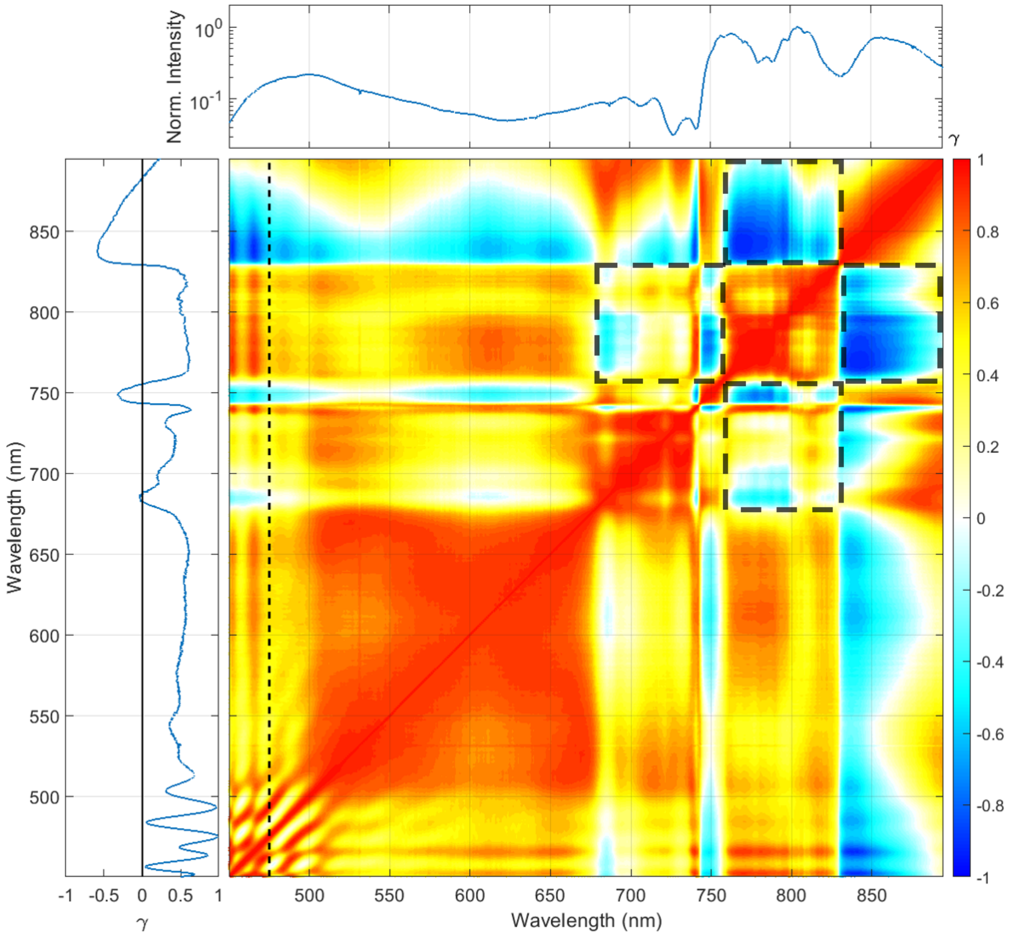

Figure B.1: Spectral correlation of the single-stage MPC where the dashed boxes indicate the regions of direct self-phase modulation and four-wave mixing.

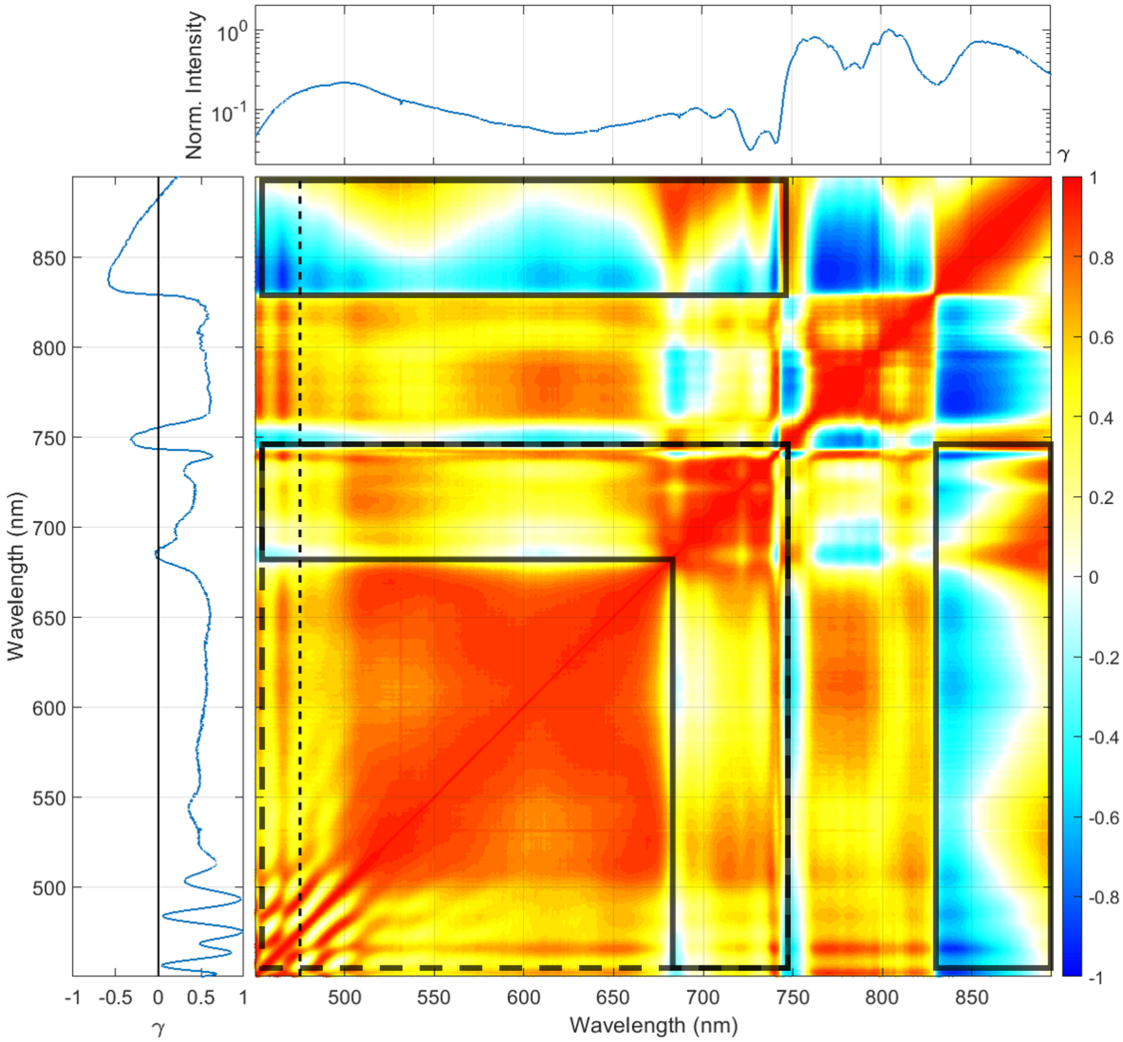

Figure B.2: Spectral correlation of the single-stage MPC where the dashed box indicates the region of self-steepening assisted self-phase modulation (450 nm to 750 nm). The solid lines indicate the competing regions of direct self-phase modulation and four-wave mixing.

B.2 Double-stage MPC

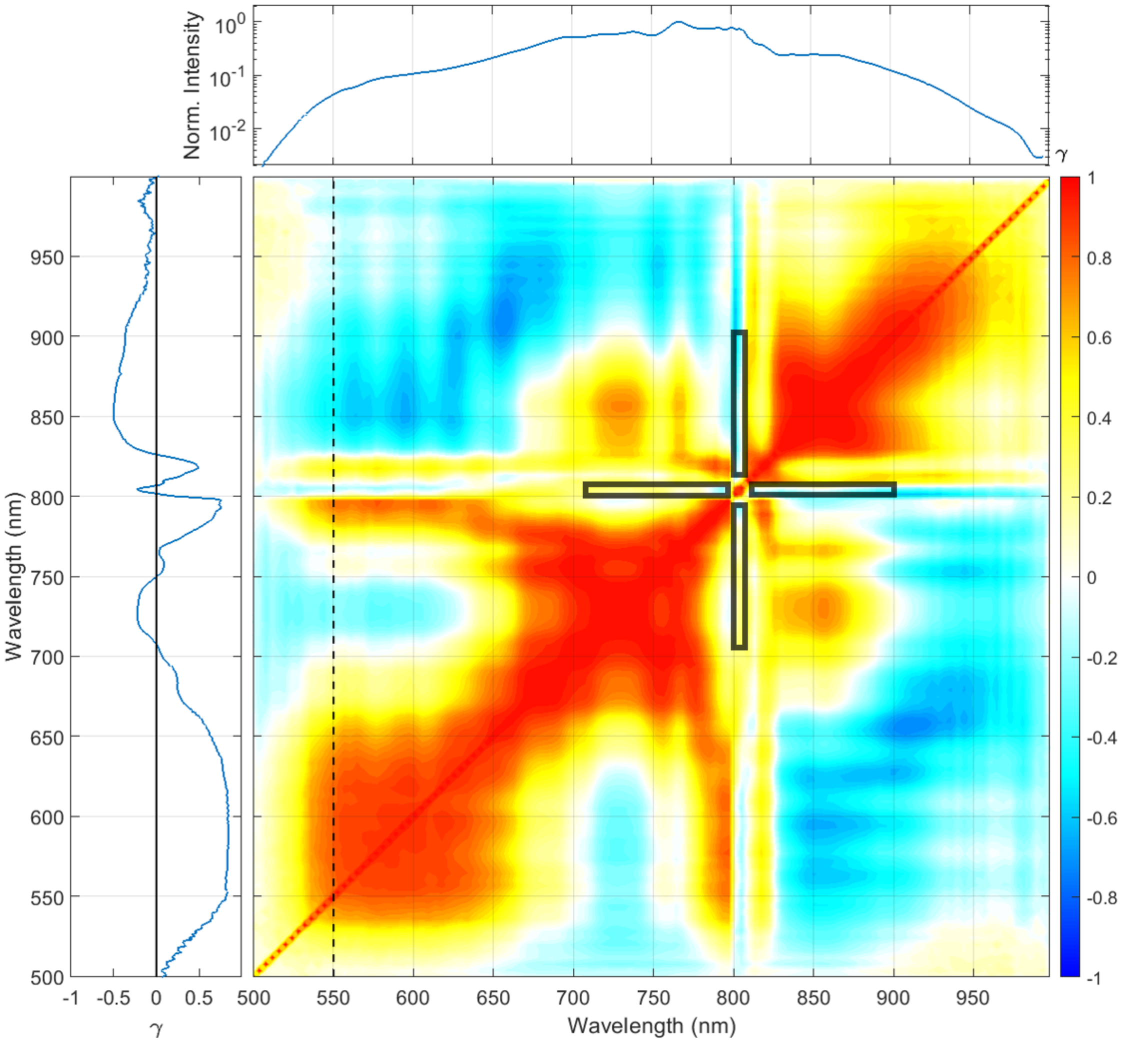

Figure B.3: Spectral correlation of the double-stage MPC where the dashed boxes indicate the regions of direct self-phase modulation and four-wave mixing of the first MPC stage.

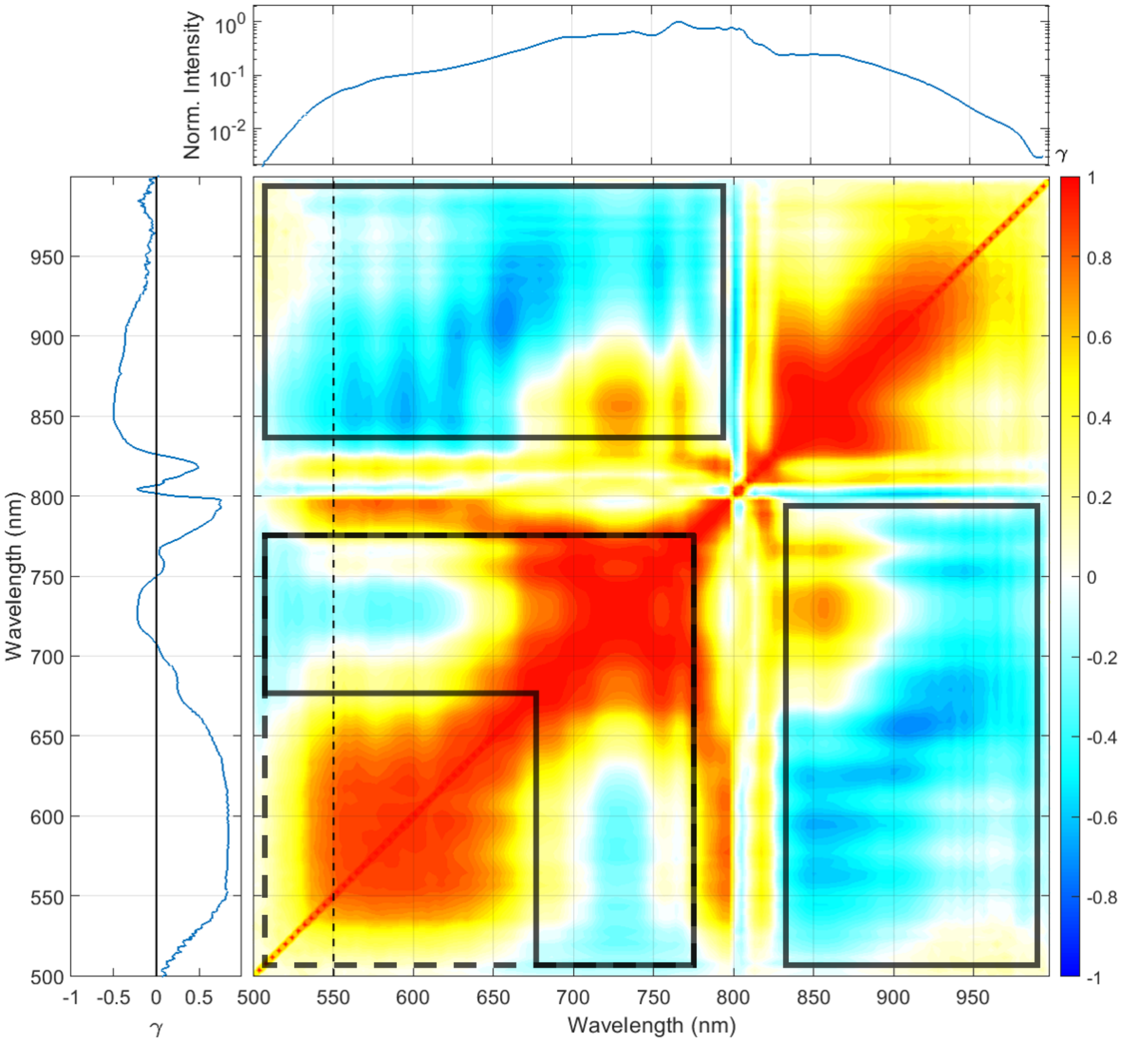

Figure B.4: Spectral correlation of the double-stage MPC where the dashed box indicates the region of self-steepening assisted self-phase modulation (500 nm to 775 nm). The solid lines indicate the competing regions of direct self-phase modulation and four-wave mixing.

Chapter 7

Bibliography

[1] PEPANZ, *New Zealand's Energy Mix: Global Consumption*, `https://www.energymix.co.nz/our-consumption/global-consumption/`, Accessed: 2021-02-01.

[2] IEA, *IEA (2019), World Energy Outlook 2019*, `https://www.iea.org/reports/world-energy-outlook-2019`, Accessed: 2021-02-01.

[3] EIA, *EIA, International Energy Outlook 2020*, `https://www.eia.gov/outlooks/ieo/`, Accessed: 2021-02-01.

[4] R. Pachauri and L. Meyer, *Climate Change 2014: Synthesis Report. Contribution of Working Groups I, II and III to the Fifth Assessment Report of the Intergovernmental Panel on Climate Change*, 2014.

[5] U.S. Global Change Research Program, *Climate science special report: Fourth national climate assessment, volume I*, U.S. Global Change Research Program **1**, 470 (2018).

[6] *United Nations Climate Change, The Paris Agreement*, Accessed: 2021-02-02.

[7] N. Mohr, A. Meijer, M. A. Huijbregts, and L. Reijnders, *Environmental impact of thin-film GaInP/-GaAs and multicrystalline silicon solar modules produced with solar electricity*, International Journal of Life Cycle Assessment **14**, 225 (2009).

[8] B. Ehrler, E. Alarcón-Lladó, S. W. Tabernig, T. Veeken, E. C. Garnett, and A. Polman, *Photovoltaics reaching for the shockley-queisser limit*, ACS Energy Letters **5**, 3029 (2020).

[9] S. K. Haque, J. A. Ardila-Rey, Y. Umar, H. Rahman, A. A. Mas'ud, F. Muhammad-Sukki, and R. Albarracín, *Polymeric materials for conversion of electromagnetic waves from the sun to electric power*, Polymers **10** (2018).

[10] T. Ibn-Mohammed, S. C. Koh, I. M. Reaney, A. Acquaye, G. Schileo, K. B. Mustapha, and R. Greenough, *Perovskite solar cells: An integrated hybrid lifecycle assessment and review in comparison with other photovoltaic technologies*, Renewable and Sustainable Energy Reviews **80**, 1321 (2017).

[11] A. Kojima, K. Teshima, Y. Shirai, and T. Miyasaka, *Organometal Halide Perovskites as Visible- Light Sensitizers for Photovoltaic Cells*, J Am Chem Soc **131**, 6050 (2009).

[12] *NREL, Best Research-Cell Efficiency Chart*, `https://www.nrel.gov/pv/cell-efficiency.html`, Accessed: 2021-02-25.

[13] J. J. Wysocki and P. Rappaport, *Effect of Temperature on Photovoltaic Solar Energy Conversion*, Journal of Applied Physics **31**, 571 (1960).

[14] J. J. Loferski, *Theoretical Considerations Governing the Choice of the Optimum Semiconductor for Photovoltaic Solar Energy Conversion*, Journal of Applied Physics **27**, 777 (1956).

[15] G. Xing, N. Mathews, S. S. Lim, N. Yantara, X. Liu, D. Sabba, M. Grätzel, S. Mhaisalkar, and T. C. Sum, *Low-temperature solution-processed wavelength-tunable perovskites for lasing*, Nature Materials

13, 476 (2014).

[16] G. Xing, N. Mathews, S. S. Lim, N. Yantara, X. Liu, D. Sabba, M. Grätzel, S. Mhaisalkar, and T. C. Sum, *Low-temperature solution-processed wavelength-tunable perovskites for lasing*, Nature Materials **13**, 476 (2014).

[17] C. C. Stoumpos, D. H. Cao, D. J. Clark, J. Young, J. M. Rondinelli, J. I. Jang, J. T. Hupp, and M. G. Kanatzidis, *Ruddlesden–Popper Hybrid Lead Iodide Perovskite 2D Homologous Semiconductors*, Chemistry of Materials **28**, 2852 (2016).

[18] J. Álvarez-Conde, E. M. García-Frutos, and J. Cabanillas-Gonzalez, *Organic Semiconductor Micro/Nanocrystals for Laser Applications*, Molecules **26**, 958 (2021).

[19] Y. W. Su, S. C. Lan, and K. H. Wei, *Organic photovoltaics*, Materials Today **15**, 554 (2012).

[20] A. Chilvery, S. Das, P. Guggilla, C. Brantley, and A. Sunda-Meya, *A perspective on the recent progress in solution-processed methods for highly efficient perovskite solar cells*, Science and Technology of Advanced Materials **17**, 650 (2016).

[21] J. Jiang, S. Wang, X. Jia, X. Fang, S. Zhang, J. Zhang, W. Liu, J. Ding, and N. Yuan, *Totally room-temperature solution-processing method for fabricating flexible perovskite solar cells using an* Nb_2O_5*–*TiO_2 *electron transport layer*, RSC Advances **8**, 12823 (2018).

[22] Z. Li, R. Liang, J. Wang, B. Na, and H. Liu, *Solution-Processable All-Small-Molecules for High-Performance Nonfullerene Organic Solar Cells with High Crystallinity Acceptor*, Journal of Physical Chemistry C **123**, 28021 (2019).

[23] F. Zhao, D. Chen, S. Chang, H. Huang, K. Tong, C. Xiao, S. Chou, H. Zhong, and Q. Pei, *Highly flexible organometal halide perovskite quantum dot based light-emitting diodes on a silver nanowire-polymer composite electrode*, Journal of Materials Chemistry C **5**, 531 (2017).

[24] M. Ylikunnari, M. Välimäki, K. L. Väisänen, T. M. Kraft, R. Sliz, G. Corso, R. Po, R. Barbieri, C. Carbonera, G. Gorni, and M. Vilkman, *Flexible OPV modules for highly efficient indoor applications*, Flexible and Printed Electronics **5** (2020).

[25] Y. Li, M. Behtash, J. Wong, and K. Yang, *Enhancing Ferroelectric Dipole Ordering in Organic-Inorganic Hybrid Perovskite* $CH_3NH_3PbI_3$*: Strain and Doping Engineering*, Journal of Physical Chemistry C **122**, 177 (2018).

[26] B. Abdollahi Nejand, P. Nazari, S. Gharibzadeh, V. Ahmadi, and A. Moshaii, *All-inorganic large-area low-cost and durable flexible perovskite solar cells using copper foil as a substrate*, Chemical Communications **53**, 747 (2017).

[27] H. Tahara, T. Aharen, A. Wakamiya, and Y. Kanemitsu, *Photorefractive Effect in Organic–Inorganic Hybrid Perovskites and Its Application to Optical Phase Shifter*, Advanced Optical Materials **6**, 1 (2018).

[28] R. Michalzik, *VCSELS; Fundamentals, Technology and Applications of Vertical-Cavity Surface-Emitting Lasers*, volume 166 of *Springer Series in Optical Sciences*, Springer Berlin Heidelberg, Berlin, Heidelberg, 2013.

[29] M. B. Price, J. Butkus, T. C. Jellicoe, A. Sadhanala, A. Briane, J. E. Halpert, K. Broch, J. M.

Hodgkiss, R. H. Friend, and F. Deschler, *Hot-carrier cooling and photoinduced refractive index changes in organic-inorganic lead halide perovskites*, Nature Communications **6**, 1 (2015).

[30] H. P. Pasanen, P. Vivo, L. Canil, A. Abate, and N. Tkachenko, *Refractive index change dominates the transient absorption response of metal halide perovskite thin films in the near infrared*, Physical Chemistry Chemical Physics **21**, 14663 (2019).

[31] J. Winter, S. Rapp, M. Spellauge, C. Eulenkamp, M. Schmidt, and H. P. Huber, *Ultrafast pump-probe ellipsometry and microscopy reveal the surface dynamics of femtosecond laser ablation of aluminium and stainless steel*, Applied Surface Science **511**, 145514 (2020).

[32] S. Chandrabose, K. Chen, A. J. Barker, J. J. Sutton, S. K. Prasad, J. Zhu, J. Zhou, K. C. Gordon, Z. Xie, X. Zhan, and J. M. Hodgkiss, *High Exciton Diffusion Coefficients in Fused Ring Electron Acceptor Films*, Journal of the American Chemical Society **141**, 6922 (2019).

[33] K. Broch, J. Dieterle, F. Branchi, N. J. Hestand, Y. Olivier, H. Tamura, C. Cruz, V. M. Nichols, A. Hinderhofer, D. Beljonne, F. C. Spano, G. Cerullo, C. J. Bardeen, and F. Schreiber, *Robust singlet fission in pentacene thin films with tuned charge transfer interactions*, Nature Communications **9** (2018).

[34] N. Kumar, J. He, D. He, Y. Wang, and H. Zhao, *Charge carrier dynamics in bulk MoS2 crystal studied by transient absorption microscopy*, Journal of Applied Physics **113** (2013).

[35] R. Kerremans, C. Kaiser, W. Li, N. Zarrabi, P. Meredith, and A. Armin, *The Optical Constants of Solution-Processed Semiconductors—New Challenges with Perovskites and Non-Fullerene Acceptors*, Advanced Optical Materials **8** (2020).

[36] E. Tokunaga, T. Kobayashi, and A. Terasaki, *Frequency-domain interferometer for femtosecond time-resolved phase spectroscopy*, Optics Letters **17**, 1131 (1992).

[37] K. Misawa and T. Kobayashi, *Femtosecond Sagnac interferometer for phase spectroscopy*, Optics Letters **20**, 1550 (1995).

[38] U. Megerle, I. Pugliesi, C. Schriever, C. F. Sailer, and E. Riedle, *Sub-50 fs broadband absorption spectroscopy with tunable excitation: putting the analysis of ultrafast molecular dynamics on solid ground*, Applied Physics B: Lasers and Optics **96**, 215 (2009).

[39] D. Polli, M. R. Antognazza, D. Brida, G. Lanzani, G. Cerullo, and S. De Silvestri, *Broadband pump-probe spectroscopy with sub-10-fs resolution for probing ultrafast internal conversion and coherent phonons in carotenoids*, Chemical Physics **350**, 45 (2008).

[40] A. Dubietis, G. Tamošauskas, R. Šuminas, V. Jukna, and A. Couairon, *Ultrafast supercontinuum generation in bulk condensed media (Invited Review)*, (2017).

[41] C. Manzoni, D. Polli, and G. Cerullo, *Two-color pump-probe system broadly tunable over the visible and the near infrared with sub-30 fs temporal resolution*, Review of Scientific Instruments **77** (2006).

[42] A. Shirakawa, I. Sakane, M. Takasaka, and T. Kobayashi, *Sub-5-fs visible pulse generation by pulse-front-matched noncollinear optical parametric amplification*, Applied Physics Letters **74**, 2268 (1999).

[43] G. Agrawal, *Nonlinear Fiber Optics*, Elsevier, 2012.

---

[44] C.-H. Lu, Y.-J. Tsou, H.-Y. Chen, B.-H. Chen, Y.-C. Cheng, S.-D. Yang, M.-C. Chen, C.-C. Hsu, and A. H. Kung, *Generation of intense supercontinuum in condensed media*, Optica **1**, 400 (2014).

[45] C.-H. Lu, W.-H. Wu, S.-H. Kuo, J.-Y. Guo, M.-C. Chen, S.-D. Yang, and A. H. Kung, *Greater than 50 times compression of 1030 nm Yb:KGW laser pulses to single-cycle duration*, Optics Express **27**, 15638 (2019).

[46] R. P. Huebener, *Conductors, Semiconductors, Superconductors*, Undergraduate Lecture Notes in Physics, Springer International Publishing, Cham, 2015.

[47] R. d. L. K. Penney and W. .G., *Quantum Mechanics of Electrons in Crystal Lattices*, Proceedings of the Royal Society of London, Series A **52**, 555 (1931).

[48] C. Kittel, *Introduction to Solid State Physics*, John Wiley & Sons, Inc, 2010.

[49] P. Dirac, *On the theory of quantum mechanics*, Proceedings of the Royal Society of London. Series A, Containing Papers of a Mathematical and Physical Character **112**, 661 (1926).

[50] Y. Kanemitsu and T. Handa, *Photophysics of metal halide perovskites: From materials to devices*, Japanese Journal of Applied Physics **090101**, 1 (2018).

[51] C. Li, X. Lu, W. Ding, L. Feng, Y. Gao, and Z. Guo, *Formability of* ABX_3 *(X = F, Cl, Br, I) halide perovskites*, Acta Crystallographica Section B: Structural Science **64**, 702 (2008).

[52] D. Bi, W. Tress, M. I. Dar, P. Gao, J. Luo, C. Renevier, K. Schenk, A. Abate, F. Giordano, J. P. Correa Baena, J. D. Decoppet, S. M. Zakeeruddin, M. K. Nazeeruddin, M. Grätzel, and A. Hagfeldt, *Efficient luminescent solar cells based on tailored mixed-cation perovskites*, Science Advances **2** (2016).

[53] P. Vashishtha, D. Z. Metin, M. E. Cryer, K. Chen, J. M. Hodgkiss, N. Gaston, and J. E. Halpert, *Shape-, Size-, and Composition-Controlled Thallium Lead Halide Perovskite Nanowires and Nanocrystals with Tunable Band Gaps*, Chemistry of Materials **30**, 2973 (2018).

[54] H. Lin, C. Zhou, Y. Tian, T. Siegrist, and B. Ma, *Low-Dimensional Organometal Halide Perovskites*, ACS Energy Letters , 54 (2017).

[55] J. Li, L. Luo, H. Huang, C. Ma, Z. Ye, J. Zeng, and H. He, *2D Behaviors of Excitons in Cesium Lead Halide Perovskite Nanoplatelets*, Journal of Physical Chemistry Letters **8**, 1161 (2017).

[56] H. Telfah, A. Jamhawi, M. B. Teunis, R. Sardar, and J. Liu, *Ultrafast Exciton Dynamics in Shape-Controlled Methylammonium Lead Bromide Perovskite Nanostructures: Effect of Quantum Confinement on Charge Carrier Recombination*, Journal of Physical Chemistry C **121**, 28556 (2017).

[57] H. J. Snaith, *Present status and future prospects of perovskite photovoltaics*, Nature Materials **17**, 372 (2018).

[58] J. Kim, S. H. Lee, J. H. Lee, and K. H. Hong, *The role of intrinsic defects in methylammonium lead iodide perovskite*, Journal of Physical Chemistry Letters **5**, 1312 (2014).

[59] R. Cheacharoen, C. C. Boyd, G. F. Burkhard, T. Leijtens, J. A. Raiford, K. A. Bush, S. F. Bent, and M. D. McGehee, *Encapsulating perovskite solar cells to withstand damp heat and thermal cycling*, Sustainable Energy & Fuels **2** (2018).

[60] J. A. Christians, P. Schulz, J. S. Tinkham, T. H. Schloemer, S. P. Harvey, B. J. Tremolet de Villers, A. Sellinger, J. J. Berry, and J. M. Luther, *Tailored interfaces of unencapsulated perovskite solar cells*

for >1,000 hour operational stability, Nature Energy **3**, 68 (2018).

[61] P. Umari, E. Mosconi, and F. De Angelis, *Relativistic GW calculations on* $CH_3NH_3PbI_3$ *and* $CH_3NH_3SnI_3$ *Perovskites for Solar Cell Applications*, Scientific Reports **4**, 4467 (2015).

[62] G. Xing, N. Mathews, S. Sun, S. S. Lim, Y. M. Lam, M. Gratzel, S. Mhaisalkar, and T. C. Sum, *Long-range balanced electron-and hole-transport lengths in organic-inorganic* $CH_3NH_3PbI_3$, Science **342**, 344 (2013).

[63] H. S. Kim, C. R. Lee, J. H. Im, K. B. Lee, T. Moehl, A. Marchioro, S. J. Moon, R. Humphry-Baker, J. H. Yum, J. E. Moser, M. Grätzel, and N. G. Park, *Lead iodide perovskite sensitized all-solid-state submicron thin film mesoscopic solar cell with efficiency exceeding 9%*, Scientific Reports **2**, 1 (2012).

[64] T. Baikie, Y. Fang, J. M. Kadro, M. Schreyer, F. Wei, S. G. Mhaisalkar, M. Graetzel, and T. J. White, *Synthesis and crystal chemistry of the hybrid perovskite* $(CH_3NH_3)PbI_3$ *for solid-state sensitised solar cell applications*, Journal of Materials Chemistry A **1**, 5628 (2013).

[65] E. Mosconi, T. Etienne, and F. De Angelis, *Rashba Band Splitting in Organohalide Lead Perovskites: Bulk and Surface Effects*, Journal of Physical Chemistry Letters **8**, 2247 (2017).

[66] E. M. Hutter, M. C. Gélvez-Rueda, A. Osherov, V. Bulović, F. C. Grozema, S. D. Stranks, and T. J. Savenije, *Direct-indirect character of the bandgap in methylammonium lead iodide perovskite*, Nature Materials **16**, 115 (2017).

[67] T. Wang, B. Daiber, J. M. Frost, S. A. Mann, E. C. Garnett, A. Walsh, and B. Ehrler, *Indirect to direct bandgap transition in methylammonium lead halide perovskite*, Energy and Environmental Science **10**, 509 (2017).

[68] T. Chen, W.-L. Chen, B. J. Foley, J. Lee, J. P. C. Ruff, J. Y. P. Ko, C. M. Brown, L. W. Harriger, D. Zhang, C. Park, M. Yoon, Y.-M. Chang, J. J. Choi, and S.-H. Lee, *Origin of long lifetime of band-edge charge carriers in organic–inorganic lead iodide perovskites*, Proceedings of the National Academy of Sciences **114**, 7519 (2017).

[69] B. E. A. Saleh and M. C. Teich, *Fundamentals op Photonics*, John Wiley & Sons, Inc., New York, 1991.

[70] L. M. Herz, *Charge-Carrier Dynamics in Organic-Inorganic Metal Halide Perovskites*, Annual Review of Physical Chemistry **67**, 65 (2016).

[71] S. D. Stranks, S. D. Stranks, G. E. Eperon, G. Grancini, C. Menelaou, M. J. P. Alcocer, T. Leijtens, L. M. Herz, A. Petrozza, and H. J. Snaith, *Electron-Hole Diffusion Lengths Exceeding 1 Micrometer in an Organometal Trihalide Perovskite Absorber*, Science (New York, N.Y.) **342**, 341 (2014).

[72] Y. Yamada, T. Nakamura, M. Endo, A. Wakamiya, and Y. Kanemitsu, *Photocarrier recombination dynamics in perovskite* $CH_3NH_3PbI_3$ *for solar cell applications*, Journal of the American Chemical Society **136**, 11610 (2014).

[73] C. Wehrenfennig, G. E. Eperon, M. B. Johnston, H. J. Snaith, and L. M. Herz, *High charge carrier mobilities and lifetimes in organolead trihalide perovskites*, Advanced Materials **26**, 1584 (2014).

[74] A. Miyata, A. Mitioglu, P. Plochocka, O. Portugall, J. T. W. Wang, S. D. Stranks, H. J. Snaith, and R. J. Nicholas, *Direct measurement of the exciton binding energy and effective masses for charge carriers*

in organic-inorganic tri-halide perovskites, Nature Physics **11**, 582 (2015).

[75] A. Mondal, J. Aneesh, V. Kumar Ravi, R. Sharma, W. J. Mir, M. C. Beard, A. Nag, and K. V. Adarsh, *Ultrafast exciton many-body interactions and hot-phonon bottleneck in colloidal cesium lead halide perovskite nanocrystals*, Physical Review B **98**, 1 (2018).

[76] T. C. Sum, N. Mathews, G. Xing, S. S. Lim, W. K. Chong, D. Giovanni, and H. A. Dewi, *Spectral Features and Charge Dynamics of Lead Halide Perovskites: Origins and Interpretations*, Accounts of Chemical Research **49**, 294 (2016).

[77] M. B. Johnston and L. M. Herz, *Hybrid Perovskites for Photovoltaics: Charge-Carrier Recombination, Diffusion, and Radiative Efficiencies*, Accounts of Chemical Research **49**, 146 (2016).

[78] Y. Yang, M. Yang, Z. Li, R. Crisp, K. Zhu, and M. C. Beard, *Comparison of Recombination Dynamics in $CH_3NH_3PbBr_3$ and $CH_3NH_3PbI_3$ Perovskite Films: Influence of Exciton Binding Energy*, Journal of Physical Chemistry Letters **6**, 4688 (2015).

[79] T. C. Sum and N. Mathews, *Advancements in perovskite solar cells: Photophysics behind the photovoltaics*, Energy Environ. Sci. **7**, 2518 (2014).

[80] W. Ming, S. Chen, and M. H. Du, *Chemical instability leads to unusual chemical-potential-independent defect formation and diffusion in perovskite solar cell material $CH_3NH_3PbI_3$*, Journal of Materials Chemistry A **4**, 16975 (2016).

[81] M. Li, S. Bhaumik, T. W. Goh, M. S. Kumar, N. Yantara, M. Grätzel, S. Mhaisalkar, N. Mathews, and T. C. Sum, *Slow cooling and highly efficient extraction of hot carriers in colloidal perovskite nanocrystals*, Nature Communications **8**, 3 (2017).

[82] M. L. De Giorgi, A. Perulli, N. Yantara, P. P. Boix, and M. Anni, *Amplified Spontaneous Emission Properties of Solution Processed CsPbBr3 Perovskite Thin Films*, The Journal of Physical Chemistry C **121**, 14772 (2017).

[83] S. Yakunin, L. Protesescu, F. Krieg, M. I. Bodnarchuk, G. Nedelcu, M. Humer, G. De Luca, M. Fiebig, W. Heiss, and M. V. Kovalenko, *Low-threshold amplified spontaneous emission and lasing from colloidal nanocrystals of caesium lead halide perovskites*, Nature Communications **6**, 1 (2015).

[84] B. R. Bennett, R. A. Soref, and J. A. Del Alamo, *Carrier-Induced Change in Refractive Index of InP, GaAs, and InGaAsP*, IEEE Journal of Quantum Electronics **26**, 113 (1990).

[85] D. Gamota, P. Brazis, K. Kalyanasundaram, and J. Zhang, *Printed Organic and Molecular Electronics*, Kluwer Academic Publishers, Boston, first edition, 2004.

[86] A. Buckley, *Organic Light-Emitting Diodes (OLEDs): Materials, Devices and Applications*, Woodhead Publishing, 2013.

[87] W. Li and H. Kwok, *Conduction Mechanisms in Organic Semiconductors*, pages 493–500, Springer Netherlands, Dordrecht, 2012.

[88] B. S. Basel, C. Hetzer, J. Zirzlmeier, D. Thiel, R. Guldi, F. Hampel, A. Kahnt, T. Clark, D. M. Guldi, and R. R. Tykwinski, *Davydov splitting and singlet fission in excitonically coupled pentacene dimers*, Chemical Science **10**, 3854 (2019).

[89] C. Voz, J. Puigdollers, I. Martín, D. Muñoz, A. Orpella, M. Vetter, and R. Alcubilla, *Optoelectronic*

devices based on evaporated pentacene films, Solar Energy Materials and Solar Cells **87**, 567 (2005).

[90] O. D. Jurchescu, J. Baas, and T. T. Palstra, *Effect of impurities on the mobility of single crystal pentacene*, Applied Physics Letters **84**, 3061 (2004).

[91] J. Breeze, K. J. Tan, B. Richards, J. Sathian, M. Oxborrow, and N. M. N. Alford, *Enhanced magnetic Purcell effect in room-temperature masers*, Nature Communications **6**, 1 (2015).

[92] B. J. Walker, A. J. Musser, D. Beljonne, and R. H. Friend, *Singlet exciton fission in solution*, Nature Chemistry **5**, 1019 (2013).

[93] M. W. Wilson, A. Rao, J. Clark, R. S. S. Kumar, D. Brida, G. Cerullo, and R. H. Friend, *Ultrafast dynamics of exciton fission in polycrystalline pentacene*, Journal of the American Chemical Society **133**, 11830 (2011).

[94] D. Di, L. Yang, J. M. Richter, L. Meraldi, R. M. Altamimi, A. Y. Alyamani, D. Credgington, K. P. Musselman, J. L. MacManus-Driscoll, and R. H. Friend, *Efficient Triplet Exciton Fusion in Molecularly Doped Polymer Light-Emitting Diodes*, Advanced Materials **29** (2017).

[95] R. Ieuji, K. Goushi, and C. Adachi, *Triplet–triplet upconversion enhanced by spin–orbit coupling in organic light-emitting diodes*, Nature Communications **10** (2019).

[96] B. Ehrler, N. Yanai, and L. Nienhaus, *Up- And down-conversion in molecules and materials*, Journal of Chemical Physics **154** (2021).

[97] P. M. Zimmerman, F. Bell, D. Casanova, and M. Head-Gordon, *Mechanism for singlet fission in pentacene and tetracene: From single exciton to two triplets*, Journal of the American Chemical Society **133**, 19944 (2011).

[98] V. O. Kim, K. Broch, V. Belova, Y. S. Chen, A. Gerlach, F. Schreiber, H. Tamura, R. G. Della Valle, G. D'Avino, I. Salzmann, D. Beljonne, A. Rao, and R. Friend, *Singlet exciton fission via an intermolecular charge transfer state in coevaporated pentacene-perfluoropentacene thin films*, Journal of Chemical Physics **151** (2019).

[99] W. Shockley and H. J. Queisser, *Detailed balance limit of efficiency of p-n junction solar cells*, Journal of Applied Physics **32**, 510 (1961).

[100] R. W. Boyd, *Nonlinear Optics*, Elsevier, New York, 2nd editio edition, 2003.

[101] M. Born and E. Wolf, *Principles of Optic*, Cambridge University Press, Cambridge, seventh edition, 1999.

[102] R. Trebino, *Frequency-Resolved Optical Gating: The Measurement of Ultrashort Laser Pulses*, Springer US, Boston, MA, 1st edition, 2000.

[103] P. A. Franken, A. E. Hill, C. W. Peters, and G. Weinreich, *Generation of optical harmonics*, Physical Review Letters **7**, 118 (1961).

[104] A. Dubietis and A. Couairon, *Ultrafast Supercontinuum Generation in Transparent Solid-State Media*, Springer, Switzerland, 2019.

[105] Alfano R.R. and Shapiro S.L., *Emission in the region 4000 to 7000Å via four-photon coupling in glass*, Physical Review Letters **24**, 584 (1970).

[106] D. Strickland and G. Mourou, *Compression of amplified chirped optical pulses*, Optics Communica-

tions **56**, 219 (1985).

[107] W. Lin, T. Lai, Y. Cheng, X. Zheng, X. Xu, and D. Mo, *19fs-pulse generation from a self mode-locked Ti:Sapphire laser*, Guangxue Xuebao/Acta Optica Sinica **15**, 1151 (1995).

[108] V. P. Kandidov, O. G. Kosareva, I. S. Golubtsov, W. Liu, A. Becker, N. Akozbek, C. M. Bowden, and S. L. Chin, *Self-transformation of a powerful femtosecond laser pulse into a white-light laser pulse in bulk optical media (or supercontinuum generation)*, Applied Physics B: Lasers and Optics **77**, 149 (2003).

[109] I. S. Golubtsov, V. P. Kandidov, and O. G. Kosareva, *Initial phase modulation of a high-power femtosecond laser pulse as a tool for controlling the pulse filamentation and generation of a supercontinuum in air*, Kvantovaya Elektronika **33**, 525 (2003).

[110] T. S. Robinson, S. Patankar, E. Floyd, N. H. Stuart, N. Hopps, and R. A. Smith, *Spectral characterization of a supercontinuum source based on nonlinear broadening in an aqueous K_2ZnCl_4 salt solution*, Applied Optics **56**, 9837 (2017).

[111] H. Schroeder and S. L. Chin, *Visualization of the evolution of multiple filaments in methanol*, Optics Communications **234**, 399 (2004).

[112] A. K. Dharmadhikari, F. A. Rajgara, N. C. S. Reddy, A. S. Sandhu, and D. Mathur, *Highly efficient white light generation from barium fluoride*, Optics Express **12**, 695 (2004).

[113] J. M. Dudley, G. Genty, and S. Coen, *Supercontinuum generation in photonic crystal fiber*, Reviews of Modern Physics **78**, 1135 (2006).

[114] A. Couairon and A. Mysyrowicz, *Femtosecond filamentation in transparent media*, Physics Reports **441**, 47 (2007).

[115] R. R. Alfano, *Supercontinuum Generation in Condensed Matter*, in *The Supercontinuum Laser Source*, pages 33–100, Springer New York, New York, NY, 2016.

[116] J.-C. Diels and W. Rudolph, *Fundamentals, Techniques, and Applications on a Femtosecond Time Scale*, in *Ultrashort Laser Pulse Phenomena*, edited by P. Liao and P. Kellye, volume 25, page 581, Elsevier, 2nd editio edition, 2006.

[117] A. Brodeur and S. L. Chin, *Ultrafast white-light continuum generation and self-focusing in transparent condensed media*, Journal of the Optical Society of America B **16**, 637 (1999).

[118] S. A. Akhmanov, A. P. Sukhorukov, and R. Khokhlov, *Self-focusing and diffraction of light in a Nonlinear medium*, Uspekhi Fizicheskih Nauk **93**, 19 (1967).

[119] M. D. Feit and J. A. Fleck, *Beam nonparaxiality, filament formation, and beam breakup in the self-focusing of optical beams*, Journal of the Optical Society of America B **5**, 633 (1988).

[120] R. R. Alfano and S. L. Shapiro, *Observation of self-phase modulation and small-scale filaments in crystals and glasses*, Physical Review Letters **24**, 592 (1970).

[121] N. Bloembergen, *The influence of electron plasma formation on superbroadening in light filaments*, Optics Communications **8**, 285 (1973).

[122] L. Jian-Hua, L. Yu-Lin, and J. Jia-Lin, *On combined self-phase modulation and stimulated Raman scattering in optical fibres*, Optical and Quantum Electronics **17**, 187 (1985).

[123] F. DeMartini, C. H. Townes, T. K. Gustafson, and P. L. Kelley, *Self-steepening of light pulses*, Physical Review **164**, 312 (1967).

[124] G. zhen Yang and V. R. Shen, *Spectral Broadening of Ultrashort Pulses in a Nonlinear Medium.*, Optics Letters **9**, 29 (1984).

[125] D. Anderson and M. Lisak, *Nonlinear Asymmetric Distortion of Short Pulses in Long Optical Fibers.*, **7**, 166 (1983).

[126] E. Yablonovitch and N. Bloembergen, *Avalanche ionization and the limiting diameter of filaments induced by light pulses in transparent media*, Physical Review Letters **29**, 907 (1972).

[127] R. Trebino and D. J. Kane, *Using phase retrieval to measure the intensity and phase of ultrashort pulses: frequency-resolved optical gating*, J. Opt. Soc. Am. A **10**, 1 (1993).

[128] D. J. Kane and R. Trebino, *Characterization of Arbitrary Femtosecond Pulses Using Frequency-Resolved Optical Gating*, IEEE Journal of Quantum Electronics **29**, 571 (1993).

[129] R. Trebino, K. W. DeLong, D. N. Fittinghoff, J. N. Sweetser, M. A. Krumbügel, B. A. Richman, and D. J. Kane, *Measuring ultrashort laser pulses in the time-frequency domain using frequency-resolved optical gating*, Review of Scientific Instruments **68**, 3277 (1997).

[130] D. Fittinghoff, J. Squier, C. Toth, B. Walker, and C. Barty, *Low-dispersion polarization gate frequency-resolved optical gating for measuring high-power <30-fs pulses*, in *Technical Digest. Summaries of Papers Presented at the Conference on Lasers and Electro-Optics. Conference Edition. 1998 Technical Digest Series, Vol.6 (IEEE Cat. No.98CH36178)*, pages 463–464, IEEE, 1998.

[131] R. Stolen and A. Ashkin, *Optical Kerr effect in glass waveguide*, Applied Physics Letters **22**, 294 (1973).

[132] K. W. DeLong, B. Kohler, K. Wilson, D. N. Fittinghoff, and R. Trebino, *Pulse retrieval in frequency-resolved optical gating based on the method of generalized projections*, Optics Letters **19**, 2152 (1994).

[133] K. W. DeLong and R. Trebino, *Improved ultrashort pulse-retrieval algorithm for frequency-resolved optical gating*, Journal of the Optical Society of America A **11**, 2429 (1994).

[134] J. Gagnon, E. Goulielmakis, and V. S. Yakovlev, *The accurate FROG characterization of attosecond pulses from streaking measurements*, Applied Physics B: Lasers and Optics **92**, 25 (2008).

[135] F. Kanal, S. Keiber, R. Eck, and T. Brixner, *100-kHz shot-to-shot broadband data acquisition for high-repetition-rate pump–probe spectroscopy*, Optics Express **22**, 16965 (2014).

[136] R. Berera, R. van Grondelle, and J. T. Kennis, *Ultrafast transient absorption spectroscopy: Principles and application to photosynthetic systems*, Photosynthesis Research **101**, 105 (2009).

[137] A. Walsh, J. L. Da Silva, and S. H. Wei, *Origins of band-gap renormalization in degenerately doped semiconductors*, Physical Review B - Condensed Matter and Materials Physics **78**, 1 (2008).

[138] K. F. Berggren and B. E. Sernelius, *Band-gap narrowing in heavily doped many-valley semiconductors*, Physical Review B **24**, 1971 (1981).

[139] A. Miller, K. Welford, and B. Daino, *Nonlinear Optical Materials and Devices for Applications in Information Technology*, Springer Science+Business Media, 1993.

[140] A. B. Djurišić and E. H. Li, *Dielectric function models for describing the optical properties of hexagonal*

GaN, Journal of Applied Physics **89**, 273 (2001).

[141] T. Ghosh, S. Aharon, A. Shpatz, L. Etgar, and S. Ruhman, *Reflectivity Effects on Pump-Probe Spectra of Lead Halide Perovskites: Comparing Thin Films versus Nanocrystals*, ACS Nano **12**, 5719 (2018).

[142] B. Anand, S. Sampat, E. O. Danilov, W. Peng, S. M. Rupich, Y. J. Chabal, Y. N. Gartstein, and A. V. Malko, *Broadband transient absorption study of photoexcitations in lead halide perovskites: Towards a multiband picture*, Physical Review B **93**, 1 (2016).

[143] J. Brazard, L. A. Bizimana, and D. B. Turner, *Accurate convergence of transient-absorption spectra using pulsed lasers*, Review of Scientific Instruments **86** (2015).

[144] H. Löslein, T. Ameri, G. J. Matt, M. Koppe, H. J. Egelhaaf, A. Troeger, V. Sgobba, D. M. Guldi, and C. J. Brabec, *Transient absorption spectroscopy studies on polythiophene-fullerene bulk heterojunction organic blend films sensitized with a low-bandgap polymer*, Macromolecular Rapid Communications **34**, 1090 (2013).

[145] R. R. Alfano, *The Supercontinuum Laser Source*, volume 53, Springer New York, New York, NY, third edit edition, 2016.

[146] G. Cerullo and S. De Silvestri, *Ultrafast optical parametric amplifiers*, Review of Scientific Instruments **74**, 1 (2003).

[147] E. Hecht, *Optics*, Pearson Education, Inc., San Francisco, 4ed edition, 2002.

[148] Y.-h. Chen, R. R. Tamming, K. Chen, Z. Zhang, F. Liu, Y. Zhang, J. M. Hodgkiss, R. J. Blaikie, B. Ding, and M. Qiu, *Bandgap control in two-dimensional semiconductors via coherent doping of plasmonic hot electrons*, Nature Communications , 6 (2021).

[149] E. Tokunaga and A. Terasaki, *Femtosecond time-resolved dispersion relations studied with a frequency-domain interferometer*, Physical Review A **47**, 4581 (1993).

[150] J. J. Fendley, *Measurement of refractive index using a Michelson interferometer*, Physics Education **17**, 209 (1982).

[151] P. A. Flournoy, R. W. McClure, and G. Wyntjes, *White-Light Interferometric Thickness Gauge*, Applied Optics **11**, 1907 (1972).

[152] S. M. Kuo and B. H. Lee, *Real-Time Digital Signal Processing; Implementations, Applications and Experiments with the TMS320C55x*, John Wiley \& Sons Ltd., London, 1st edition, 2001.

[153] J. Butkus, *Excited State Properties of Novel Solution Processed Inorganic and Hybrid Photovoltaic Materials*, PhD thesis, Victoria University of Wellington, 2018.

[154] R. R. Tamming, J. Butkus, M. B. Price, P. Vashishtha, S. K. K. Prasad, J. E. Halpert, K. Chen, and J. M. Hodgkiss, *Ultrafast Spectrally Resolved Photoinduced Complex Refractive Index Changes in CsPbBr 3 Perovskites*, ACS Photonics (2019).

[155] M. M. Lee, J. Teuscher, T. Miyasaka, T. N. Murakami, and H. J. Snaith, *Efficient hybrid solar cells based on meso-superstructured organometal halide perovskites*, Science **338**, 643 (2012).

[156] M. Liu, M. B. Johnston, and H. J. Snaith, *Efficient planar heterojunction perovskite solar cells by vapour deposition*, Nature **501**, 395 (2013).

[157] Z.-K. Tan, R. S. Moghaddam, M. L. Lai, P. Docampo, R. Higler, F. Deschler, M. Price, A. Sadhanala, L. M. Pazos, D. Credgington, F. Hanusch, T. Bein, H. J. Snaith, and R. H. Friend, *Bright light-emitting diodes based on organometal halide perovskite*, Nature Nanotechnology **9**, 687 (2014).

[158] P. Vashishtha and J. E. Halpert, *Field-Driven Ion Migration and Color Instability in Red-Emitting Mixed Halide Perovskite Nanocrystal Light-Emitting Diodes*, Chemistry of Materials **29**, 5965 (2017).

[159] F. Deschler, M. Price, S. Pathak, L. E. Klintberg, D. D. Jarausch, R. Higler, S. Hüttner, T. Leijtens, S. D. Stranks, H. J. Snaith, M. Atatüre, R. T. Phillips, and R. H. Friend, *High photoluminescence efficiency and optically pumped lasing in solution-processed mixed halide perovskite semiconductors*, Journal of Physical Chemistry Letters **5**, 1421 (2014).

[160] K. Chen, A. J. Barker, F. L. Morgan, J. E. Halpert, and J. M. Hodgkiss, *Effect of carrier thermalization dynamics on light emission and amplification in organometal halide perovskites*, Journal of Physical Chemistry Letters **6**, 153 (2015).

[161] X. Jia, J. Jiang, Y. Zhang, J. Qiu, S. Wang, Z. Chen, N. Yuan, and J. Ding, *Observation of enhanced hot phonon bottleneck effect in 2D perovskites*, Applied Physics Letters **112** (2018).

[162] E. Serpetzoglou, I. Konidakis, G. Kakavelakis, T. Maksudov, E. Kymakis, and E. Stratakis, *Improved Carrier Transport in Perovskite Solar Cells Probed by Femtosecond Transient Absorption Spectroscopy*, ACS Applied Materials & Interfaces , acsami.7b15195 (2017).

[163] J. G. Mendoza-Alvarez, R. H. Yan, and L. A. Coldren, *Contribution of the band-filling effect to the effective refractive-index change in double-heterostructure GaAs/AlGaAs phase modulators*, Journal of Applied Physics **62**, 4548 (1987).

[164] E. Y. Lin and T. S. Lay, *Empirical model including band-to-band Coulomb interaction for refractive index spectra of quaternary semiconductors*, Journal of Applied Physics **105** (2009).

[165] P. Löper, M. Stuckelberger, B. Niesen, J. Werner, M. Filipič, S.-J. Moon, J.-H. Yum, M. Topič, S. De Wolf, and C. Ballif, *Complex Refractive Index Spectra of $CH_3NH_3PbI_3$ Perovskite Thin Films Determined by Spectroscopic Ellipsometry and Spectrophotometry*, The Journal of Physical Chemistry Letters **6**, 66 (2015).

[166] D. C. Hutchings, M. Sheik-Bahae, D. J. Hagan, and E. W. Van Stryland, *Kramers-Krönig relations in nonlinear optics*, Optical and Quantum Electronics **24**, 1 (1992).

[167] A. Djorović, M. Meyer, B. L. Darby, and E. C. Le Ru, *Accurate Modeling of the Polarizability of Dyes for Electromagnetic Calculations*, ACS Omega **2**, 1804 (2017).

[168] Y. Q. Zhao, Q. R. Ma, B. Liu, Z. L. Yu, and M. Q. Cai, *Pressure-induced strong ferroelectric polarization in tetra-phase perovskite CsPbBr3*, Physical Chemistry Chemical Physics **20**, 14718 (2018).

[169] A. B. Kuzmenko, *Kramers–Kronig constrained variational analysis of optical spectra*, Review of Scientific Instruments **76**, 083108 (2005).

[170] M. Ahmad, G. Rehman, L. Ali, M. Shafiq, R. Iqbal, R. Ahmad, T. Khan, S. Jalali-Asadabadi, M. Maqbool, and I. Ahmad, *Structural, electronic and optical properties of $CsPbX_3$ (X=Cl, Br, I) for energy storage and hybrid solar cell applications*, Journal of Alloys and Compounds **705**, 828 (2017).

[171] E. A. Pogna, M. Marsili, D. De Fazio, S. Dal Conte, C. Manzoni, D. Sangalli, D. Yoon, A. Lombardo, A. C. Ferrari, A. Marini, G. Cerullo, and D. Prezzi, *Photo-induced bandgap renormalization governs the ultrafast response of single-layer MoS2*, ACS Nano **10**, 1182 (2016).

[172] Y. Yang, D. P. Ostrowski, R. M. France, K. Zhu, J. Van De Lagemaat, J. M. Luther, and M. C. Beard, *Observation of a hot-phonon bottleneck in lead-iodide perovskites*, Nature Photonics **10**, 53 (2016).

[173] S. Nah, B. M. Spokoyny, C. M. Soe, C. C. Stoumpos, M. G. Kanatzidis, and E. Harel, *Ultrafast Imaging of Carrier Cooling in Metal Halide Perovskite Thin Films*, Nano Letters **18**, 1044 (2018).

[174] J. Fu, Q. Xu, G. Han, B. Wu, C. H. A. Huan, M. L. Leek, and T. C. Sum, *Hot carrier cooling mechanisms in halide perovskites*, Nature Communications **8** (2017).

[175] M. L. De Giorgi, F. Krieg, M. V. Kovalenko, and M. Anni, *Amplified Spontaneous Emission Threshold Reduction and Operational Stability Improvement in CsPbBr3 Nanocrystals Films by Hydrophobic Functionalization of the Substrate*, Scientific Reports **9**, 1 (2019).

[176] C. Li, Z. Zang, C. Han, Z. Hu, X. Tang, J. Du, Y. Leng, and K. Sun, *Enhanced random lasing emission from highly compact CsPbBr3 perovskite thin films decorated by ZnO nanoparticles*, Nano Energy **40**, 195 (2017).

[177] A. Balena, A. Perulli, M. Fernandez, M. L. De Giorgi, G. Nedelcu, M. V. Kovalenko, and M. Anni, *Temperature Dependence of the Amplified Spontaneous Emission from CsPbBr3 Nanocrystal Thin Films*, Journal of Physical Chemistry C **122**, 5813 (2018).

[178] B. G. F. Burkhard, E. T. Hoke, and M. D. Mcgehee, *Accounting for Interference, Scattering, and Electrode Absorption to Make Accurate Internal Quantum Efficiency Measurements in Organic and Other Thin Solar Cells*, **94305**, 3293 (2010).

[179] Z. Wang, Q. Lin, B. Wenger, M. G. Christoforo, Y. H. Lin, M. T. Klug, M. B. Johnston, L. M. Herz, and H. J. Snaith, *High irradiance performance of metal halide perovskites for concentrator photovoltaics*, Nature Energy **3**, 855 (2018).

[180] L. A. Pettersson, L. S. Roman, and O. Inganäs, *Modeling photocurrent action spectra of photovoltaic devices based on organic thin films*, Journal of Applied Physics **86**, 487 (1999).

[181] P. Peumans, A. Yakimov, and S. R. Forrest, *Small molecular weight organic thin-film photodetectors and solar cells*, Journal of Applied Physics **93**, 3693 (2003).

[182] L. Zhou, J. Chang, Z. Liu, X. Sun, Z. Lin, D. Chen, C. Zhang, J. Zhang, and Y. Hao, *Enhanced planar perovskite solar cell efficiency and stability using a perovskite/PCBM heterojunction formed in one step*, Nanoscale **10**, 3053 (2018).

[183] L. C. Chen, J. C. Chen, C. C. Chen, and C. G. Wu, *Fabrication and Properties of High-Efficiency Perovskite/PCBM Organic Solar Cells*, Nanoscale Research Letters **10**, 2 (2015).

[184] T. Narushima and H. Okamoto, *Circular Dichroism Microscopy Free from Commingling Linear Dichroism via Discretely Modulated Circular Polarization*, Scientific Reports **6**, 1 (2016).

[185] R. R. Tamming, C.-Y. Lin, K. Chen, C.-H. Lu, J. M. Hodgkiss, and S.-D. Yang, *Multiple-Plate Compression used in Transient Absorption Spectroscopy*, in *14th Pacific Rim Conference on Lasers and*

Electro-Optics (CLEO PR 2020), page C6B_4, Washington, D.C., 2020, OSA.

[186] J. B. Ashcom, R. R. Gattass, C. B. Schaffer, and E. Mazur, *Numerical aperture dependence of damage and supercontinuum generation from femtosecond laser pulses in bulk fused silica*, Journal of the Optical Society of America B **23**, 2317 (2006).

[187] M. Kato, T. Fujiseki, T. Miyadera, T. Sugita, S. Fujimoto, M. Tamakoshi, M. Chikamatsu, and H. Fujiwara, *Universal rules for visible-light absorption in hybrid perovskite materials*, Journal of Applied Physics **121** (2017).

[188] L. Krückemeier, P. Kaienburg, J. Flohre, K. Bittkau, I. Zonno, B. Krogmeier, and T. Kirchartz, *Developing design criteria for organic solar cells using well-absorbing non-fullerene acceptors*, Communications Physics **1**, 1 (2018).

[189] D. Wegkamp, D. Brida, S. Bonora, G. Cerullo, J. Stähler, M. Wolf, and S. Wall, *Phase retrieval and compression of low-power white-light pulses*, Applied Physics Letters **99** (2011).

[190] T. Witting, F. J. Furch, and M. J. Vrakking, *Spatio-temporal characterisation of a 100 kHz 24 W sub-3-cycle NOPCPA laser system*, Journal of Optics (United Kingdom) **20** (2018).

[191] A. Zaukevičius, V. Jukna, R. Antipenkov, V. Martinėnaitė, A. Varanavičius, A. P. Piskarskas, and G. Valiulis, *Manifestation of spatial chirp in femtosecond noncollinear optical parametric chirped-pulse amplifier*, Journal of the Optical Society of America B **28**, 2902 (2011).

[192] J. M. Dudley, *Coherence properties of supercontinuum spectra generated in photonic crystal and tapered optical fibers*, Optics Letters **27**, 1180 (2002).

[193] R. D. Engelsholm and O. Bang, *Supercontinuum noise reduction by fiber undertapering*, Optics Express **27**, 10320 (2019).

[194] G. Chang, H. G. Winful, and T. B. Norris, *Optimization of supercontinuum generation in photonic crystal fibers for pulse compression*, OSA Trends in Optics and Photonics Series **88**, 1810 (2003).

[195] Y.-C. Cheng, C.-H. Lu, Y.-Y. Lin, and A. H. Kung, *Supercontinuum generation in a multi-plate medium*, Optics Express **24**, 7224 (2016).

[196] P. He, Y. Liu, K. Zhao, H. Teng, X. He, P. Huang, H. Huang, S. Zhong, Y. Jiang, S. Fang, X. Hou, and Z. Wei, *High-efficiency supercontinuum generation in solid thin plates at 0.1TW level*, Optics Letters **42**, 474 (2017).

[197] C.-H. Lu, W.-H. Wu, S.-H. Kuo, J.-Y. Guo, M.-C. Chen, S.-D. Yang, and A. H. Kung, *Greater than 50 times compression of 1030 nm Yb:KGW laser pulses to single-cycle duration*, Optics Express **27**, 15638 (2019).

[198] M. Seidel, G. Arisholm, J. Brons, V. Pervak, and O. Pronin, *All solid-state spectral broadening: an average and peak power scalable method for compression of ultrashort pulses*, Optics Express **24**, 9412 (2016).

[199] W. Liu, S. Petit, A. Becker, N. Aközbek, C. M. Bowden, and S. L. Chin, *Intensity clamping of a femtosecond laser pulse in condensed matter*, Optics Communications **202**, 189 (2002).

[200] H.-S. Tan, I. R. Piletic, and M. D. Fayer, *Polarization selective spectroscopy experiments: methodology and pitfalls*, Journal of the Optical Society of America B **22**, 2009 (2005).

[201] R. R. Tamming, C.-Y. Lin, J. M. Hodgkiss, S.-D. Yang, K. Chen, and C.-H. Lu, *Single 3.3-fs Multiple-Plate Compression Light Source in Ultrafast Transient Absorption Spectroscopy*, Research Square (2021).

[202] M. Bradler, P. Baum, and E. Riedle, *Femtosecond continuum generation in bulk laser host materials with sub-μJ pump pulses*, Applied Physics B: Lasers and Optics **97**, 561 (2009).

[203] N. Yarita, H. Tahara, T. Ihara, T. Kawawaki, R. Sato, M. Saruyama, T. Teranishi, and Y. Kanemitsu, *Dynamics of Charged Excitons and Biexcitons in CsPbBr3Perovskite Nanocrystals Revealed by Femtosecond Transient-Absorption and Single-Dot Luminescence Spectroscopy*, Journal of Physical Chemistry Letters **8**, 1413 (2017).

[204] M. Bradler and E. Riedle, *Temporal and spectral correlations in bulk continua and improved use in transient spectroscopy*, Journal of the Optical Society of America B **31**, 1465 (2014).

[205] A. L. Dobryakov, S. A. Kovalenko, A. Weigel, J. L. Pérez-Lustres, J. Lange, A. Müller, and N. P. Ernsting, *Femtosecond pump/supercontinuum-probe spectroscopy: Optimized setup and signal analysis for single-shot spectral referencing*, Review of Scientific Instruments **81** (2010).

[206] L. Blanchet, J. Réhault, C. Ruckebusch, J. P. Huvenne, R. Tauler, and A. de Juan, *Chemometrics description of measurement error structure: Study of an ultrafast absorption spectroscopy experiment*, Analytica Chimica Acta **642**, 19 (2009).

[207] P. Béjot, J. Kasparian, E. Salmon, R. Ackermann, and J. P. Wolf, *Spectral correlation and noise reduction in laser filaments*, Applied Physics B: Lasers and Optics **87**, 1 (2007).

[208] A. van de Walle, M. Hanna, F. Guichard, Y. Zaouter, A. Thai, N. Forget, and P. Georges, *Spectral and spatial full-bandwidth correlation analysis of bulk-generated supercontinuum in the mid-infrared*, Optics Letters **40**, 673 (2015).

[209] T. Godin, B. Wetzel, T. Sylvestre, L. Larger, A. Kudlinski, A. Mussot, A. Ben Salem, M. Zghal, G. Genty, F. Dias, and J. M. Dudley, *Real time noise and wavelength correlations in octave-spanning supercontinuum generation*, Optics Express **21**, 18452 (2013).

[210] A. L. Gaeta, *Catastrophic collapse of ultrashort pulses*, Physical Review Letters **84**, 3582 (2000).

[211] M. Klimczak, G. Soboń, K. Abramski, and R. Buczyński, *Spectral coherence in all-normal dispersion supercontinuum in presence of Raman scattering and direct seeding from sub-picosecond pump*, Optics Express **22**, 31635 (2014).

[212] M. Klimczak, G. Soboń, R. Kasztelanic, K. M. Abramski, and R. Buczyński, *Direct comparison of shot-to-shot noise performance of all normal dispersion and anomalous dispersion supercontinuum pumped with sub-picosecond pulse fiber-based laser*, Scientific Reports **6**, 1 (2016).

[213] R. L. Milot, G. E. Eperon, H. J. Snaith, M. B. Johnston, and L. M. Herz, *Temperature-Dependent Charge-Carrier Dynamics in CH3NH3PbI3 Perovskite Thin Films*, Advanced Functional Materials **25**, 6218 (2015).

[214] X. Chen, H. Lu, Y. Yang, and M. C. Beard, *Excitonic Effects in Methylammonium Lead Halide Perovskites*, The Journal of Physical Chemistry Letters **9**, 2595 (2018).

[215] K. Chen, A. J. Barker, F. L. C. Morgan, J. E. Halpert, and J. M. Hodgkiss, *Effect of Carrier*

Thermalization Dynamics on Light Emission and Amplification in Organometal Halide Perovskites, Journal of Physical Chemistry Letters (2015).

[216] J. M. Richter, F. Branchi, F. Valduga De Almeida Camargo, B. Zhao, R. H. Friend, G. Cerullo, and F. Deschler, *Ultrafast carrier thermalization in lead iodide perovskite probed with two-dimensional electronic spectroscopy*, Nature Communications **8**, 1 (2017).

[217] M. Cho, T. Brixner, I. Stiopkin, H. Vaswani, and G. R. Fleming, *Two dimensional electronic spectroscopy of molecular complexes*, Journal of the Chinese Chemical Society **53**, 15 (2006).

[218] A. H. Hamad, *Effects of Different Laser Pulse Regimes (Nanosecond, Picosecond and Femtosecond) on the Ablation of Materials for Production of Nanoparticles in Liquid Solution*, High Energy and Short Pulse Lasers (2016).

[219] P. Hariharan, *Basics of Interferometry*, Elsevier Inc., London, second edi edition, 2007.

[220] C.-H. Lu, T. Witting, A. Husakou, M. J. Vrakking, A. H. Kung, and F. J. Furch, *Sub-4 fs laser pulses at high average power and high repetition rate from an all-solid-state setup*, Optics Express **26**, 8941 (2018).

[221] V. Lucarini, J. Saarinen, K.-E. Peiponen, and E. Vartiainen, *Kramers-Kronig relations in Optical Materials Research*, Springer, Berlin, Heidelberg, first edition, 2005.

[222] T. Sai, M. Saba, E. R. Dufresne, U. Steiner, and B. D. Wilts, *Designing refractive index fluids using the Kramers-Kronig relations*, Faraday Discussions **223**, 136 (2020).

[223] J. C. Ku and J. D. Felske, *Determination of refractive indices of Mie scatterers from Kramers–Kronig analysis of spectral extinction data*, Journal of the Optical Society of America A **3**, 617 (1986).

[224] X. Ziang, L. Shifeng, Q. Laixiang, P. Shuping, W. Wei, Y. Yu, Y. Li, C. Zhijian, W. Shufeng, D. Honglin, Y. Minghui, and G. G. Qin, *Refractive index and extinction coefficient of CH_3NH_3PbI_3 studied by spectroscopic ellipsometry*, Optical Materials Express **5**, 29 (2015).

[225] T. G. Mayerhöfer and J. Popp, *Improving Poor Man's Kramers-Kronig analysis and Kramers-Kronig constrained variational analysis*, Spectrochimica Acta - Part A: Molecular and Biomolecular Spectroscopy **213**, 391 (2019).

[226] M. Kepenekian and J. Even, *Rashba and Dresselhaus Couplings in Halide Perovskites: Accomplishments and Opportunities for Spintronics and Spin-Orbitronics*, Journal of Physical Chemistry Letters **8**, 3362 (2017).

[227] D. Eimerl, L. Davis, S. Velsko, E. K. Graham, and A. Zalkin, *Optical, mechanical, and thermal properties of barium borate*, Journal of Applied Physics **62**, 1968 (1987).

[228] *United Crystals*, `https://www.unitedcrystals.com/BBOProp.html`, Accessed: 2021-01-15.

[229] J. K. Cooper, S. E. Reyes-Lillo, L. H. Hess, C. M. Jiang, J. B. Neaton, and I. D. Sharp, *Physical Origins of the Transient Absorption Spectra and Dynamics in Thin-Film Semiconductors: The Case of BiVO4*, Journal of Physical Chemistry C **122**, 20642 (2018).

[230] N. Menke, B. Yao, Y. Wang, W. Dong, M. Lei, Y. Chen, M. Fan, and T. Li, *Spectral relationship of photoinduced refractive index and absorption changes in fulgide films*, Journal of Modern Optics **55**, 1003 (2008).

[231] R. Kubo and M. Ichimura, *Kramers-Kronig relations and sum rules,* Journal of Mathematical Physics **13**, 1454 (1972).

[232] A. Rao, M. W. Wilson, S. Albert-Seifried, R. Di Pietro, and R. H. Friend, *Photophysics of pentacene thin films: The role of exciton fission and heating effects,* Physical Review B - Condensed Matter and Materials Physics **84**, 1 (2011).

[233] J. Puigdollers, C. Voz, A. Orpella, I. Martin, M. Vetter, and R. Alcubilla, *Pentacene thin-films obtained by thermal evaporation in high vacuum,* Thin Solid Films **427**, 367 (2003).

[234] T. Basché, S. Kummer, and C. Bräuchle, *Optical spectroscopy of single pentacene molecules in an ordered and a disordered p-terphenyl crystal,* Chemical Physics Letters **225**, 116 (1994).

[235] C. Sturm, D. Tanese, H. S. Nguyen, H. Flayac, E. Galopin, A. Lemaître, I. Sagnes, D. Solnyshkov, A. Amo, G. Malpuech, and J. Bloch, *All-optical phase modulation in a cavity-polariton Mach-Zehnder interferometer,* Nature Communications **5**, 1 (2014).

[236] A. Gelzinis, R. Augulis, V. Butkus, B. Robert, and L. Valkunas, *Two-dimensional spectroscopy for non-specialists,* Biochimica et Biophysica Acta - Bioenergetics **1860**, 271 (2019).

[237] H. Kuramochi, S. Takeuchi, and T. Tahara, *Femtosecond time-resolved impulsive stimulated Raman spectroscopy using sub-7-fs pulses: Apparatus and applications,* Review of Scientific Instruments **87** (2016).

[238] P. C. Tapping, Y. Song, Y. Kobayashi, G. D. Scholes, and T. W. Kee, *Two-Dimensional Electronic Spectroscopy Using Rotating Optical Flats,* Journal of Physical Chemistry A **124**, 1053 (2020).

[239] G. Chang and Z. Wei, *Ultrafast Fiber Lasers: An Expanding Versatile Toolbox,* iScience **23**, 101101 (2020).

[240] *Lasers for industry: Tangor,* `https://amplitude-laser.com/products/lasers-for-industry/tangor/`, Accessed: 2021-02-15.

[241] K. Chen, J. K. Gallaher, A. J. Barker, and J. M. Hodgkiss, *Transient grating photoluminescence spectroscopy: An ultrafast method of gating broadband spectra,* Journal of Physical Chemistry Letters **5**, 1732 (2014).

[242] D. P. Khatua, S. Gurung, A. Singh, S. Khan, T. K. Sharma, and J. Jayabalan, *Filtering noise in time and frequency domain for ultrafast pump-probe performed using low repetition rate lasers,* Review of Scientific Instruments **91** (2020).

[243] F. Korte, S. Adams, A. Egbert, C. Fallnich, A. Ostendorf, S. Nolte, M. Will, J.-P. Ruske, B. Chichkov, and A. Tuennermann, *Sub-diffraction limited structuring of solid targets with femtosecond laser pulses,* Optics Express **7**, 41 (2000).

[244] J. Singh and S. Thakur, *Laser-Induced Breakdown Spectroscopy,* Elsevier B.V., Oxford, 2007.

[245] M. Hashmi, editor, *Comprehensive Materials Processing - 13 volume set,* Elsevier Ltd., Oxford, 2014.

[246] Q. McCulloch, J. G. Gigax, and P. Hosemann, *Femtosecond Laser Ablation for Mesoscale Specimen Evaluation,* Jom **72**, 1694 (2020).

[247] S. Döring, S. Richter, A. Tünnermann, and S. Nolte, *Influence of pulse duration on the hole formation*

during short and ultrashort pulse laser deep drilling, Frontiers in Ultrafast Optics: Biomedical, Scientific, and Industrial Applications XII **8247**, 824717 (2012).

[248] G. T. Reed, G. Mashanovich, F. Y. Gardes, and D. J. Thomson, *Silicon optical modulators*, Nature Photonics **4**, 518 (2010).

[249] M. C. Estevez, M. Alvarez, and L. M. Lechuga, *Integrated optical devices for lab-on-a-chip biosensing applications*, Laser and Photonics Reviews **6**, 463 (2012).

[250] Y. Wang, F. Zhang, X. Tang, X. Chen, Y. Chen, W. Huang, Z. Liang, L. Wu, Y. Ge, Y. Song, J. Liu, D. Zhang, J. Li, and H. Zhang, *All-Optical Phosphorene Phase Modulator with Enhanced Stability Under Ambient Conditions*, Laser and Photonics Reviews **12**, 1 (2018).

[251] S. Reineke, M. Thomschke, B. Lüssem, and K. Leo, *White organic light-emitting diodes: Status and perspective*, Reviews of Modern Physics **85**, 1245 (2013).

[252] A. Kellerer, S. Wright, and S. Lacour, *Coherence and information in a fiber interferometer*, American Journal of Physics **85**, 6 (2017).

[253] I. Mingareev, D. Wortmann, A. Brand, and A. Horn, *Time-resolved white-light interferometry for ultrafast metrology*, AIP Conference Proceedings **1278**, 891 (2010).

[254] M. Yue, L. Yan, Y. Xu, V. Nguyen, and T. Chen, *Intense and Collimated Supercontinuum Generation Using Microlens Array*, IEEE Photonics Technology Letters **29**, 2031 (2017).